Multifractal analysis and simulation of wind energy fluctuations

George Fitton

UNIVERSITÉ PARIS-EST

laboratoire eau environnement systemes urbains

École des Ponts ParisTech

Thèse présentée pour obtenir le grade de

Docteur de l'Université Paris-Est

Spécialité : Sciences et Techniques de l'Environnement

par

George Fitton

Ecole Doctorale : SCIENCES, INGENIERIE ET ENVIRONNEMENT

Analyse multifractale et simulation des fluctuations de l'énergie éolienne

Multifractal analysis and simulation of the fluctuations of wind energy

Thèse soutenue le 16/09/13 devant le jury composé de :

Annick Pouquet	*Rapporteur*
Joachim Peinke	*Rapporteur*
Peter Tavner	*Rapporteur*
Yuli Chashechkin	*Examinateur*
Philippe Drobinski	*Examinateur*
Ioulia Tchiguirinskaia	*Co-encadrant*
Daniel Schertzer	*Directeur de thèse*

I would like to dedicate this thesis to my loving family... specifically[1]
Mum, Dad, Grace-Case and Goldi

[1] A shout-out also to Venky, Hubert and Yeng Feng, Plant-pot, Soggy, Cookie and Lee-Lee who have all, if indirectly, helped to motivate me.

Acknowledgements

Thank you to all of my colleagues at LEESU for their support. You are my second family. A thank you also to Annick Pouquet, Joachim Peinke and Peter Tavner for not only finding the energy to read this lengthy piece but for also providing me with some insightful additions.

A special thank you to Daniel and Ioulia who have challenged me and 'encouraged' me throughout my time here. I have learnt a great deal from you both at the sacrifice sometimes of my sanity. Thank you for that.

This research is part of the EU-FP7 ITN WAUDIT (http://www.waudit-itn.eu).

Abstract

Renewable energy is the new black. Countries all over the world are investing in renewable energy solutions in a bid to become sustainable. Wind energy is one of the major contributors to this green revolution with an annual increase of around 20%. Although this increase is indeed impressive, wind energy is still unable to compete against cheap fossil fuels. With current technologies, extracting energy (or torque) from the wind is difficult, intermittent and unpredictable in many respects. This unpredictability makes it - even now - a risky industry to invest in.

The european union would like to reduce the uncertainties in wind resource assessment and forecasting to below 3% by 2030. If this is managed wind energy will be competitive. Among the wide range of multidisciplinary topics on wind energy technology, the European Technology Platform for Wind Energy identifies wind conditions as one of the key thematic areas for the development of future research activities in the sector. This term should encompass all of the relevant wind aspects that have an impact on the economic and technical feasibility of a wind farm deployment, notably: wind resource, turbulence characteristics (intensity, spectra as well as higher order statistics) and wind shear extremes.

A common way to evaluate the wind conditions of a test site is to place wind-measuring masts in the potential turbine locations. The potential power is then estimated with the combination of mast-based measurements, numerical engineering models and a significant portion of field experience. The latter is motivated mainly by the unreliability of the numerical models; models originally developed for mildly complex terrain under neutral atmospheric conditions.

In this dissertation we have made use of two such atmospheric wind measurement campaigns from two very topographically different nest sites: the German Growian experiment in a near homogenous terrain setting and the French Ersa wind park experiment where measurements were taken from within a wind farm on top of a mountain in Corsica. Both sites are subject to convective sea breezes

and both exhibit wind shear distributions where even coarse time-scale extremes are much more frequent than those previously predicted by Gaussian distributions. These frequent intermittent bursts are the major source of wind energy's unpredictability and the reason there are mechanical overloads, deviations from expected power production and large short-time power fluctuations.

From the governing equations of the velocity field, one can not only expect a (highly) non-Gaussian wind but also one that is scaling. By scaling we mean a given (statistical) self-similarity; a turbulent cascade of eddies. Stochastic multifractals (with multiple singularities and co-dimensions) easily reproduce the scaling, heavy-tailed probabilities that are ubiquitous with the wind and essential to quantify for the wind energy community. The few parameters that define these models can be derived either from theoretical considerations or from statistical data analysis.

For multifractal data analyses, the main aim is to determine the statistics of the velocity shears. It is sometimes possible to do this with the universal multifractal (UM) parameters: α - the index of multifractality ($0 \leq \alpha \leq 2$), C_1 - the co-dimension of the mean intermittency ($C_1 \geq 0$) and H - the degree of non-conservation. The latter of the three parameters is often called the Hurst exponent. We inter-compare the results from the rather standard method of empirical estimation of the UM parameters, the Double Trace Moment (DTM) method, with that of the Double Structure Function (DSF), a newly developed method.

We found that flux proxies based on the modulus of the wind velocity shears yield non-scaling statistical moments and therefore spurious multifractal parameter estimates. DSF does not require this proxy approximation thus providing parameters that describe the non-linearity of the structure-function to an extent. We found no truly stable estimate of alpha using standard methods. Moreover, the apparent agreement of the departure of the semi-analytic function with that of the empirical at the theoretically predicted order for a finite sample is not linear, contradictory to the classical UM theory.

This no longer occurs when we locally optimise (by fractionally differentiating) the DTM scaling behaviour. We then obtain very stable estimates of the multifractality index that are furthermore consistent (smaller than two) with other literature. On the contrary, the two other parameters (C_1 and H) become non-

linear functions of the order q of the statistical moments. These results suggest that the isotropic UM model cannot be used to reproduce the velocity shears in the atmospheric surface-layer.

To investigate the above hypothesis we use a rotated frame of reference to analyse the anisotropy of the horizontal velocity in the atmospheric surface-layer. This enables us to quantify the angular dependency of a Hurst exponent. Despite being anisotropic the Hurst exponent is consistent with other surface-layer literature. For time-scales above a few seconds, both data exhibit a strong, scaling anisotropy that decreases with height. We put forward an analytical expression for the angular variation of the Hurst exponent based on the correlation of the horizontal components. It determines the generation of wind shear extremes, including those in the wake of a turbine. We find that the turbulent wind shears are so extreme that their probability distributions follow a power law. The corresponding exponent (q_D) is rather the same in both sites at 50m heights ($4 \leq q_D \leq 5$), inspite of very different orographic conditions. We also discuss its consequences when analysing the stability of the atmospheric boundary-layer and propose a new method for its classification.

Finally, we analytically demonstrate that anisotropy increases the extremes' probability. This finding reveals one of the many possible turbulence mechanisms in the atmospheric surface-layer that may seemingly over-generate wind shear extremes if they are studied in an isotropic UM framework. We theoretically analyse the consequences of this on the UM estimates for the DTM method. The obtained analytical results fully support empirical findings. We then discuss how to take into account all of these considerations when simulating multifractal fields of the wind in the atmospheric boundary-layer. The overall results of this dissertation go beyond wind energy, they open up new perspectives for the theoretical predictions of extremes in the general case of strongly correlated data.

Keywords

wind energy, atmospheric turbulence, multifractal intermittence, surface-layer stability, anisotropy, extremes

Résumé

Les énergies renouvelables sont à la mode. Partout dans le monde les pays investissent dans ces énergies pour devenir durables. Avec une croissance annuelle d'environ 20%, l'énergie éolienne est un des principaux acteurs de cette révolution verte. Bien que cette augmentation soit impressionnante, l'énergie éolienne ne parvient toujours pas à être compétitive face aux combustibles fossiles bon marché. Avec les technologies actuelles, extraire l'énergie du vent est difficile, intermittent et imprévisible à bien des égards. Cette imprévisibilité fait de l'énergie éolienne - même maintenant - un investissement risqué.

L'Union européenne voudrait réduire les incertitudes à moins de 3% à l'horizon 2030 dans l'évaluation et la prévision des ressources éoliennes. Cela permettrait à l'énergie éolienne d'être enfin compétitive. Parmi la vaste gamme de sujets pluridisciplinaires sur la technologie éolienne, la Plate-forme Technologique européenne pour l'énergie éolienne identifie 'les conditions du vent' comme une des thématiques clés pour le développement des futures activités de recherche dans le domaine. Ce terme devrait englober tous les aspects du vent qui ont un impact sur la faisabilité économique et technique d'un parc éolien, notamment: la ressource, les caractéristiques de turbulence et les cisaillements extrêmes.

Un moyen classique d'évaluation du potentiel éolien sur un site choisi consiste à installer des mâts météorologiques dans les emplacements potentiels d'éoliennes. Dans cette thèse, nous avons exploité des mesures de vents atmosphériques réalisés pendant deux compagnes sur deux sites topographiquement très différents: Growian en Allemagne sur un terrain à peu près plat, et le parc éolien Ersa, où les mesures ont été prises entre les éloliennes situées au sommet d'une montagne en Corse (France). Les deux sites sont soumis à des brises de mer convectives et présentent des distributions de cisaillement où même à basse résolution les extrêmes sont plus fréquents que ceux précédemment prévus avec des distributions Gaussienne. Ces fréquentes poussées intermittentes de vent sont la principale cause de l'imprévisibilité de l'énergie éolienne et la raison sous-jacente

aux surcharges mécaniques, aux écarts entre production d'énergie attendue et mesurée, ainsi qu'aux fluctuations importantes de puissance sur de courtes durées.

A partir des équations gouvernant le champ de vitesse, on peut non seulement s'attendre à un vent (fortement) non-gaussien, mais aussi à un vent présentant un comportement scalant. Par scalant' ou invariant d'échelle, nous faisons référence à un comportement statistique auto-similaire particulier; les cascades de tourbillons. Les multifractales stochastiques (avec des singularités et des co-dimensions multiples) reproduisent facilement le comportement scalant et les distributions de probabilités à queues épaisses omniprésentes dans le vent et dont la quantification est essentielle pour la communauté. Les quelques paramètres qui définissent ces modèles peuvent êtres déduits soit de considérations théoriques, soit de l'analyse statistique de données.

Il est parfois possible de caractériser les statistiques de cisaillement du vent à l'aide des paramètres des multifractals universelles (UM) : α - l'indice de multifractalité ($0 \leq \alpha \leq 2$), C_1 - la co-dimension de l'intermittence moyenne ($C_1 \geq 0$) et H - le degré de non-conservation. Le dernier des trois paramètres est souvent appelé exposant de Hurst. Nous comparons les résultats issus des estimations empiriques des paramètres UM via la méthode plutt standard du Double Moment Trace (DTM), avec celle nouvellement développée de la Double Fonction de Structure (DSF).

Nous avons constaté que les approximations de flux basées sur le module du cisaillement du vent donnent des moments statistiques non-scalants et donc des estimations faussées des paramètres multifractals. La méthode DSF n'exige pas cette approximation et garantit un comportement scalant sur une certaine gamme d'échelles. Nous n'avons trouvé aucune estimation véritablement stable de α en utilisant des méthodes standards. Ceci n'arrive plus quand nous optimisons localement (par la différenciation fractionnaire) le comportement scalant du DTM. Nous obtenons alors des estimations très stables de l'indice de multifractalité qui sont en outre en accord ($\alpha \leq 2$) avec des résultats publiés. Au contraire, les deux autres paramètres (C_1 et H) deviennent des fonctions non-linéaires de l'ordre q des moments statistiques. Ces résultats suggèrent que le modèle UM isotrope ne peut être utilisé pour reproduire le cisaillement de vent dans la couche de surface atmosphérique.

Lesdites hypothèses sont examinées en utilisant un repère tournant pour analyser

l'anisotropie de la vitesse horizontale dans la couche de surface atmosphérique. Cela permet de quantifier la dépendance angulaire de l'exposant de Hurst. Les valeurs de cet exposant restent tout de même conformes aux résultats précédemment publiés. Pour des échelles de temps supérieures à quelques secondes, les deux jeux de données présentent une anisotropie scalante forte, qui décrot avec l'altitude. Nous mettons en évidence une expression analytique de la variation angulaire de l'exposant de Hurst, reposant sur les corrélations entre les composantes horizontales. Ceci pilote la formation des extrêmes du cisaillement, y compris dans le sillage d'une éolienne. Les cisaillements turbulents du vent sont si extrêmes que leur loi de probabilité est une loi de puissance. L'exposant correspondant (q_D) est similaire pour les deux sites à une hauteur de 50m ($4 \leq q_D \leq 5$), malgré des conditions orographiques très différentes. Nous discutons aussi de ses conséquences en analysant la stabilité de la couche limite atmosphérique et proposons une nouvelle méthode pour sa classification.

Enfin, nous démontrons analytiquement que l'anisotropie augmente la probabilité des extrêmes. Ce résultat met en lumière un des nombreux mécanismes de turbulence possibles dans la couche de surface qui peut apparemment surproduire les cisaillements extrêmes du vent, s'ils sont étudiés dans le cadre des UM isotropes. Nous en analysons théoriquement les conséquences sur les estimations des paramètres multifractales par la méthode DTM. Les résultats analytiques obtenus sont en parfait accord avec les observations empiriques. Nous discutons alors de la prise en compte de toutes ces considérations pour faire des simulations multifractales des champs du vent dans la couche limite atmosphérique.

Les résultats de cette thèse vont au-delà de la question de l'énergie éolienne. Ils ouvrent de nouvelles perspectives sur les prévisions théoriques d'extrêmes dans le cas général de données fortement corrélées.

Mots Clés

énergie éolienne, turbulence atmosphérique, intermittence multifractale, stabilité de la couche-limit, anisotropie, extrêmes

Contents

Chapter 1

1.1 The Challenge In Wind Resource Assessment: Turbulence

Although the effects of wakes add additional complexity to the problem, the wind energy community is facing the same problems as the turbulence community. This can easily be seen by considering the state of art wind resource assessment deliverable D7 (Rodrigo [2011]). The conclusions of the report use the results from a survey of 72 wind analysts from 48 different organisations to highlight problematic areas in the wind industry. A comparison of these conclusions with the "*recent advances and key issues in wall-bounded turbulence*" discussed in Marusic et al. [2010] confirms there is an overlap of joint issues that question:

- the existence of universal principal model parameters as a result of the advent of new methods that provide higher resolution more reliable data (through remote sensing and post-processing techniques),
- the validity of approximations to Reynolds stresses and whether they represent micro-scale wind conditions and extremes and
- the effect of non-neutral stability effects and complex topographical features.

An appropriate response would be to now focus on the state of art in statistical turbulence modelling, listing the advantages and disadvantages of applying such

methods to these sort of problems. This is appropriate because the key ideas in statistical turbulence modelling were developed over 50 years ago (see §1.2) and are well established within the turbulence community. Moreover, one would expect the wind energy community to also be well aware of the alternatives to the Reynolds decomposition given the explicit relationship between the two areas of research, i.e. the wind.

In reality we find there is an apparent lack of even the most basic statistical approaches to the aforementioned problems, a blind dependency on the results of numerical simulations that seems to have been fast translated from the numerical weather prediction (NWP) community.

A fine example of this is in the very questionnaire that we have used to highlight the joint issues being faced between both communities. In the list of questions we find three categories: numerical modelling, physical modelling and field measurements for validation. Although some of the questions within each category are indirectly related to statistical mechanics it is clear 'statistical methods' is a category of atmospheric science that is either unheard of, or not regarded as, one of sufficient importance to be included. The irony of this situation is that the very area of research that is left out, is the very area that is the most feasible option for obtaining a real solution to the aforementioned problems. It is therefore for this reason that we have endeavoured to give a more pedagogical discussion in what follows.

The Need For Higher Resolutions

Although being left out of a questionnaire is not of great importance, the fact is that similar opinions are reflected throughout the wind energy community. Most commercial, site nesting, models are slightly modified versions of NWP models (see §1 of Holmes [2011] for an overview of current models). Due to computational expenses, NWP models are forced to truncate the space-time scales of simulations resulting in a somewhat ad-hoc parameterisation of the unresolved scales. This same parametrisation of unresolvable scales has also been refashioned into the wind energy community in the form of the so called 'turbulence intensity' (TI) (Wallbank [2008]). A second order approximation (typically done on ten-

minute supervisory control and data acquisition (SCADA) measurements) that is accepted as a sufficient means by which to quantify extreme wind velocities. For the NWP community a parameterisation like this *may* be deemed acceptable because the typical space-time scales being resolved (greater than 1km by 1 day) are assumed *not* to be greatly influenced by a second order approximation.

It fast became clear that the scales being resolved by such models and the necessary parameterisation of small-scale velocity fluctuations do not correspond to the scales needed to model wind turbines (see for example Schertzer et al. [2011]). Wind turbines have blades of length and width in the order of metres interacting with strong intermittent wind increments that have been shown (Fitton et al. [2011b]) to fluctuate wildly at resolutions of Hertz's let alone minutes or even days. In response to this the wind industry has focused on obtaining better predictions with higher resolution models. The solution to this problem then becomes dependent on the latest and most innovative cluster of processors. One benefit of this initiative is the need for higher resolution boundary and initial condition data. This in turn has led to higher resolution measurements which in turn has allowed us to highlight the extreme variability of the wind.

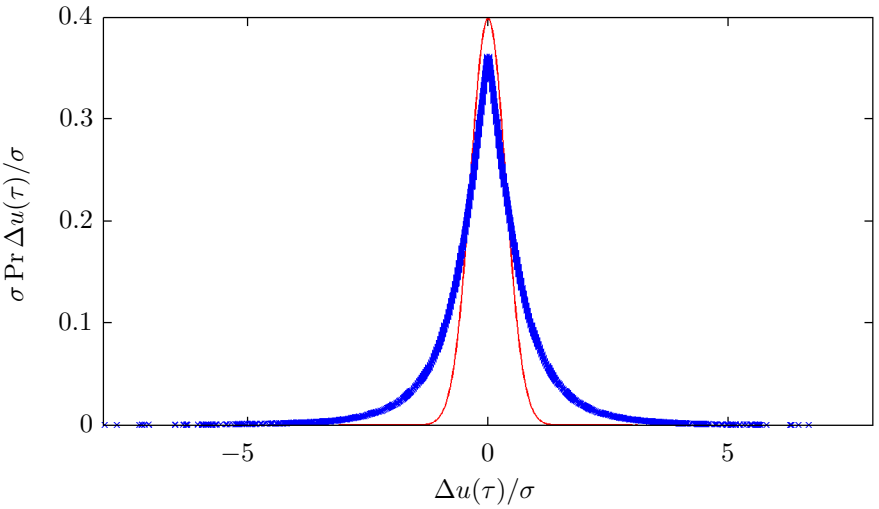

Figure 1.1: Empirical probability distribution (blue crosses) of the normalised horizontal velocity increments, $\Delta u(\tau)/\sigma$ (the velocity increments are defined as $\Delta \boldsymbol{u}(\tau) = \boldsymbol{u}(t+\tau) - \boldsymbol{u}(t)$), measured in a high-resolution experimental campaign at a wind turbine test site in Corsica. Red solid line is the corresponding Normal distribution, $\mathcal{N}(\mu, \sigma^2)$, for the sample mean, μ, and the variance, σ^2.

Figure 1.1 displays the (heavy-tailed) probability distribution of the time increments of the horizontal wind velocity. The winds were measured in a high-resolution experimental campaign at a wind turbine test-site in Corsica (for details see §2.1). The heavy tails are a result of the large ratio of scales i.e. a high sampling frequency and a long sampling run (over one hour of measurements at 10Hz). Observing the same heavy tails with SCADA data would require nearly a continuous year of measurements. An easy way to check whether the tails of a distribution are heavy is to plot the logarithm of the probability.

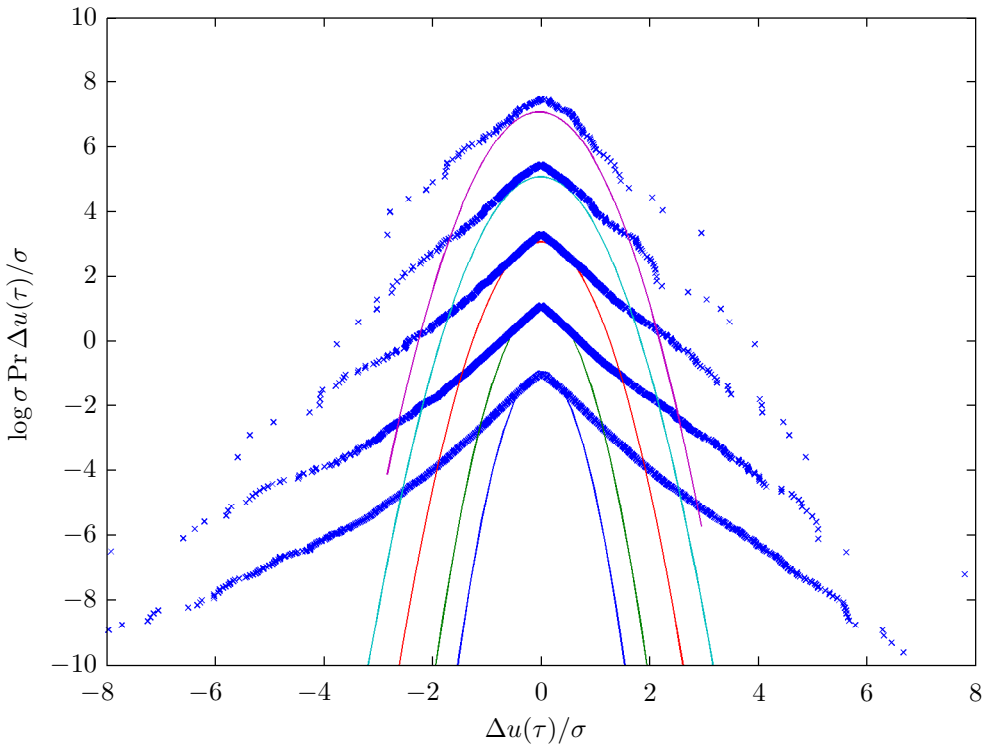

Figure 1.2: Same distribution as in figure 1.1 but with a logarithmic vertical axis and for increasing time-scales: $\tau = 0.1, 0.4, 1.6, 6.4$ seconds.

Figure 1.2 plots the same distribution but for log-probabilities. In addition we have upscaled the data through temporal averaging in order to show that the heavy tails are persistent in time. As the resolution is decreased up to the final lowest resolution (upper-most plot at 6.4 seconds), the empirical data 'appears' to better fit the normal distribution curve due to the lack of extreme events (a result of the smoothing effect from the averaging procedure).

A Matter Of Scales

In the previous section we defined three areas that require significant development. But why, if the governing equation of the problem does not change, is there a separation of focus on the development of a better solution? Why can't we find a solution to three-dimensional fluid flow? Starting first with the latter of the two questions, the answer is given typically by example. Since there is no known (as of yet) analytical solution to the governing equation of fluid flow – the Navier-Stokes equation – a popular alternative is to numerically approximate the time-evolution. In the atmosphere, the Reynolds Number, Re, is usually estimated to be 10^{12}. This estimate can be obtained by using the following relation

$$Re \approx (L/\ell_K)^{4/3}$$

and considering the horizontal scaling range as ranging from the dissipation/Kolmogorov scale ($\ell_K \approx 1$ millimetre) to planetary scales ($L \approx 10^4$ kilometres). The number of grid points therefore required to completely compute the flow in three dimensions is the cube of this, i.e. 10^{36} grid points. Given the largest direct numerical simulation (DNS) to date (Yokokawa et al. [2002]) was done on 10^{11} grid points for up to five times the eddy turnover time, to follow the evolution of all of the details would take many thousands of years on even the fastest modern computers.

Thus, we find direct numerical simulation is confined to flows of relatively small Reynolds numbers with relatively simple geometry. In order to fit the models into a given volume there is a requirement to make a compromise between acceptable resolutions and simulation run-times. This is typically done by truncating the space-time scales and approximating the remaining unresolved scales using one of the following models Speziale [2011]:

1. *Reynolds-stress models, allow for the calculation of one-point first and second moments such as the mean velocity, mean pressure, and turbulent kinetic energy.*
2. *sub-grid scale models for large-eddy simulations, wherein the large, energy-containing eddies are computed directly and the effect of*

the small scales – which are more universal in character – are modelled.

3. *two-point closures or spectral models, which provide more detailed information about the turbulence structure, since they are based on the two-point velocity correlation tensor.*

With any of the above methods the 'closure of the system' is the outstanding difficulty i.e. there are more unknowns than there are equations (see for example Tsinober [1993]). In other words the order of information produced by the model will never exceed the order of information that is input. Since the models in question 'in general' do not resolve all of the scales of the system, we find the numerical models are adjusted to fit space-time resolutions that maximise the information for different flow scenarios. It is here therefore that we find the answer to the first of our questions: why, if the governing equation of the problem does not change, is there a separation of focus on the development of a better solution? Scale dependency.

What Is The Alternative?

We discussed how traditional numerical approaches are forced to truncate their scales by transforming partial differential equations (PDEs) into (more easily solvable) ordinary differential equations (ODEs) that implicitly impose regularity and homogeneity assumptions through parameterisation methods. The problem encountered with these assumptions is the violation of the fundamental symmetries of the non-linear PDEs that thus leads to a reduction in variability. This then questions the relevance of the resulting numerical codes because their range of scales are different from those of the observations.

Multifractals on the other hand are independent of scale providing the velocity field scales as a power law. This allows us to understand and to model extremely variable space-time fields over wider (if not all) ranges of scales, thus accounting for extreme events or gusts. However, before delving into the intricacies of the universal multifractal (UM) framework (§4.1) we will attempt to summarise some of the main ideas that led to its development (see also Fitton).

Governing PDE

The equation that governs turbulence is generally referred to as the Navier-Stokes equation (1823) and is essentially the extension of the basic symmetries of Newton's laws for continuum media:

$$\frac{\partial \boldsymbol{u}}{\partial t} + (\boldsymbol{u} \cdot \nabla)\boldsymbol{u} = -\nabla p + \nu \nabla^2 \boldsymbol{u} + \boldsymbol{f}, \tag{1.1}$$

where $\boldsymbol{u}$ is the velocity vector, with components (u, v, w), which, in general, depend on the three spatial coordinates, (x, y, z), of the position vector $\boldsymbol{r}$, and time t; p is the reduced or kinematic pressure (i.e. pressure divided by density ρ considered as constant, according to an acceptable approximation in the boundary layer), ν is the kinematic viscosity and $\boldsymbol{f}$ represents the body forces acting on the fluid. Since we will consider only atmospheric flows with velocities much smaller than the speed of sound, we also have the incompressibility condition:

$$\nabla \cdot \boldsymbol{u} = 0.$$

Although the elementary properties of the solutions (including existence and uniqueness) of the Navier-Stokes equations are still unknown, their symmetries have been considered for a while, see in particular Sedov [1972], Frisch [1980].

Symmetries

The Navier-Stokes equation has the following six known symmetries:

1. Space-translations: $t, \boldsymbol{r}, \boldsymbol{u} \mapsto t, \boldsymbol{r} + \ell, \boldsymbol{u}, \ \ \ell \in \mathbb{R}^3$
2. Time-translations: $t, \boldsymbol{r}, \boldsymbol{u} \mapsto t + \tau, \boldsymbol{r}, \boldsymbol{u}, \ \ \tau \in \mathbb{R}$
3. Galilean transformations: $t, \boldsymbol{r}, \boldsymbol{u} \mapsto t, \boldsymbol{r} + \boldsymbol{U}t, \boldsymbol{u} + \boldsymbol{U}, \ \ \boldsymbol{U} \in \mathbb{R}^3$
4. Parity: $t, \boldsymbol{r}, \boldsymbol{u} \mapsto t, -\boldsymbol{r}, -\boldsymbol{u}$.
5. Rotations: $t, \boldsymbol{r}, \boldsymbol{u} \mapsto t, R\boldsymbol{r}, R\boldsymbol{u}, \ \ R \in \mathrm{SO}(3, \mathbb{R})$
6. Scaling: $t, \boldsymbol{r}, \boldsymbol{u} \mapsto e^{1-a}t, e\boldsymbol{r}, e^a\boldsymbol{u}, \ \ e \in \mathbb{R}_+, \ \ a \in \mathbb{R}$

The symmetries (1-4) can be merely understood as direct consequences of the Galilean invariance of the Navier-Stokes equation. The scaling symmetry is formally rather straightforward for infinite Reynolds numbers and no forcing i.e. $\nu = 0$ and $f = 0$ (Frisch [1980]). However, it can also be argued (Herring et al. [1982], Lilley et al. [2004]) that this also applies to non-zero eddy/renormalised viscosity and forcing, without keeping the Reynolds number constant contrary to Sedov [1972]. Let us also mention that a more systematic way to find the appropriate scaling symmetries, including anisotropic scaling ones, of a differential system can be obtained with the help of the pullback transforms of the field and the differential operators generated by (possibly generalised) dilations/contractions of the space (Schertzer et al. [2011]).

Conservation Laws

We have seen in the previous section that for an infinite Reynolds number, no forcing and constant density, the equations of hydrodynamic turbulence are scaling under isotropic scale changes (symmetry 6). Consider now the energy flux whose density is given by:

$$\varepsilon = -\frac{1}{2}\frac{\partial}{\partial t}(\boldsymbol{u}\cdot\boldsymbol{u}). \tag{1.2}$$

Under the same conditions we find the energy flux density is conserved by the non-linear 'inertial' terms (see appendix A.1). This is important because we will be interested in situations where these terms are dominant. The dominance of the terms are classically estimated by the ratio of the non-linear term and the dissipative (viscous) term in the Navier-Stokes equation using the 'Reynolds' number

$$Re \sim \frac{\text{Non-linear terms}}{\text{Linear damping}} \sim \frac{U\cdot L}{\nu}$$

where U is a 'typical' horizontal velocity of the largest scale motions and L is the corresponding 'outer' scale. The Reynolds number is the non-linear 'coupling constant' for the problem. Since Re is usually estimated to be 10^{12} (as previously calculated) we may anticipate, in this strong coupling limit, that many standard methods such as perturbation techniques (which work by solving the easy linear

problem and treating the non-linear term as a perturbation) will not converge.

1.2 A Statistical Approach To Turbulence

At the beginning of the 20$^{\text{th}}$ century, V. Bjerknes (1904) and then L. F. Richardson (1922) laid the first blueprints for combining the equations of thermodynamics with those of hydrodynamics in the form of a closed set of governing non-linear partial differential equations. At roughly the same time an alternative stochastic 'turbulent' approach was being developed by Taylor (1920), Richardson (1926), Kolmogorov (1930) and others (see both Davidson et al. [2011] and Lovejoy and Schertzer [2013a] for a more in-depth historical background). The idea behind this was that just as in statistical mechanics where huge numbers of degrees of freedom exist, only certain 'emergent' macroscopic qualities are of interest. In the corresponding turbulent systems therefore, new theories sought to discover emergent laws that in principle could be characterised by simple statistical quantities, such as averages, probability distribution functions, spectra, correlations, etc.

The first person to discover one of these laws was Lewis Fry Richardson (1926). In an experiment using two small balloons releasing seeds *simultaneously* at different distances apart, he derived a general law in which the rate of increase of the square of the separation (i.e. the rate of diffusion) between objects diffusing on a turbulent stream increases in proportion to the separation raised to the power 4/3, i.e.,

$$D(L) \propto L^{4/3},$$

or equivalently $\nu(L) = KL^{4/3}$ where $D(L)$ and $\nu(L)$ are the mass and momentum diffusivity (viscosity) respectively, related through the Schmidt number at scale L; K is a constant of proportionality.

The result of this discovery was conclusive evidence that turbulent motion was unlike that of molecular motion in that it was contained in the motion of eddies with many length scales and that in the limit of small viscosity the trajectories cease to be deterministic and other methods of analysis are needed. Understanding this non-determinism properly requires the understanding of the

zero-viscosity limit. It was this very question that was the precursor to the law of 3D isotropic homogeneous turbulence (Kolmogorov [1941a] and Kolmogorov [1941b]).

Although Richardson's discovery was of great importance, it was the audacity with which he conceived a unique scaling (power) law (i.e. a law without characteristic length scales) that could operate from millimetres to thousands of kilometres, that was of the greatest significance. In accordance with this, Richardson believed that the corresponding diffusing particles had 'Weierstrass function like' (i.e. fractal) trajectories (see section §3.1). In fact in the very same pioneering book "*Weather Prediction by Numerical Process*" (Richardson [2007], reprinted version) in which he essentially wrote down the modern equations of the atmosphere (Lynch [2006]) and attempted a manual integration; he also slyly inserted the following –

"Big whorls have little whorls,
Which feed on their velocity;
And little whorls have lesser whorls,
And so on to viscosity
-in the molecular sense."

–implying the notion of cascades seldom left his thoughts. It is thanks to this now iconic poem, Richardson, is often considered the grandfather of the modern cascade theories. Had Richardson been encumbered by the later notions of the mesoscale, or of isotropic turbulence in either two or three dimensions, he might never have discovered his law.

The Kolmogorov Self-Similarity Hypothesis (K41)

In 1941, inspired by Richardson's energy cascade, Andrei Kolmogorov (Kolmogorov [1941a] and Kolmogorov [1941b]) made claim to the famous 5/3 law. He assumed that with each step in the energy transfer to smaller and smaller scales, the anisotropic influence of the large scales would be gradually lost, such that at sufficiently small scales the distribution of increments would be statistically homogeneous and isotropic (see appendix A.2). This steady situation,

characterised by a mean flux of energy $\langle\varepsilon\rangle = \bar{\varepsilon}$, was postulated by Kolmogorov to be universal and determined by only one parameter, $\bar{\varepsilon}$. With respect to Richardson's 4/3 law, Kolmogorov's contribution was to find a proportionality constant, K, that depends on the mean energy flux density i.e. $K = \bar{\varepsilon}^{1/3}$.

Kolmogorov's 2/3 Law

Kolmogorov formulated his famous heuristic scaling theory of the inertial range in turbulence, with the help of the second-order structure function.

> *In a turbulent flow at very high Reynolds number, the mean-square velocity increment $\left\langle \Delta\boldsymbol{u}(\ell)^2 \right\rangle$ between two points separated by a distance ℓ behaves approximately as the two-thirds power of the distance.*

Thus, the second-order structure function is defined somewhat heuristically as the second-order moment, of the ensemble average, of the velocity increment separated by a distance ℓ:

$$S_2(\ell) \equiv \left\langle \Delta\boldsymbol{u}(\ell)^2 \right\rangle = \left\langle (\boldsymbol{u}(\boldsymbol{r}+\ell) - \boldsymbol{u}(\boldsymbol{r}))^2 \right\rangle. \tag{1.3}$$

Under Kolmogorov's second universality assumption, in the limit of infinite Reynolds number, the statistics of turbulence depend only on the length scale ℓ and the mean energy flux density $\bar{\varepsilon}$. Dimensional analysis (remembering equation 1.2 gives $\varepsilon \propto \boldsymbol{u}^2/\tau = \boldsymbol{u}^2/(\ell/\boldsymbol{u}) = \boldsymbol{u}^3/\ell$) of equation 1.3 thus yields

$$S_2(\ell) = C(\bar{\varepsilon}\ell)^{2/3} \tag{1.4}$$

where C is a universal constant.

The Energy Spectrum

The second-order structure function, equation 1.3, is a special case in that it can be expressed in terms of the auto-correlation function

$$R(\ell) = \langle \boldsymbol{u}(\boldsymbol{r}+\ell) \cdot \boldsymbol{u}(\boldsymbol{r}) \rangle \propto \ell^{2H},$$

where H is a measure of correlation. Using the Wiener-Khinchin theorem

$$R(\ell) = \mathcal{F}(E(k)) \text{ i.e. } \langle \boldsymbol{u}(\boldsymbol{r}+\ell) \cdot \boldsymbol{u}(\boldsymbol{r}) \rangle = \int_{-\infty}^{\infty} e^{-ik\ell} \cdot E(k) \cdot dk.$$

The second-order structure function is then

$$\begin{aligned} S_2(\ell) &= \left\langle (\boldsymbol{u}(\boldsymbol{r}+\ell) - \boldsymbol{u}(\boldsymbol{r}))^2 \right\rangle \\ &= 2\Big[\langle \boldsymbol{u}(\boldsymbol{r}+\ell) \cdot \boldsymbol{u}(\boldsymbol{r}) \rangle - \left\langle |\boldsymbol{u}(\boldsymbol{r})|^2 \right\rangle \Big] \\ &= \int_{-\infty}^{\infty} E(k) \cdot (1 - e^{-ik\ell}) \cdot dk. \end{aligned} \tag{1.5}$$

Equating equations 1.4 and 1.5 yields the Kolmogorov-Obukhov inertial range spectrum:

$$E(k) \propto \bar{\varepsilon}^{2/3} k^{-\beta}, \tag{1.6}$$

where k is the wavenumber (related to the scale separation by $k \propto 1/\ell$) and $\beta = 5/3$. Based on the general relationship between the power-spectrum exponent β and the second-order-moment structure function exponent $\zeta(2)$:

$$\beta = 1 + \zeta(2) \approx 1 + 2H. \tag{1.7}$$

This spectral law is best visualised as the slope of the energy spectrum in a log-log plot (see figure 1.3).

It has been verified in the atmosphere (Gurvich and Yaglom [1967b]) and in laboratory experiments (Champagne [1978]). The spectral form, equation 1.6, has become quite universal for describing fully developed turbulence. However, as we will see later significant deviations from the exponent 5/3 are expected due to intermittency. We will see later that the models describing intermittency, imply $\zeta(2) < 2/3$, which leads to values smaller than the theoretical $\beta = 5/3$ respectively.

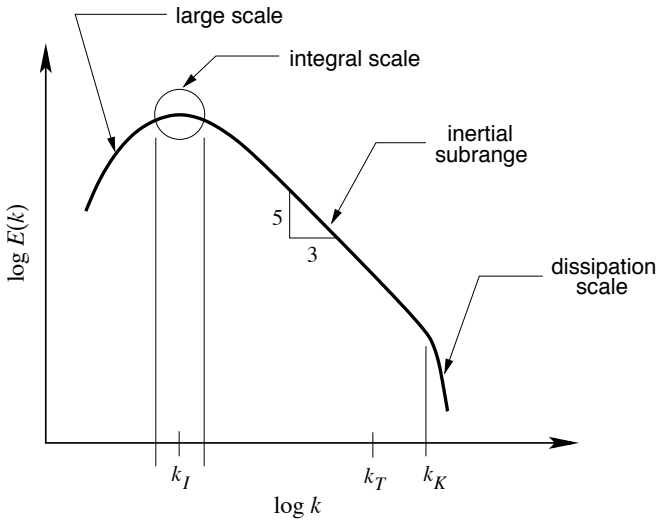

Figure 1.3: Schematic diagram of the turbulence energy wavenumber spectrum, $E(k) \propto k^{-\beta}$, where k_I, k_T and k_K are the equivalent wave numbers of the Integral, Taylor and Kolmogorov scales.

Kolmogorov's 4/5 Law

Starting from the Karman-Howarth-Monin relation Kolmogorov derived a rigorous result for the third-order structure function, the famous 'four-fifths law', considered to be one of only a few exact results satisfying the Navier-Stokes equation (equation 1.1).

> *In the limit of infinite Reynolds number the third-order (longitudinal) structure function of homogeneous isotropic turbulence, evaluated for increments small compared to the integral scale, is given in terms of the mean energy dissipation per unit mass by*
>
> $$S_3(\ell) \equiv \langle |\Delta \boldsymbol{u}(\ell)|^3 \rangle = -\frac{4}{5}\bar{\varepsilon}\ell.$$

The four-fifths law also allows us to determine the value of the scaling exponent ($H = 1/3$) for isotropic and homogeneous turbulence, although this requires supplementary assumptions on the rigorous definition of the involved averaged energy flux density $\bar{\varepsilon}$, as discussed below. Frisch [1980] considered the derivation based on Kolmogorov [1941b] as more rigorous than that given in Kolmogorov [1941a], whereas Chigirinskaya et al. [1998] emphasised that in both cases there

is an ad hoc hypothesis of a unique scaling exponent, which turn out to be fully irrelevant.

The Structure Function

A more general form of the structure function, for moments of order q, is given by:

$$S_q(\ell) \equiv \langle |\Delta \boldsymbol{u}(\ell)|^q \rangle = \langle |\boldsymbol{u}(\boldsymbol{r}+\ell) - \boldsymbol{u}(\boldsymbol{r})|^q \rangle. \tag{1.8}$$

Assuming $\bar{\varepsilon}$ is constant and can be determined, the second of Kolmogorov's hypotheses i.e. self-similarity, suggests that structure functions of an arbitrary (but finite) order q should scale as:

$$S_q(\ell) \propto (\bar{\varepsilon}\ell)^{\zeta(q)}, \tag{1.9}$$

with a linear scaling exponent $\zeta(q) = q/3$ for K41 (no intermittency).

Bolgiano-Obukhov Theory (BO)

To take into account the dominant role of the vertical motion of large scale atmospheric structures Bolgiano Jr [1959] and Obukhov [1959] considered the buoyancy force variance flux, ξ. This flux plays the same role as the energy flux, ε, in 3D turbulence along the vertical

$$\Delta u(\Delta z) \stackrel{d}{=} \xi(\Delta z)^{1/5} \Delta z^{3/5}. \tag{1.10}$$

Dimensional arguments of the energy spectrum, as with K41, give a Bolgiano-Obukhov (BO) -11/5 scaling exponent. In the first attempts to observe an 11/5s power law, due to the isotropic-homogeneous statistical conditions imposed, the predicted 11/5s exponent was rarely observed in three dimensions and therefore easily disregarded. Generalised scaling invariance (GSI) on the other hand does not require an isotropic-homogeneous condition, in fact quite the inverse. In GSI, equation 1.10 is used only to define the iso-scale. A variety of scaling anisotropies can then be postulated for different scenarios. We see later that this is a more appropriate model for our empirical observations.

1.3 The Challenge In Turbulence: Intermittency

The general notion of an intermittent process is one that is scarcely active. In fluid dynamics, due to Batchelor and others, this notion has become much more precise, i.e. the activity of a process is confined to smaller and smaller fractions of the available space-time when observed at a higher and higher resolution. Examples of intermittency can easily be observed in wind farm wind velocity data (see figure 1.4). This is mainly due to the high Reynolds numbers associated with the atmospheric conditions at wind farm locations. As discussed in the following sections, rigorous definitions of intermittency can be obtained with the help of fractals and multifractals.

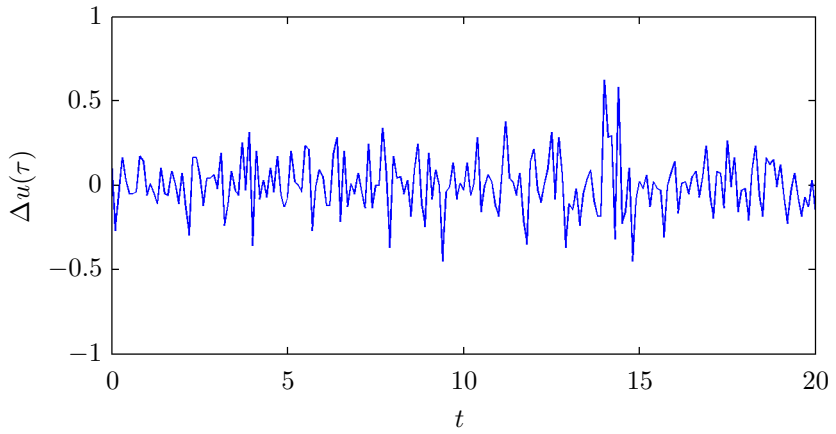

Figure 1.4: A twenty-second time-series of wind velocity increments, $\Delta u(\tau)$, taken from a wind farm test site in Corsica. The sporadic/intermittent nature of the large fluctuations is characteristic of turbulent processes.

The Energy Flux Density And Intermittency

Under K41 we have assumed that the mean of the energy flux density is sufficient to characterise the statistical properties of a fully developed turbulent flow. Although the instantaneous value of $\Delta \boldsymbol{u}(\ell)$ might be expressed as a universal function of the dissipation, ε, at the instant considered, when we average these

expressions, an important part will be played by the manner of variation of ε over time. Such variations in time at a given point in space are also easily observed, as with the intermittent nature of the wind velocity, in empirical data (see for example figure 1.5). Thus we find neither the velocity increments, $\Delta \boldsymbol{u}(\ell)$, nor the energy flux density, ε, are constant in time or space. Within a turbulent flow field, ε may vary widely in space, sometimes by orders of magnitude. The highest values of ε (relative to the mean) will tend to increase with increasing Reynolds number. These values may be of an order 15 times greater than the average energy flux at laboratory scale flows and 50 times that of the average energy flux in atmospheric flows.

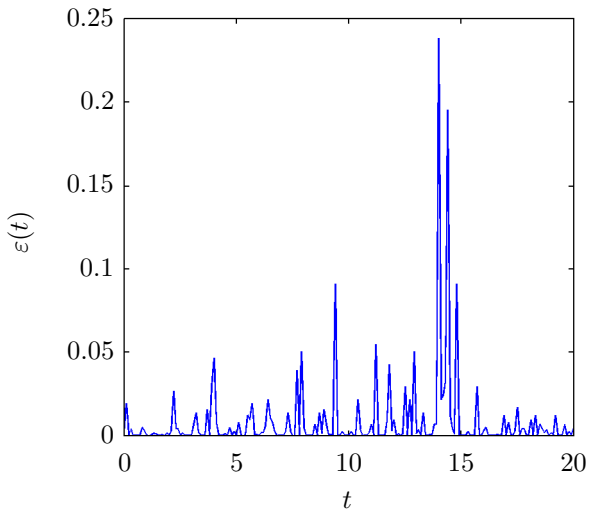

Figure 1.5: The rate of energy transfer (energy flux density), $\varepsilon(t) = |\Delta u(t)|^3$, from large to small scales for atmospheric turbulence. The energy flux density is very intermittent.

Limitations To The K41 Hypothesis

To take intermittency into account, Kolmogorov [1962] (denoted K62) and Obukhov [1962] considered that the structure function of velocity increments is a function of a locally averaged energy flux density for a sphere of radius ℓ and therefore ε_ℓ. They hypothesised that ε_ℓ was log-normally distributed with the variance σ_ℓ^2 of $\log(\varepsilon_\ell)$ given by

$$\sigma_\ell^2 = B + \pi \log(L/\ell),$$

where B is a constant associated with the macrostructure of the flow, π a universal constant, and L the largest external scale. One may note here that this hypothesis has been presented without real theoretical foundations. Kolmogorov did not provide any justification for this hypothesis, just stating that "*it is natural to suppose that...*" (Kolmogorov [1962]). Obukhov was more specific, indicating that the distribution of any positive quantity should be approximated by a log-normal distribution with the appropriate values for the first and second moments of the logarithm of this quantity (Obukhov [1962]).

Thus, under the K62 hypothesis, equation 1.9 becomes

$$S_q(\ell) = \varepsilon_\ell^{q/3} \ell^{q/3}, \tag{1.11}$$

also known as the refined similarity hypothesis (RSH). Although a log-normal distribution was hypothesised the 'refinement' can be generalised to any distribution.

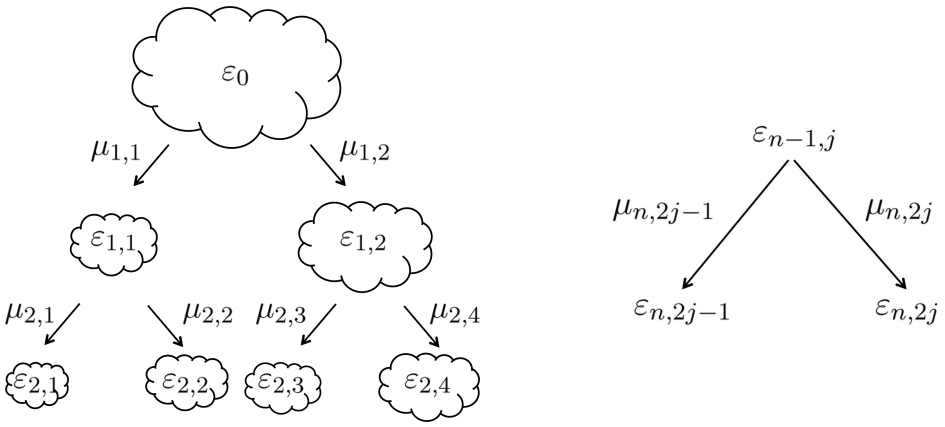

(a) First two steps in the RSH cascade i.e. for $n, j = 1, 2$.

(b) General case of the RSH for the energy density flux, ε_n, at any scale, n.

Figure 1.6: One dimensional schematic diagram of the RSH. The energy flux $\varepsilon_\ell = \varepsilon_{n,j}$ is fractionally distributed through the randomly distributed multiplicative increment $\mu_{n,j}$ where n is the level corresponding to the discrete scale ℓ_n and j is the position in the cascade.

Thus, the energy flux density simply becomes a function of the positive randomly distributed variable μ_n, where n is the position in the cascade i.e. the

local scale (see figure 1.6 for a schematic of the RSH). In comparison, K41 was previously assumed to be a homogenous and uniform distribution. Comparing the two expressions makes the subtle difference slightly clearer:

- K41: $\Delta \boldsymbol{u}(\ell) = \bar{\varepsilon}^{1/3}\ell^{1/3}$
- RSH: $\Delta \boldsymbol{u}(\ell) = \varepsilon_\ell^{1/3}\ell^{1/3}$

The statistics of $\Delta \boldsymbol{u}(\ell)^3$ are equivalent to that of ε_ℓ in both cases, but only in K62 are these statistics expected to correspond to a wide spread probability distribution, e.g. a fat-tailed distribution. This wide spread distribution corresponds to the non-linear forms of the structure-function exponent, $\zeta(q)$, thus characterising intermittency.

Discrete Cascades

Although Kolmogorov mentioned turbulence cascades in his derivation of the first universal law for the velocity fluctuations no explicit cascade model was referred to. It was not until Yaglom [1966] and Gurvich and Yaglom [1967b] made his first attempt at a multiplicative cascade model that a quantitative description of the Richardson cascade was produced. It is this model therefore that is the root of all the cascade models developed subsequently.

Multiplicative Processes

The key assumption in phenomenological models of turbulence is that successive steps define (independently) the 'fraction' of the flux of energy density distributed over smaller scales (this implies the use of a multiplicative process rather than an additive one). The small scales do not add energy they only modulate the energy passed down from larger scales. In the case where the scales are discretised this is rather simple to express. More precisely if one is using an elementary fixed ratio of scales, $\lambda = L/\ell$, and the discrete scales are, $\ell_n = L/\lambda^n$, the corresponding energy flux density, ε_ℓ, is replaced by $\varepsilon_n = \varepsilon_{\ell_n}$, which will be on constant volumes of size ℓ_n; notice we have defined our discrete energy flux density for any arbitrary position in the cascade, i.e. we neglect the j indexing used in figure 1.6. For a

multiplicative process the n^{th} energy flux density is recursively defined by

$$\varepsilon_n = \big(\mu_n\big)\varepsilon_{n-1} \tag{1.12}$$

where μ is a scale independent multiplicative increment analogous to Δ for additive increments and equation 1.12 is analogous (equivalent in logarithmic coordinates) to a forwards difference operation i.e. $\Delta\varepsilon = \varepsilon_n - \varepsilon_{n-1}$, which yields:

$$\varepsilon_n = \mu_1\mu_2\mu_3...\mu_n\varepsilon_0 = \left(\prod_{i=1}^{n}\mu_i\right)\varepsilon_0$$

Scaling Moment Function

Following the previous hypothesis of independence of variables, it is straightforward to calculate the moment of the energy flux density ε_n at the step n (and as discussed later, the corresponding result for the limit $n \to \infty$):

$$\begin{aligned}\langle(\varepsilon_n)^q\rangle &= \left\langle\left(\prod_{i=1}^{n}\mu_i\right)^q\right\rangle\langle\varepsilon_0\rangle^q \\ &= \prod_{i=1}^{n}\langle(\mu_i)^q\rangle\langle\varepsilon_0\rangle^q \\ &= \langle\mu_1^q\rangle^n\langle\varepsilon_0\rangle^q. \end{aligned} \tag{1.13}$$

We can predict that the moments of the energy density flux are related to the scale ratio through a scaling moment function $K(q)$

$$\langle\varepsilon_\lambda^q\rangle \propto \lambda^{K(q)}. \tag{1.14}$$

For $\lambda = 2^n$ between the external scale L and the reference scale $\ell > \ell_K$, from equation 1.13 we find that $K(q) = \log_2\langle\mu_1^q\rangle$. We can use this result to derive a general relationship between the scaling moment function and the structure function as follows.

Consider the relationship between the velocity increments and the energy flux density at scale ratio $\lambda = L/\ell$ for arbitrary scaling exponents a and H

$$\Delta \boldsymbol{u}_\lambda = \varepsilon_\lambda^a \lambda^{-H}. \tag{1.15}$$

Calculating their moments, equation 1.15 becomes

$$\langle \Delta \boldsymbol{u}_\lambda^q \rangle = \langle \varepsilon_\lambda^{aq} \rangle \lambda^{-qH}.$$

Substituting equation 1.9 into the l.h.s – we can easily normalise λ by the largest scale such that $\lambda = 1/\ell$ – and equation 1.14 into the r.h.s

$$\lambda^{-\zeta(q)} = \lambda^{K(aq)} \lambda^{-qH} \implies \zeta(q) = qH - K(aq). \tag{1.16}$$

Because we know the turbulent energy is conserved over the inertial subrange during the cascade process, we have

$$\langle \varepsilon_\lambda \rangle = \langle \varepsilon_0 \rangle = k, \ \forall \lambda \text{ where } k \text{ is a constant} \ldots$$
$$\ldots \implies K(1) = 0 \text{ (following from equation 1.14)}$$

One may note that this is a necessary and sufficient condition for a cascade developed on a finite ratio of scale, whereas it is only necessary for an infinite ratio of scale (for a more in-depth discussion on this see Schertzer [1987]). If we define $a = 1/3$ and $H = 1/3$ we obtain K41 which satisfies the exact relationship $\zeta(3) = 1$ (equation 1.9).

In the next chapter we will discuss two experimental datasets that contain wind measurements from a wide range of complex conditions. However, as we will see in the later sections of the chapter, through scaling analysis we have a means by which to simplify these complexities. Through scaling we can give an alternative interpretation to that of classical methodologies; an interpretation that provides both contrasting yet complimentary results.

1.4 Summary Of Chapter 1

Our goal is to reduce uncertainties in wind resource assessment. We claim that, based on the state of the art in wind energy, poor approximations to the high-number of degrees of freedom that arise in a bounded, turbulent, atmosphere are the main cause of uncertainty. Numerical attempts to model these complex and highly non-linear processes typically require a truncation of scales and more often than not complex parameterisations. Even if all of the scales were resolved (i.e., if we were given an infinitely powerful computer so that we could resolve all scales down to the dissipation scale) this will not prevent the uncertainties that would occur from the upscaled initial/boundary conditions at infinitely small scales. A statistical understanding of the corresponding simulations of the Navier-Stokes equations is therefore still required. We argue that due to the symmetries of the governing equations of fluid motion for a high-Reynolds number flow, the statistics of the wind are scaling and multifractal. It is therefore unnecessary to truncate the scales of the process.

From the governing equations that define the forces driving the wind, it is natural to not only expect a highly non-Gaussian wind but also one that it is scaling. By scaling we mean a process that has (statistical) self-similitude. This isn't such an abstract concept to conceive if we consider for an instance the cascading eddies of a smoke plume. Typical atmospheric turbulence modelling approaches micro-scale wind effects within the ranges of 1 to 1000 metres or 1 to 100 seconds. Such models naturally rely on stochastic multifractal cascade processes. This is because multifractals (multiple co-dimension self-similar subdivisions) easily reproduce the intermittency, heavy-tailed probabilities that are ubiquitous with the wind and essential to quantify for the wind energy community.

References: Chapter 1

R. Bolgiano Jr. Turbulent spectra in a stably stratified atmosphere. *J. Geophys. Res.*, 64(12):2226–2229, January 1959. URL http://www.google.fr/search?client=safari&rls=10_7_4&q=Turbulent+spectra+in+a+stably+stratified+atmosphere&ie=UTF-8&oe=UTF-8&redir_esc=&ei=qiyJUP_kK4HL0QWil4CgBQ.

F. H. Champagne. The fine-scale structure of the turbulent velocity field. *Journal of Fluid Mechanics*, 86(1):67–108, 1978.

Y. Chigirinskaya, D. Schertzer, and S. Lovejoy. An alternative to shell-models: More complete and yet simple models of intermittency. pages 263–266, 1998. URL http://link.springer.com/chapter/10.1007/978-94-011-5118-4_65.

P. A. Davidson, Y. Kaneda, K. Moffatt, and K. R. Sreenivasan. A voyage through turbulence. 2011. doi:10.1017/CBO9781139018241. URL http://books.google.com/books?hl=en&lr=&id=04QIthkkPf0C&oi=fnd&pg=PR11&dq=a+voyage+through+turbulence&ots=Jc7udrSjYE&sig=67Q8bJJrZcm7G0Y-6oEBP6eA0xI.

G. Fitton, I. Tchiguirinskaia, D. Schertzer, and S. Lovejoy. Scaling Of Turbulence In The Atmospheric Surface-Layer: Which Anisotropy? *Journal of Physics: Conference Series*, 318(7):072008, January 2011. doi:10.1088/1742-6596/318/7/072008. URL http://www.google.fr/search?client=safari&rls=en-us&q=Scaling+Of+Turbulence+In+The+Atmospheric+Surface+Layer+Which+Anisotropy&ie=UTF-8&oe=UTF-8&redir_esc=&ei=b5hUT8DlGsOF8gO5kJTwBQ.

G. F. Fitton. Multifractal Analysis And Simulation Of Wind Energy Fluctuations. URL http://www.google.fr/search?client=safari&rls=10_7_4&q=MULTIFRACTAL+ANALYSIS+AND+SIMULATION+OF+WIND+ENERGY+FLUCTUATIONS&ie=UTF-8&oe=UTF-8&gws_rd=cr&ei=o2E4UuuUHtSN7Abi8IH4DQ.

U. Frisch. Fully developed turbulence and intermittency. *Annals of the New York Academy of Sciences*, 357(1):359–367, 1980. URL http://onlinelibrary.wiley.com/doi/10.1111/j.1749-6632.1980.tb29703.x/abstract.

A. Gurvich and A. Yaglom. Breakdown of eddies and probability distributions for small-scale turbulence. *Phys. Fluids*, 10:S59, January 1967. URL http://www.google.fr/search?client=safari&rls=10_7_4&q=Breakdown+of+eddies+and+probability+distributions+for+small+scale+turbulence&ie=UTF-8&oe=UTF-8&redir_esc=&ei=HzKJUI6hLZOQhQes7ICwAg.

J. R. Herring, J. P. Chollet, G. R. Newman, M. Lesieur, D. Schertzer, and M. Larcheveque. Comparative assessment of spectral closures as applied to passive scalar diffusion. *Journal of Fluid Mechanics*, 124(235):411–437, 1982. URL http://journals.cambridge.org/production/action/cjoGetFulltext?fulltextid=390001.

H. Holmes. WAUDIT Guidance Report - WP6 Deliverable D24. *Public*, pages 1–30, October 2011. URL http://www.waudit-itn.eu/newsAndEventsDetail.php?idn=47.

A. Kolmogorov. The local structure of turbulence in incompressible viscous fluid for very large Reynolds numbers. In *Dokl. Akad. Nauk SSSR*, pages 9–13, January 1941a. URL http://www.google.fr/search?client=safari&rls=10_7_4&q=The+local+structure+of+turbulence+in+incompressible+viscous+fluid+for+very+large+Reynolds+numbers&ie=UTF-8&oe=UTF-8&redir_esc=&ei=XiiJUOr5CaKI0AXmxoGoDA.

A. Kolmogorov. Dissipation of energy in the locally isotropic turbulence. reprinted 1991. In *Proc R Soc Lond A*, pages 15–17, January 1941b.

A. Kolmogorov. A refinement of previous hypothesis concerning the local structure of turbulence in a viscous incompressible fluid at high Reynolds number. *J. Fluid Mech*, 13:S2, 1962. URL http://scholar.google.com/scholar?q=related:TrvmATypJ4gJ:scholar.google.com/&hl=en&num=30&as_sdt=0,5.

M. Lilley, S. Lovejoy, K. Strawbridge, and D. Schertzer. 23/9 dimensional anisotropic scaling of passive admixtures using lidar aerosol data. *Phys. Rev. E*, 70(3):036307, January 2004. URL http://www.google.fr/search?client=safari&rls=10_7_4&q=23+9+dimensional+anisotropic+scaling+of+passive+admixtures+using+lidar+aerosol+data&ie=UTF-8&oe=UTF-8&redir_esc=&ei=8ymJUInPBsqb0QWLzYGgBQ.

S. Lovejoy and D. Schertzer. *The weather and Climate: emergent laws and multifractal cascades*. Cambridge University Press, 2013.

P. Lynch. *The emergence of numerical weather prediction: Richardson's dream*. Cambridge University Press, 2006.

I. Marusic, B. J. McKeon, P. A. Monkewitz, H. M. Nagib, A. J. Smits, and K. R. Sreenivasan. Wall-bounded turbulent flows at high Reynolds numbers: Recent advances and key issues. *Phys. Fluids*, 22(6):065103, 2010. doi:10.1063/1.3453711. URL http://link.aip.org/link/PHFLE6/v22/i6/p065103/s1&Agg=doi.

A. Obukhov. Effect of Archimedean forces on the structure of the temperature field in a turbulent flow. In *Dokl. Akad. Nauk SSSR*, page 1246, 1959.

A. Obukhov. Some specific features of atmospheric turbulence. *J. Geophys. Res.*, 67(8):3011–3014, 1962.

L. F. Richardson. Weather prediction by numerical process. 2007. URL http://books.google.com/books?hl=en&lr=&id=D52d3_bbgg8C&oi=fnd&pg=PA3&dq=weather+prediction+by+numerical+process&ots=6_OwhW5IZp&sig=_iwiOtMACeMce0k_Ixrd7aIjJ0E.

J. S. Rodrigo. State-of-the-Art of Wind Resource Assessment. *N/A*, pages 1–25, January 2011. URL http://www.waudit-itn.eu/download.php?id=103&parent=79.

D. Schertzer. Physical modeling and analysis of rain and clouds by anisotropic scaling multiplicative processes. *J. Geophys. Res.*, January 1987. URL http://www.physics.mcgill.ca/~gang/eprints/eprintLovejoy/neweprint/JGR.SL.1987.good.pdf.

D. Schertzer, I. Tchiguirinskaia, S. Lovejoy, and A. Tuck. Quasi-geostrophic turbulence and generalized scale invariance, a theoretical reply. *Atmos. Chem. Phys. Discuss*, 11(1):3301–3320, 2011. doi:10.5194/acpd-11-3301-2011. URL http://www.google.fr/search?client=safari&rls=10_7_4&q=Quasi+geostrophic+turbulence+and+generalized+scale+invariance+a+theoretical+reply&ie=UTF-8&oe=UTF-8&redir_esc=&ei=Ru6HUIyfEanA0QWG1YCwBQ.

L. I. Sedov. Methods of similitude and dimensionality in mechanics. 1972.

C. G. Speziale. Analytical Methods for the Development of Reynolds-Stress Closures in Turbulence. *Annu. Rev. Fluid Mech.*, 23(1):107–157, January 2011. doi:doi: 10.1146/annurev.fl.23.010191.000543. URL http://dx.doi.org/10.1146/annurev.fl.23.010191.000543.

A. Tsinober. New approaches and concepts in turbulence. 1993. doi:10.1007/978-3-0348-8585-0. URL http://books.google.com/books?hl=en&lr=&id=E5YPi4GhhEMC&oi=fnd&pg=PP13&dq=New+approaches+and+concepts+in+turbulence&ots=RqCWd0MsHv&sig=tmCr_jgFjFApGYBhv3s1qrkMzds.

T. Wallbank. WindSim Validation Study. *CFD validation in Complex terrain*, January 2008. URL http://www.google.fr/search?client=safari&rls=10_7_4&q=WindSim+Validation+Study&ie=UTF-8&oe=UTF-8&redir_esc=&ei=DzaJUMCEG4Wi0QXQi4CYBA.

A. M. Yaglom. The influence of fluctuations in energy dissipation on the shape of turbulence characteristics in the inertial interval. In *Soviet Physics Doklady*, page 26, 1966.

M. Yokokawa, K. Itakura, A. Uno, T. Ishihara, and Y. Kaneda. 16.4-Tflops direct numerical simulation of turbulence by a Fourier spectral method on the Earth Simulator. pages 50–50, 2002. URL http://ieeexplore.ieee.org/xpls/abs_all.jsp?arnumber=1592886.

Chapter 2

2.1 Wind Energy Experimental Settings

For data analysis we have made use of two datasets of atmospheric measurements from two very topographically different locations. The first (Growian) dataset was introduced to us by Professor Joachim Peinke of the Oldenburg Institute of Physics and ForWind. It consists of wind turbine inflow measurements taken in a near homogenous terrain surrounding. The second (Corsica) dataset was provided by a WAUDIT partner enterprise, Électricité de France (EDF), and it consists of measurements taken from within a wind farm on top of a mountain. This means that unlike the Growian site, the measurements will have been subject to both wake and orographic effects. Although both test sites differ topographically, both are located within two kilometres of the sea, suggesting both will be influenced by convective sea breezes.

The Growian Experiment

The Growian wind turbine experiment (Günther and Hennemuth [1988]; Körber et al. [1988]) was a German Federal Ministry of Research and Technology's project that took place over the years 1983 to 87. A two-bladed, 3-megawatt, wind turbine was constructed for research purposes in Kaiser-Wilhelm-Koog, near the German coastline of the North Sea.

Figure 2.1: Aerial photograph of the Growian experiment taken by Schleswig-Holstein (www.panoramio.com).

This particular experiment is of great interest to us, not because of the turbine, but, because of the two 150m measuring masts, positioned 65m West-South-West of the turbine. Sixteen cup anemometers and wind vanes, eight-per-mast, were installed on the ends of 12m booms at 50, 75, 100, 125 and 150m from the ground; covering an effective area of 75-by-100m as can be seen in figure 2.2. This grid-like set-up meant that (limited) space-time measurements were possible. Finally,

near-surface measurements were taken at 10m on just one of the masts.

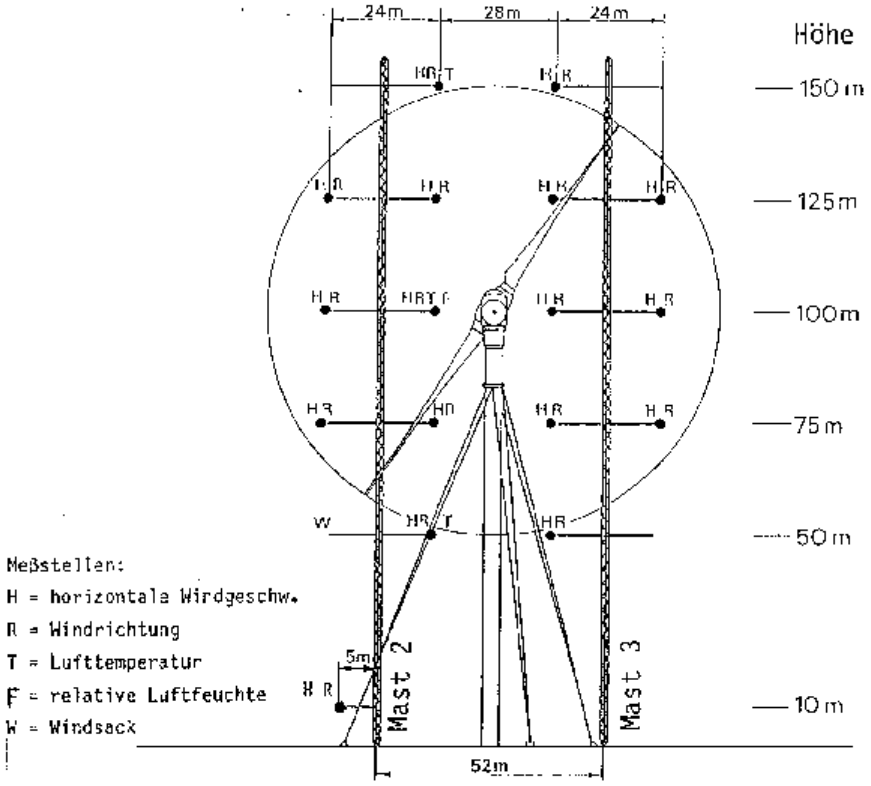

Figure 2.2: Site view and ground plan of the Growian experiment. Image is taken from the 1984 European Wind Energy Conference.

The data available from the experiment came in the form of a horizontal wind speed measured from the cup anemometer and a simultaneously measured wind direction from the wind vane. A vertical velocity was also measured, but only at 75 and 125m. In addition to wind measurements, temperature and relative humidity were measured at 50, 100 and 150m. The rate of measurement was the same for all of the variables, 2.5Hz, and the duration of one measuring run was approximately twenty minutes. A total of 300 runs were made altogether.

Figure 2.3 plots a ten-minute time-series of the wind speed, direction, temperature and relative humidity taken from the same inner-most position of the second mast ("Mast 2") at 100m. The wind speed, direction and temperature appear intermittent and stationary. The relative humidity on the other hand, while

also fairly intermittent, is sloped suggesting the larger time-scales are displaced.

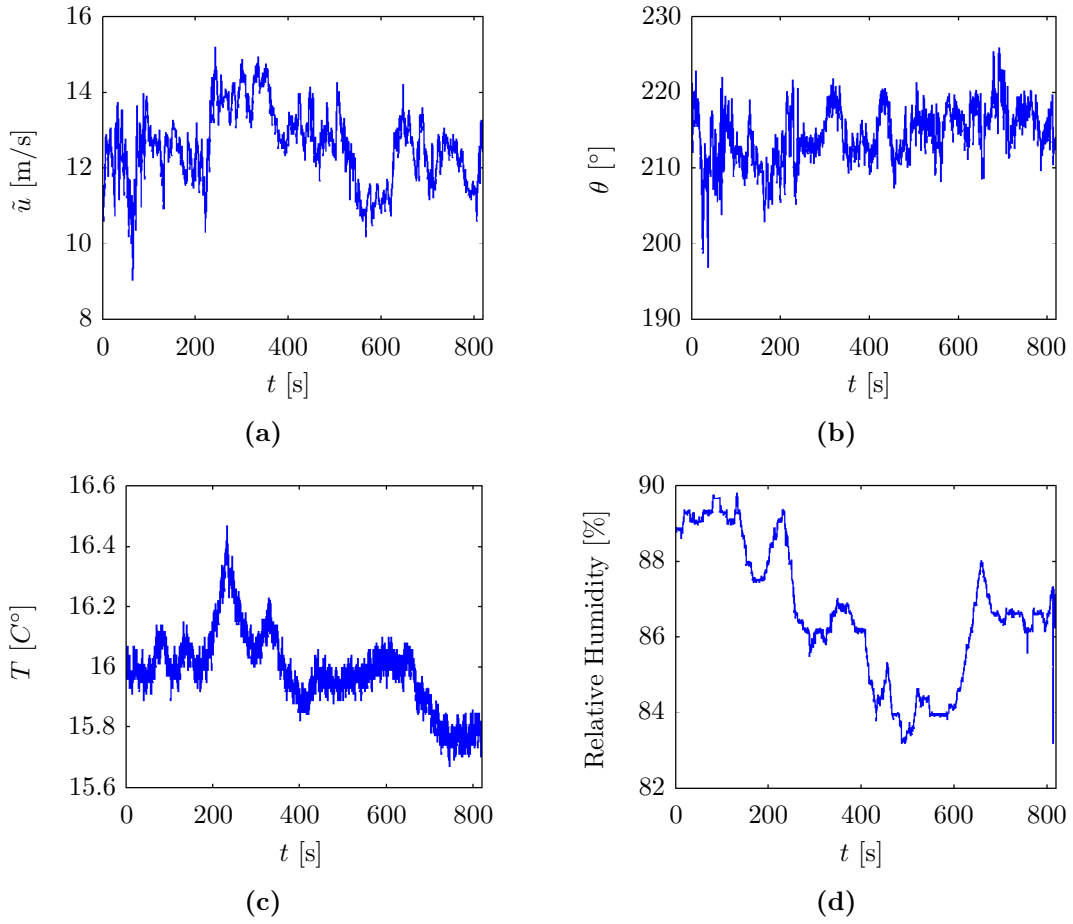

Figure 2.3: Plots of the ten-minute time-series of the wind speed (a), direction (b), temperature (c) and relative humidity (d). All of the measurements are taken from the inner-most position of the second mast ("Mast 2") at 100m.

Topographical Features

From figure 2.1 we can see that the terrain surrounding the masts consists mainly of fields, small buildings, bushes and a few sparsely positioned trees. Although far from wind-tunnel-like ideal conditions, a homogenous boundary condition can be assumed. This becomes more evident when we compare the flat terrain of the Growian experiment to the starkly contrasting mountainous, rocky, outcrops of the Ersa wind farm. The second of our two datasets that will be described in

more detail in section 2.1.

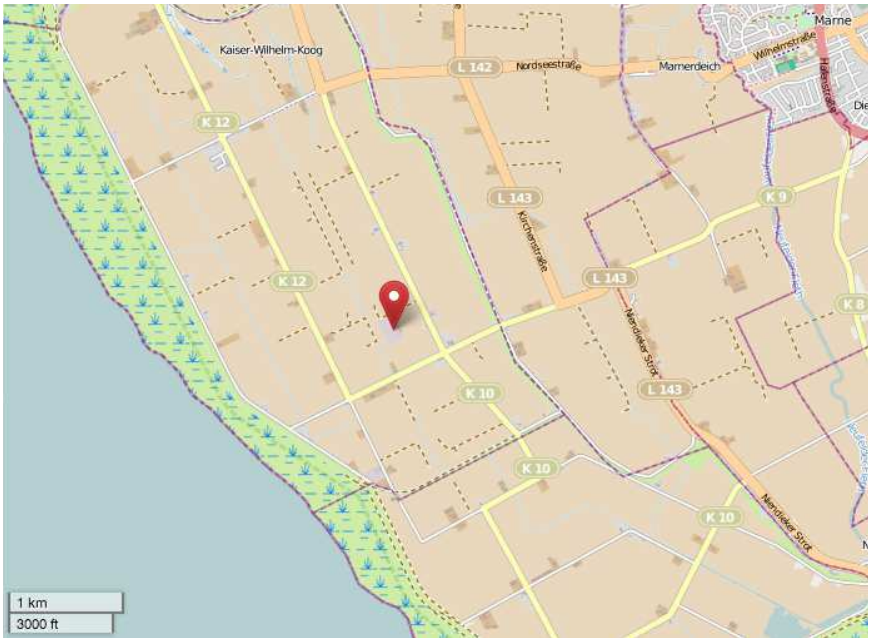

Figure 2.4: Location of the Growian experiment (red marker) with respect to the nearby coast. Map was generated at www.openstreetmap.org.

A second interesting topographical feature of the Growian dataset is the nearby sea. Figure 2.4 shows the position of the masts with respect to the sea. The masts lie approximately two kilometres East-North-East of the sea. Due to the close proximity to the sea one would expect to observe strong convective winds, the so-called 'sea breeze' phenomena (see Simpson [1994] and Levi et al. [2011] for a more recent overview). Sea breezes are a commonly observed phenomena that occur during periods of solar heating where albedo differences between the land and sea result in strong convective winds. Moreover, after periods of solar heating, differences in conductive properties cause counter-directional winds and inversion layers. Because the Growian experiment has vertically spaced wind and temperature measurements, we can easily test some of the classical measures for stability that aim to classify the corresponding physical processes associated with this phenomena.

Data Quality

Errors in the Growian experiment data meant the number of usable twenty-minutes samples varied between 174 to 290 (see tables 2.1 and 2.2). The errors in the data consisted of either large numbers of zeros or 9999s. No documentation could be found describing why there were errors of this sort, we can however speculate that it was due to mechanical failure because of the consistency of the error values. For simplicity if either one of the two values was detected in the full twenty-minute measuring run, the full measuring run was discarded.

	Mast 2								
	Inner					Outer			
Height [m]	50	75	100	125	150	10	75	100	125
# Discarded Samples	31	25	30	28	126	10	21	40	50

Table 2.1: Number of twenty-minute runs discarded due to errors (Mast 2).

	Mast 3							
	Inner					Outer		
Height [m]	50	75	100	125	150	75	100	125
# Discarded Samples	28	58	71	62	49	26	35	61

Table 2.2: Number of twenty-minute runs discarded due to errors (Mast 3).

The Wind Direction And Shadow Effect

Figure 2.5 plots the mean raw (no post-processing) wind direction data, $\bar{\theta}_{\text{raw}}$, per twenty-minute measuring run, sorted into ascending order. The majority (about two-thirds) of the values of the direction lie between 180 and 300°. A comparison with the site plan of the experiment (figure 2.6) and a meteorological compass (positioned on the same figure) confirms that the raw directional data measures the meteorological wind direction θ_M. The documentation that came with the data made no reference to what kind of direction was being measured hence our

need to check its correspondence. We define the meteorological wind direction, θ_M, to be the direction that the wind comes from i.e. if the wind blows *from* the North then $\theta_M = 0°$, and is measured clockwise thereafter.

With this in mind we can see that the general directional tendency of the wind is perpendicular to the positioning of the mast array. It is likely that the original positioning of the array (and turbine) was done according to long-term mean wind directions similar those displayed in figure 2.5, i.e. with a prevailing West-South-Westerly wind. Note that the West-South-West direction of the wind enforces our previous expectation that sea-land and land-sea winds are likely to occur.

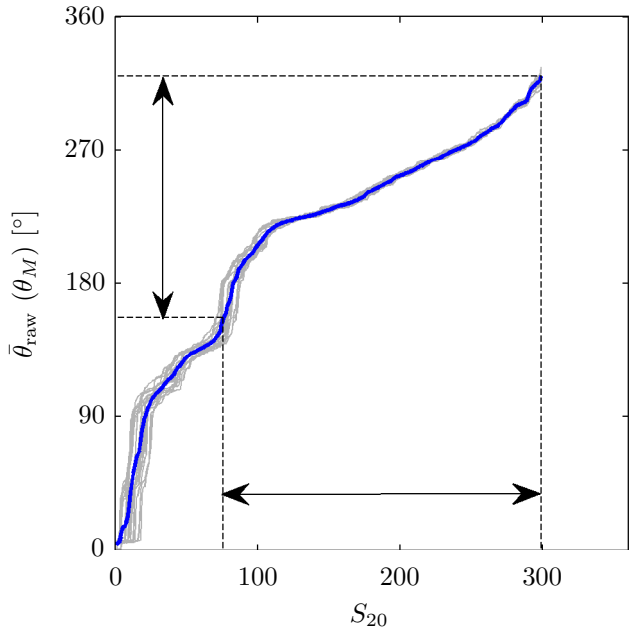

Figure 2.5: Plot of the mean measured wind direction, $\bar{\theta}_M$, per twenty minute measuring run, S_{20}, sorted into ascending order. The grey plots are the means for each individual wind vane and the blue plot is, furthermore, the corresponding mean over all of the individual wind vanes. The dashed lines correspond to a $\pm 90°$ tolerance about the assumed perpendicular-to-the-array direction, $\theta_M = 247.5°$.

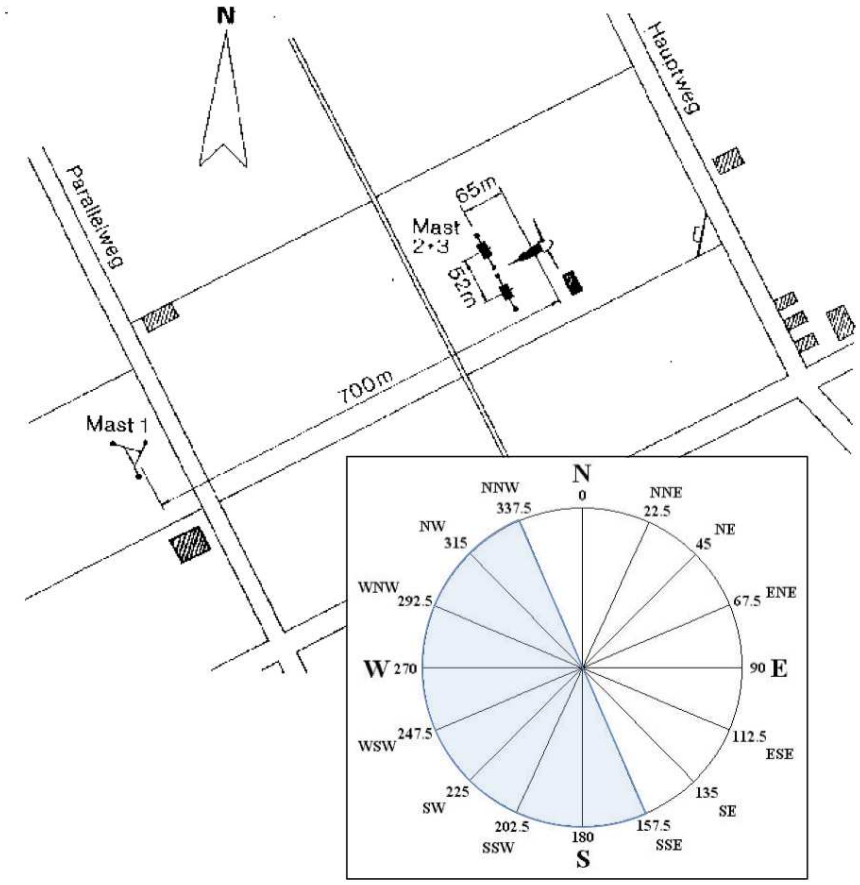

Figure 2.6: Top view of the measuring site with wind rose. The blue highlighted area on the wind rose corresponds to winds with direction assumed to have the least influence from the masts and the nearby turbines.

In order to calculate and plot the vector components of the wind we need, instead of the meteorological direction, the azimuthal direction θ_A. Figure 2.7 shows the relation between the meteorological, azimuthal and polar directions. The azimuthal direction, i.e. the direction *towards* which the wind is blowing, is related to the meteorological direction by $\pm 180°$. The two-dimensional wind vector polar angle on the other hand increases in an anti-clockwise direction from the positive x-axis. A two-dimensional polar coordinate system will be used to statistically define the component-wise anisotropy later on. The radial and directional components of the polar coordinate system are: $\tilde{u} = \sqrt{u^2 + v^2}$ and $\theta_P = \tan^{-1}(v/u)$ respectively.

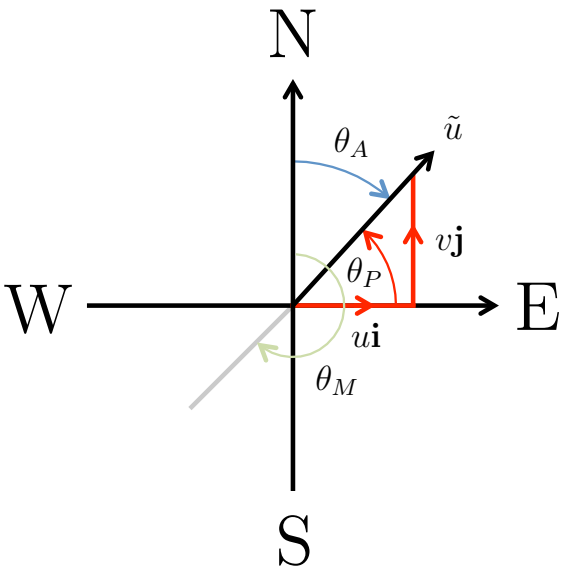

Figure 2.7: Diagram illustrating the relation between the meteorological, azimuthal and polar directions; θ_M, θ_A and θ_P respectively.

Table 2.3 shows how the components u and v are calculated for either the meteorological wind direction or azimuthal wind direction and vice versa. Figure 2.8 then plots the mean wind vectors – averaged in height and over 25 twenty-minute measuring runs at a time – corresponding to the (increasing) change in direction seen in figure 2.5. Some additional information we gain from the vector plot is the apparent increase or decrease in wind speed with clockwise or anti-clockwise rotation.

Wind Vector Azimuth	Meteorological Wind Direction
$u = \tilde{u} \cdot \sin\theta_A$	$u = -\tilde{u} \cdot \sin\theta_M$
$v = \tilde{u} \cdot \cos\theta_A$	$v = -\tilde{u} \cdot \cos\theta_M$

Table 2.3: Table relating the horizontal wind components u and v to the meteorological and azimuthal wind directions and vice versa. The symbol $\tilde{u}$ corresponds to wind speed.

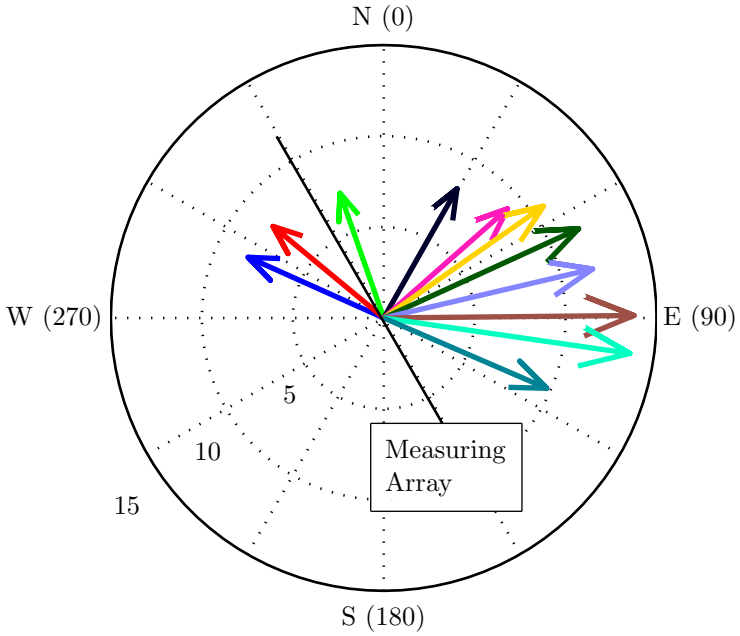

Figure 2.8: Mean wind vectors averaged in height (10, 50 75, 100, 125 and 150; inner-most position of Mast 2), and over 25 twenty-minute measuring runs i.e. $S_\theta = S_i \leq S \leq S_{i+1}$ for $i \in [1:25:300]$. Corresponding time-scale $\tau = 12$ hours. The radial units of measurements are in m/s.

It is possible the wind speed decreases with rotation due to the influence of the mast on the measurements. In both figures 2.6 and 2.8 the position of the array with respect to the mean wind vector over all of the data can be seen to be approximately perpendicular. When there is a mast array set-up, such as the one in the Growian experiment, it is important to make sure that the wind

measurements are unimpeded by the structure of the array. If the winds do pass through the array, additional turbulent mixing will be generated in the wake of the structure resulting in an increase in fluctuations at a given scale – typically the scale corresponding to the size of the structure. This behaviour is easily observed when a scaling analysis is performed. We will discuss this in more detail later on.

To ensure this doesn't happen we can take data with direction close to perpendicular to the array. However, because of the limited number of measurements, it is in our interest to maximise the amount of usable data. We therefore set our direction bounds to be within $\pm 90°$ of the perpendicular direction. Although the mean direction over all of the error free data files is approximately perpendicular to the mast, there are a number of sub-samples, within the dispersion of the direction estimates, whose mean direction suggests the measurements were influenced by the mast i.e. $\bar{\theta} \in [0° : 157.5°]$ (see figure 2.5). Applying the $\pm 90°$ bound as a means to preselect the data we get a subset (denoted $S_\perp$) consisting of 225 sub-samples of the total database as shown (again) in figure 2.5.

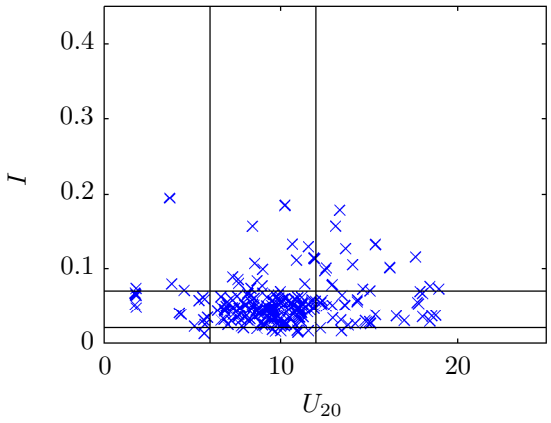

Figure 2.9: Plot of the relative turbulence intensity, I, vs. the mean twenty minute wind speed, U_{20}. The plot corresponds to the dataset $S_\perp$. The black lines correspond to the selection criteria used by Mücke et. al [2011].

In Mücke et al. [2011] the authors suggested the use of a selection criteria based on the twenty-minute mean interpolated wind speed, U_{20}, and the turbulence intensity, $I = \sqrt{\langle u_\delta^2 \rangle}/U_{20}$, where $\langle \cdot \rangle$ is an averaging procedure and $\sqrt{\langle u_\delta^2 \rangle}$ is the average fluctuating component. The exact bounds given to U_{20} and I aren't

formally presented. We can however get a rough approximation from the plots in the publication. We approximated these values to be: $8 \leq U_{20} \leq 12$ and $0.05 \leq I \leq 0.12$. The criteria is supposedly used to remove measurements subject to a 'shadow effect' from the mast. We tested the criteria against $S_{\perp}$ (figure 2.9) and they do not correspond.

Vertical Wind and Temperature Profiles

One of the more fascinating aspects of the Growian dataset is the possibility to compare measurements in space as well as in time. It is therefore always of interest to perform the analyses in space in order to fully utilize the available information. In this section we will look at the vertical profiles of the wind and temperature and compare them with classical surface and boundary-layer theory. Figure 2.10 plots the vertical profiles of the mean horizontal wind components and their corresponding mean (azimuthal) directions and temperatures. The plots are in fact complimentary to the wind vector plots in figure 2.8 of the previous section. There are two interesting features to note from this figure.

The first, is that the direction remains unquestionably constant with height. This isn't altogether shocking since the sub-samples have indeed been sorted by direction. What is surprising is the complete lack of variability. This suggests that the wind velocities and temperature are not coupled to the direction (since they *do* change with height) at this time-scale (12 hours). The second surprising observation is the appearance of a temperature inversion at 50m for the two most South-South-Easterly winds (the red and blue plots). Since the wind vectors' directions would mean they would displace from land to sea it seems plausible that the temperature inversion is the result of the so called 'sea-breeze' phenomena. This result further strengthens the argument that strong convective winds will influence the measurement site. However, based on the discussion in the previous section, the inversion may also be due to shadow effects caused by the mast – since the wind vector directions suggest there will have been an impediment caused by the structure. Using scaling analysis we later provide evidence that the mast obstruction doesn't change the scaling of the temperature.

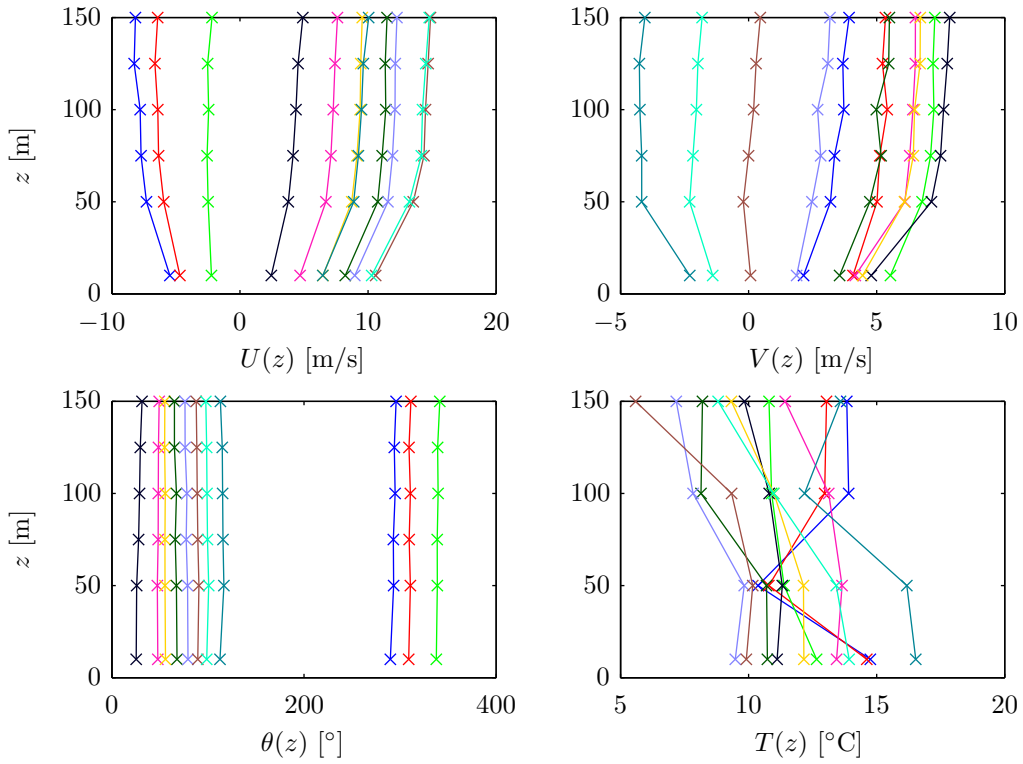

Figure 2.10: Vertical profiles of the mean horizontal wind components $U(z)$ and $V(z)$ (top left and top right), the corresponding mean (azimuthal) directions $\theta(z)$ (bottom left) and similarly their related temperatures $T(z)$ (bottom right). The color-coding matches the wind vectors plotted in figure 2.8. Also as in figure 2.8 the time-scale $\tau = 12$ hours.

We have included the vertical profiles of the wind in the description of the data as it is now a standard means of data pre-processing, particularly in the fields of numerical simulation and data assimilation. In the case of numerical simulation it is often simpler to simulate wind fields under neutral atmospheric conditions since under stable or unstable conditions additional heat flux equations must be added to the forcing term of the governing equations. The vertical wind profile boundary conditions are therefore chosen such that a neutral atmospheric condition is satisfied. If the boundary conditions do exhibit discontinuities corresponding to temperature inversions etc. there is more chance (depending on the complexity of the terrain) that the in-situ measurements used for model validation will deviate from the simulated wind field. Nonetheless, even if the model does deviate from validation measurements data assimilation tools can be used

to 'nudge' the results back to their desired profiles Laporte et al. [2009]!

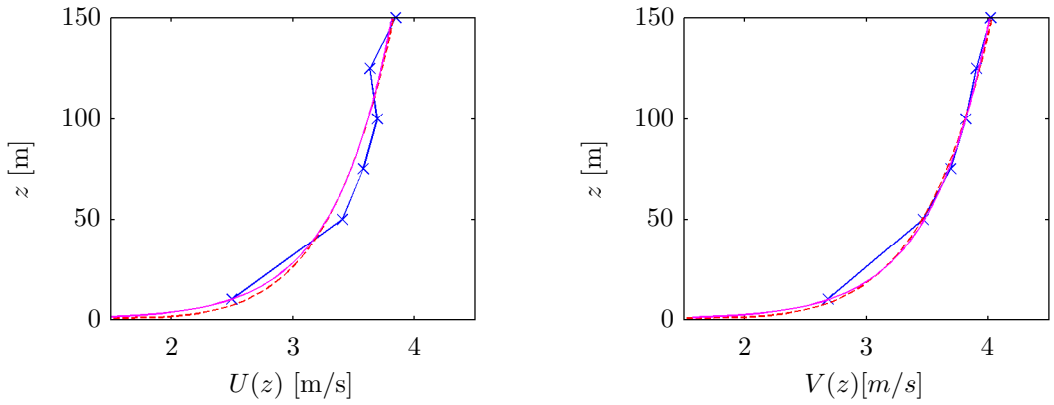

Figure 2.11: The mean (over $S_\perp$) horizontal wind vertical profiles for the Growian experiment (blue crosses). Classical logarithmic (red dashed lines) and power law (pink solid lines) expressions approximate the profiles.

Figure 2.11 shows the mean (over $S_\perp$) horizontal wind velocity vertical profiles, for the Growian experiment. The most basic (excluding temperature forcing) logarithmic profile model for approximating the vertical wind speed profile within the surface-layer is defined by:

$$U(z) = \frac{u_*}{\kappa} \log(z/z_0) \tag{2.1}$$

where $U(z)$ is the mean wind speed as a function of height, z, z_0 is the surface roughness; a parameter that varies from 0.001 to 0.7 depending on the whether the ground is flat or rough respectively, $u_* = \sqrt{S/\rho}$, is the friction velocity (1/10 of the mean flow velocity), S is the shear stress, and κ is the the Von Kármán constant (~ 0.41). Alternatively, Burton et al. [2001] states that a power law approximation is often used in the wind energy community. In this case

$$U(z) \propto z^\pi, \tag{2.2}$$

where π is typically 0.14 for 'normal' conditions and 0.20 for turbulent conditions. No reason is given for this approximation more than it fits! Figure 2.11 compares the empirical vertical wind profile with $U(z)$ estimated from equations 2.2 and 2.1. The parameters used in equation 2.2 are $\pi = 0.14$ with proportionality

coefficient 2 for both U and V. For equation 2.1 we have used $z_0 = 0.04$ and 0.06 for $U(z)$ and $V(z)$ respectively with $u_* = 0.2$ in both cases. Indeed, it seems that, at a time-scale of three days (68 hours) i.e. averaged over all of the available measuring runs, the vertical wind profile can be approximated with either a power law *or* logarithmic profile depending on the choice of parameters.

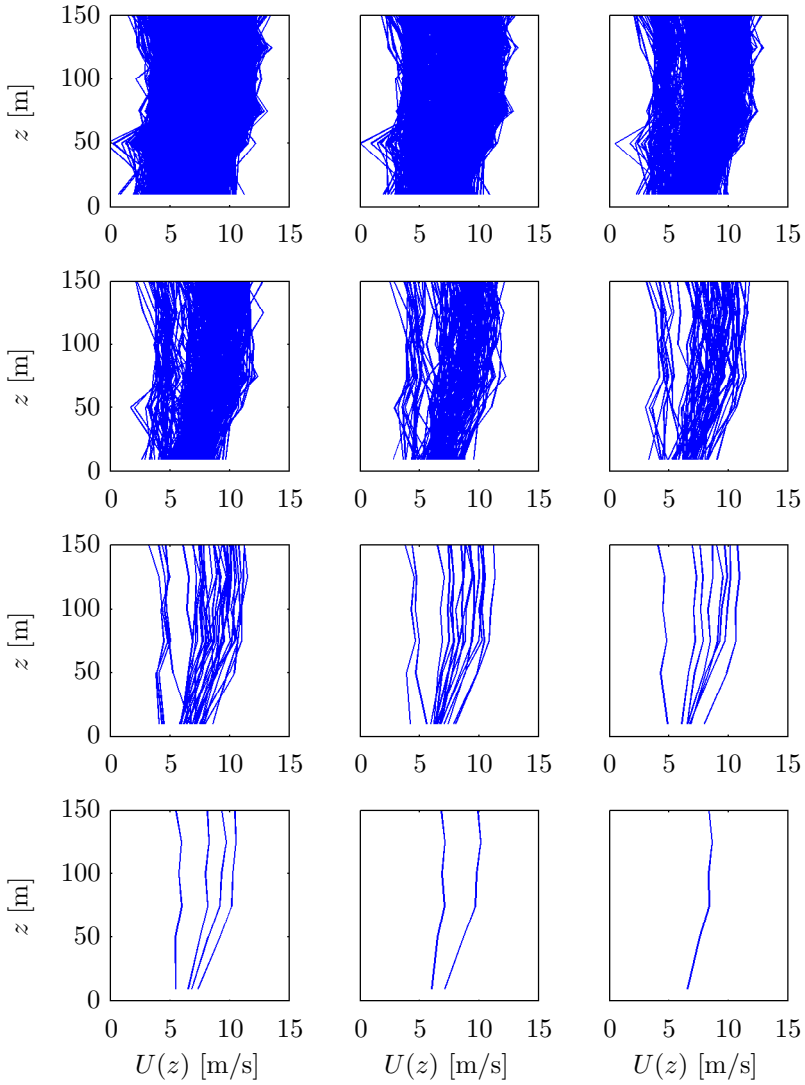

Figure 2.12: Vertical profile of the mean horizontal wind component, $U_y(z)$, at $\tau = 0.4\text{s}\times 2^i$ for $i \in [0:11]$ (from left to right; top to bottom).

Although fitting the vertical wind profile at a three-day time-scale seems achievable within the recommendations of the IEC, the information it provides is somewhat misleading. In Wächter et al. [2012], they calculate that, using Taylor's hypothesis (a topic we will return to ourselves in the coming sections), a one second temporal increment corresponds to a 10 to 20m spatial increment. This suggests that if we want to even begin to truly quantify the effects of wind shear across the diameter of a wind turbine blade an understanding, of vertical wind profiles at a three-day time-scale simply will not do. Moreover, quantifying the effects of wind shear across the width of a blade (1 to 2m) will require an understanding of the properties of temporal wind increments at scales much smaller than a second.

Figure 2.12 shows the vertical profiles of the horizontal u-component for time-scales between 0.4 seconds and 15 minutes. It is clear from the plots that, not only at the highest resolution, but up to time-scales of approximately a minute, a smooth power law approximation cannot be used. Below time-scales of a minute the profiles are not only without a general form, they are chaotic; turbulent one might say. If time-averaging a velocity until it becomes smooth is representative only of the time-scale it is averaged up to, what other means do we have to describe the chaotic profiles observed at higher frequencies? We may take note from a discussion I once overheard – "it is always interesting to first look at the probability distributions [before a more complex approach is attempted]".

Vertical Probability Distribution Profiles

Figure 2.13 shows the exceedance probabilities of the temporal velocity increments, $\Delta u(\tau) = u(t+\tau, z) - u(t, z)$, of six twenty-minute samples taken at different heights but for the same measuring run. The time-scale of the increment is 0.4 seconds and the differing sample heights are 10, 50, 75, 100, 125 and 150m (from top to bottom and shifted vertically for clarity). The probability of exceedance is calculated using the Weibull plotting position

$$\Pr(X \geq s) = i/(N+1), \tag{2.3}$$

where i is the index of the random variable X_i, N is the length of $\{X_i\}$ and s is X_i sorted into descending order. Although the distributions in figure 2.13 correspond to one measuring run out of a total of 300 it is representative of the majority ($> 70\%$) of the probability distributions for the other measuring runs.

The vertical scale of the plot is logarithmic so as to emphasise the heavy-tails of the distribution. Interestingly we can see that the tails of the distribution of $\Delta u(\tau)$ do not vary (if but a little) with height unlike the mean velocity profiles that showed a clear decrease with height. In fact, on the contrary, the tails of the distributions of $\Delta u(\tau)$ are heavier – where a heavier tail corresponds to a more frequent occurrence of extremes – closer to the ground than they are above. This isn't particularly unexpected if we consider the temporal increments to be transformed from velocity increments in space using Taylor's hypothesis.

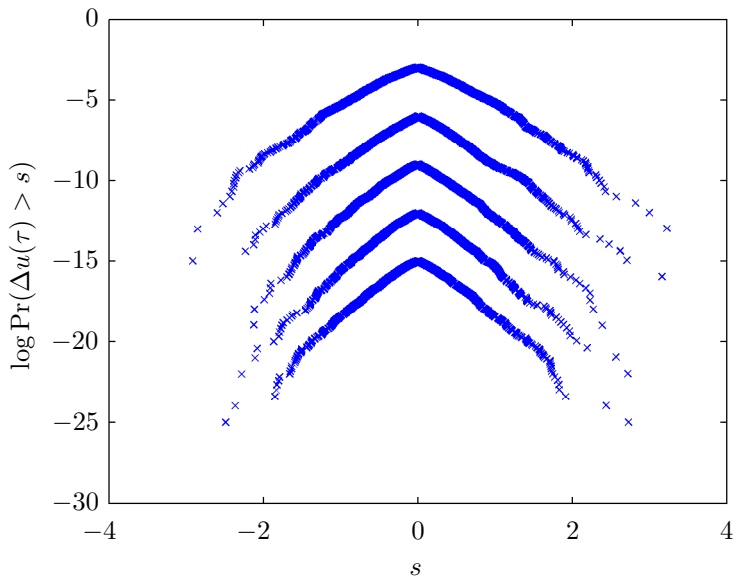

Figure 2.13: Logarithm of exceedance probabilities of $\Delta u(\tau)$, from six twenty-minute samples taken at different heights but for the same measuring run. The time-scale of the increments is 0.4 seconds and the differing sample heights are 10, 50, 75, 100, 125 and 150m (from top to bottom and shifted vertically for clarity).

Re-emphasising now the interest of the Growian experiment, figure 2.14 plots the exceedance probabilities of the vertical increments, $\Delta v(r_z) = v(z_0 + r_z, t) - v(z_0, t)$, where $r_z = 40$, 65, 90, 115 and 140 (again from top to bottom and also shifted vertically for clarity) and $z_0 = 10$m. By performing this kind of an analysis

we are effectively looking at the statistical properties of the different layers of the vertical velocity increments.

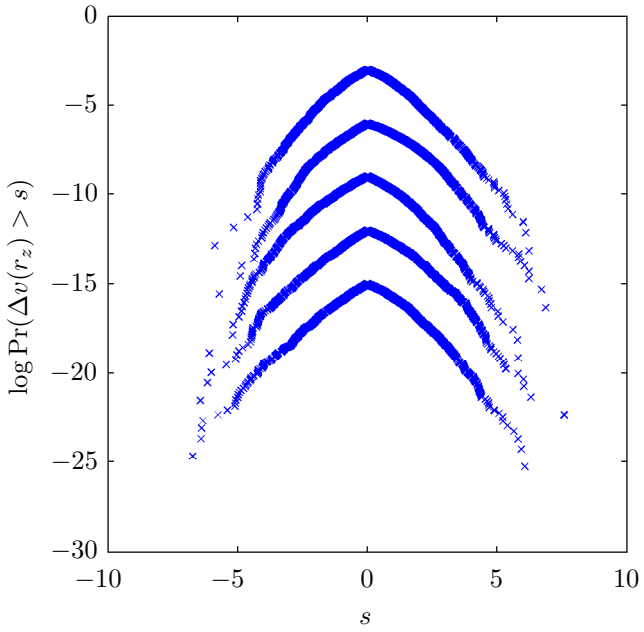

Figure 2.14: The exceedance probabilities of $\Delta v(r_z)$ in a semi-log plot, for r_z = 40, 65, 90, 115 and 140 (from top to bottom; shifted vertically for clarity). Mean meteorological direction for the measuring run is 270°.

	$200 < \bar{\theta}_M \leq 250$	$250 < \bar{\theta}_M \leq 300$	$\bar{\theta}_M > 300$
$\Delta v(r_z)$	anti-symmetric w/ heavier +ve tails	symmetric	anti-symmetric w/ heavier -ve tails
$\Delta u(r_z)$	——— anti-symmetric w/ heavier +ve tails ———		

Table 2.4: Classification of the kinds of (anti-)symmetries observed for different ranges of direction for $\Delta u(r_z)$ and $\Delta v(r_z)$.

The mean meteorological direction of the measuring run used for the distributions in figure 2.14 was 270°. The result, as you can see, is a symmetrical distribution of increments with heavy-tails similar to those observed in the temporal velocity increments. However, although symmetric for $\bar{\theta}_M = 270°$, the general form of the distribution of the increments of $\Delta v(r_z)$ is very much dependent on the

value of $\bar{\theta}_M$. In order to observe a symmetric distribution the value of $\bar{\theta}_M$ needed to be within 270 to 300°, i.e. when $U \approx V$. The slight bias arises due to the prevailing wind direction (there are very few files with $\bar{\theta}_M > 300$. For measuring runs with $\bar{\theta}_M$ outside of this range the distributions became highly asymmetric in $\Delta v(r_z)$. Interestingly $\Delta u(r_z)$ was always asymmetrically distributed in that the heavy-tails of the positive increments were much larger than those of the negative increments (see figure 2.15b). Table 2.4 shows what kind of (anti-)symmetries are observed for different ranges of direction.

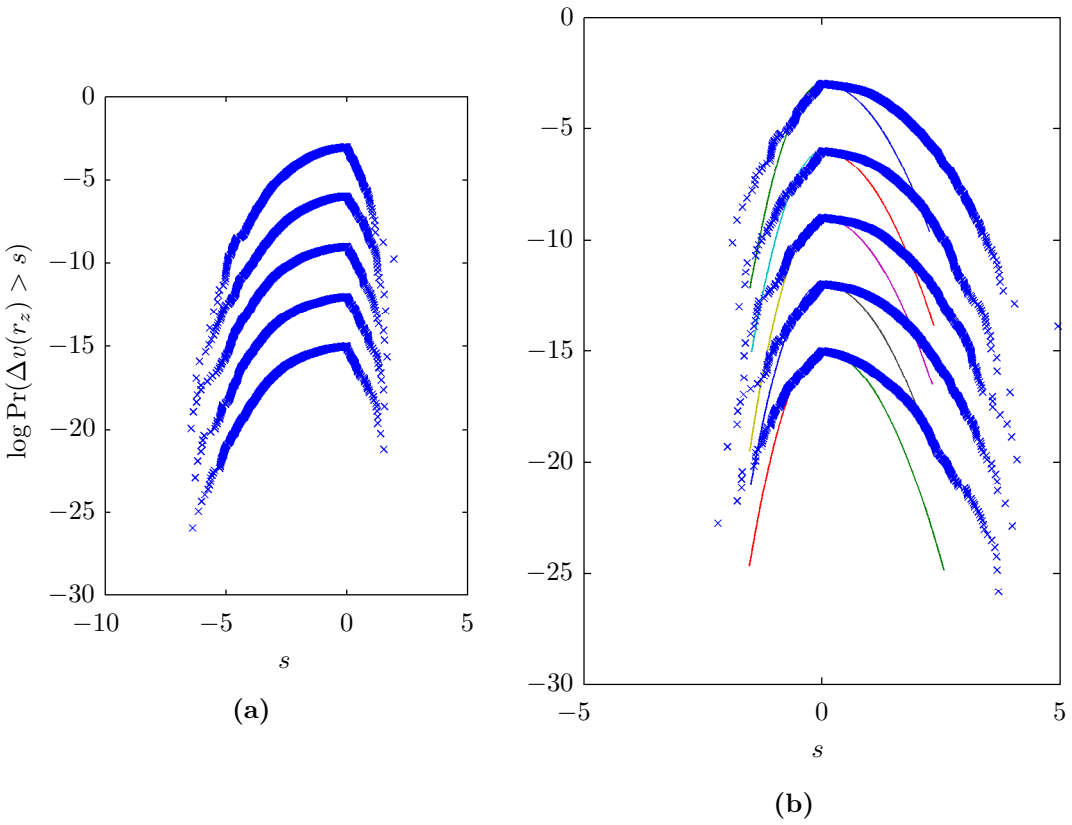

Figure 2.15: The exceedance probabilities of $\Delta v(r_z)$ in a semi-log plot, for $r_z = 40$, 65, 90, 115 and 140 (from top to bottom; shifted vertically for clarity). Mean meteorological directions for the measuring runs are 310° (a) and 220° (b). Solid lines in plot (b) correspond to the Gaussian distribution approximations for the negative and positive increments.

We can suggest that the changes in the skewness of the distribution for $\Delta v(r_z)$ i.e. from heavier positive tails (figure 2.15b) to heavier negative tails (figure

2.15a), for an increasing angle θ_M are the result of a change in sign in v that occurs when the vector passes through the x-axis. Either way we can interpret both kinds of distribution as an increase in velocity with height due to the largely biased number of positive increments. In figure 2.15b we have also included the Gaussian distribution approximations for both the negative and positive increments as a reminder that although skewed they are still non-Gaussian.

Finally, figure 2.16 shows another fairly frequent occurrence that was observed when looking to the distributions. For both vector component increments $\Delta u(r_z)$ and $\Delta v(r_z)$, when the distributions were largely asymmetric a number of measuring runs exhibited a flip in the shape of the distribution at the largest vertical scale (140m) i.e. the lowest plot in figure 2.16 corresponding to the difference between the velocity at 150m and the velocity at 10m. One explanation for this phenomena could be the occurrence of an inversion layer.

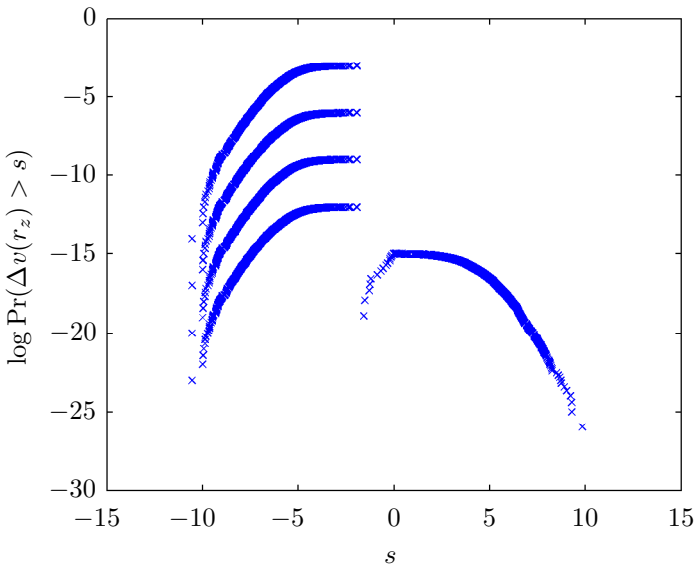

Figure 2.16: Exceedance probability distribution of $\Delta v(r_z)$ in a semi-log plot, for $r_z = 40$, 65, 90, 115 and 140 (from top to bottom; shifted vertically for clarity).

The aim of this section has not been to explain every physical process behind our observations. The aim has instead been to show that there are alternative methods to time-averaging data that enable us to better extract a representative description of the available information. The application of simple statistical

methods to wind data can easily show that the more frequent occurrence of extremes ubiquitous with turbulent phenomena are not only persistent in changing time-scales (with regular vertical spacings), but also persistent in space (with regular time-spacings). This heavy-tailed persistence is strong evidence of a highly intermittent space-time scaling process; a scaling that is not easily observed through mean statistics.

The Corsica Dataset

The 'Corsica dataset' is the result of a wind measurement campaign performed by EDF in the Ersa wind park from the 16th November to the 15th of May. With respect to the measurements, sonic anemometers at 22, 23 and 43m measured three-component wind velocities and temperature at 10Hz. The first anemometer at 22m was positioned directly on the mast. The second, at 23m, was positioned at the end of a horizontal pole with length 2.5m and azimuth 134°. The highest mast at 43m was positioned on a 3m pole on top of the mast. Preliminary analyses on the dataset were also performed by Fuchs [2008].

(a)

(b)

Figure 2.17: (a) photo of the mast and the vertical positioning of the sonic anemometers in the Ersa wind farm; (b) the crest of Torricella over which the turbines are lined up.

Figure 2.18 plots the daily means of the three wind velocity components, temperature, and azimuthal direction over the six-month measuring period. The horizontal velocity components exhibit fairly violent fluctuations when compared to the vertical component. The vertical velocity component remains at about two-orders of magnitude smaller than the horizontal components; this is consistent with classical literature and the reason why the geostrophic approximation is

commonly used.

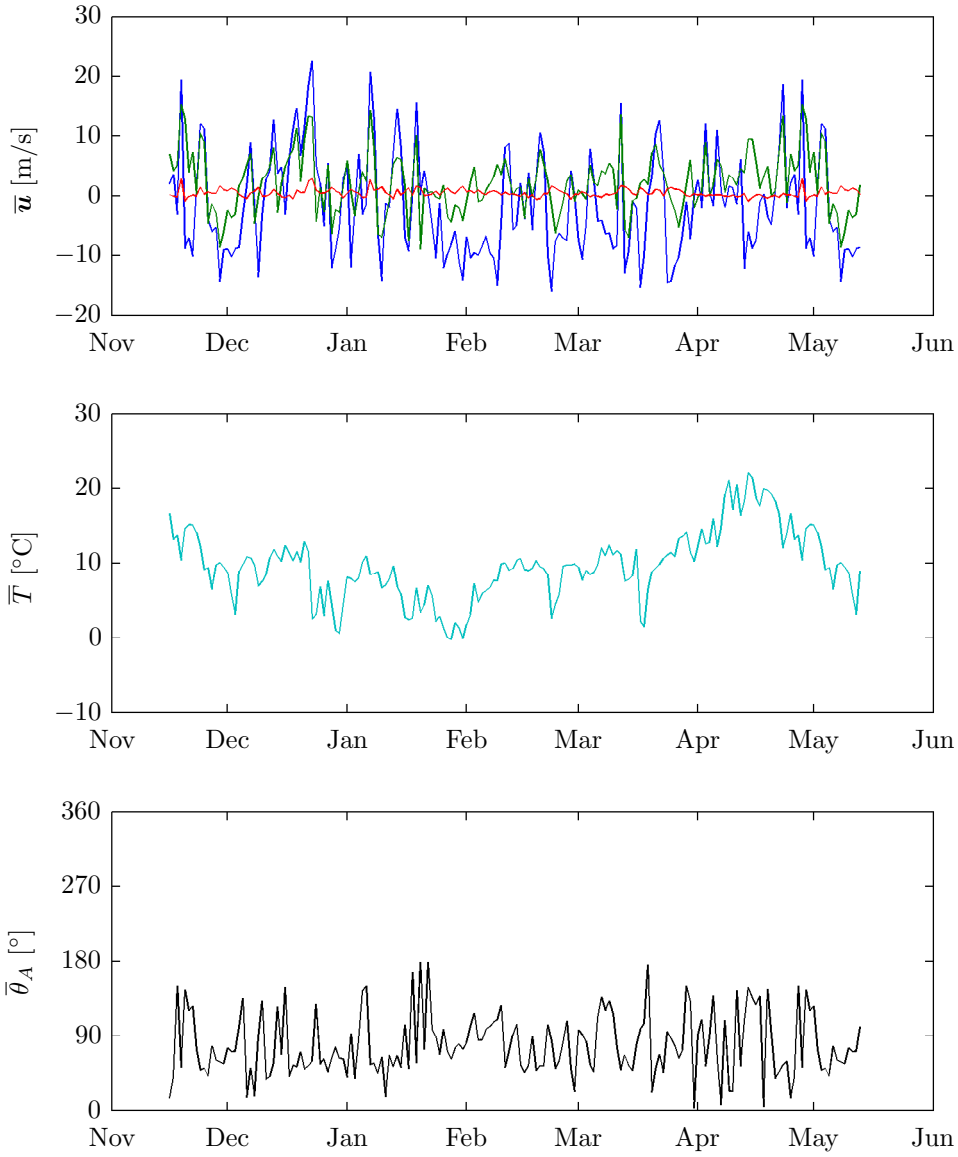

Figure 2.18: Daily means of the three wind velocity components (top most plot) – u (blue), v (green) and w (red), temperature (central plot), and azimuthal direction (lower most plot) taken over the six-month measuring period.

Table 2.5 displays the mean estimates of the variables taken over six-months.

z [m]	$\overline{u}$ [m/s]	$\overline{v}$ [m/s]	$\overline{w}$ [m/s]	$\overline{T}$ [°C]	$\overline{\theta}_A$ [°]
23m	-1.44	1.65	0.23	10.08	77.15
43m	-1.60	2.16	0.49	9.66	78.84

Table 2.5: Six-month mean velocities, temperature and direction.

Topographical Features

The Ersa wind farm is located in the North of Corsica (France), approximately 2km from the coast on the West and 4km on the North and East. Figure 2.19 shows the position of the 13 turbines situated along the crest of Torricella with respect to the measuring mast. The altitudes of the crest range from 480 to 520m with a 30° incline across the East and West faces (see figure 2.20). All of the turbines have a hub height of 60m and are positioned approximately 117m apart from each other.

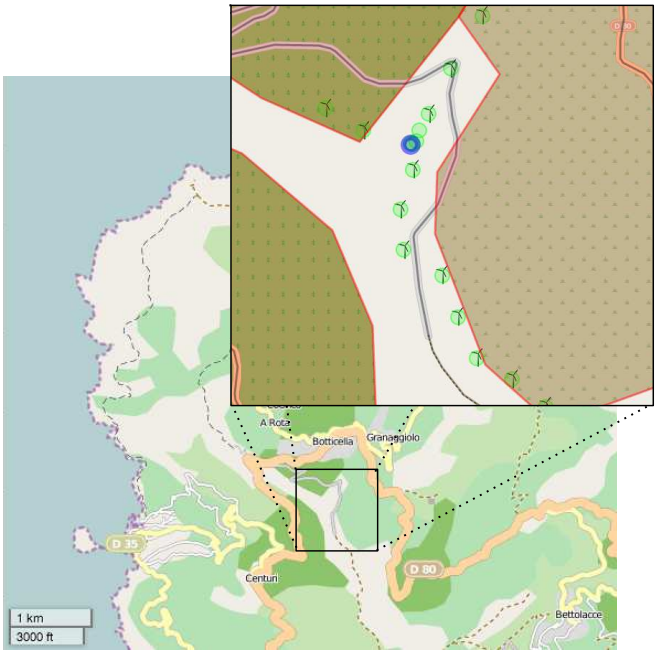

Figure 2.19: Map of the Ersa wind farm. The zoomed portion of the map shows the positioning of the 13 turbines (highlighted by green circles) situated along the crest of Torricella. The blue circle shows where the measuring mast was positioned during the experiment. The exact coordinates of the mast are 42°58.153'N by 9°22.809'E

Figure 2.20: Contour map of the Torricella crest. The red marker plots the location of the measuring mast.

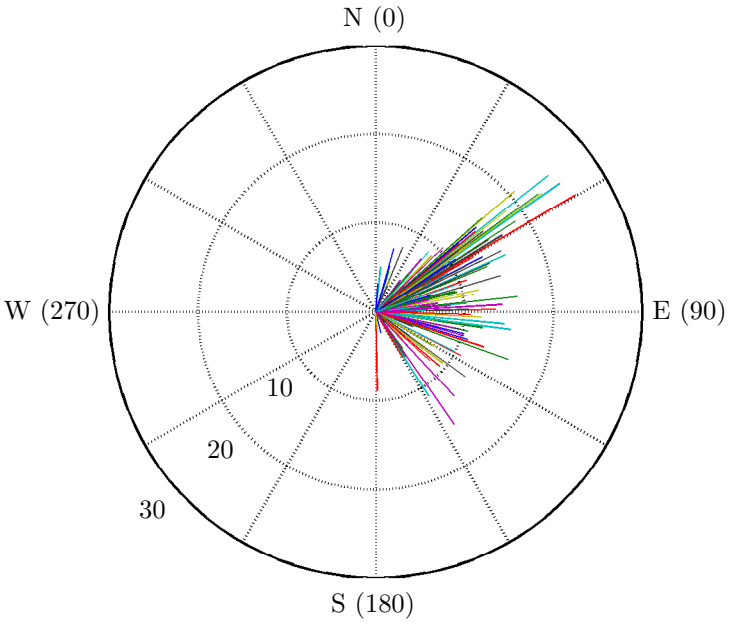

Figure 2.21: Daily mean wind azimuth vectors at 43m. The radial component is measured in [m/s].

Figure 2.21 shows the daily mean wind azimuth vectors at 43m. The predominant Westerly wind direction suggests that, as with the Growian experiment, the wind directions are mainly determined by land-sea temperature gradients. However, unlike the Growian experiment, the returning land-sea breezes that were associated with a temperature inversion are not observed for the Corsica dataset; possibly due to the mountain ranges East of the site. Figure 2.20 is a contour map of the Torricella crest. If we compare the wind vectors with the contour map it is clear the measured winds will have been subject to some sort of orographic lifting.

Smith [1979] gives an overview of some of the phenomena commonly observed when orographic winds arise however the focus of the text is mainly on the buoyancy waves that are created in the wake of the lift which is not much concern to us in this study. In Wu [1985] they suggest that the upper boundaries of different mixing layers undulates with the ridge. We will use this later to show that the increased height of the surface-layer can be seen in scaling analyses of the Corsica dataset. This so-called undulation of the ridge may explain why. Other phenomena associated with orographic winds can be seen in figure 2.22. It illustrates that the winds over hills will be, cooler, faster and more humid.

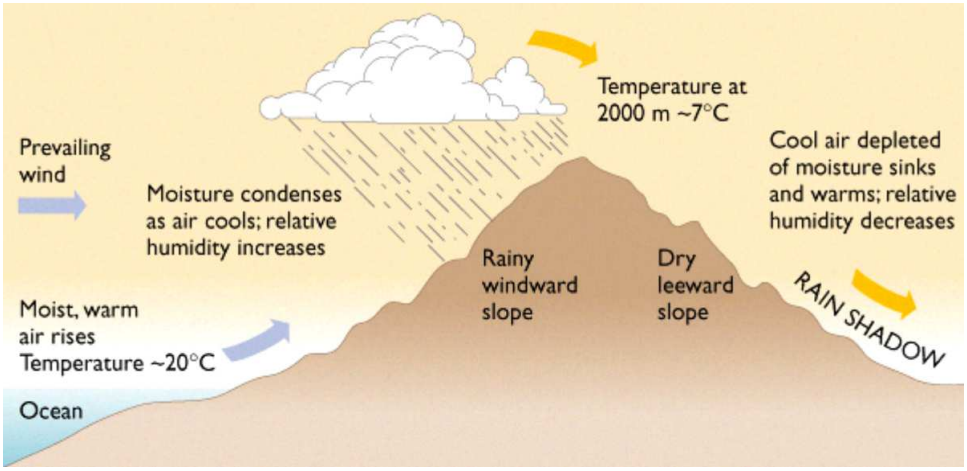

Figure 2.22: A simple diagram of the processes that occur in orographic lifting. Picture is publicly sourced from the internet, the author of the original is unknown.

Data Quality

When using data from devices not positioned directly on top of the mast (those at 22 and 23m), it was necessary to take into account the shadow effects caused by the wind impacting on the mast, thus destroying the quality of the measurements. To check for this problem we took data with daily mean wind passing directly through the mast (48 of the 102 days) and did a cross comparison at different heights. We observed large numbers of anomalous small fluctuations in the vertical component (high frequency noise through spectral representation) being measured at 22m. On closer inspection the anemometer at 22m was found to be positioned directly on the mast unlike the measurements at 23m that were distanced from the mast by a few meters. For simplicity, we decided not to include the 22m measurements in our analyses.

Although confident our data was free of physical interference, corrupt and missing data files made it difficult to have long runs of continuous error free (*clean*) data. Out of the 181 days of data only 10 of the days were time-continuously clean. For non-time-continuous data (independent samples) there were 161 days of clean data.

2.2 Preliminary Scaling Tests

In this section a spectral representation is used to determine the overall scaling behaviour of our data. This is because a random field is *scaling* when its spectrum follows the power law defined in equation 1.6. In equation 1.6 our energy spectrum is a function of the wavenumber $k \propto 1/\ell$. Although we do have measurements in space allowing for separations ℓ, they are insufficient in quantity to merit a spectral analysis. We must therefore invoke Taylor's hypothesis of frozen turbulence on the time-series' of the velocities. To emphasise our analyses dependence on time rather than space we use the frequency $\omega \propto 1/\tau$ instead of the wavenumber. The exponent β of equation 1.6 can be estimated by plotting the spectra on a log-log graph. Computing the (co)-spectrum of two fields (which are identical for the spectrum) is the real part of the scalar product of their Fourier transforms. The Fourier transforms were computed using the fast Fourier transform (FFT) algorithm.

With the use of the FFT algorithm we were restricted (in order to avoid padding) to data of sizes 2^n where $n \leq \log_2(N_s)$ and N_s is the sample size. Thus, given the longest time continuous sample was six-months, the maximum range of scales achievable was of about eight orders of magnitude. While a spectral representation of long runs of data is indispensable to evaluate the overall scaling behaviour and its limitations, sample averaged estimates are used to define the spectral exponents more precisely. Since averaging requires more than one sample, given such a large discontinuous dataset, it was important to choose a suitable sub-sample size to obtain the most amount of information from the data. For the majority of this study we focused on analyses with $\lambda = 2^{15}$ with a brief discussion on the benefits of a larger sample in §2.2.

In the following figures containing spectra, co-spectra and integrated spectra, the frequency is normalised such that $\omega = 2^N/\tau_n = \lambda/\tau_0$, where $\tau_n = 2^n \times \tau_0$ for $n \in [0 : N]$. The smallest time-scale, τ_0, is 0.1 seconds for the Corsica dataset and 0.4 seconds for the Growian dataset.

Scaling In The Growian Data

The Wind

Because the Growian dataset has the wind speed and direction recorded into separate files it was straight forward to calculate their corresponding energy spectrum to check whether either of the quantities scaled as independent variables. It is well known that the velocity exhibits an inertial range assumed to be isotropic and homogeneous. Under these conditions an analysis of the scaling properties of the direction and magnitude (wind speed) separately is useless. However, as we endeavour to show in the remaining section of this chapter, both scale-by-scale, and component-wise scaling properties are far from homogenous and isotropic.

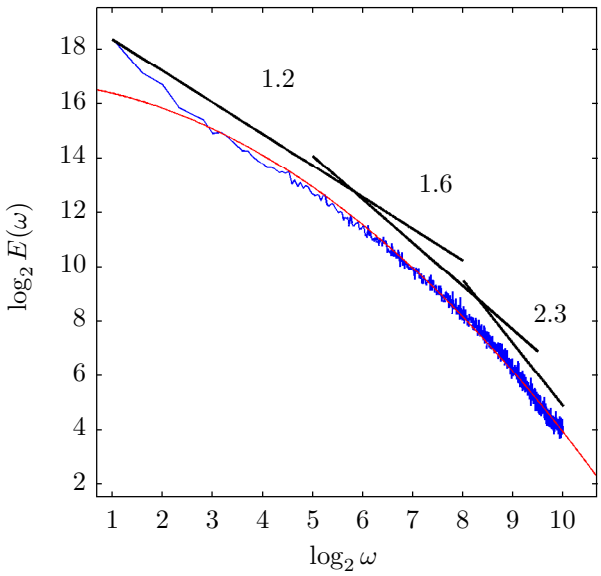

Figure 2.23: Energy spectrum of the wind speed, $\tilde{u}$, taken at 50m from a single twenty-minute measuring run. Only the first 2^{11} measurements are used in the calculation of the spectra. Smallest time-scale corresponds to 0.8 seconds ($\log_2 = 10$). The red line attempts to fit the spectra with a quadratic.

If we consider the wind speed with scaling exponent $\tilde{u}^{H_{\tilde{u}}} = [u^{2H_u} + v^{2H_v}]^{H_{\tilde{u}}/2}$, where H_u and H_v are the scaling parameters computed from equation 1.7, the most likely case that $\tilde{u}$ will be scaling is when u and v are equally correlated i.e. $H_u = H_v$. However, as figures 2.23 and 2.24 show, surprisingly it seems that

only the direction exhibits scaling. The wind speed doesn't really display a single inertial range, rather a mixture of different scaling ranges that we have tried to fit with a series of linear regressions.

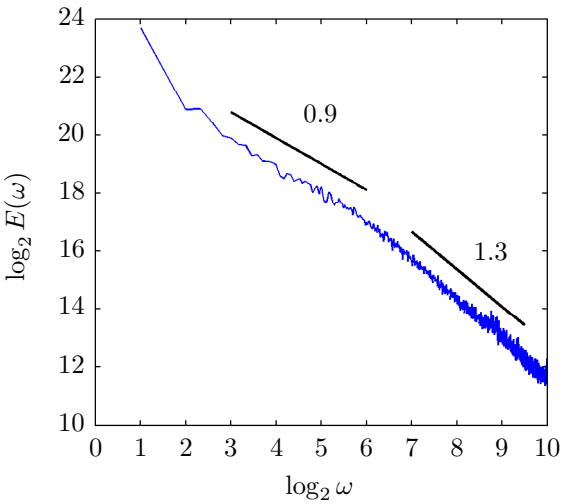

Figure 2.24: Energy spectra of the meteorological direction, θ_M, taken at 50m from the same single twenty-minute measuring run as taken for the wind speed in figure 2.23.).

Figure 2.25 shows the velocity components calculated from the wind speeds and directions of figure 2.23 and 2.24. The statistical scaling exponents for the two fields show that indeed $H_u = H_v$. This is contradictory to our previous statement, implying that there must be a factor that is unaccounted for. In the later sections of this chapter we attempt to explain this behaviour through the anisotropic scaling properties of the horizontal wind components u and v. For now we can consider the mixture of inertial ranges as the combination of the two statistics of two variables with two different scaling exponents valid over two different ranges of scales. The result will be something that looks curved.

The horizontal velocity components exhibit two inertial ranges, the first from 0.8 seconds to 10 seconds, has a scaling exponent close that predicted by Kolmogorov's homogeneous and isotropic hypothesis. The second scaling sub-range starts at 10 seconds and persists up to 10 minutes with a scaling exponent close to -1. In order to explain a -1 power law we remind ourselves first of the dimensional derivation of the K41 spectrum. For high Reynolds number turbulent flows the conservation of the energy flux in the inertial range implies that the energy spec-

trum depends only on the frequency, ω, and the rate of energy dissipation, ε, i.e. $E(\omega, \varepsilon) \propto \omega^{p_1} \varepsilon^{p_2}$. The corresponding dimensions of the variables are: $[\omega] = 1/\ell$, $[\varepsilon] = \ell^2/\tau^3$ and $[E] = \ell^3/\tau^2$. Using the dimensional arguments $\ell^3 = \ell^{-p_1} \ell^{2p_2}$ and $\tau^{-2} = \tau^{-3\eta}$ we find $p_1 = -5/3$ and $p_2 = 2/3$.

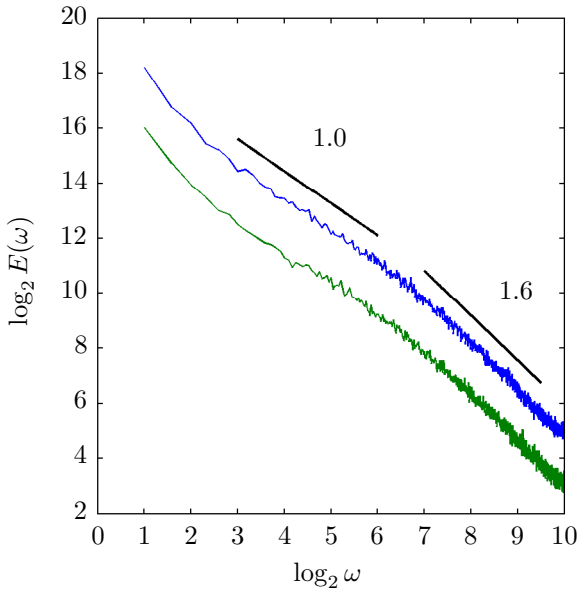

Figure 2.25: Energy spectrums of the u (blue) and v (green) component velocities calculated from the wind speeds and directions (at 50m) of figures 2.23 and 2.24.

Korotkov [1976] postulates that for near-wall length-scales i.e. for $\ell \ll \delta$ (δ is the boundary-layer depth), the effect of self-similarity is no longer total but local, i.e., near the wall, the flow is determined directly by the viscosity, depending only on the length scale ℓ defined through the friction velocity u_*.

It follows that the power spectrum then becomes independent of the distance from the wall and is fully determined by the friction velocity and frequency. Using the same dimensional arguments as we did for the K41 inertial range we find that $E(\omega) \propto u_*^2 \omega^{-1}$. In Korotkov [1976], their results are based on a laboratory experiment boundary-layer. The Reynolds numbers from the experiment are therefore much lower compared those observed in the atmosphere. Also the time-scales of measurement in their experiment are much smaller than the scales we are working with. In fact their largest scale corresponds exactly to our smallest scale (10Hz). They also hypothesise the continuation of the -1 power law when

in fact a steeper slope is observed at their higher frequencies.

Drobinski et al. [2004] is a more recent publication on the atmospheric surface-layer. In their measurements the same high-frequency K41 inertial range is observed followed by an adjoining -1 subrange. An attempt is made to explain these observations through rapid distortion theory (see **?**) requiring a statistical homogeneity assumption. This is contrary to the results we describe in the third chapter of this thesis. Moreover, as in Korotkov [1976], the theory predicts a -1 sub-range but does not account for the increase in scaling exponent empirically observed over the higher frequencies.

A Matter Of Direction

As we discussed in §2.1, the Growian dataset consists of samples containing measurements that may have been influenced by the nearby mast structures. Figure 2.26 shows the velocity spectra taken over the full dataset, i.e. without removing the files that may have been influenced. Both of the plots exhibit a spectral spike at approximately $\log_2 \omega = 9$ (two seconds). Using the mean velocity profiles of the previous sections we get a characteristic length scale of 30m. This is approximately the distance between the anemometer and mast or simply the length of the boom.

Figure 2.27 plots the power spectra of the velocity taken from the outer-most point of mast 3 at 75m with (top) and without (bottom) pre-selecting according to direction, i.e. within the $\pm 90°$ bounds we defined in section §2.1. It is clear that removing the measuring runs whose winds are displaced through the structure results in the disappearance of the spike. This confirms that the spectral spike is due to a shadow effect.

Although pre-selecting the data removes the spectral spike the white noise visible in the spectra of the inner position of mast 3 at 125m does not disappear. We checked the direction and wind speed scaling at this position and it seems that the noise appears only in the directional data. One explanation for this could be weathering, decreasing the inertia of the device.

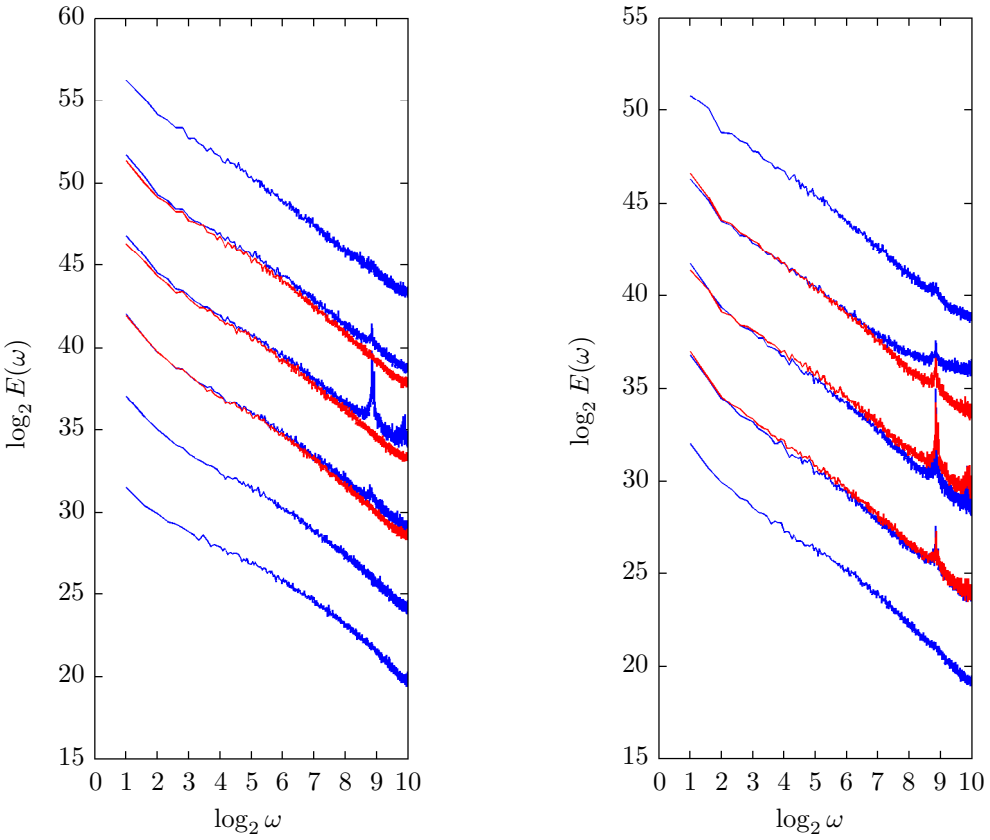

Figure 2.26: Log-log plots of averaged u-component spectra, $E_u(\omega)$, for all $S_{20} \in S$. The plots (shifted) from bottom to top correspond to wind speeds at 50, 75, 100, 125 and 150m measured on Mast 3. The blue and red correspond again to inner and outer positions.

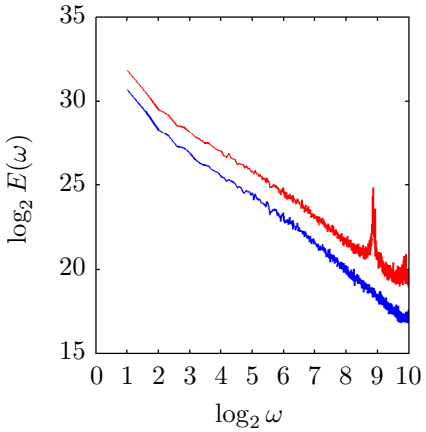

Figure 2.27: Log-log plot of averaged horizontal wind velocity spectra, $E_{u_\perp}(\omega)$, for samples with direction approximately perpendicular to the array (blue) and the corresponding spectra taken for all measuring runs in the dataset.

Performing simple scaling analyses on data proves to be a very powerful and useful tools of analysis. Our previous methods for checking whether there are

influences from the nearby masts consisted of sorting, filtering, and looking for erroneous measurements. The mean velocity profiles showed no real means by which to distinguish between the usable and unusable profiles. On the other hand, using scaling analysis quickly allows us to profit by removing non-scaling data.

Temperature

Figure 2.28 plots the averaged temperature spectra at four heights: 10, 50, 100 and 150m. Unlike the velocity spectra the temperature spectra have a unique scaling exponent over almost all of the time-scales with the exception of the higher frequencies, i.e. from 0.8 to 3.2 seconds, where a white noise behaviour occurs. The scaling exponent, $\beta \approx 2$, is much higher than that of the velocity (1.6) suggesting the temperature fluctuations are dominated by a different process. A scaling exponent of 2 is close to the scaling exponent predicted for a convective process (a BO scaling exponent of 11/5).

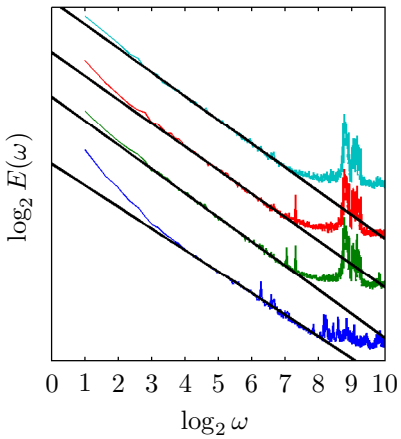

Figure 2.28: Spectral slopes of the temperature at 10, 50, 100 and 150m are: β =1.84, 2.05, 2.00 and 2.02 from bottom to top.

Scaling In The Corsica Dataset

The Corsica dataset is divided into single day sub-samples. In each of these sub-samples there are approximately 860,000 wind and temperature measurements.

We perform the spectral analyses on samples with an integer power of two length. This is because for the scaling analyses that involve the trace and double trace moment methods in the next chapter an integer power of two is necessary so that the upscaling procedure converges to a single value. As previously mentioned this is also useful for the FFT. Calculating the spectra on files with the same length makes it easier therefore to directly compare the scales. Thus, from a file of 860,000 we get a maximum integer power of two sample length 2^{19}. Figure 2.29 compares the ensemble average of the energy spectra of the three wind velocity components and temperature, at the heights 23 and 43m.

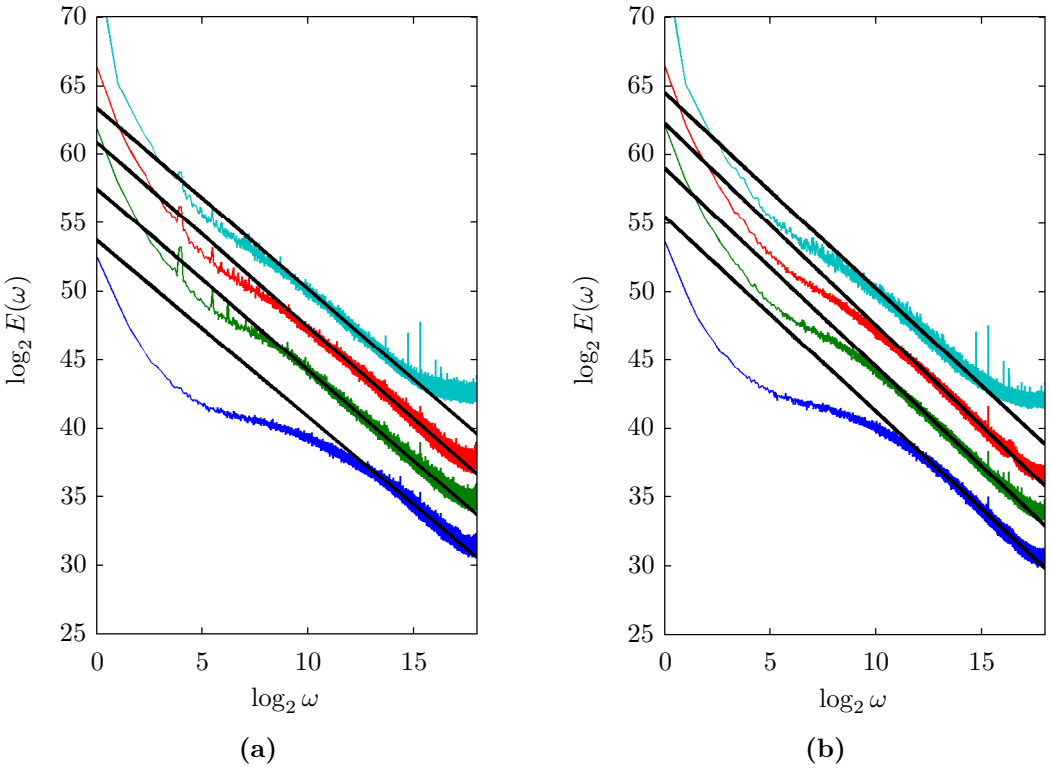

Figure 2.29: Comparison of the ensemble averaged energy spectra of the three wind velocity components u (red), v (green), w (blue) and temperature (turquoise), at the heights 23 (a) and 43m (b).

The spectral analyses show a similar scaling behaviour to that observed in the Growian dataset. The first two subranges over high and mid-frequencies respectively, are again partially in agreement with Kolmogorovs -5/3 law of locally isotropic turbulence. Moreover, for all three velocity components we can

observe an adjoining -1 power law over smaller frequencies. What is particularly striking about this result is the repeatability of the processes for two completely topographical different sites. One of the difficulties that arises with numerical simulation is a need to choose the scales and processes that need to be simulated separately. In order to understand the processes at many scales and for different temperature and topographical situations, numerical computational fluid dynamics models are coupled together (usually even without quantifying numerical error since validation and nudging techniques can be used to correct any error). What is becoming more and more clear is that there are underlying, reproducible (being the key word here) phenomena, independent of location, that arise. The histograms of the scaling exponents of the velocity temperature can be found in Fitton et al. [2011b]. Over the high-frequency range (between 5 and 100 seconds) we find $0.4 < \beta < 1.4$ with mean 1.21 and over the lower-frequency range (between 10 minutes and 2 hours) $0.5 < \beta < 4$). We found no obvious dependence between scaling exponent and wind strength although some slight dependence was observed between the scaling exponent and temperature.

Scaling At Low Frequencies

One of the most interesting features of the Corsica dataset is the continuous-time sample length. Having a continuous run of measurements over a six-month period measured at 10Hz means that an extremely large ratio of scales can be observed. Because of the fluctuating nature of the spectra it is usually better to average the spectra over a few samples to help smooth out the spectral spikes. This unfortunately meant that we couldn't take full advantage of the whole 6-month time-scale. We were however able calculate power spectrums up to the time-scales of a month (averaged over six files). This required the concatenation of around thirty daily samples giving 2^{26} data points in total. Working on files of this size on a basic desktop computer can be very computationally expensive and therefore time consuming. Since it is only the largest scales we are interested in for this kind of analysis we found it was easier to concatenate the multiple files just once and then upscale them to the largest minimum scale, thus reducing the size of the files considerably. Scaling analysis methods can then be calculated on

the – much reduced in size – upscaled data.

Figure 2.30 plots the spectra of the horizontal u-component calculated for three ranges of increasing scale: 0.2 seconds to 15 hours, 15 minutes to $2\frac{1}{2}$ days and 4 hours to a month. For the smallest scale spectral plot we have pre-selected the files to have no scaling break using a simple algorithm. The algorithm determined the position of the breaks based on the minimum and maximum of $\Delta\beta = \beta_{n+1} - \beta_n$ over the range i of $E(\omega_i) \approx \omega_n^\beta$ (from equation 1.6) where $i = 2^n, ..., 2^{n+\Delta n}$ and $n = 1, ..., \log_2(N - \Delta n)$. The value $\Delta n = 5$ was found to be the most appropriate compromise between the best fit and the loss of information at the sample bounds. By pre-selecting the data to scale we have effectively forced a single scaling range.

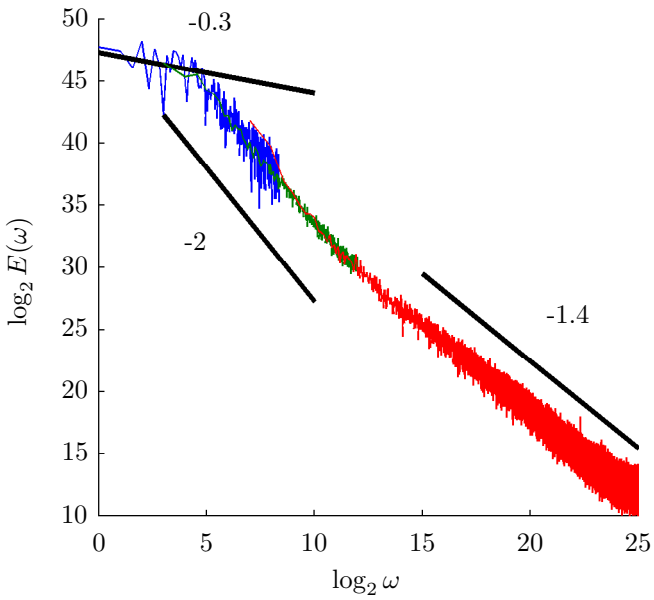

Figure 2.30: Plots of the horizontal u component spectra calculated for three ranges of increasing scale: 0.2 seconds to 15 hours, 15 minutes to $2\frac{1}{2}$ days and 4 hours to a month. For the smallest scale spectral plot we have pre-selected the files to have no scaling break.

From figure 2.30 we can discern three distinct ranges of scaling. A high frequency inertial range similar to K41 as we had also showed in the previous section (but with an adjoining -1 subrange which we have in fact filtered out). The mid-frequency range corresponds to a -2 power law. This is usually associated with Bolgiano-Obhukov buoyancy force effects. Although, alternatively it could also be the result of the break down of Taylor's hypothesis. Taylor's hypothesis

is not applicable when: the mean wind is displaced and/or $u_\delta \sim U$. If Taylor's hypothesis breaks down it may be that we are observing the temporal fluctuations of the large-scale structures themselves (i.e. $u_\delta = U_\delta$) resulting in a Lagrangian scaling exponent $\Delta u(\ell) = \varepsilon^{1/2}\ell^{1/2}$ (see **?**). Moreover, in Wyngaard and Cote [1972] a -7/3 scaling exponent is derived for the turbulent momentum $\langle u_\delta w_\delta \rangle$ and heat flux $\langle w_\delta \theta_\delta \rangle$ co-spectrum in the inertial subrange. Thus, we may try to decide which of the three scaling laws is the most applicable.

Over the very largest scales (4 hours to a month) we find power laws almost exactly comparable with the transitions shown to be climate to weather-climate-plateaus in the century reanalysis of the temperature spectrum in Lovejoy and Schertzer [2013a] (see also Lovejoy and Schertzer [2013b]). The time-scales used for the analysis are from 6 hours to 10 years with scaling exponents $\beta = 2$ and 0.2 from six-hours to $3\frac{1}{2}$ days and from $3\frac{1}{2}$ days to ten years respectively. The exponents and break in scaling are in good agreement with figure 2.30 where the break is at three days with exponents 2 and 0.3 over the same time-scales (largest time-scale is one-month in our case). One thing to note is that the spectra in Lovejoy and Schertzer [2013a] correspond to temporal temperature measurements whereas the spectra in figure 2.30 correspond to the velocity. This suggests that the temperature acts as a passive scalar of the wind over these lower temporal resolutions.

In Pinel et al. [2013] Thermal IR MTSAT-1R images allowed for space-time spectral analyses to be made on thermal IR radiances. The horizontal scaling exponents were found to be the same $\beta = 1.55$ for the space and time-scales 120-5000km and 3-100hrs. Assuming that the thermal IR radiances also act as a passive scalar, the scaling exponents are then much higher than the 'weather-climate-plateau' exponents estimated in Lovejoy and Schertzer [2013a] and in figure 2.30. This suggests that scaling exponents for the temperature and velocity may differ. A result we look into in more detail later in §3.3. In the overlap of time frequencies between figure 2.30 and the thermal IR radiances spectra (<3hrs), a departure to a higher power law ($\beta = 2$) can be seen in both the space and time spectra of the thermal IR radiances. The position of the break occurs at the same temporal scales we have observed in figure 2.30.

The reason we have and will focus on the explanation of this scaling region

is that it is a phenomena that occurs in both of our datasets for all of the measured quantities: 3D velocity, temperature, direction, relative humidity and even vorticity. The latter of these quantities we will come back to later. Figure 2.31 compares the low-frequency ranges from both of the datasets. As was done in figure 2.30 for the Corsica dataset, we have increased the largest time-scale of the Growian dataset by concatenating eight measuring runs ($\lambda = 2^{14}$), giving thirty larger samples when using all of the available files. This was done at 50m so it could be compared with the 43m measurements of the Corsica dataset.

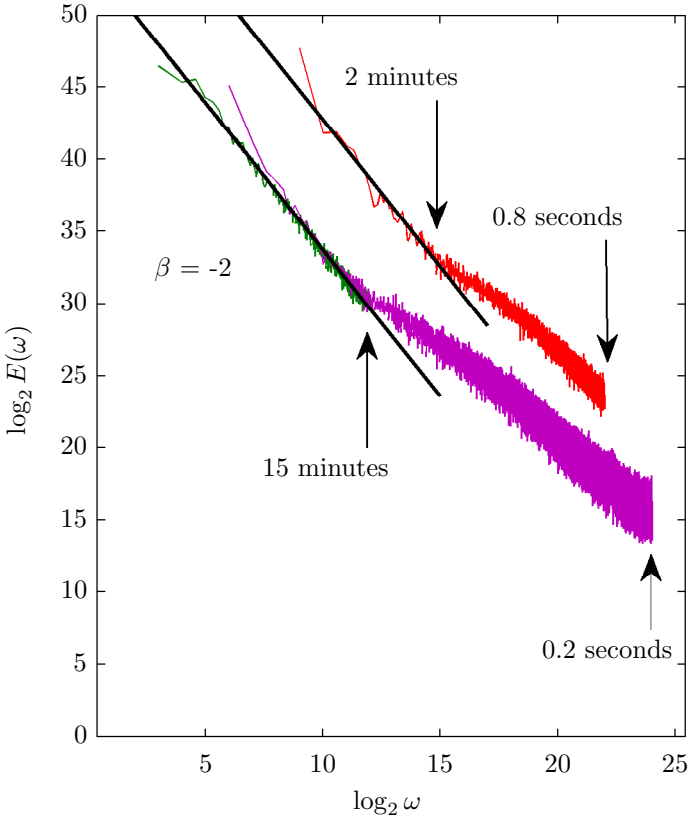

Figure 2.31: Comparison of the low-frequency, u-component, spectral ranges from the Growian (red) and Corsica (purple and green) dataset. The measurements from the Growian dataset are taken from the innermost point of mast at 50m. The Corsica dataset measurements are taken at 43m.

As we can see from figure 2.31 both spectra exhibit a -2 scaling power law over the lower frequencies. In the Growian case the power law starts at two-minutes

and in the Corsica spectra it starts at the lower frequency of 15 minutes. It is possible that this is the effect of an increased surface-layer height; a consequence of the complex terrain of the mountain. Over the higher frequencies we have omitted the filtering criteria that was used to obtain a unique scaling range for the Corsica data of figure 2.30. The result is a very much comparable adjoining -1 range in both of the spectra. Again, it is surprising to see that two very different datasets can result in very similar scaling behaviours. On a final note, we can see that at approximately one hour, in the overlap of the two spectra (green and purple) a discrepancy occurs in the last value of the spectra taken for higher frequencies. A discrepancy that suggests the energy spectra at k_0 is poorly defined.

In order to determine whether or not either the scaling exponent or the onset of the -2 scaling range has some dependence on height figure 3.32 plots the compensated spectra $\omega^{-2}E(\omega)$ at 10, 50, 75, 100, 125 and 150m (Growian). It seems that both the scaling exponent and the frequency of the onset occur independently of any space scale (we can infer a horizontal space-scale separation due to the fixed frequency) in the surface-layer. Because the fixed frequency (30 seconds) corresponds to larger space scales (between 120 and 360m using Taylor's hypothesis) it is possible that we require a larger change in height in order to observe any real change with height.

As previously mentioned the occurrence of a -2 scaling range is not restricted only to the velocity field. Figure 2.33 plots the horizontal u-component velocity and temperature spectra of the Growian dataset at 50m. We can see that for time-scales above 2-minutes both spectra superimpose with scaling exponent 2. This suggests both the temporal fluctuations of the velocity and temperature are dominated by the same process over these time-scales whereas for higher frequencies the processes are different. We see later that this divergence of scaling processes results in a strong component-wise anisotropy. For the lower frequencies one can hypothesis that it is a Bolgiano-Obukhov process that dominates the fluctuations of the horizontal wind. Indeed the geostrophic approximation predicts that the variation in the horizontal velocity components will solely be determined from pressure/temperature differences between layers.

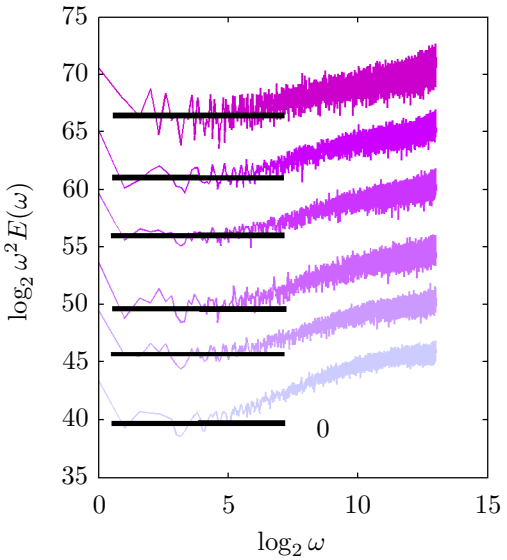

Figure 2.32: Plot of the compensated spectra, $\omega^2 E_(\omega)$, of the u-component velocity at 10, 50, 75, 100, 125 and 150m (Growian). In order to observe the -2 scaling range eight samples have been put together such that $\lambda = 2^{14}$.

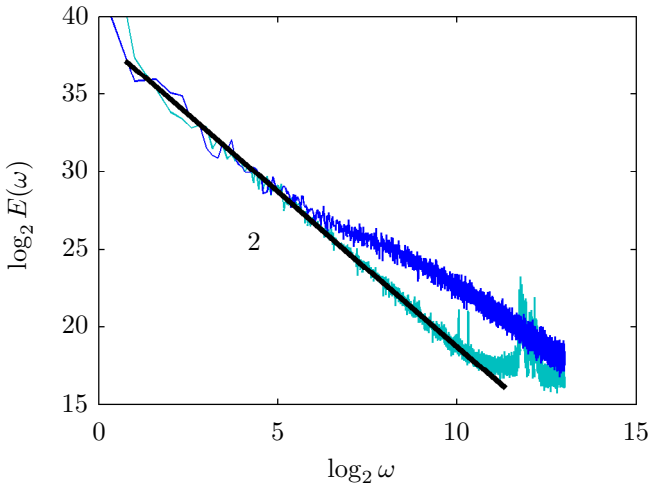

Figure 2.33: Comparison of the horizontal u-component velocity and temperature spectra of the Growian dataset at 50m.

2.3 Scaling Inputs To Wind Industry Community

Wakes

Because the Growian experiment was aimed mainly towards inflow conditions, there are very few samples (20) that displace past the turbine. Our analysis of wakes is therefore based only on the Corsica dataset. In order to analyse the wind data in the wake of the turbines we need to know which data has been influenced by the turbines. This requires the sorting of the data by direction. We sorted the Corsica data according to their hourly means. Figure 2.34 plots the horizontal u-component velocity spectra for files with mean wind directions $\bar{\theta}_M$ that pass in and out of the path of the turbine according to the map in figure 2.19.

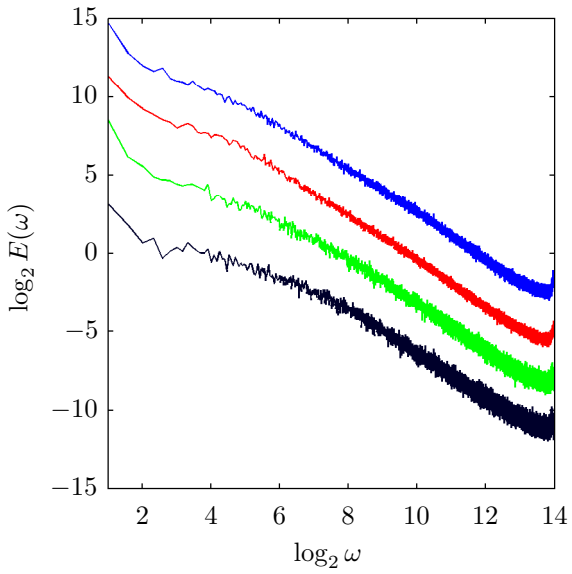

Figure 2.34: Plot of the u-component velocity spectra for samples with $\bar{\theta}_M$ that pass in (blue to red plots) and out (green to black) of the path of the turbine according to the map in figure 2.19.

As we transition in an out of the path of the turbine from the uppermost (blue) plot through to the lowermost (black) plot it is the range of time-scales that scale as approximately -1 that are influenced the most. For the uppermost spectra,

corresponding to samples directly in the wake of the turbine, the adjoining -1 range stops at 10-minutes ($\log_2 \omega = 5$). This is then followed by a highly intermittent ($\beta = 1.3$) Kolmogorov range. For the lowermost plot the -1 adjoining extends up to the much smaller time-scale of one minute ($\log_2 \omega = 8$). The reason for this is explained in terms of a disc approximation to the blades of a turbine. If we imagine that all eddies larger than the disc will be broken into smaller eddies (as is done with grid-generated turbulence) we are increasing the space-time scales of the Kolmogorov range; a range of scales that would normally scale as -1. This process is discussed in more detail in Fitton et al. [2011a] where in particular we show that the largest frequency of the Kolmogorov range corresponds approximately to the diameter of the turbine blades. In Fitton et al. [2011a] we also propose that this break-up of larger structures homogenises the turbulence. A result that could be of use for the wind industry community as it suggest that only the front most turbines in an array need to be resilient to strong wind shearing.

Nacelle Direction And Speed Measurements

Figure 2.35 compares the energy spectra of the wind turbine nacelle direction (blue) and the wind speed measured at the nacelle (green). Over the lower frequencies we loose the -1 scaling range as observed for the inflow conditions of the Growian velocity spectra. This is in agreement with our previous wake observations that hypothesise a forced Kolmogorov range due to the break up of eddies. Remembering that for nacelle measurements we are in the wake due the wake of the complex measuring mast structure in front of the turbine. Over higher frequencies there are indeed complex behaviours that arise that we shall not attempt to explain. What is of particular importance is that there is evidence of scaling. This result could be very important for designing turbine control systems (see Fitton et al. [2012] for other applications of scaling methods to wind energy related topics). At approximately one and two seconds there is evidence of spectral leakage. It may be that at these higher-frequency rapid changes in direction the turbine resonates thus fatiguing the structure. This is mere speculation, however, it would be interesting to find out exactly what this behaviour

corresponds to and how it may affect the turbine.

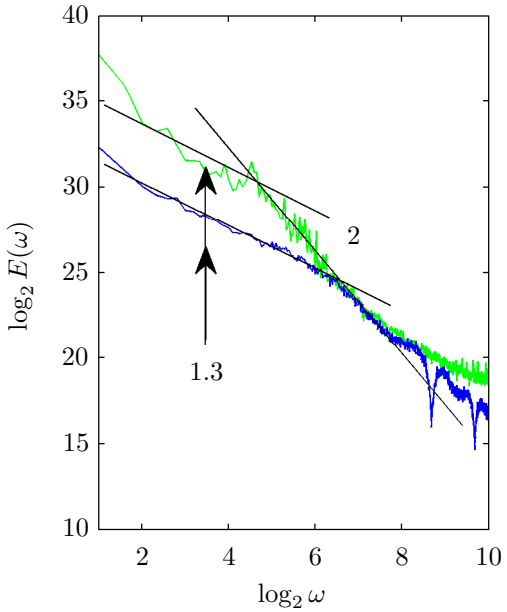

Figure 2.35: Energy spectra of the wind turbine nacelle direction (blue) and the wind speed measured at the nacelle (green).

A Matter Of Distributions

The quantitative nature of the so-called intermittent correction introduced by the function $K(q)$ into the K41 theory (cf. equations 1.9 and 1.16) and into the corresponding values of the spectral exponent β, remembering $\beta = 1 + \zeta(2)$, is detailed throughout the following sections and will directly and indirectly be the focus of the remaining topics. Following the second refined similarity hypothesis, a variety of non-linear velocity structure functions were introduced in order to study the intermittent statistical properties of turbulence (Monin and Yaglom [1975]). The critical point here is that...

> *...the scaling moment functions of turbulent velocity are directly related to the probability distribution functions (PDF's) of the local dissipation rate ε_λ. A proper model of the PDF of ε_λ is sufficient to describe the whole of the statistics of turbulent velocity.* **?**

The prediction of the original log-normal proposal is in reasonable agreement with empirical data for q of sufficiently low order (i.e. $q \leq 3$) for the energy flux density. This also implies for $q > 9$, the discrepancies for the velocity increment, are attributed to the deficiencies in the log-normal assumption, which has been roundly criticised (e.g. Mandelbrot [1974], Yamazaki [1990]; Frisch [1980], Schertzer and Lovejoy [1985a]). With the introduction of discrete and continuous cascade models, a variety of distributions (including improvements on the initial log-normal proposal) have been proposed for ε_λ. We discuss some examples in the next section.

2.4 Summary Of Chapter 2

In this chapter we have made use of the data from two atmospheric wind measurement campaigns from two very topographically different nest sites: the German Growian experiment in a near homogenous terrain setting and the French Ersa wind park experiment where measurements were taken from within a wind farm on top of a mountain in Corsica. Both sites exhibit velocity increment distributions where even coarse time-scale extremes are much more frequent than those previously predicted by Gaussian distributions. It is these frequent intermittent bursts that characterise wind energy's unpredictability, e.g., additional mechanical loads, deviations from expected power production and large short-time power fluctuations.

Since we had a number of different interesting measurements at our disposal we were inclined to see whether or not they were all scaling. The first and most common method for checking whether or not a process is scaling – synonymous with power law probabilities – is to look at the spectra. Analyses on the three-dimensional velocity confirmed it is scaling and that its scaling power laws are in agreement with other literature. The spectral exponent being something that resembled a high-frequency Kolmogorov range with an adjoining lower frequency -1 subrange. Other not so frequently analysed quantities such as the temperature, relative humidity, direction, nacelle wind speed and nacelle direction were also scaling, proving that, particularly for the wind industry, the application of scaling methods to any dimensional combination of the wind velocity can give remarkable insights into a number of different processes, including wake effects.

References: Chapter 2

P. Bernardara, D. Schertzer, E. Sauquet, I. Tchiguirinskaia, and M. Lang. The flood probability distribution tail: how heavy is it? *Stochastic Environmental Research and Risk Assessment*, 22(1):107–122, 2008. URL http://link.springer.com/article/10.1007/s00477-006-0101-2.

T. Burton, D. Sharpe, and N. Jenkins. *Wind energy*. John Wiley&Sons, 2001. URL https://cdp.pageplace.de/cdp/public/publications/DT0154/9781119992721/PREVIEW/9781119992721_preview.pdf.

A. Clauset, C. R. Shalizi, and M. E. Newman. Power-law distributions in empirical data. *SIAM review*, 51(4):661–703, 2009. URL http://www.google.fr/search?client=safari&rls=10_7_4&q=Power+law+distributions+in+empirical+data&ie=UTF-8&oe=UTF-8&redir_esc=&ei=xIt_UcHBD4KIhQeS8oHgCw.

P. Drobinski, P. Carlotti, R. K. Newsom, R. M. Banta, R. C. Foster, and J. L. Redelsperger. The structure of the near-neutral atmospheric surface layer. *Journal of the atmospheric sciences*, 61(6):699–714, 2004. doi:10.1175/1520-0469(2004)061¡0699:TSOTNA¿2.0.CO;2. URL http://dx.doi.org/10.1175/1520-0469(2004)061<0699:TSOTNA>2.0.CO;2.

G. Fitton, I. Tchiguirinskaia, D. Schertzer, and S. Lovejoy. The Anisotropic Multifractal Model and Wind Turbine Wakes. *7th PhD Seminar on Wind Energy in Europe*, pages 115–118, 2011a. URL http://hal.archives-ouvertes.fr/hal-00696108/.

G. Fitton, I. Tchiguirinskaia, D. Schertzer, and S. Lovejoy. Scaling Of Turbulence

In The Atmospheric Surface-Layer: Which Anisotropy? *Journal of Physics: Conference Series*, 318(7):072008, January 2011b. doi:10.1088/1742-6596/318/7/072008. URL http://www.google.fr/search?client=safari&rls=en-us&q=Scaling+Of+Turbulence+In+The+Atmospheric+Surface+Layer+Which+Anisotropy&ie=UTF-8&oe=UTF-8&redir_esc=&ei=b5hUT8DlGsOF8gO5kJTwBQ.

G. Fitton, I. Tchiguirinskaia, D. Schertzer, and S. Lovejoy. Torque Fluctuations In The Framework Of A Multifractal 23/9-Dimensional Turbulence Model. In *EUROMECH Colloquium 528*, 2012. URL http://www.google.fr/search?client=safari&rls=10_7_4&q=Torque+Fluctuations+In+The+Framework+Of+A+Multifractal+23+9+Dimensional+Turbulence+Model&ie=UTF-8&oe=UTF-8&gws_rd=cr&ei=WWI4UqfLIIeN7Qbao4DQCQ.

U. Frisch. Fully developed turbulence and intermittency. *Annals of the New York Academy of Sciences*, 357(1):359–367, 1980. URL http://onlinelibrary.wiley.com/doi/10.1111/j.1749-6632.1980.tb29703.x/abstract.

K. Fuchs. *Multifractal Analysis of the wind in the wind park ERSA*. PhD thesis, Carl von Ossietzky Universitat Oldenburg, 2008.

H. Günther and B. Hennemuth. Erste Aufbereitung von flächenhaften Windmessdaten in Höhen bis 150m. *Deutscher Wetter Dienst, BMBF-Projekt A*, 329372: 1998, 1988.

F. Körber, G. Besel, and H. Reinhold. *Meßprogramm an der 3 MW-Windkraftanlage GROWIAN: Förderkennzeichen 03E-4512-A*. Große Windenergieanlage Bau-u. Betriebsges., 1988.

B. N. Korotkov. Kinds of local self-similarity of the velocity field of prewall turbulent flows. *Fluid Dynamics*, 11(6):850–856, 1976. URL http://link.springer.com/article/10.1007/BF01026403.

L. Laporte, É. Dupont, B. Carissimo, L. Musson-Genon, and C. Sécolier. Atmospheric CFD simulations coupled to mesoscale analyses for wind resource assessment in complex terrain. In *Proceedings of the European wind energy*

conference, Marseille, France, 2009. URL http://www.google.fr/search?client=safari&rls=10_7_4&q=Atmospheric+CFD+simulations+coupled+to+mesoscale+analyses+for+wind+resource+assessment+in+complex+terrain&ie=UTF-8&oe=UTF-8&redir_esc=&ei=BHF-Ue3hNdHB7AaH3ICQAg.

Y. Levi, E. Shilo, and I. Setter. Climatology of a summer coastal boundary layer with 1290-MHz wind profiler radar and a WRF simulation. *Journal of Applied Meteorology and Climatology*, 50(9):1815–1826, 2011. URL http://www.google.fr/search?client=safari&rls=10_7_4&q=Climatology+of+a+summer+coastal+boundary+layer+with+1290+MHz+wind+profiler+radar+and+a+WRF+simulation&ie=UTF-8&oe=UTF-8&redir_esc=&ei=5beDUZqrIaSh7AbOjoHgCw.

S. Lovejoy and D. Schertzer. *The weather and Climate: emergent laws and multifractal cascades*. Cambridge University Press, 2013a.

S. Lovejoy and D. Schertzer. The climate is not what you expect. *Bull. Amer. Meteor. Soc*, 2013b.

B. B. Mandelbrot. Intermittent turbulence in self-similar cascades- Divergence of high moments and dimension of the carrier. *Journal of Fluid Mechanics*, 62(2):331–358, 1974. doi:10.1017/S0022112074000711. URL http://journals.cambridge.org/production/action/cjoGetFulltext?fulltextid=385759.

A. Monin and A. M. Yaglom. Statistical Fluid Mechanics: Mechanics of Turbulence, vol. 2, 874 pp. 1975.

T. Mücke, D. Kleinhans, and J. Peinke. Atmospheric turbulence and its influence on the alternating loads on wind turbines. *Wind Energ.*, 14(2):301–316, March 2011. doi:10.1002/we.422. URL http://onlinelibrary.wiley.com/doi/10.1002/we.422/full.

J. Pinel, S. Lovejoy, and D. Schertzer. The horizontal space-time scaling and cascade structure of the atmosphere and satellite radiances. *Atmos. Res.(submitted)*, 2013. URL http://www.physics.mcgill.ca/~gang/eprints/eprintLovejoy/neweprint/AtmosRes_15.2.13.final.pdf.

D. Schertzer and S. Lovejoy. Generalised scale invariance in turbulent phenomena. *PhysicoChemical Hydrodynamics*, 6:623–635, January 1985. URL http://www.google.fr/search?client=safari&rls=10_7_4&q=Generalised+scale+invariance+in+turbulent+phenomena&ie=UTF-8&oe=UTF-8&redir_esc=&ei=4jSJUMnJA4jIhAfYwoCoCw.

D. Schertzer, P. Bernardara, A. Biaou, I. Tchiguirinskaia, M. Lang, E. Sauquet, H. Bendjoudi, P. Hubert, S. Lovejoy, and J. M. Veysseire. Extrêmes et multifractals en hydrologie: résultats, validations et perspectives. *La Houille Blanche*, (5):112–119, 2006. doi:10.1051/lhb. URL http://www.shf-lhb.org/articles/lhb/abs/2006/05/lhb2006095/lhb2006095.html.

J. E. Simpson. *Sea breeze and local winds*. Cambridge University Press, 1994.

R. B. Smith. The influence of mountains on the atmosphere. *Advances in geophysics.*, 21:87–230, 1979.

M. Wächter, H. Heißelmann, M. Hölling, A. Morales, P. Milan, T. Mücke, J. Peinke, N. Reinke, and P. Rinn. Wind Energy and the Turbulent Nature of the Atmospheric Boundary Layer. *arXiv*, February 2012. doi:10.1080/14685248.2012.696118. URL http://arxiv.org/abs/1202.2245v2.

R. Wu. The influences of orography upon the flow within Ekman boundary layer under the approximation of geostrophic momentum. *Advances in Atmospheric Sciences*, 2(1):1–7, 1985. URL http://link.springer.com/article/10.1007/BF03179731.

J. C. Wyngaard and O. R. Cote. Cospectral similarity in the atmospheric surface layer. *Q.J.R. Meteorol. Soc.*, 98(417):590–603, 1972.

H. Yamazaki. Breakage models: Lognormality and intermittency. *Journal of Fluid Mechanics*, 219:181–193, 1990. URL http://www.google.fr/search?client=safari&rls=10_7_4&q=Breakage+models+Lognormality+and+intermittency&ie=UTF-8&oe=UTF-8&redir_esc=&ei=ZbfnUeaFK4LdOsLOgcgL.

Chapter 3

3.1 Intermittency, Multifractals And Extremes Of The Wind

In §1.2 we mentioned how Richardson believed that the corresponding diffusing particles had 'Weierstrauss-function-like' trajectories. Figure 3.1 illustrates the Weierstrauss-function whose behaviour is seemingly comparable to that of wind farm wind velocity data (figure 3.2). A comparison of such may have validated the assumption made by Richardson. However, further inspection shows the fractal like self-similarity of the function results in a periodic trajectory. This sort of unique periodic behaviour is generally not found in the very intermittent high frequency velocity data that is usually measured. This suggests a more realistic solution may be the combination of more than one fractal function.

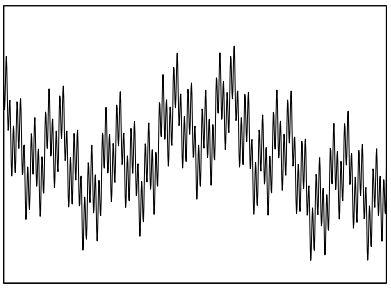

Figure 3.1: Weierstrauss function (fractal).

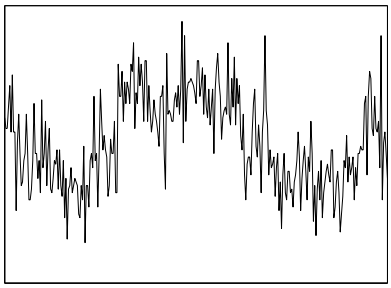

Figure 3.2: Data from wind farm in Corsica (multifractal).

Fractal Geometry

Fractal geometry (Mandelbrot [1977] and Mandelbrot [1982]) provides the simplest non-trivial example of scale invariance and is useful for characterising fractal sets. Unfortunately in wind resource assessment (and more generally geophysics) we are usually much more interested in fields. However, over a wide range of scales, fractal dimensions can still be useful in 'counting the occurrences of a given phenomena' as long as this question is properly posed.

There are several definitions of fractal dimensions that were initially thought of as rather equivalent (see appendix A.3). Fractal dimensions are non-integer generalisations of the concept of the dimension, intuitively understood as measuring the number of points of a given geometrical set A (e.g. a square has more points than a segment, but less than a cube). Most of them correspond to a (non-integer) scaling exponent, with respect to the increasing resolution, λ, of a given estimate of the number of points

$$N_\lambda \simeq \lambda^{D_F(A)} \tag{3.1}$$

where $D_F(A) = 1$ for a segment, 2 for a square, 3 for a cube.

The Co-dimension

In the previous section we defined $D_F(A)$ as the fractal dimension of the fractal set A. We now define the geometrical co-dimension, $c(A)$, of the fractal set A (Mandelbrot [1967], Mandelbrot [1977], Mandelbrot [1982], Falconer [1986], Barnsley [1988], Feder and Bak [1989]) in an analogous way to the definition of a linear sub-space of a finite-dimensional vector space;

$$c(A) = D - D_F(A). \tag{3.2}$$

A similar relation can be derived for the probability that a ball, B_λ, with scale ratio, λ, is contained in the fractal set A such that

$$P(B_\lambda \cap A) \simeq \lambda^{-c(A)}.$$

The corresponding definition of the statistical co-dimension is in fact much more general than the geometrical one (Schertzer and Lovejoy [1994]). The details of the relationship between the geometrical and probabilistic definition of the co-dimension are not discussed here but can be found in appendix A.4. The reason for using the co-dimension as opposed to the fractal dimension will become clearer in the following sections.

The β-Model

One of the simplest cascade models that takes the intermittency of turbulence into account using fractals is the β-model by Novikov and Stewart [1964], Mandelbrot [1974] and Frisch et al. [1978]. This is done by assuming the cascading eddies are in either a 'dead' or 'alive' state where the probability of being alive corresponds to the number of occurrences out the total, i.e., by equation 3.1

$$P(\mu_\varepsilon = \lambda^c) \simeq \frac{N_\lambda(\textsc{Alive})}{N_\lambda(\textsc{Total})} = \frac{\lambda^{D_F}}{\lambda^D} = \lambda^{-c}, \tag{3.3}$$

where the index, ε, of the multiplicative increment, μ_ε, indicates that we are producing the energy flux field and not the velocity field. The corresponding dead state probability is therefore simply

$$P(\mu_\varepsilon = 0) \simeq 1 - \lambda^{-c} \quad (\textsc{Dead}). \tag{3.4}$$

The *boost*, $\mu_\varepsilon = \lambda^c > 1$ of equation 3.3, is chosen such that the probability of all events occurring satisfies the conservation of the energy flux density defined in equation 1.3, i.e.

$$\langle \varepsilon_n \rangle = \langle \varepsilon_0 \rangle \implies \langle \mu_\varepsilon \rangle = 0 \cdot (1 - \lambda^{-c}) + \lambda^c \cdot \lambda^{-c} = 1.$$

Thus we have a cascade where the number of *daughters* of a given *mother-eddy* are chosen such that the fraction of the volume occupied is decreased by the factor $\beta = \lambda^{-c}$ $(0 < \beta < 1)$ hence the name β-model. In terms of the co-dimension, we see from equation 3.2 in the previous section, that the larger the co-dimension, c, the less of the fraction of space is occupied by the fractal set

of the support dimension (see figure 3.3). A consequence of the variation in c is that as $n \to \infty$ so does ε_λ, i.e. ε_λ is singular in an analogous way to the Dirac δ-function for example. For any n, the energy density flux depends on the same fractal co-dimension.

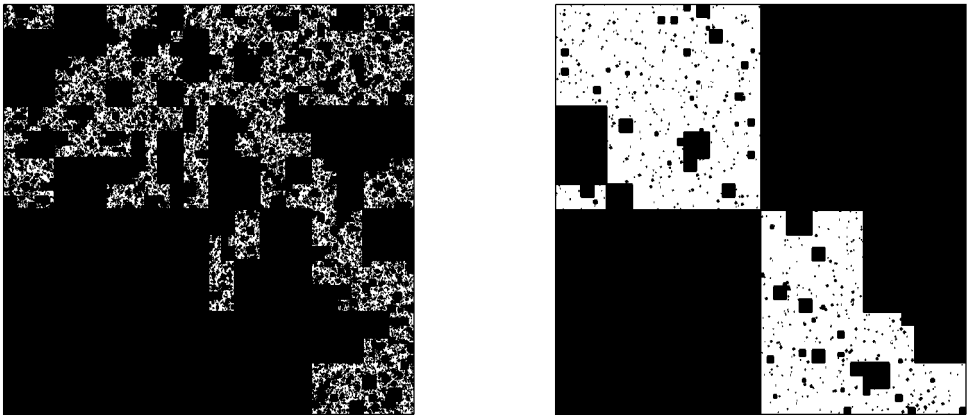

(a) **(b)**

Figure 3.3: Plots of the energy density flux, ε_n, cascade using the two-dimensional β-model for varying co-dimensions, $c = 0.4$ and 0.9, (plots a and b respectively) and scale ratio, $\lambda = 2^7$. Notice that even for the most basic of cascade models we see realistic comparisons with turbulent energy flux density distributions in that they are proportional to the intensity of the flux at small scales, i.e. for low $c = 0.1$ – abundant and evenly distributed energy flux densites, and for high $c = 0.9$ – sparse and concentrated.

Multifractal co-dimension Functions

In the β-model example we calculated the fractal dimension of the occurrences of eddies in a support dimension for two possible states 'alive' and 'dead'. The result is an intermittency occurrence quantified by the unique co-dimension as seen in figure 4.1. A comparison of figure 3.3a and 3.3b with the energy flux density in figure 1.5 shows that although the field we are generating with the β-model *is* 'intermittent' the magnitude of the distribution of the flux is homogeneous (in contrast to the highly variable energy flux density of figure 1.5).

The reason for the homogeneity or lack of heterogeneity is simply because we did not consider the intensity of each of the eddies, only their presence or absence. It has previously been reported by Schertzer and Lovejoy [1984a] that a better concept than the fractal object is that of the multifractal field. The phenomenon studied in this case are characterised by a hierarchy of many fractals (hence multi-fractal) corresponding to regions over which the field intensity exceeds a given threshold (by taking the logarithm base λ of this intensity, we obtain the corresponding singularity which is singular for the homogeneous case). For a non-homogeneous case each singularity is then characterised by a fractal dimension. The non-uniqueness of a fractal dimension requires a co-dimension function dependent on the orders of singularities. It will be this function that will be discussed in detail throughout the following sections.

The α-Model

Because the β-model turns out to be a poor approximation to turbulence (unstable under perturbation) we must consider a more realistic alternative to the simplicity of the 'dead' or 'alive' dichotomy. One such consideration was the α-model (Schertzer and Lovejoy [1984b, 1985b]) named because of the divergence of moments (we will come back to this later, also see appendix A.5) with exponent α. Rather than only allowing eddies to be either 'dead' or 'alive' the α-model considers a more realistic α-instability in which each state can be either 'more' or 'less' active (see figures 3.5a, 3.5b, and Lovejoy and Schertzer [1986] for further examples).

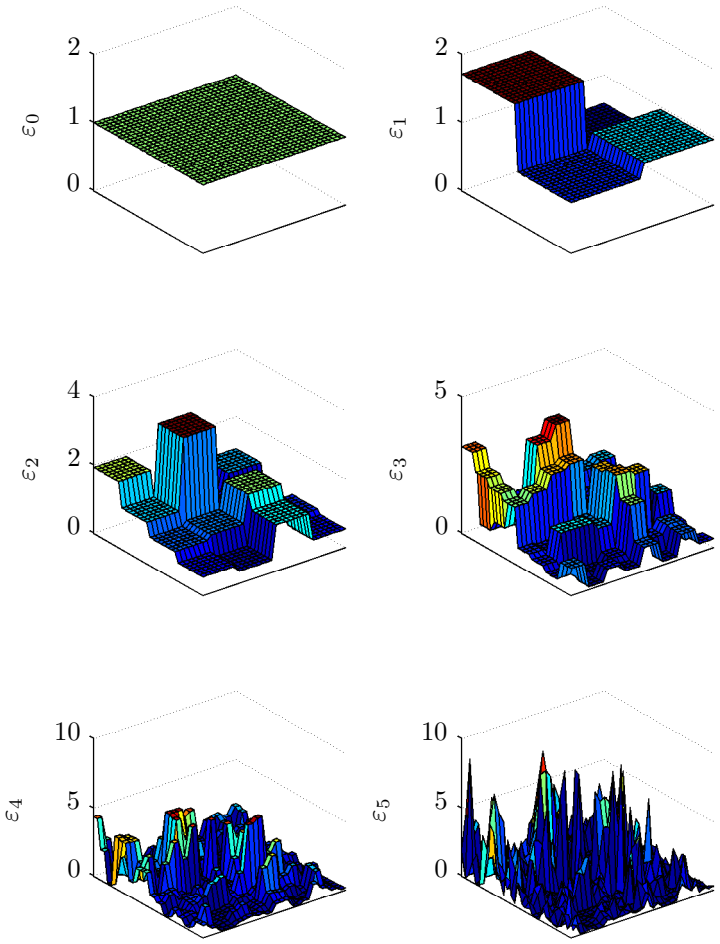

Figure 3.4: Plots of the energy density flux, ε_n, cascade using the two-dimensional α-model for co-dimension, $c = 0.2$ and $\alpha = 1.5$; the scale ratio, $\lambda = 2^6$. Comparisons show varying divergences of moments, α, with fixed co-dimension and fixed scale ratio. We can see from the final step of the model at ε_6 (and in fact all steps prior to) we have a much more heterogeneous distribution of energy flux densities contrary to the homogeneous distribution of the β-model (figure 3.3). As with the β-model, the magnitude of each energy flux density is proportional to a singularity exponent i.e. defined by a unique co-dimension. Because we have a non-unique singularity we must therefore have many fractal dimensions (and therefore a co-dimension function, hence multifractality).

The model randomly distributes the occurrence of each eddy at each generation corresponding to the following binomial process (see figure 3.4):

$$P(\mu_\varepsilon = \lambda^{\gamma_+}) \simeq 1 - \lambda^{-\gamma_+} \quad \text{(INCREASE)} \tag{3.5}$$

$$P(\mu_\varepsilon = \lambda^{\gamma_-}) \simeq \lambda^{-\gamma_-} \quad \text{(DECREASE)} \tag{3.6}$$

where

$$\gamma_+ = \frac{c}{\alpha}, \quad \gamma_- = \frac{c}{\alpha'} \quad \text{and} \quad \frac{1}{\alpha} + \frac{1}{\alpha'} = 1.$$

Note the β-model is a special case of the α-model in which $\gamma_- \to -\infty$ and $\gamma_+ = c$. Because the β-model has a unique singularity, c, corresponding to a unique fractal dimension, D_F, it is defined as a mono-fractal model.

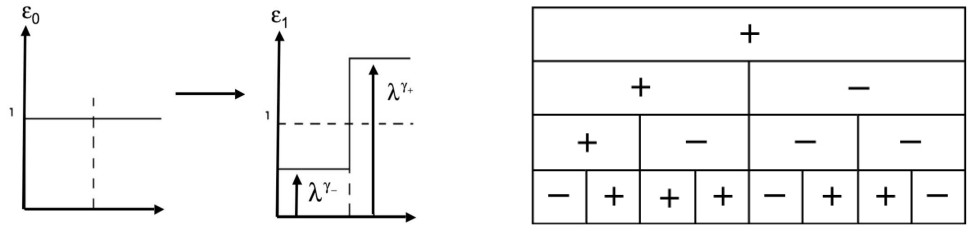

(a) A schematic picture of the α-model. At each step, uniform intervals (left) are divided into fixed λ subintervals (where $\lambda = 2$ here) and then each is randomly multiplied by either λ^{γ_+} or λ^{γ_-} (with $\gamma_+ > 0$, an increase, or $\gamma_- < 0$, a decrease).

(b) Schematic of a tree of increases ('+') or decreases ('-') for a one-dimensional α- or β-model with probabilities defined by equations 3.5 and 3.6.

Figure 3.5: Schematics of the α- and β-model.

As with the β-model it is necessary to satisfy the condition $\langle \mu_\varepsilon \rangle = 1$ such that:

$$\langle \mu_\varepsilon \rangle = \lambda^{\gamma_+}\lambda^{-c} + \lambda^{\gamma_-}(1 - \lambda^{-c}) = 1. \tag{3.7}$$

The above equation is in itself evidence that the α-model is a multifractal model since there exist two singularities, λ^{γ_+} and λ^{γ_-}. Again this means there is more

than one fractal dimension related to the singularities through the co-dimension hence validation of the terming 'multifractal model').

Defining Multifractals

By re-normalising discrete cascades (see appendix A.6) the multifractal field, ε_λ, at the ratio of scale λ can be written

$$P(\varepsilon_\lambda \geq \lambda^\gamma) \simeq \lambda^{-c(\gamma)}. \tag{3.8}$$

Each value of ε_λ corresponds to a singularity (where strictly speaking 'singularity' applies only to $\gamma > 0$ i.e. when $\varepsilon \to \infty$ for $\lambda \to \infty$, when $\gamma < 0$ it is a 'regularity') of order γ and co-dimension $c(\gamma)$. Moreover, we can define the multifractality with respect to $c(\gamma)$, i.e. the multifractality corresponds to the non-uniqueness of c. It is beyond fractal geometry, where uniqueness of the fractal (co)-dimension is the rule. Figure 3.6 illustrates why for a multifractal field two scaling thresholds, γ_1 and γ_2, do not correspond to the same co-dimension.

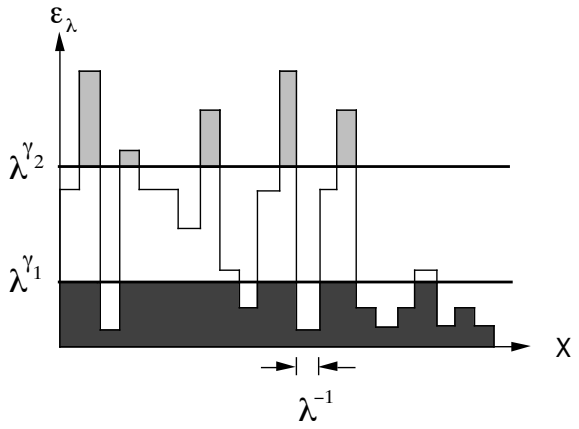

Figure 3.6: A schematic illustration of a multifractal field analysed over a scale ratio λ, with two scaling thresholds λ^{γ_1} and λ^{γ_2}, corresponding to two orders of singularity: $\gamma_1 > \gamma_2$.

On a final note, equation 3.8, considers the probability distribution of events above a given (scaling) threshold; therefore we consider 'exceedance probability distributions', $p(\varepsilon_\lambda) = P(\varepsilon_\lambda \geq \lambda^\gamma)$, rather than the the standard 'cumulative probability distribution function' (CDF), $F(\varepsilon_\lambda) = P(\varepsilon_\lambda < \lambda^\gamma)$. Both are obviously related by $p(\varepsilon_\lambda) = 1 - F(\varepsilon_\lambda)$. Throughout the rest of the report we will use

the term 'probability distribution' in the sense of exceedance probability distribution (and therefore for events above a given (scaling) threshold). This is in fact a more appropriate form of notation anyway since it is usually velocity thresholds we require.

Lets consider now some of its general properties; the first being that due to its very definition, $c(\gamma)$ is an increasing function of γ. The second also readily derived by considering moments, is that it must be convex. Thus, because $\langle \varepsilon_\lambda \rangle \simeq \lambda^{\gamma_1 - c(\gamma_1)}$ where γ_1 is the singularity contributing to the mean ($q = 1$); the derivative of the function (now denoted using Leibniz's notation) is unity i.e. $c'(\gamma_1) = 1$ and since $\langle \varepsilon_\lambda \rangle = 1$, we obtain $\gamma_1 = c(\gamma_1) = C_1$. The properties of the $c(\gamma)$ function will be discussed in more detail in section §4.1.

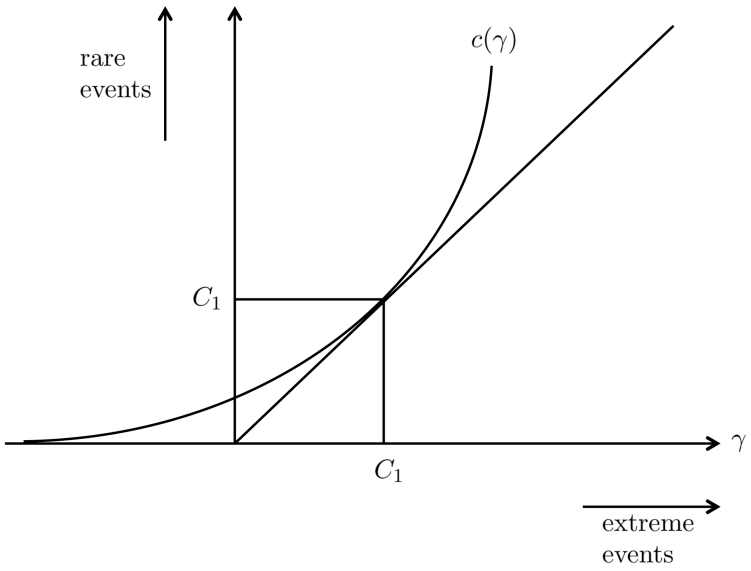

Figure 3.7: A schematic illustration of a conserved multifractal $c(\gamma)$, showing relations $c(C_1) = C_1$ and $c'(C_1) = 1$ where C_1 is the singularity of the mean.

Above we defined the co-dimension function as the statistical scaling exponent of the probability distribution of the energy flux density. A schematic illustration of a multifractal co-dimension function is given by figure 3.7.

Bare And Dressed Cascades

From the α-model we were able to derive a continuous distribution relationship between the probability of exceedence of the energy flux density and the co-dimension function at non-finite scales λ i.e.

$$P(\varepsilon_\lambda \geq \lambda^\gamma) \simeq \lambda^{-c(\gamma)}.$$

However, we must now pose the question:

> What are the consequences of the singular behaviour when reaching the small scale limit $\lambda \to \infty$ and where does this fit into reality?

We must pose this question simply because in reality we will never come across an infinitely small sample. To deal with this Schertzer [1987] introduced the terms 'bare' and 'dressed' (see figure 3.8):

1. Respecting $\varepsilon_\lambda \simeq \lambda^\gamma$ for all $\gamma > 0$, one has $\varepsilon_\lambda \to \infty$ as $\lambda \to \infty$; and $\langle \varepsilon_\lambda \rangle = \lambda^{K(q)} \to \infty$ for all $q > 1$ (since $K(q) > 0$ for $q > 1$). This singular behaviour means that if a limit exists, it is not in the sense of functions. We really have something analogous to a Dirac delta-function, as was discussed with the β-model. This is a 'generalised' function defined as a limit of functions and only meaningful if we integrate over it. The limit is in fact a density of measure, i.e. well defined limits only exist for the fluxes $\Pi_\lambda(A) \to \Pi_\infty(A)$ which are integrals over the flux densities, ε:

$$\Pi_\infty(A) = \lim_{\lambda \to \infty} \Pi_\lambda(A) = \lim_{\lambda \to \infty} \int_A \varepsilon_\lambda . d^D \boldsymbol{r}.$$

   What we find is the integration has a drastic calming effect on the variability of the energy flux density. The singular nature of the limit $\lambda \to \infty$ and the possibility of smoothing by integration distinguishes the 'bare' cascade quantities, obtained after proceeding down to scale λ (downscaling), from the 'dressed' cascade quantities obtained after integration of the complete cascade over the same scale $\ell = L/\lambda$ (upscaling). In general, the divergence implies the dressed quantities will have much larger fluctuations.

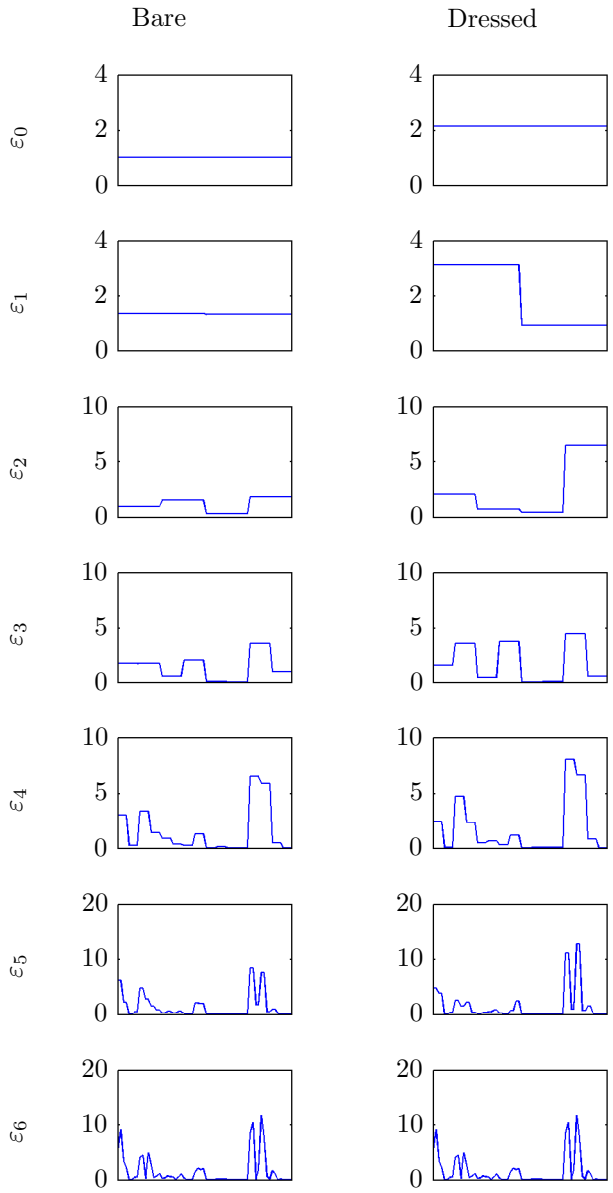

Figure 3.8: An example of an α-model cascade. The left hand side shows the step by step construction of a ('bare') multifractal cascade starting with an initially uniform unit flux density. The right hand side shows the result of spatial averaging (to the same scale as the left image) of the cascade developed over the full range (a factor 2^7 here, bottom centre): the 'dressed' cascade discussed in the text. The vertical axis represents the density of energy flux density ε to smaller scales which is conserved by the non-linear terms in the dynamical equations governing fluid turbulence. At each step the horizontal scale is divided by two, and independent random factors are chosen either < 1 or > 1.

2. If ε is considered at individual points, then as we add in more and more cascade steps, the 'incipient' singularity values, defined at finite λ, are

$$\gamma_\lambda = \frac{\log \varepsilon_\lambda}{\log \lambda},$$

and will not converge to a value γ_∞ but will undergo random walks as λ is increased.

Divergence Of Moments

In the previous section we defined the fundamental difference between the 'bare' and 'dressed' cascade properties i.e. the former all have moments finite (since by definition, for bare quantities λ is finite) whereas the latter will generally have divergence for all moments greater than a critical value q_D which depend on the dimension of space over which the process is integrated (see figure 3.8 for a schematic).

To define the dressed flux, start by defining the resolution flux $\Pi_\Lambda(A)$ over the set A:

$$\Pi_\Lambda(A) = \int_{A\varepsilon_\Lambda} d^D\boldsymbol{r},$$

where Λ is the highest resolution. We can now define the 'partially dressed' flux density $\varepsilon_{\lambda,\Lambda(d)}$ as:

$$\varepsilon_{\lambda,\Lambda(d)} = \frac{\Pi_\lambda(B_\lambda)}{\mathrm{vol}(B_\lambda)}$$

where $\mathrm{vol}(B_\lambda) = \lambda^{-D}$ is the D-dimensional volume of a ball (interval, square, cube etc.) of size L/λ and the '(fully) dressed flux density' as:

$$\varepsilon_{\lambda,\Lambda(d)} = \lim_{\Lambda\to\infty} \varepsilon_{\lambda,\Lambda(d)}$$

Now we can use the factorisation property of the cascade; the independence of the large and small scale multiplicative factors

$$\varepsilon_\Lambda = \varepsilon_\lambda T_\lambda(\varepsilon_{\Lambda/\lambda})$$

where the operator T_λ increases the scale – 'zooms' by a factor λ. This equation should be understood in the following way – to obtain a fine scale cascade (resolution Λ) we may take a lower resolution (λ) cascade and multiply each of the λ resolution boxes (balls) by independent cascade processes each developed over a range of scales Λ/λ and reduced in size by factors of λ. This leads to:

$$\varepsilon_{\lambda,\Lambda(d)} = \varepsilon_\lambda \cdot \varepsilon_{\Lambda,\lambda(h)}$$

where ε_λ is the usual bare density (accounting for variability at scales larger than the observation scale) and the density $\varepsilon_{\Lambda,\lambda(h)}$ (accounting for variability at scales smaller than the observation scale) can be said to be 'hidden' (hence h) since it corresponds to the scales with which we average over.

It can be shown (Schertzer [1987]) that the integration of ε_λ on sets of dimension D leads to statistical discrepancies ($\lambda \to \infty$) as soon as the order of moments q becomes greater than a certain critical value q_D defined by:

$$K(q_D) = (q_D - 1)D; \quad q_D > 1. \tag{3.9}$$

The divergence of moments of a random variable X i.e. ($\langle X^q \rangle = \infty$ for $q > q_D$) is the 'hyperbolic' (algebraic) fall off of the probability distribution. The exponent of this q_D tail of probability, which characterises the relative frequency of extreme events (Schertzer [1987], Schertzer and Lovejoy [1991]), is therefore nothing but the order of the critical statistical discrepancy; thus we have:

$$P(X \geq s) \approx s^{q_D} \iff \langle X^q \rangle = \infty, \quad q > q_D \tag{3.10}$$

where s is a threshold of intensity. This statistical behaviour is a consequence of the fact that the sum of the contributions is dominated by the contribution that is the strongest, that is, rare events have a dominant contribution (Tessier et al. [1993]). We may note that using thermodynamic analogues of a multifractal scaling moment function (e.g. where $K(q)$ is the analogue of a thermodynamic potential, q; the inverse of temperature – discussed in more detail in §4), the divergence of the theoretical moments (i.e. for an infinite number of samples) corresponds to a first-order transition over finite samples at the temperature $1/q$

(see Schertzer et al. [1993] and Schertzer and Lovejoy [1993]).

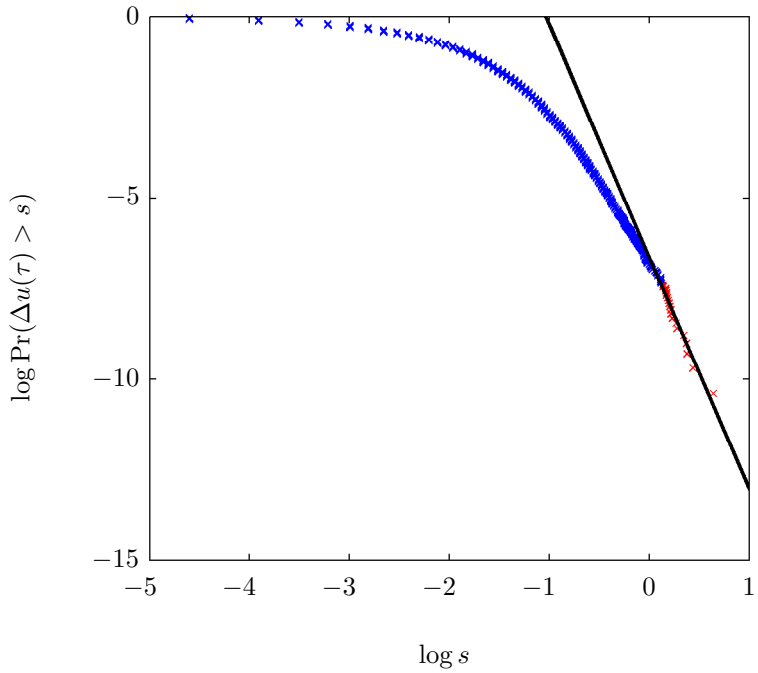

Figure 3.9: Log-log plot of the exceedance probability, $\Pr(\Delta u(\tau) > s)$, of the horizontal velocity increments, $\Delta u(\tau)$, of the twenty-second time-series in figure 1.4. The slope of the dashed line is approximately -6 i.e. $q_D = 6$. This means velocity increment statistics above an order of 6 are random.

The physical significance of these differences is that the event is more violent the smaller the exponent q_D. Figure 3.9 illustrates the divergence of statistical moments on empirical data. If we consider now estimating the power, P, through the fluctuations i.e. $P(u) \propto u^3$ as is typically done (see for example Peinke et al. [2006]) we can only consider the second order moment as a usable statistic.

Empirical Power Law Estimation

As was discussed in the first chapter of this thesis, one way to quantify the behaviour of the extremes of a distribution is to try to fit a power law of the form of equation 3.10 to the (heavy) tail(s). We can estimate the exponent by taking the linear regression of the same probabilities in 2.13 versus s however in a log-log plot. In order to estimate the regression we require a minimum s value, $s_{\min}$ say, over which to perform the regression. Choosing a value of $s_{\min}$ too small we underestimate the power law, too large and the quality of regression is diminished.

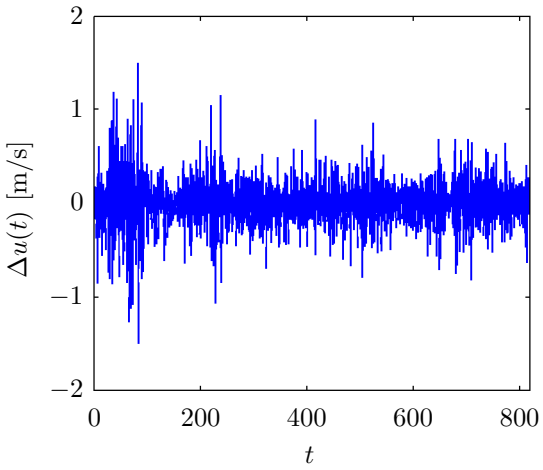

Figure 3.10: A ten-minute time-series of the u-component velocity increments calculated from the wind speeds and directions in figures 2.3a and b.

Figures 3.10 and 3.11 plot a ten-minute time-series of $\Delta u(\tau)$ and its corresponding probability of exceedance in log-log plot. Figure 3.12 plots the probability of exceedance of the positive and negative velocity increments of figure 2.15b; the different distributions correspond to increasing vertical spacings, i.e. $r_z = 40$, 65, 90, 115 and 140m. In both cases $s_{\min}$ has been selected visually; a time-consuming method that cannot be performed on a very large dataset.

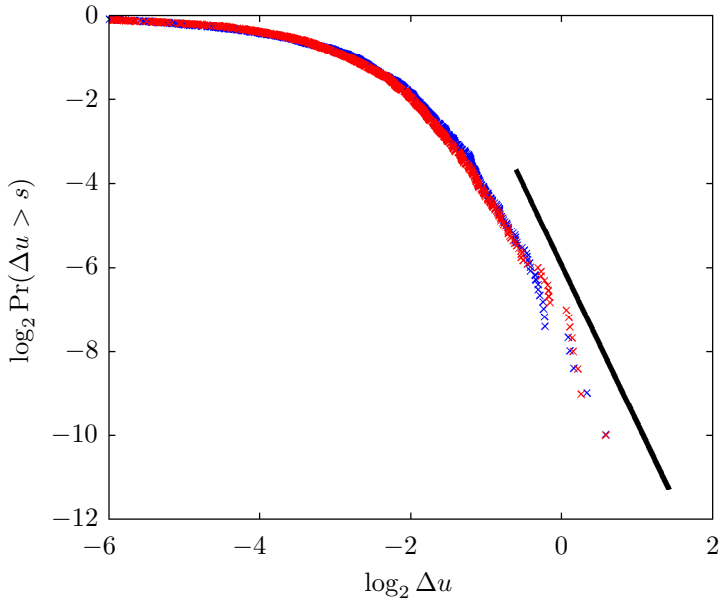

Figure 3.11: The exceedance probability of the positive (red) and negative (blue) velocity increments in figure 3.10, in log-log plot. The slope of the tail corresponding to the power law of the distribution is -3.7.

In Schertzer et al. [2006], Bernardara et al. [2008] and Clauset et al. [2009] a selection of methods are tested concluding that classical estimators of probability tails have two problems. First, all methods consider samples of independent outcomes, an assumption that does not fit with long range dependence. Second, most methods assume the existence of a power-law, i.e. they always yield a given estimate of its exponent, independently of its relevance (see Schertzer et al. [2006] and Bernardara et al. [2008] for a discussion on a 'generalized Hill estimator' that yields a signed shape parameter that helps to avoid this problem). In Clauset et al. [2009] it is shown that a combination of the Kolmogorov-Smirnov or KS statistic for the estimation of $s_{\min}$ followed by a maximum likelihood estimator (MLE) gives the best results. The details of why this is will not be discussed here more than the accuracy of the MLE can decrease for sample sizes $N < 500$. If this is the case a third criteria must be used. However, since the minimum sample length for this study is 3500 (truncated to a base two power integer in general for scaling analysis, e.g. $N = 2^{11}$) we are well within the recommended number of samples. Finally, the programs can be directly downloaded from the

authors' website http://tuvalu.santafe.edu/~aaronc/powerlaws/, however, it is important to note that their estimated parameter is the exponent of the probability density function, $p(x) \propto x^{-\alpha}$, as opposed to the exponent of the exceedance probability. Thus, for the estimation of q_D we needed to slightly modify the program.

The estimates of the slopes in figures 3.11 and 3.12 are much lower than previous surface-layer estimates. In Schmitt et al. [1994], q_D was estimated to be 7.5, on 10Hz velocity measurements taken at 25m, just above a pine forrest. Remembering that the smaller the value q_D the more wild the extremes, we can easily say the Growian test site exhibited much wilder extremes. Tables 3.1 and 3.2 show the average statistics of q_D with error bars for absolute $\Delta u(\tau, z)$. Figure 3.11 is not far from the average statistic.

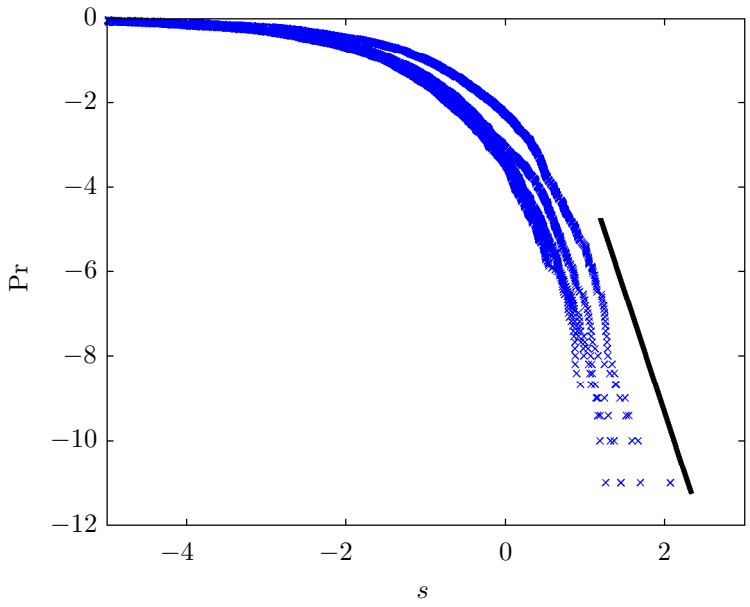

Figure 3.12: The exceedance probability of the absolute velocity increments in figure 2.13, in log-log plot. The slope of the tail is -5.

Tables 3.3 and 3.4 show the average statistics of q_D (with error bars) for absolute $\Delta u(t, r_z)$ and $\Delta v(t, r_z)$. Because the distributions seemed to vary so much in terms of asymmetry for either u or v we included them both. The mean values show a large increase in the values of q_D suggesting that vertical increments

of the horizontal wind are much less wild. This is not surprising given the vertical wind velocity fluctuations are often measured to be an order of magnitude less than the horizontal component. This is later also observed in the Corsica dataset.

	Mast 2 (Inner) $\Delta u(\tau)$				
z [m]	50	75	100	125	150
q_D	4.0±2.1	4.1±2.3	4.2±2.7	4.2±2.1	4.2±2.2

Table 3.1: Table of mean power law tail exponents for $\Delta u(\tau)$ at 50, 75, 100, 125 and 150m, on the inner measurement locations of mast 2.

	Mast 2 (Outer) $\Delta u(\tau)$			
z [m]	10	75	100	125
q_D	4.3±2.5	3.7±2.0	4.1±2.2	4.0±2.3

Table 3.2: Table of mean power law tail exponents for $\Delta u(\tau)$ at 50, 75, 100, 125 and 150m, on the outer measurement locations of mast 2.

	Mast 2 (Inner) $\Delta u(r_z)$				
r_z [m]	40	65	90	115	140
q_D	10.3±10.8	11.8±11.4	12.2±11.7	13.5±16.1	17.4±21.1

Table 3.3: Table of mean power law tail exponents for $\Delta u(r_z) = 40$, 65, 90, 115, and 140. The measurements were taken on the inner measurement locations of mast 2.

	Mast 2 (Inner) $\Delta v(r_z)$				
r_z [m]	40	65	90	115	140
q_D	10.2±11.7	10.2±11.8	11.2±12.5	10.9±11.6	12.8±14.0

Table 3.4: Table of mean power law tail exponents for $\Delta v(r_z) = 40$, 65, 90, 115, and 140. The measurements were taken on the inner measurement locations of mast 2.

Estimates of q_D For The Corsica Dataset

As we have done with the Growian dataset, we use the MLE to find q_D. Because of the limited lengths of the time-series for the Growian dataset we were only

able to calculate q_D at the highest resolution. Trying to estimate q_D on larger (upscaled) time-scales returned errors on the estimation of the parameters. The Corsica dataset on the other hand has much longer data time-series ($\lambda = 2^{19}$). This meant that q_D could be calculated over a range of time-scale resolution ($\lambda < \Lambda$).

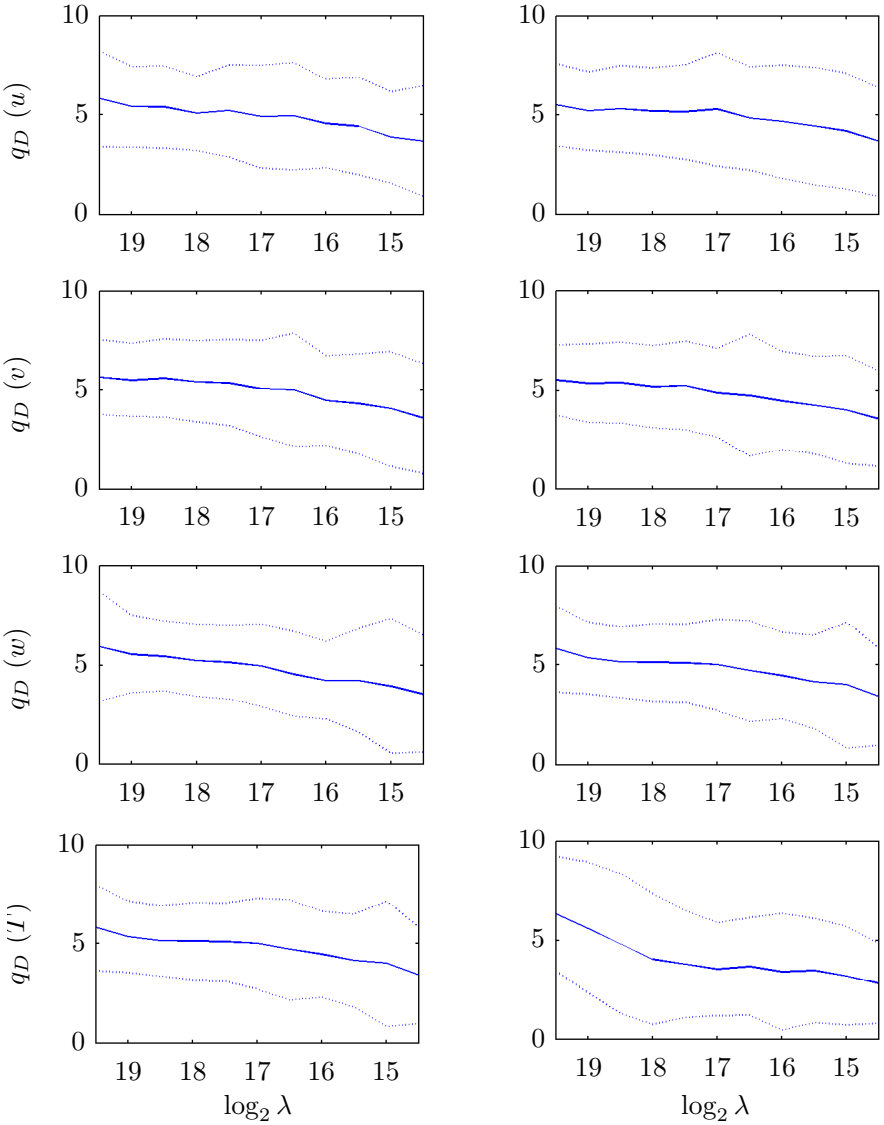

Figure 3.13: Plots of q_D at decreasing resolutions λ (by decreasing resolutions we mean an upscaled fixed sample size with resolution Λ), for $\boldsymbol{u}$ and T at 23 and 43m (left and right columns). Solid blue line is the mean with $\pm$ error bars (dotted lines) either side.

Figure 3.13 shows the estimates of q_D for increasingly smaller resolutions for the different increments of $\boldsymbol{u}$ and T. Interestingly we see that with increasing time-scales the velocity increments become more wild i.e. q_D decreases. At first thought one might think this is due to less and less values being used for the estimator. However, this is in fact the inverse behaviour that we would expect if it a was bias in the estimator. For fewer and fewer samples we would expect larger and larger q_D would there be a bias.

Although 3.13 exhibits a slight dependence of the empirical estimate of q_D on the *resolution* λ, one should not confuse this dependence with that of the largest resolution of the data (Λ) or with the sample size. Indeed, the theoretical q_D is independent of the sample size, but, requires a large sample size to be (easily) observable. The λ-dependence could be related to the lack of a unique scaling regime although the observed fluctuations might simply be inside of the error bars. It is worthwhile noting that large numerical simulations (Ishihara et al. [2009], one of the largest direct numerical simulations with 4096^3 grid points) hint at the existence of a probability distribution power-tail with $q_D \approx 8.3$ (see figure 3.14).

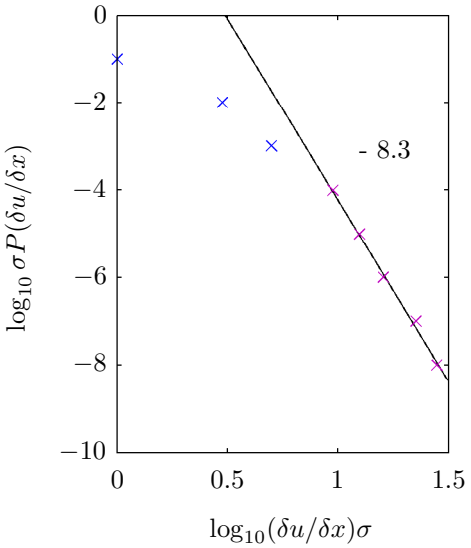

Figure 3.14: Log-log plot of the normalised probability density functions of the longitudinal velocity gradients simulated in Ishihara et al. [2009].

3.2 The Effects Of Scaling Anisotropy On Extremes

Growian

For the Growian dataset the Cartesian wind components are not directly measured, but are easily obtained from the wind velocity modulus, $\tilde{u} = \|\boldsymbol{u}\|^2$, and the instantaneous meteorological angle θ_M with respect to a fixed reference frame R:

$$u = -\tilde{u} \cdot \sin(\theta_M) \text{ and } v = -\tilde{u} \cdot \cos(\theta_M). \tag{3.11}$$

Figure 3.15 compares the scaling properties of the u and v components from the Growian dataset at 100m.

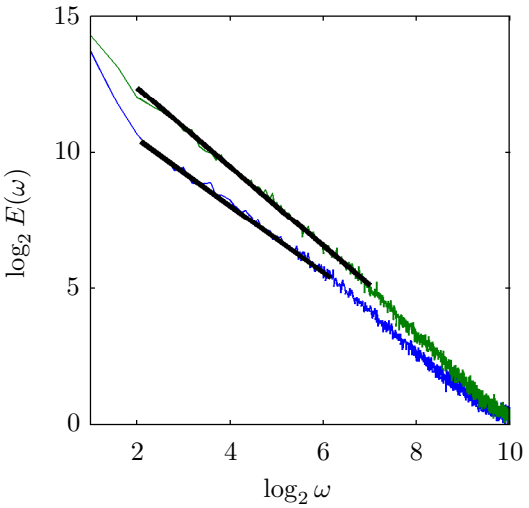

Figure 3.15: Energy spectra of the velocity components u (blue) and v (green) for the Growian dataset. The corresponding spectral exponents for u over low and high frequency ranges respectively are 1.25 and 1.45; and for v are 1.45 and 1.70.

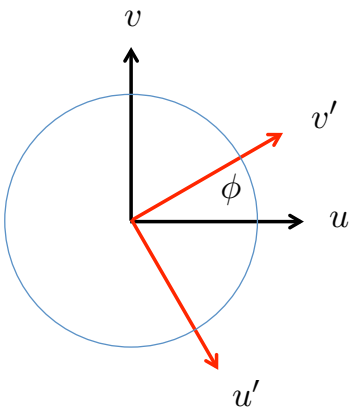

Figure 3.16: Diagram showing a comparison between the initial two-dimensional Cartesian frame of reference R (black) with horizontal velocity vector components u and v and the rotated frame of reference $R'(\phi)$ (red) and its corresponding rotated velocities u' and v'.

Both components show two scaling sub-ranges: a small scale sub-range from 1 to 10 seconds and a larger scale sub-range from 10 seconds to 15 minutes. The scaling exponents for u over low and high frequency ranges respectively are

1.25 and 1.45; and for v are 1.45 and 1.7. The significant differences in scaling exponents correspond to a scaling anisotropy that is much stronger than a trivial anisotropy with a constant ratio of components different from one. Moreover, there is no evidence of $\beta = 5/3$ predicted by homogeneous isotropic turbulence.

The aforementioned scaling anisotropy is in sharp contrast to the 'local isotropy' assumption commonly used in turbulence since Kolmogorov. In Pouquet et al. [1976] they show that helicity can strongly modify the spectral slope, however, due to the complexity of the problem, it is analysed in an isotropic framework that introduces limitations w.r.t. to surface-layer. The relevance of an isotropic atmospheric turbulence has been brought into question numerous times, eventually leading to the birth of the concept of generalised scale invariance (GSI). GSI first posits scaling, not isotropy Schertzer and Lovejoy [1985a]. Statistical isotropy, i.e. $u \overset{d}{=} v$ (the symbol $\overset{d}{=}$ denotes equality in probability distribution), would correspond to rotational invariance of the statistics at all scales.

In order to quantify the scaling anisotropy (by means of the parameter H) we can rotate the frame of reference R by an angle ϕ giving the rotated frame of reference $R'(\phi)$ (see figure 3.16). We then compute the corresponding statistical exponents $H_u(\phi)$ and $H_v(\phi)$. This is in some way the inverse of the procedure typically performed in order to ensure isotropy, i.e. $E_u = E_v$ (see Drobinski et al. [2004]).

The Cartesian components, defined through the direction and modulus, in a rotated reference frame $R'(\phi)$, are then simply given by:

$$u'(\phi) = -\tilde{u} \cdot \sin(\theta_M + \phi), \quad v'(\phi) = -\tilde{u} \cdot \cos(\theta_M + \phi). \tag{3.12}$$

Since we are using the spectral exponent, β, to quantify statistical properties, it will be of interest to look at the analytical properties of the rotated vectors' energy spectra. The rotated time-dependent u-component is:

$$u'_\phi(t) = \cos(\phi)u(t) - \sin(\phi)v(t), \tag{3.13}$$

and its Fourier transform (due to the linearity of the Fourier transform) is:

$$\widehat{u'_\phi}(\omega) = \cos(\phi)\hat{u}(\omega) - \sin(\phi)\hat{v}(\omega). \tag{3.14}$$

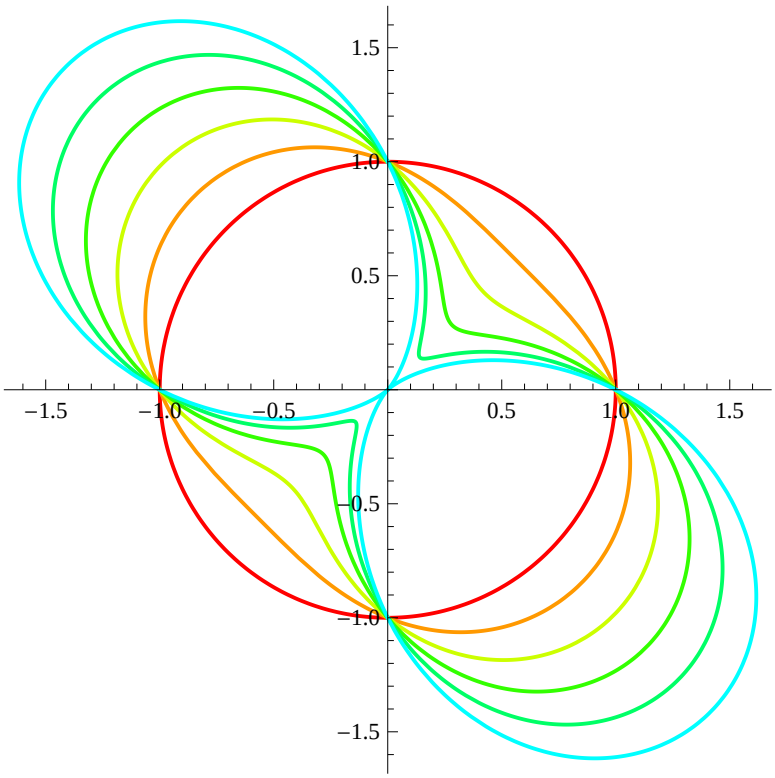

Figure 3.17: Plot of the function $\rho(\phi)$ in polar coordinates $(\rho, -\phi)$ for the correlation coefficient r. The coefficient is increased in increments 0.2 from $r = 0$ (red) to $r = 1$ (turquoise). The red circle corresponds to the isotropic case of independent identically distributed variables.

Considering now either the variance or the spectra of the field, their quadratic nature yields the following relations: for the variance

$$< |u'_\phi(t)|^2 >= \mathrm{Var}_\phi(t) = \cos^2(\phi)\mathrm{Var}_0(t) + \sin^2(\phi)\mathrm{Var}_{\pi/2}(t) - \sin(2\phi)\mathrm{Cov}_{u,v}(t), \tag{3.15}$$

where $\mathrm{Cov}_{u,v}$ is the covariance of u and v and, Var_0 and $\mathrm{Var}_{\pi/2}$ are the variances of u and v respectively; and for the spectra

$$|\widehat{u'_\phi}(\omega)|^2 = E_\phi(\omega) = \cos^2(\phi)E_0(\omega) + \sin^2(\phi)E_{\pi/2}(\omega) - \sin(2\phi)E_{u,v}(\omega), \tag{3.16}$$

where $E_{u,v}$ is the co-spectrum of u and v and, E_0 and $E_{\pi/2}$ are the spectra of u and v respectively.

When the two velocity components u and v are identically distributed, but not independent, equations 3.15 and 3.16 become

$$\mathrm{Var}_\phi = \rho(\phi)\mathrm{Var}_0, \tag{3.17}$$

$$\text{and } E_\phi = \rho(\phi)E_0, \tag{3.18}$$

where

$$\rho(\phi) = 1 - r\sin(2\phi), \tag{3.19}$$

and r is the correlation coefficient of u and v.

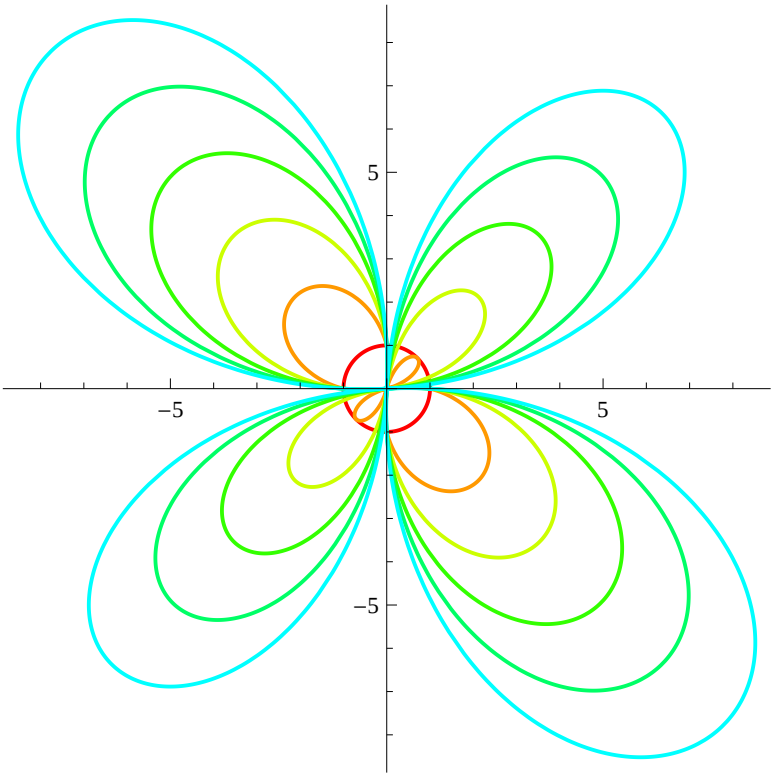

Figure 3.18: Plot of the function $\rho(\phi)$ in polar coordinates $(\rho, -\phi)$ for the correlation coefficient r. The coefficient is increased in increments 2 from $r = 0$ (red) to $r = 10$ (turquoise). The red circle corresponds to the isotropic case of independent identically distributed variables.

Equations 3.15 and 3.16 correspond to a given anisotropy of the velocity field u. This anisotropy becomes a scaling anisotropy if we consider, instead of the

velocity field itself, similar relations for the singularities, $\gamma = \log_\lambda u$, where λ is the ratio of the total sample length and the time-scale of observation. If we consider the same rotations for the singularities, the equivalent equation to equation 3.15 readily holds for the (misnamed) log-normal model and therefore for the scaling exponent of the moment of order two, i.e., $K_\phi(2) = \rho(\phi)K_0(2)$. A more general, universal multifractal (UM) case isn't yet shown, however, we may mention that the generalisation should lead to

$$K_\phi(q) = \rho(\phi)K_0(q) \tag{3.20}$$

when considering the full hierarchy of multifractal singularities. Note that the UM scaling moment function $K_\phi(q)$ statistically describes the intermittency of atmospheric flows. From the above equation, this intermittency varies with $\rho(\phi)$. Initial analysis of the function shows that the most intermittent fields do not correspond to the largest values of r. We wind that the most intermittent fields are those when $r = 0.2$.

As expected in the isotropic turbulence model the scaling exponent will remain the same for varying ϕ. Note, even though the scaling exponent is isotropic it could remain far from being homogeneous. This is due to strong intermittency corrections assimilated into H estimates that make them differ from the expected $H = 1/3$! Figures 3.17 and 3.18 show the continuous squeezing of the isotropic, circular structures due to an increase of the correlation coefficient (see equation 3.19) in the case of identically distributed, but not independent velocities. With the Growian data, the scaling anisotropy of this type is empirically visible, in particular over larger time-scales (10 seconds to 5 minutes).

Figures 3.19 and 3.20 display the scaling exponents H_u and H_v as a function of the rotation, ϕ, of the frame of reference. The scaling exponents have been estimated over the (larger) scales (figure 3.19), 10 seconds to 5 minutes ($\log_2 \omega$ from 2 to 6) and the (smaller) scales (figure 3.20), 0.2 to 10 seconds ($\log_2 \omega$ from 7 to 10). Each plot (from left to right and from top to bottom) corresponds to an increasing height of 10, 50, 75, 100, 125 and 150m. The black solid line corresponds to the scaling exponent expected in the isotropic homogeneous case i.e. $H = 1/3$.

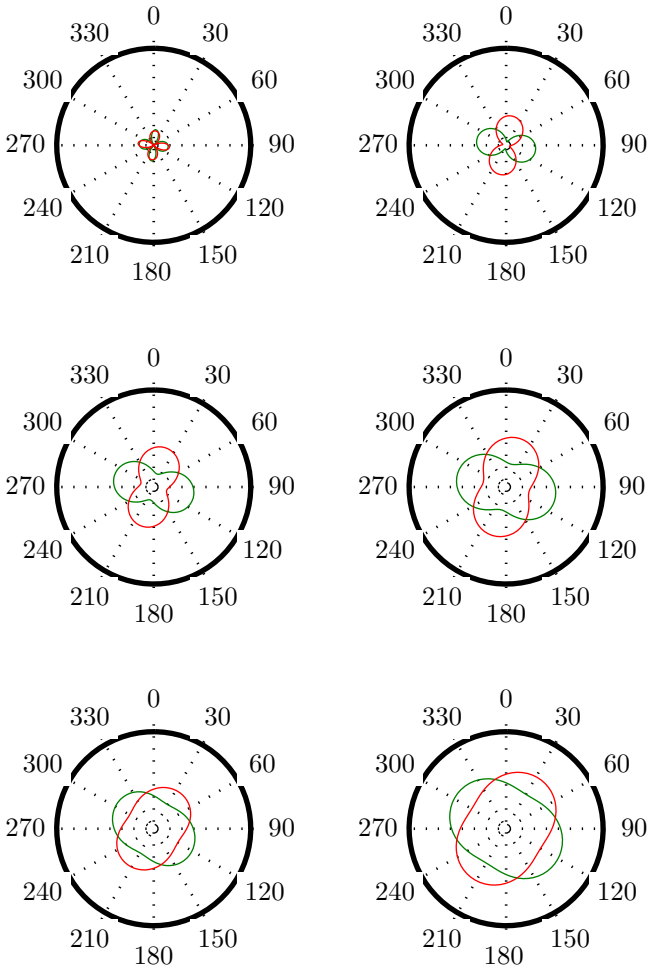

Figure 3.19: Plots of empirically estimated H_u (red) and H_v (green), as a function of ϕ. Exponents are estimated over the (larger) scales, 10 seconds to 5 minutes ($\log_2 \omega$ from 2 to 6). The different plots correspond to the heights 10, 50, 75, 100, 125 and 150m from left to right and from top to bottom. The black solid line corresponds to the scaling exponent expected in the isotropic homogeneous case i.e. $H = 1/3$.

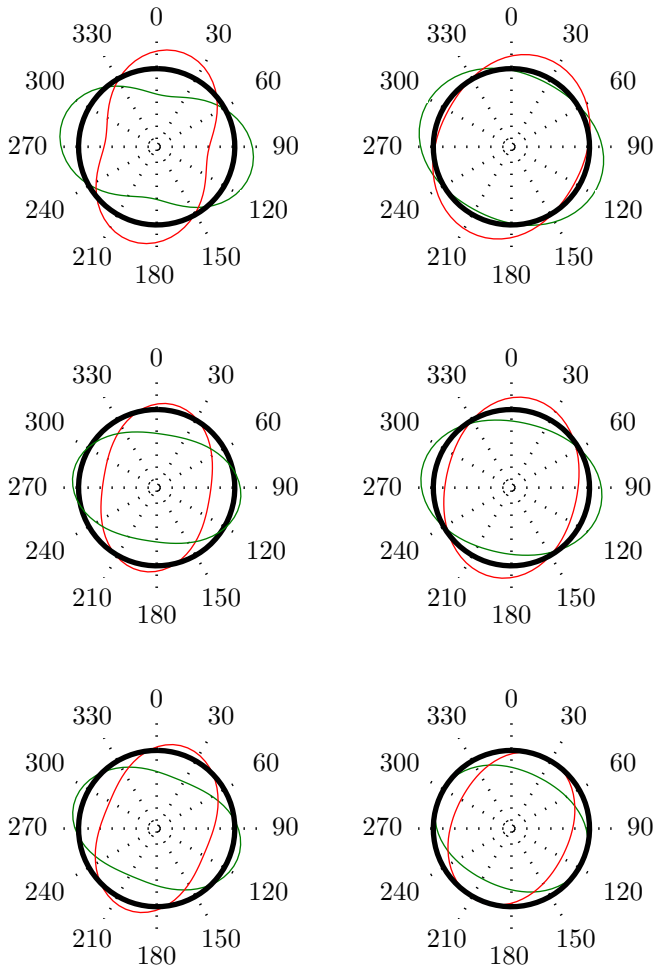

Figure 3.20: Plots of empirically estimated H_u (red) and H_v (green), as a function of ϕ. Exponents are estimated over the (smaller) scales, 0.2 to 10 seconds ($\log_2 \omega$ from 7 to 10). The different plots correspond to the heights 10, 50, 75, 100, 125 and 150m from left to right and from top to bottom. The black solid line corresponds to the scaling exponent expected in the isotropic homogeneous case i.e. $H = 1/3$.

The increasing values of H_u and H_v with height in figure 3.19 are, although well below the exponent predicted for homogeneous turbulence, consistent with other literature (see for example Drobinski et al. [2004]). What is of particular interest is the clearly decreasing anisotropy between exponents with height. At 10m (top left) we see the scaling exponents exhibit the largest (relative) difference. The anisotropy exhibits symmetries consistent with the symmetries of equation 3.16. At 150m (bottom right) it is rather clear that with the addition of another 100m in height the scaling exponents would become isotropic to a point.

A further strange observation is the apparent rotation of the point of statistical isotropy i.e. where $H_u = H_v$ with height. This is strange because the preferential direction (θ) is fixed with a mean at all heights that does not vary outside of $250 \pm 1°$. From 10 to 150m the degree of ϕ for which the scaling is isotropic varies from 30 to 90°. This rotation most presumably results from the Coriolis force, as in the classical Ekman surface-layer.

With respect to figure 3.20 we can see that the smaller scales also show an increase in anisotropy with a decrease in height although not to the same extent as the larger scales. Also, the increase in r does not seem as steady as was observed over the larger scales in that the increase is mainly at the lowest height with very little change in r (not H) over the remaining heights.

Corsica

Figure 3.21a shows the energy spectra of the velocity component $u'(\phi)$ at 43m for $\phi \in [0 : \pi/10 : \pi/2]$ for the Corsica dataset. As expected in the isotropic turbulence model the scaling exponent remains the same ($\beta = 1.3$) for varying ϕ over the time-scales 5 seconds to 5 minutes. Even though the scaling exponent is isotropic over these scales it is far from being homogeneous due to strong intermittency corrections! The horizontal velocity at 23m showed identical behaviour and has therefore not been shown.

Because there is no real component-wise scale separation we estimate H_u over just one range of scales, 3 seconds to a minute ($\log_2 \omega = 6$ to 10). Although in the spectra the scaling exponent seems isotropic when we plot the exponent H_u as a function of ϕ (figure 3.21b) we can see that a slight anisotropy arises. When

calculating θ using the inverse tangent function it is important to map θ from the $[-\pi : \pi]$ plane onto the $[0 : 2\pi]$ plane. Not doing so will result in spurious values of u' and v'. We mention this specifically for the Corsica dataset as it was unnecessary to compute the direction for the Growian dataset as it was already available.

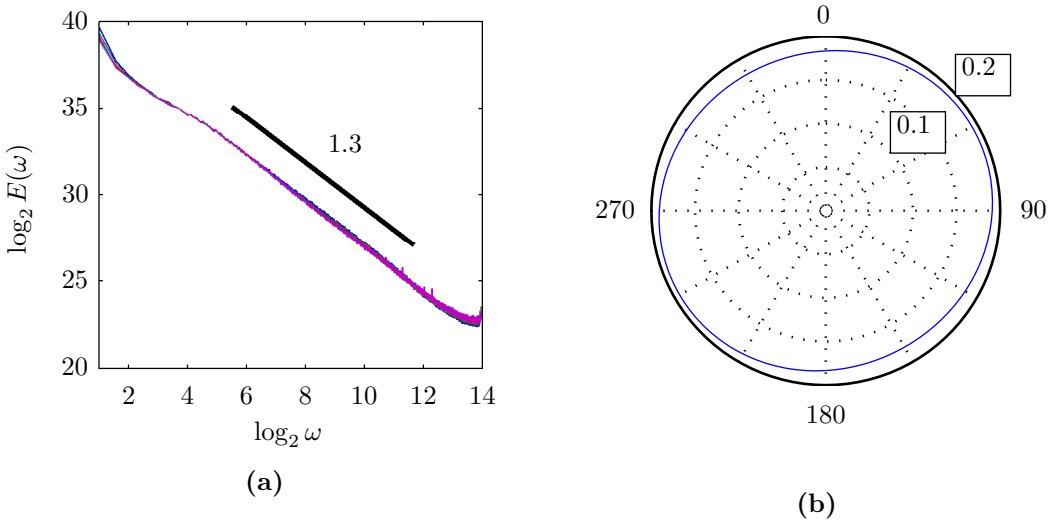

Figure 3.21: (a) Energy spectra of the velocity component $u'(\phi)$ for $\phi \in [0 : \pi/10 : \pi/2]$ from the Corsica dataset; (b) Plot of empirical $H_u(\phi)$ calculated at 43m.

Although the Corsica dataset exhibited less anisotropy than the Growian dataset on the ensemble averaged spectra this was not the case for individual samples. Figure 3.22 plots $u'(\phi)$ for the first thirty single samples in the Corsica dataset. We can see that the near isotropic scaling is lost and instead the deformed structures seen in the Growian data at 50m are matched. What is particularly interesting is the rotation of the structures with ϕ. Indeed it seems that the majority of individual samples exhibit a stronger anisotropy than the mean; when averaged together, however, due to their rotations the anisotropy is cancelled out. There is one single file in figure 3.22 that exhibits a much stronger anisotropy than the others.

In the next section we investigate the possible physical processes responsible for the anisotropic behaviour in the Growian dataset and why this doesn't occur in the Corsica dataset. We have already briefly mentioned that the Ekman-

layer is a well studied surface/boundary-layer phenomena that induces a rotation. Moreover, due to the measurements' (fairly) close proximity to the land surface it likely that convection plays a key role. If we are to determine if convection contributes to the anisotropy of the observations we must quantify the stability of the atmosphere.

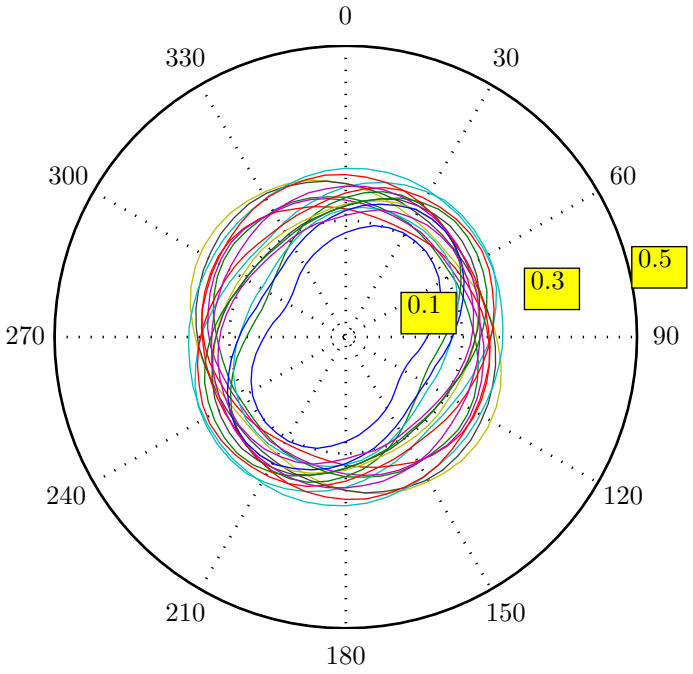

Figure 3.22: Plots of $u'(\phi)$ for $\phi \in [0 : \pi/10 : \pi/2]$ for the first thirty single samples in the Corsica dataset.

3.3 Atmospheric Stability

The limits for stability classification through the Richardson number and the Obukhov-length are widely discussed in Xue-yan et al. [2005]. We will show that the distributions of both parameters correspond to unwieldy statistics that are difficult to classify. We will then attempt to create our own classification by relating the scaling of the temperature and velocity to the anisotropy of the horizontal velocity components for an appropriate choice of the physical mechanism.

In the previous section we have clearly illustrated that the two datasets exhibit similar scaling exponents ($\beta = 1.3$, given we take the isotropic case at 50m from the Growian dataset) from 10 seconds to 5 minutes. In addition, we have also observed that the two datasets exhibit very different component-wise scaling properties. Since our measurements are well within the surface-layer (SL) we can expect that the instability of the atmosphere will contribute significantly to anisotropic changes in shear stresses (see Drobinski et al. [2004]).

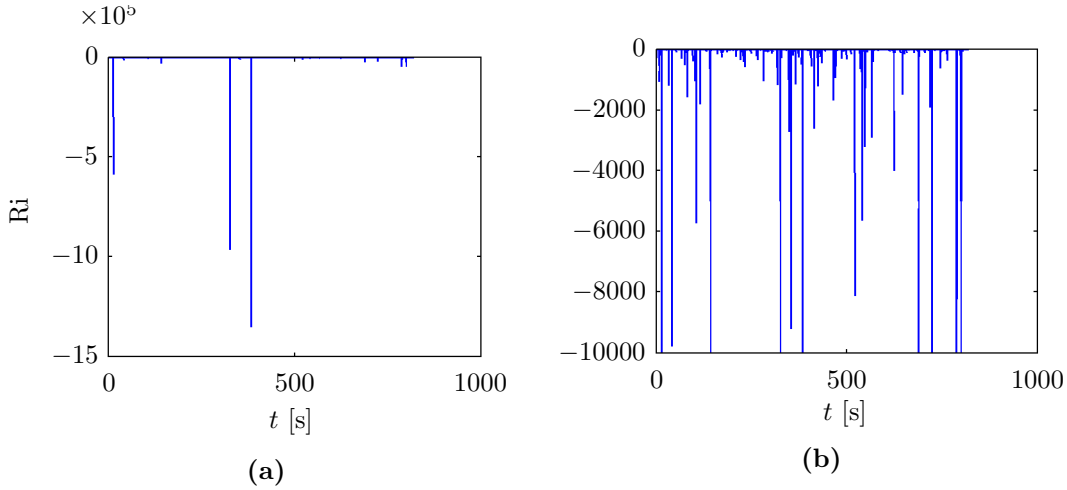

Figure 3.23: (a) Plot of the (Growian) time-series of the instantaneous Richardson number, $\mathrm{Ri} = g/T(\Delta T/\Delta u^2)$, calculated from 2^{11} velocity and temperature time-series observations at 75m. The velocity and temperature measurements were taken at the same rate of 2.5Hz giving a total measuring time of about fifteen minutes. Plot (b) shows the same time-series but for values greater than -10^4. This was done in order to further expose the extreme and intermittent nature of the quantity.

A fairly classical means by which to quantify the vertical (or buoyancy) forces in the atmosphere is the gradient Richardson number (effectively the ratio be-

tween buoyancy and friction forces)

$$\mathrm{Ri} = \frac{g}{T(z)} \frac{\Delta T(z)}{\Delta u(z)^2} \Delta z, \tag{3.21}$$

where g is gravitational acceleration. Figure 3.23 shows a time-series (3.23a) and zoomed time-series (3.23b) of the Richardson number taken at 75m from the Growian dataset. Note since temperature measurements are only available at 50, 100 and 150m and a difference is required to compute the Richardson number we must use a 75m proxy. Large negative Richardson numbers correspond to unstable layers i.e. strong vertical motion. The majority of files for both Growian and Corsica data exhibit this kind of behaviour.

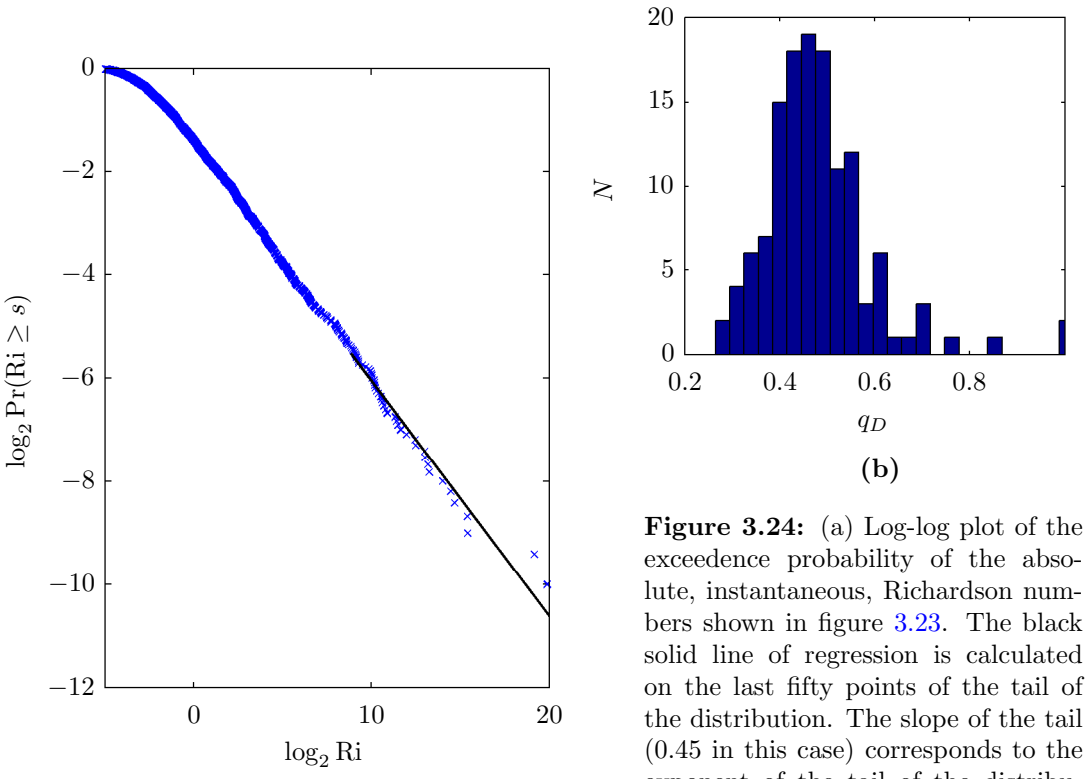

Figure 3.24: (a) Log-log plot of the exceedence probability of the absolute, instantaneous, Richardson numbers shown in figure 3.23. The black solid line of regression is calculated on the last fifty points of the tail of the distribution. The slope of the tail (0.45 in this case) corresponds to the exponent of the tail of the distribution of the Richardson numbers i.e. $\mathrm{Pr}(\mathrm{Ri} \geq s) \approx s^{-q_D}$ $q_D = 0.45$; (b) Histogram of q_Ds taken over 131 samples with $\langle q_D \rangle = 0.5 \pm 0.4$.

Figure 3.23 shows the extremely intermittent nature of the instantaneous Richardson number, suggesting that its empirical average estimate is random and sample size dependent. Figure 3.24 displays the log-log plot of the exceedance probability of the absolute, instantaneous, Richardson numbers shown in figure 3.23. The histogram of q_D in figure 3.24 gives an average exponent of less than one (0.5). This value is comparable also for the Corsica dataset. Since q_D is estimated to be less than one for both the Growian and the Corsica datasets, neither the mean of the Richardson number is defined, nor the Monin-Obukhov length that depends on it.

We infer also that other parameters, e.g. the Froude number or the Brunt Vaissala frequency, that are typically used to measure the state of systems will also be extremely intermittent. Numerical arguments such as those found in Laval et al. [2003] are typically restricted in scale ratio (computed on low Reynolds number systems) and are thus difficult to compare to the highly-intermittent fluctuations of the atmosphere.

This analysis was tested over larger scales (by averaging and spectral damping) to take into account the changes in scaling at 10 seconds. For increasingly larger time-scales there is a slight increase in the number of files for which $q_D > 1$, however, never to the extent in which it is the majority.

Temperature Scaling

As an alternative to using the unwieldy statistics of the Richardson number and the Obukhov-length we instead compare the scalings of the temperature and the u-component velocity. Figure 3.25 plots the average spectra of the temperature (turquoise) and the velocity (red) at 43m for the Corsica dataset. Over high frequencies the temperature spectra displays instrumental noise up to a second. Over the larger scales, the two spectra should have the same slope if the temperature behaves as a passive scalar.

Looking now to the average temperature and u-component velocity spectra (for $\phi = 0$) of the Growian dataset (figure 3.26) we can see that over the same larger time-scales there is a remarkable difference. Not only does the temperature scale uniquely i.e. without sub-ranges, but it scales with a much steeper

slope ($\beta = 2$). This implies that the temperature fluctuations are not only more correlated at all scales but also the temperature is presumably an active scalar.

To quantify this behaviour we have taken the difference between the two scaling exponents i.e. $\Delta H = H_u - H_T$, estimated over the larger time-scales – 10 seconds to 15 minutes. The three plots in figure 3.26 correspond to the heights 50, 100 and 150m. The decrease in ΔH at each height seems to be related to the decreasing anisotropy seen in figure 3.19. We can also see over the smaller scales that the lower the ΔH, the closer the scaling is to that of the larger scales. A final important observation is that in the isotropic case we loose this dependence on height i.e., ΔH is constant at 0.9.

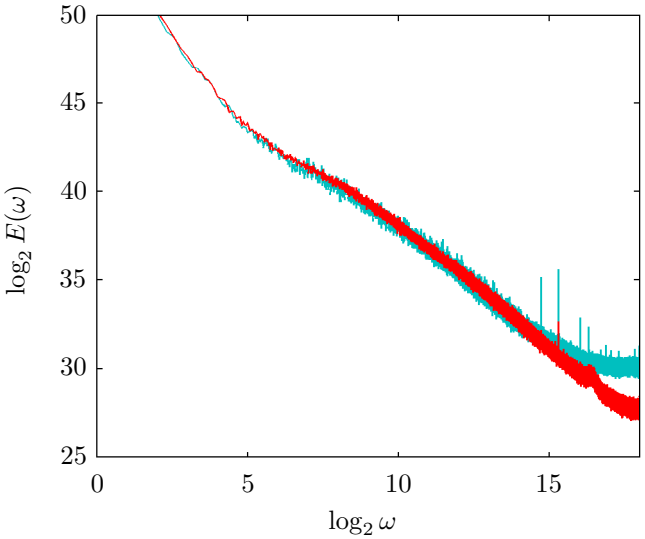

Figure 3.25: Average temperature (turquoise) and u velocity (red) spectra from the Corsica dataset at 43m.

Quickly summarising these results – we find that when the temperature is an active scalar, i.e. $\Delta H > 0$, over larger scales (specifically from scales larger than 10 seconds) wind scaling anisotropy entails. One can also hypothesise that the point of intersection of the two spectra at approximately 10 seconds is in fact a good estimation of the so called Obukhov-length or spheroscale for GSI (Schertzer and Lovejoy [1985a]), whose frequency we denote $\omega_L = 1/\tau_L$. For time-scales τ larger than τ_L the turbulent statistics are dominated by the fluid motions, *but*, the latter are strongly influenced by convection (i.e. active temperature due to surface

heat fluxes etc.). This combination of processes results in a scaling, statistical anisotropy. For time-scales $\tau < \tau_L$ the larger the ΔH the closer the scaling is to the theoretical Bolgiano-Obukhov value 11/5 for an (isotropic) buoyancy range. Being able to quantitatively relate the breaking of symmetry in the near boundary-layer to the type of convective process is a topic that has been discussed in Chashechkin [1989]. In the next section we will attempt a similar classification based on scaling exponents.

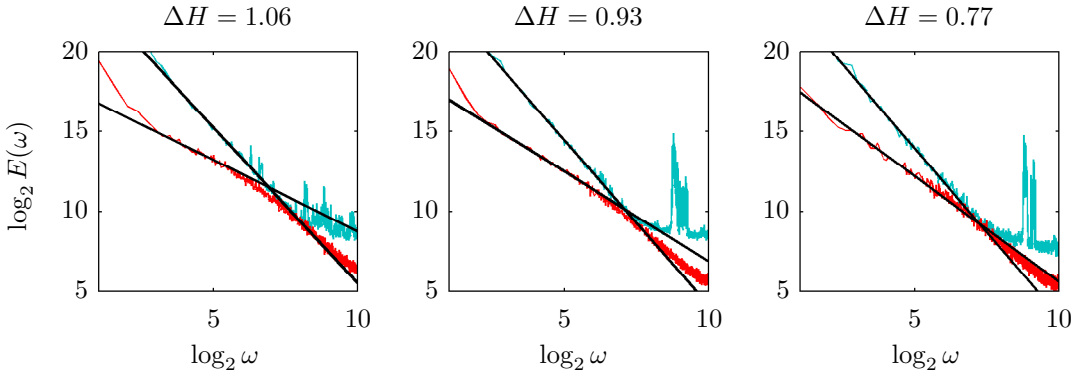

Figure 3.26: Average temperature (turquoise) and u velocity (red) spectra from the Growian dataset at 50, 100 and 150m (left to right).

More On The Convective Surface-Layer

We have just shown in the previous section that, for the two datasets, the onset of anisotropy may be determined solely by the difference found between the scaling of the temperature and the velocity. If the two scaling exponents diverge, i.e. $\Delta H > 0$, then component-wise anisotropy entails. What we haven't shown yet is whether the anisotropy occurs at large scales and is cascaded down to the smaller scales or whether there are other processes at work. This is something we will look at in the next section, i.e. what is the relationship between the two scale separations. Before that, we want to look more closely at the differences between the scaling of other variables within the two datasets.

In the Corsica dataset $\boldsymbol{u}$ appears component-wise isotropic up to ten seconds and isotropic over all scales for u, v with T scaling as a passive scalar of u and v also over all of the time-scales. The reason why w doesn't scale over all scales

is due to a well known phenomena where the height limitation of the mast does not permit the (vertical shear) fluctuations of structures larger than the mast to be observed.

Figure 3.27 compares the temperature spectra of the Growian dataset with the vertical velocity spectra. We haven't included the vertical component in the majority of the analyses due to the poor quality of data (approximately 100 usable files available at only 75 and 125m). Moreover, because the vertical velocity component is calculated at 75 and 125m and, since the temperature is measured only at 50, 100 and 150m, an average across heights the 75 and 125m was taken so that a comparison could be made.

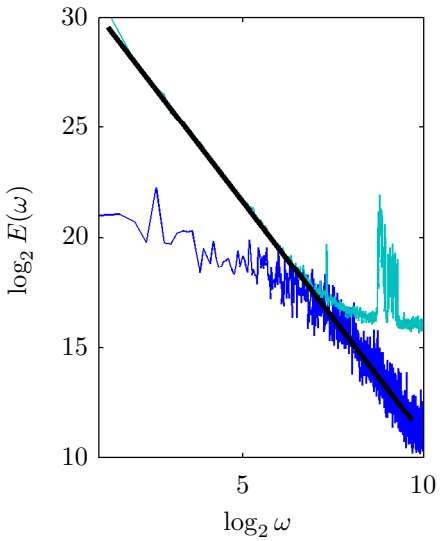

Figure 3.27: Comparison of the vertical velocity and temperature spectra of the Growian dataset at 100m. The vertical velocities are measured at 75 and 125m therefore a vertical average was taken in order to make the comparison.

We can see that over higher frequencies the vertical velocity component scales as the lower frequencies of the temperature. We can assume that if there wasn't the problem of instrumental noise in the temperature spectra and the height of the mast was increased the two spectra would superimpose. Evidence of a Bolgiano-Obukhov scaling exponent of the vertical increments of the horizontal wind have been observed from 150m to 12km in Lovejoy et al. [2009] and Hovde et al. [2011], further confirming this idea. We now propose the three following

hypotheses:

H1 For physical processes where the buoyancy forces dominate the vertical increments of the horizontal wind ($\Delta u(\Delta z)$), the vertical velocity component and the temperature will both scale as Bolgiano-Obhukov (11/5). When this occurs, if the horizontal components do not scale as the vertical component (which as an unlikely occurrence in the surface-layer), anisotropy will entail.

H2 The degree of anisotropy will be of a factor ΔH, which under the first hypothesis corresponds not only to the temperature but to the vertical wind velocity providing sufficient measurements in space can be made.

H3 In the case when turbulent mixing is the dominant physical process the scaling of the three-dimensional velocity will be component-wise isotropic and temperature will scale as a passive scalar of the dominant horizontally fluctuating velocity components.

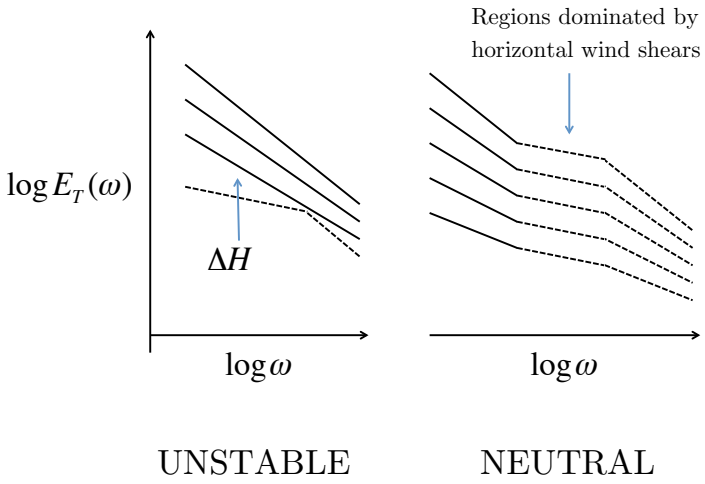

Figure 3.28: Diagram illustrating the temperature spectra in a stable and neutral atmosphere.

The three hypotheses in fact correspond to either a neutral or unstable atmosphere. For a stratified stable atmosphere H1 will be applied but over the

space-time scales corresponding to the stratification. Figure 3.28 illustrates the temperature spectra in a stable and neutral atmosphere.

Let us mention that temporal spectra are insufficient to empirically distinguish (non-linear) waves (e.g. the universal internal-wave energy spectrum first described by Garrett and Munk [1972]. Space and time are instead required (see Lovejoy et al. [2008] for a more detailed discussion).

Relative Humidity

Figure 3.29 plots the spectra of horizontal u and v-components (red and blue), the temperature (turquoise) and the relative humidity (orange).

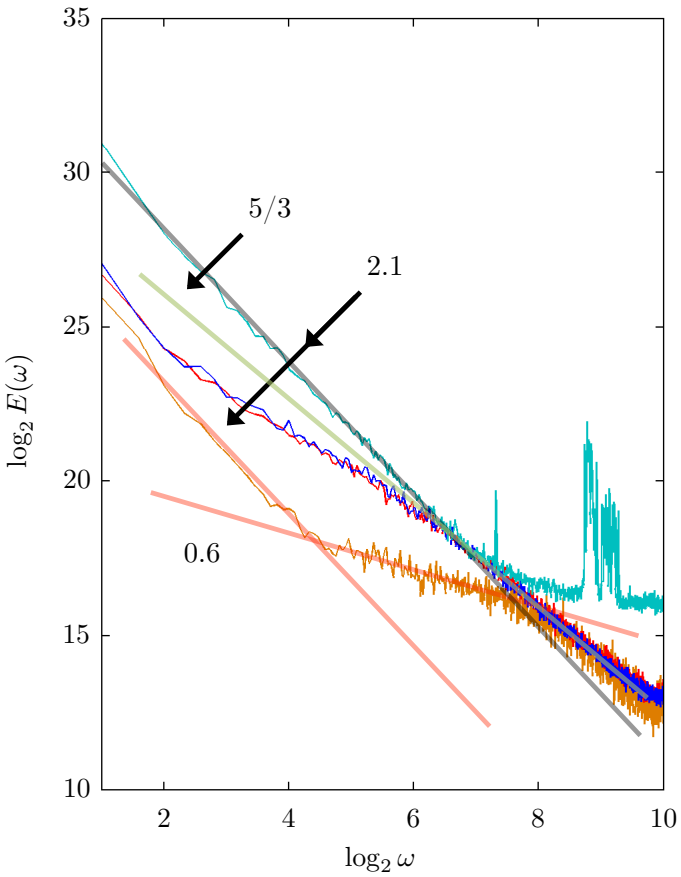

Figure 3.29: Plots of the horizontal u and v-components (red and blue), the temperature (turquoise) and the relative humidity (orange) spectra.

The spectra of the relative humidity has three scaling ranges: from 0.4 to 2 seconds with scaling exponent 5/3, from 2 seconds to half a minute with scaling exponent 0.6 and from half a minute to the largest scale (15 minutes) with scaling scaling exponent 2.1.

We have already proposed that over the time-scales of 10 seconds to 10 minutes vertical fluctuations of the horizontal wind are driven by buoyancy force effects, i.e. a convective surface-layer. Therefore the scaling of the relative humidity shows that the moisture content of the surface-layer is defined by the vertical increments of the horizontal wind at scales larger than half a minute and the horizontal increments for time-scales smaller than 2 seconds. It isn't clear where the scaling exponent of the mid-frequency comes from since it doesn't correspond to the scaling ranges or exponents of any of the other parameters. Since the quantity is cascading through the scales it may correspond to a latent heat process that occurs during the transition from buoyancy force flux to energy flux.

Relating The Two Scale Separations

In the previous section we managed to show that anisotropy entails in both the high-frequency and low-frequency sub-ranges of the horizontal velocity spectra from the Growian experiment. What was omitted from the analysis was how the two sub-ranges are related in terms of anisotropy and scaling exponents, i.e. do the changes in the lower frequencies change the scaling of the higher frequencies (they should if we are within the framework of cascade phenomena). If so, how can we quantify these changes. However, before we attempt to quantify the behaviour of the scaling exponents it is important to clearly differentiate between two of the velocity scaling exponent's properties.

- How does the process generate anisotropy? This is defined by the parameter r whose value will determine the shape of the potatoide.
- What do the magnitudes of H mean? The magnitude of the Hurst exponent can be seen as a scale parameter of the potatoide, but we would still like to quantify it!

Figure 3.30 plots the scaling exponents from the higher frequency range, H_H, and the lower frequency range, H_L, against each other at the heights 50, 100 and 150m. These are the heights that ΔH was calculated at. Taking the centre of the ellipses as some approximation of the mean of the parameters H_L and H_H we can see that $H_L(z)$ increases by a factor of about 0.1 at each 50m increase in height giving $\Delta H_L(z) = 0.2$ over a 150m vertical distance. The high frequency scaling exponent, H_H, remains about the same. We can consider the horizontal and vertical widths of the ellipsoids, $\Delta H_L(r)$ and $\Delta H_H(r)$ say, as a qualitative measure of anisotropy.

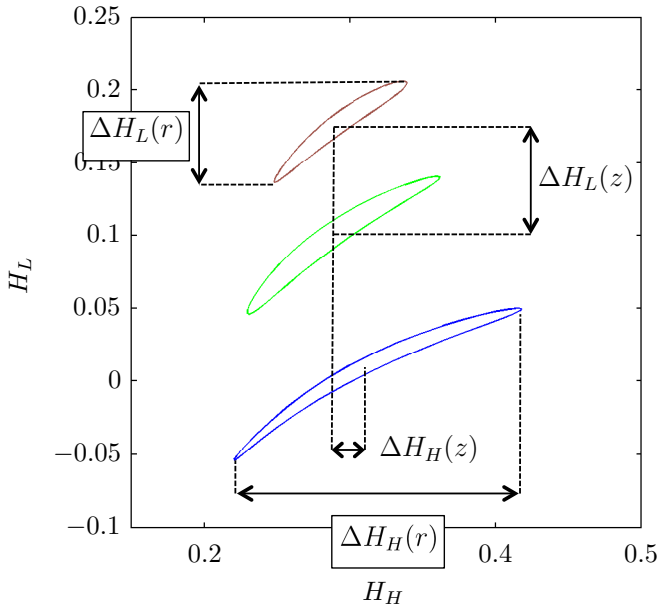

Figure 3.30: Plots of H_H versus H_L at 50 (blue), 100 (green) and 150m (brown).

In agreement with our previous observations we find therefore that both $\Delta H_L(r)$ and $\Delta H_H(r)$ decrease with height but with varying factors: $\Delta H_L(r)$ decreases from 0.1 at 50m to 0.05 at 150m and $\Delta H_H(r)$ decreases from 0.2 to 0.1. This result suggests that

$$\Delta H_L(\Delta z) = 2\Delta H_H(r) \text{ and } \Delta H_H(r) = 2\Delta H_L(r). \tag{3.22}$$

Moreover, since for all three parameters $\Delta H_L(\Delta z)$, $\Delta H_H(r)$ and $\Delta H_L(r)$ have a fairly stable (although agreeably based on only three heights) negative gradient with height we can attempt to interpolate the gradient in order to find a height at which all three become equal; an equilibrium exponent, H_0 say, where $\Delta H_L(\Delta z) = \Delta H_H(r) = \Delta H_L(r)$, i.e. the isotropic H. Figure 3.31 first plots H_H versus H_L at 50 (blue) and 100m (red), then extrapolates the line connecting $H_H(\phi), H_L(\phi)$ at 50 and 150m for larger H_L and for $\phi \in [0 : 2\pi]$.

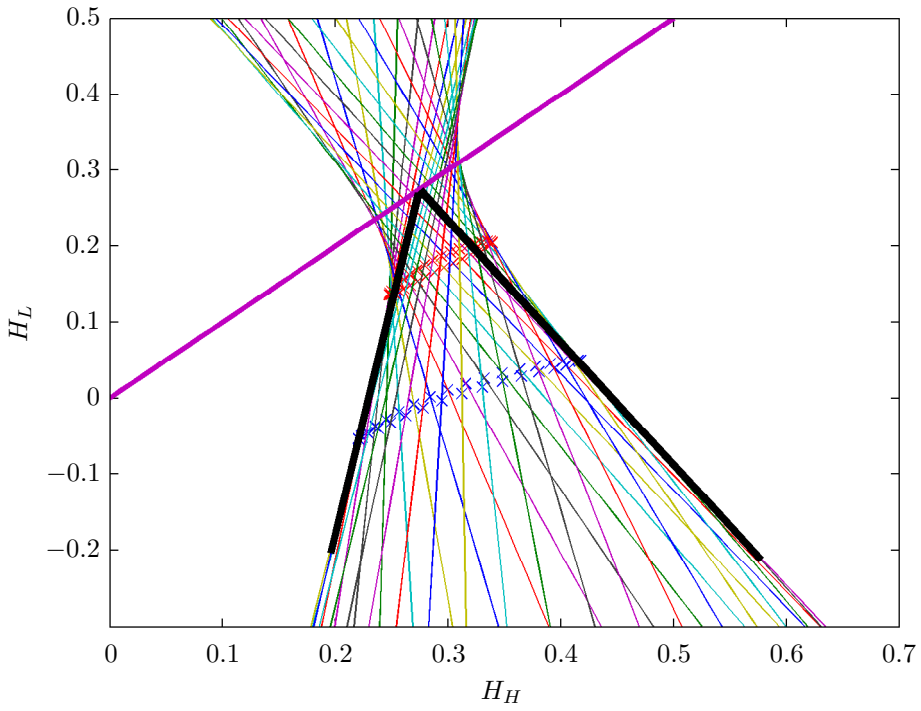

Figure 3.31: Plots of H_H versus H_L at 50 (blue) and 150m (red). Each point $(H_H(\phi), H_L(\phi))$ at 50m is then fitted and extrapolated to the same $H_H(\phi), H_L(\phi)$ at 150m. The purple solid line corresponds to the bisectrix $H_H = H_L$. The black solid lines are suggested paths of convergence.

We can see that a general form arises in the interpolation of $H_H(\phi)$ and $H_L(\phi)$ and that H_0 can be estimated to be 0.3, not far from the K41 theory's 1/3 exponent with an intermittency correction!

The Domain Of Impinging Eddies

So what exactly is H_0? In order to explain what H_0 is we must first explain why H_L decreases the closer we are to the wall. The explanation for this comes from the proposition of Korotkov [1976], that is, for near-wall length-scales the spectrum is defined solely through the friction velocity u_*. If this is true we must have a frequency ω_* that is also a function of the near-wall velocity (see also Kader and Yaglom [1989] and Yaglom [1993] for similar dimensional arguments and **?** for arguments using rapid distortion theory). Figure 3.32 shows the integrated spectra of the u-component velocity at 10, 50, 75, 100, 125 and 150m (from top to bottom). Taking the peaks as approximations of a minimum frequency ω_* we can see that the log-relation to height is approximately linear i.e. a power law in a linear plot. We showed in section §2.1 that for scales larger than a minute a power law approximation could be used. Loosely speaking therefore we can argue that the lower frequency velocities are indeed in agreement with this proposition, i.e., that ω_* depends on height.

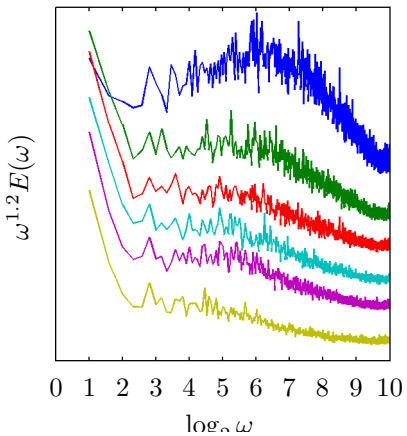

Figure 3.32: Log-linear plot of compensated, perpendicular, horizontal wind spectra, $\omega^{1.2}E(\omega)$, vs. the normalised frequency, ω; Plots correspond to horizontal wind speeds at 10, 50, 75, 100, 125 and 150m, on the inner position of Mast 2 (shifted from top to bottom).

We can now answer the question – what is H_0? It is the scaling exponent of the velocities above the height of the surface-layer, i.e. the height at which we are no longer able to observe eddies whose length-scale depend on a surface-friction velocity. Using, the blue and red plots in figure 3.31 at 50 and 150m we can get a

rough estimate of the height of the surface-layer; 50m above 150m, therefore our surface-layer height is 200m.

A Near-Wall Model

We know that for scales $\omega > \omega_*$ the eddies are 'impinged' eddies. Why we don't observe an exact -1 power is a topic we will come back to very shortly. For scales $\omega < \omega_*$ we have a scaling parameter and anisotropy relation defined by equation 3.22. Note that, even in Korotkov [1976] he mentions that if the advecting wind is $U(x)$, the friction velocity will (anisotropically) deform the length scales $\ell_{*,x} = u_{*,x}\tau$ of the structures.

For structures of size $\ell > \ell_*$, where $\ell_* = 1/\omega_*$, we have spectra that scale as k^{-1} i.e. have lower energy flux due friction forces. The structures are anisotropic if $\Delta H_L(\Delta z) > 0$ (the difference in low frequency exponents at two heights). Within a cascade framework the energy they contain is (anisotropically) passed down to smaller scales up to the scale $\ell < \ell_*$ in which there exist only unimpeded eddies with scaling exponents H_0. Due to the higher energy flux in these eddies anisotropy must be compensated, i.e. increase (with a loss factor of 2) due to conservation

$$H_0(z) - H_L(z) \propto H_H(r). \tag{3.23}$$

Moreover, one would expect therefore that the increase in anisotropy from large scales to small scales is proportional to the difference in energy between the two scale separations with the same loss factor 2. Since the energy at high frequencies is quantified by H_0 we find that

$$H_L(r) \propto H_0 - H_L(z). \tag{3.24}$$

Note we do not need H_0 to calculate the proportionality constant, only the spectral exponents at two heights. Figures 3.33 and 3.34 are diagrams that attempt to conceptually explain this phenomena.

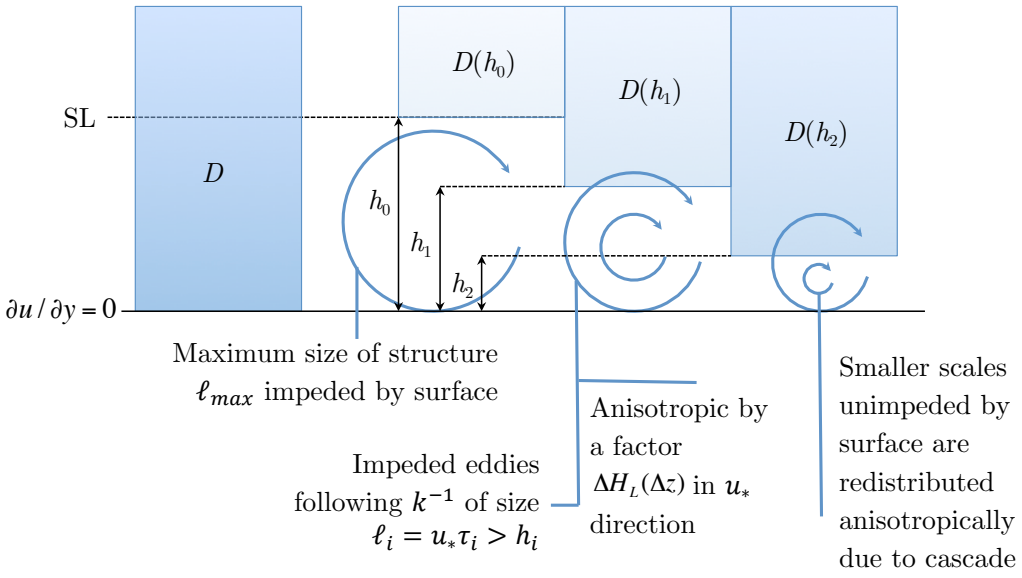

Figure 3.33: Diagram of surface-layer scalings.

In the diagrams we have also attempted to explain the transition from H_0 to k^{-1} through an observable domain space. If we start from H_0 – a height higher than the largest impinged eddy – and we move our point of measurement closer and closer to the surface we find that we are in fact increasing the number of impinged eddies we observe. However, the number of impinged eddies we observe are a subset of the fully mixed domain. The intersection of the sets D_I and D_U will be defined by the minimum size of the impinged structure $h_{\min}$. The closer we are to the surface therefore the larger the contribution of the set D_I. This an important idea because it implies that we will never truly converge to -1 (excluding corrections for intermittency). Observations of the -1 power law therefore infer the occurrence of intermittency at the near-wall. Other boundary-layer observations, specifically Koprov et al. [2005], of the velocity have shown similar scaling behaviour. In Koprov et al. [2005] however the longitudinal component of the helicity is also measured to be a passive scalar. They argue that the observation of a non-zero helicity is characteristic of an enstrophy cascade over larger scales. This questions therefore the direction of the cascade of the flux (i.e. the sign). A possible explanation for the complexities that arise later on in this thesis.

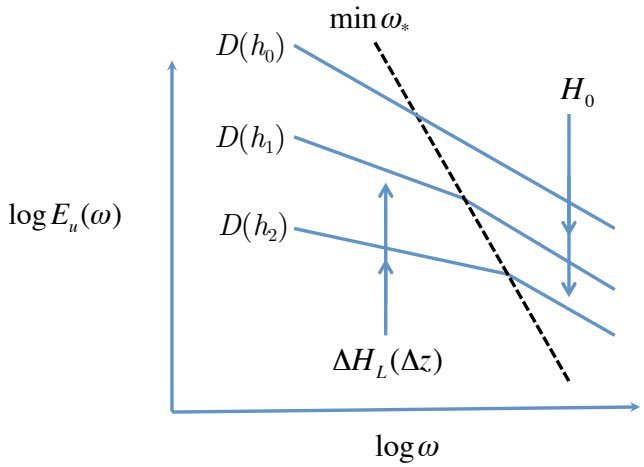

Figure 3.34: Diagram of spectra corresponding to the domains $D(h_0)$, $D(h_1)$ and $D(h_2)$.

A consequence of impinging eddies is that the cascade ceases to be local (i.e. interaction between eddies of similar sizes) become non-local (large size difference of interacting eddies) and the transfer time is no longer the usual eddy-turn over time (e.g. a time defined with the help of u_*). This drastically changes the relationship between the energy flux and the energy co-variance (and spectrum). We later see that the standard methods for estimating universal multifractal parameters using the usual energy flux density proxy – based on the third order structure function – fail. Intermittency may also drastically change this picture: u_* may fluctuate much more than the usual Gaussian assumption and therefore yield a different spectral slope.

Figure 3.35 compares the average spectra of the u-component at 23 and 43m. We can note that the lesser observed anisotropy in figure 3.21 is consistent with our proposal since $\Delta H_L(\Delta z) = 0$. One possible explanation for this is the much lower spectral exponent found over the lower frequencies (-0.8 instead of -1) due to the extraction of energy from the turbines. In the wake of a turbine the drag forces are generated in a different way to friction forces resulting in a more three-dimensionally isotropic velocity field.

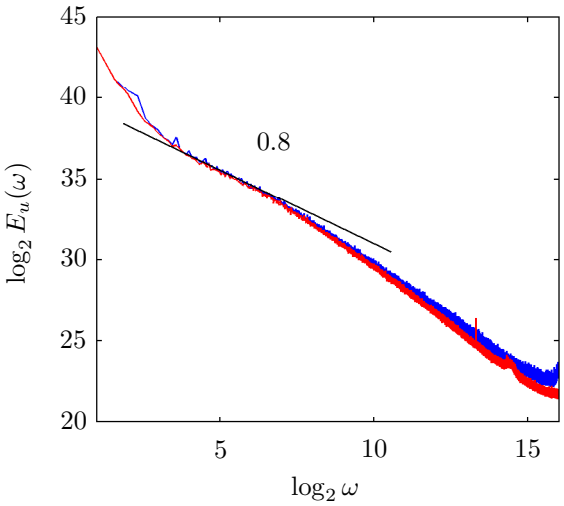

Figure 3.35: Comparison of the average spectra of the u-components at 23 and 43m for the Corsica dataset.

The results of all of the above analyses are summarised in Fitton et al. [b].

3.4 Summary Of Chapter 3

We found that turbulent wind increments are so extreme that their probability distributions follow a power law. In spite of very different orographic conditions at 50m heights, empirical estimates of the power law exponent vary between 4 and 5. To investigate this question, we use a rotated frame of reference to analyse the anisotropy of the horizontal velocity. We found that the scaling anisotropies of the velocity were far beyond that of mere scaling subranges. Due to the prevailing direction of the wind the horizontal velocity components of the wind cannot be treated as i.i.d.s. For time-scales above a few seconds, both data exhibit a strong, scaling anisotropy that decreases with height. The horizontal velocity components are in fact so correlated ($r > 1$) that their statistics are component-wise anisotropic.

As with the 23/9 dimensional model, the anisotropy reduces the total dimension of the system that moreover has an immediate effect on the extremes of a given process. We analytically demonstrate that the power law exponent decreases when anisotropy increases, corresponding to wilder and wilder extremes. This finding gives a first glimpse into one of the many possible turbulence mechanisms in the atmospheric surface-layer that may seemingly over-generate wind increment extremes if they are studied in an isotropic (scaling) framework. We put forward an analytical expression for the angular variation of the Hurst exponent that determines the generation of wind increment extremes, including those in the wake of a turbine.

We discuss the surface-layer model that integrates the consequences of the scaling anisotropies when analysing the atmospheric stability. Although as of yet we cannot directly quantify the intermittency of a field based on its stability we have suggested its component-wise anisotropy, and therefore extremes, can be quantified by ΔH. This brings some particularly useful applications for wind energy: a means to evaluate surface-layer height and a meaningful parameter with which to quantify stability.

References: Chapter 3

M. Barnsley. *Fractals everywhere*. Academic Press Inc., Boston, MA, 1988. ISBN 0-12-079062-9. URL http://www.ams.org/mathscinet-getitem?mr=MR977274.

Y. D. Chashechkin. Hydrodynamics of a sphere in a stratified fluid. *Fluid Dynamics*, 24(1):1–7, 1989. URL http://www.google.fr/search?client=safari&rls=10_7_4&q=Hydrodynamics+of+a+sphere+in+a+stratified+fluid&ie=UTF-8&oe=UTF-8&redir_esc=&ei=2ZznUcubCKi30QWCxYDYAQ.

P. Drobinski, P. Carlotti, R. K. Newsom, R. M. Banta, R. C. Foster, and J. L. Redelsperger. The structure of the near-neutral atmospheric surface layer. *Journal of the atmospheric sciences*, 61(6):699–714, 2004. doi:10.1175/1520-0469(2004)061¡0699:TSOTNA¿2.0.CO;2. URL http://dx.doi.org/10.1175/1520-0469(2004)061<0699:TSOTNA>2.0.CO;2.

K. J. Falconer. *The geometry of fractal sets*, volume 85 of *Cambridge Tracts in Mathematics*. Cambridge University Press, Cambridge, 1986. ISBN 0-521-25694-1; 0-521-33705-4. URL http://www.ams.org/mathscinet-getitem?mr=MR867284.

J. Feder and P. Bak. Fractals. *Physics Today*, 42:90, 1989.

G. F. Fitton, I. Tchiguirinskaia, D. Schertzer, and S. Lovejoy. Scaling Anisotropy And Extremes In The Wake Of A Turbine (submitted). In *21eme Congres Francais de Mecanique: Journal of Mechanics and Industry*.

U. Frisch, P. Sulem, and M. Nelkin. A simple dynamical model of intermittent fully developed turbulence. *Journal of Fluid Mechanics*, 87(04):

719–736, January 1978. URL http://www.google.fr/search?client=safari&rls=10_7_4&q=A+simple+dynamical+model+of+intermittent+fully+developed+turbulence&ie=UTF-8&oe=UTF-8&redir_esc=&ei=E9eHUK2mMeSp0QWJnIDYBA.

C. Garrett and W. Munk. Oceanic mixing by breaking internal waves. In *Deep Sea Research and Oceanographic Abstracts*, pages 823–832. Elsevier, 1972. URL http://www.google.fr/search?client=safari&rls=10_7_4&q=Oceanic+mixing+by+breaking+internal+waves&ie=UTF-8&oe=UTF-8&gws_rd=cr&ei=jUErUoquO6en0wWFzYCIBg.

S. J. Hovde, A. F. Tuck, S. Lovejoy, and D. Schertzer. Vertical scaling of temperature, wind and humidity fluctuations: dropsondes from 13 km to the surface of the Pacific Ocean. *International Journal of Remote Sensing*, 32(20):5891–5918, October 2011. doi:10.1080/01431161.2011.602652. URL http://www.tandfonline.com/doi/abs/10.1080/01431161.2011.602652.

T. Ishihara, T. Gotoh, and Y. Kaneda. Study of high-Reynolds number isotropic turbulence by direct numerical simulation. *Annual review of fluid mechanics*, 41:165–180, 2009. URL http://www.google.fr/search?client=safari&rls=10_7_4&q=Study+of+high+Reynolds+number+isotropic+turbulence+by+direct+numerical+simulation&ie=UTF-8&oe=UTF-8&gws_rd=cr&ei=0sspUuKpDfDb7Aa65YGYCw.

B. A. Kader and A. M. Yaglom. Spatial correlation functions of surface-layer atmospheric turbulence in neutral stratification. *Boundary-Layer Meteorol*, pages 1–17, 1989. URL http://www.springerlink.com/index/R23468231254223N.pdf.

B. M. Koprov, V. M. Koprov, V. M. Ponomarev, and O. G. Chkhetiani. Experimental studies of turbulent helicity and its spectrum in the atmospheric boundary layer. *Dokl. Phys.*, 50(8):419–422, August 2005. doi:10.1134/1.2039983. URL http://link.springer.com/10.1134/1.2039983.

B. N. Korotkov. Kinds of local self-similarity of the velocity field of prewall

turbulent flows. *Fluid Dynamics*, 11(6):850–856, 1976. URL http://link.springer.com/article/10.1007/BF01026403.

J. P. Laval, J. McWilliams, and B. Dubrulle. Forced stratified turbulence: Successive transitions with Reynolds number. *Phys. Rev. E*, 68(3):036308, September 2003. doi:10.1103/PhysRevE.68.036308. URL http://link.aps.org/doi/10.1103/PhysRevE.68.036308.

S. Lovejoy and D. Schertzer. Scale invariance, symmetries, fractals, and stochastic simulations of atmospheric phenomena. *Bulletin of the American meteorological society*, 67(1):21–32, 1986. URL http://www.google.fr/search?client=safari&rls=10_7_4&q=Scale+invariance+symmetries+fractals+and+stochastic+simulations+of+atmospheric+phenomena&ie=UTF-8&oe=UTF-8&redir_esc=&ei=YW8aUZXIF8uS0QWN6YGoBA.

S. Lovejoy, D. Schertzer, M. Lilley, K. B. Strawbridge, and A. Radkevich. Scaling turbulent atmospheric stratification. I: Turbulence and waves. *Q.J.R. Meteorol. Soc.*, 134(631):277–300, 2008. doi:10.1002/qj.201. URL http://doi.wiley.com/10.1002/qj.201.

S. Lovejoy, A. F. Tuck, S. J. Hovde, and D. Schertzer. Vertical cascade structure of the atmosphere and multifractal dropsonde outages. *Journal of Geophysical Research: Atmospheres (1984–2012)*, 114(D7), 2009. doi:10.1029/2008JD010651. URL http://onlinelibrary.wiley.com/doi/10.1029/2008JD010651/full.

B. Mandelbrot. How long is the coast of Britain? Statistical self-similarity and fractional dimension. *Science*, 156(3775):636, January 1967. URL http://www.google.fr/search?client=safari&rls=10_7_4&q=How+long+is+the+coast+of+Britain+Statistical+self+similarity+and+fractional+dimension&ie=UTF-8&oe=UTF-8&redir_esc=&ei=-SqJUO2EJcHS0QXl8IHYAw.

B. Mandelbrot. Fractals, Chance and Dimension. 1977.

B. B. Mandelbrot. Intermittent turbulence in self-similar cascades- Divergence of high moments and dimension of the carrier. *Journal of Fluid*

Mechanics, 62(2):331–358, 1974. doi:10.1017/S0022112074000711. URL http://journals.cambridge.org/production/action/cjoGetFulltext?fulltextid=385759.

B. B. Mandelbrot. *The fractal geometry of nature*. W. H. Freeman and Co., San Francisco, Calif., 1982. ISBN 0-7167-1186-9. URL http://www.ams.org/mathscinet-getitem?mr=MR665254.

E. A. Novikov and R. W. Stewart. The intermittency of turbulence and the spectrum of energy dissipation fluctuations. *Izv. Geophys. Ser*, 3:408–413, 1964.

J. Peinke, P. Schaumann, and S. Barth. *Wind energy: proceedings of the euromech colloquium*. Springer, 2006.

A. Pouquet, U. Frisch, and J. Léorat. Strong MHD helical turbulence and the nonlinear dynamo effect. *Journal of Fluid Mechanics*, 77(321-354): 44, 1976. URL http://www.google.fr/search?client=safari&rls=10_7_4&q=Strong+MHD+helical+turbulence+and+the+nonlinear+dynamo+effect&ie=UTF-8&oe=UTF-8&redir_esc=&ei=oJznUeLjN4mX1AWGzICIBg.

D. Schertzer. Physical modeling and analysis of rain and clouds by anisotropic scaling multiplicative processes. *J. Geophys. Res.*, January 1987. URL http://www.physics.mcgill.ca/~gang/eprints/eprintLovejoy/neweprint/JGR.SL.1987.good.pdf.

D. Schertzer and S. Lovejoy. Elliptical turbulence in the atmosphere. In *Symposium on Turbulent Shear Flows, 4 th, Karlsruhe, West Germany*, page 11, January 1984a. URL http://www.google.fr/search?client=safari&rls=10_7_4&q=Elliptical+turbulence+in+the+atmosphere&ie=UTF-8&oe=UTF-8&redir_esc=&ei=4jSJUNnnA4-GhQe62YGQBg.

D. Schertzer and S. Lovejoy. On the dimension of atmospheric motions. *Turbulence and Chaotic phenomena in Fluids*, pages 505–512, 1984b. URL http://scholar.google.com/scholar?q=related:JvT9pIKaPsgJ:scholar.google.com/&hl=en&num=20&as_sdt=0,5&as_ylo=1983&as_yhi=1983.

D. Schertzer and S. Lovejoy. Generalised scale invariance in turbulent phenomena. *PhysicoChemical Hydrodynamics*, 6:623–635, January 1985a. URL http://www.google.fr/search?client=safari&rls=10_7_4&q=Generalised+scale+invariance+in+turbulent+phenomena&ie=UTF-8&oe=UTF-8&redir_esc=&ei=4jSJUMnJA4jIhAfYwoCoCw.

D. Schertzer and S. Lovejoy. The dimension and intermittency of atmospheric dynamics. *Turbulent shear flow*, 4(7):7–33, January 1985b. URL http://www.google.fr/search?client=safari&rls=10_7_4&q=The+dimension+and+intermittency+of+atmospheric+dynamics&ie=UTF-8&oe=UTF-8&redir_esc=&ei=4jSJUOzlA4exhAfks4HwAQ.

D. Schertzer and S. Lovejoy. Scaling nonlinear variability in geodynamics: multiple singularities, observables and universality classes. *Nonlinear Variability and Geophysics: Scaling and Fractals. Kluwer, Dordrecht*, pages 41–92, 1991.

D. Schertzer and S. Lovejoy. Multifractal Generation of Self-Organized Criticality. *Fractals In the natural and applied ...*, 1993. URL http://www.physics.mcgill.ca/~gang/eprints/eprintLovejoy/neweprint/Novak.all.pdf.

D. Schertzer and S. Lovejoy. EGS Richardson AGU Chapman NVAG3 Conference: Nonlinear variability in geophysics: scaling and multifractal processes. *Nonlinear Processes in Geophysics*, 1(2/3):77–79, 1994.

D. Schertzer, S. Lovejoy, and D. Lavallée. Generic multifractal phase transitions and self-organized criticality. *Cellular Automata: prospects in ...*, 1993. URL http://132.206.6.11/~gang/eprints/eprintLovejoy/neweprint/Schert93.all.pdf.

F. Schmitt, D. Schertzer, S. Lovejoy, and Y. Brunet. Empirical study of multifractal phase transitions in atmospheric turbulence. *Nonlinear Processes in Geophysics*, 1(2/3):95–104, 1994. URL http://www.google.fr/search?client=safari&rls=10_7_4&q=Empirical+study+of+multifractal+phase+transitions+in+atmospheric+turbulence&ie=UTF-8&oe=UTF-8&redir_esc=&ei=yROKUdWoJsGg0QXAl4D4CQ.

Y. Tessier, S. Lovejoy, and D. Schertzer. Universal multrifractals: Theory and observations for rain and clouds. *Journal of Applied Meteorology;(United States)*, 32(2), January 1993. URL http://www.google.fr/search?client=safari&rls=10_7_4&q=Universal+multrifractals+Theory+and+observations+for+rain+and+clouds&ie=UTF-8&oe=UTF-8&redir_esc=&ei=yDWJUJ74LpGLhQe-nYDgCA.

B. I. Xue-yan, L. Feng, and W. Dui. Comparison of Some Limits for Stability Classification. *Journal Of Tropical Meteorology*, 11(2), 2005. URL http://d.wanfangdata.com.cn/periodical_rdqxxb-e200502006.aspx.

A. M. Yaglom. Similarity laws for wall turbulent flows: their limitations and generalizations. In *New Approaches and Concepts in Turbulence*, pages 7–27. Springer, 1993. ISBN 3764329246. URL http://www.google.fr/search?client=safari&rls=10_7_4&q=Similarity+laws+for+wall+turbulent+flows+their+limitations+and+generalizations&ie=UTF-8&oe=UTF-8&gws_rd=cr&redir_esc=&ei=fmrpUdr5BoiChQeM4oHgCQ.

Chapter 4

4.1 Background Material On Universal Multifractals (UM)

In the previous chapter we showed that the processes involved in the surface-layer are scaling, and anisotropic. Although it was important to show that the atmosphere is much, much more complicated than the standard homogeneous isotropic model – a model that is used regularly both in the wind industry and other applied fluid dynamics related research – it does not bring us any closer to understanding the true intermittent and multifractal statistics of the wind; the original task that we had set out to do. Now that we have lots of evidence that the surface-layer is scaling, multifractals are the next step to take in our understanding of this complex system. Throughout the first chapter we presented the historical developments that led to the well-posed problem that is the non-linearity of the structure function. Understanding and being able to reproduce this non-linearity is the fundamental problem that must be addressed. If we can understand how the moments of the structure function are related to the scale separation ℓ through its scaling moment function we may easily reproduce the probabilities (and its extremes) of the velocity field.

Figure 4.1 compares empirical data with: the log-normal model (Gurvich and Yaglom [1967a]), the random β-model (Benzi et al. [1984]), the p-model (Meneveau and Sreenivasan [1987]) and the B-model (Yamazaki [1990]). We see that for the β and K41-models we have linear scaling of moments as a result of the unique co-dimension. For the other four models we clearly have non-linear structure functions. This gives us our first taste of reproducible multifractality and its affect on the $\zeta(q)$ due to the scaling moment function, $K(q)$. For the log-normal and p-models, although non-linear, they struggle to fit the empirical function due to the lower value of H (i.e. lower than $H = 1/3$). The random β-model and B-model do well to fit the curve (note the random β-model required a renormalisation).

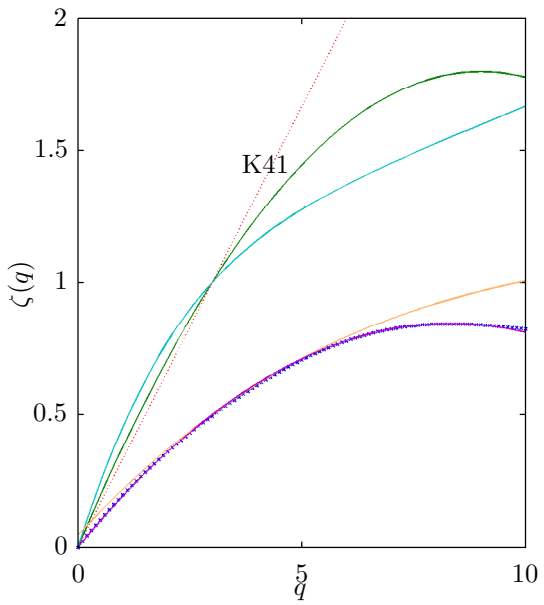

Figure 4.1: Exponent $\zeta(q)$ of the structure function. Blue crosses are the empirical structure function exponents for wind velocities measured in a wind farm test site in Corsica. Time-scales are from 2 seconds to a minute. The semi-analytical curves are: the log-normal model (green curve for $\Phi = 0.1$), the random β-model (orange curve for $C = 0.63$), the p-model (turquoise for $p = 0.13$) and the B-model (red curve for $\xi = 0.39$ and $\Theta = 0.22$). See table 4.1 for the $K(q)$ functions corresponding to the parameters.

In order to develop a multifractal contribution to the above diagram we must remind ourselves of the form of the co-dimension function derived for a cascading energy flux. Two general properties of the co-dimension function are that it is an

increasing function of γ and that it is convex. Because there is only the convexity constraint on $K(q)$ and $c(\gamma)$ (an increasing non-linear function), there are thus an infinite number of parameters required in order to determine a multifractal process.

So far, all the cascades that have been described have been discrete. This is because the scale ratio λ remains unsolved, leading to the construction of cubes that contain arbitrary properties of the generated structures. In these models the cascade, i.e. the structure function and thus the co-dimension function's moments, because of the weakness of the convexity constraint, require an infinite number of parameters.

If we simply iterate the model with a fixed ratio of scale λ, we indefinitely increase the overall range of scales $\Lambda \to \infty$. On the contrary by fixing the total scale range of the cascade processes such that λ is finite and then introduce more and more intermediate scales, the scale ratio between two consecutive cascade steps converges to 1. In this way, the densification of the cascade can yield universal behaviour. Schertzer [1987] proposed a continuous model for which three parameters were relevant enough to fully determine the function $K(q)$, and thus the co-dimension function (through the Legendre transformation [see appendix A.7]).

Universal Multifractal Parameters

We have already noted that the three parameters (H, C_1 and α) are of fundamental significance where: H characterises the deviation from conservation ($\langle\varepsilon_\lambda\rangle = \lambda^{-H}$; $K(1) = -H$, C_1 is the order and co-dimension of the mean singularities of the corresponding conservative flux (fixed point of the corresponding $c(\gamma)$), it is the local trend of the normalised $K(q)$ near the mean ($K(q) = C_1(q-1)$ for $(q-1)$) and H and C_1, thus define the best mono-fractal approximation to the mean of the process (see figure 4.2 [reproduced from Tessier et al. [1993]]).

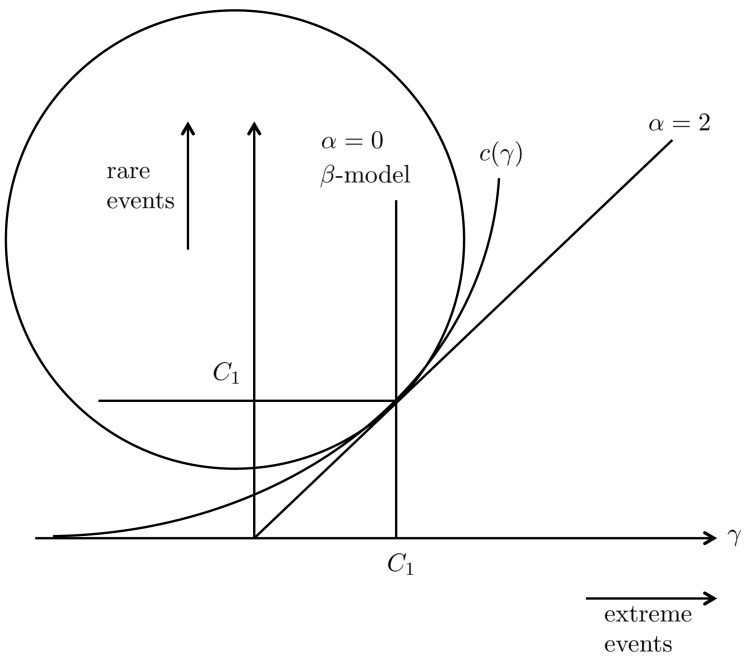

Figure 4.2: A schematic illustration showing how the $c(\gamma)$ curve can be locally characterised near the mean singularity C_1.

The parameter α continues this local description by characterising the local radius of curvature R_c of $c(\gamma)$, hence deviation from mono-fractality:

$$R_c(\gamma = C_1) = \frac{(1 + c'(C_1))^{3/2}}{c''(C_1)} = 2^{3/2}\alpha C \tag{4.1}$$

where the factor $2^{3/2}$ is introduced for convenience. Using the fact that $c(C_1) = C_1$ and $c'(C_1) = 1$ we see that the above definition of α is equivalent to:

$$\frac{d^2c(C_1)}{d\gamma^2} = \frac{1}{\alpha C_1}. \tag{4.2}$$

We can establish the corresponding relations for the second derivation and local radius of curvature of $K(q)$ near $q = 1$. Hence, we obtain

$$\frac{d^2K(1)}{dq^2} = C_1\alpha; \;\; R_K(1) = \frac{(1 + C_1^2)^{3/2}}{C_1\alpha} \tag{4.3}$$

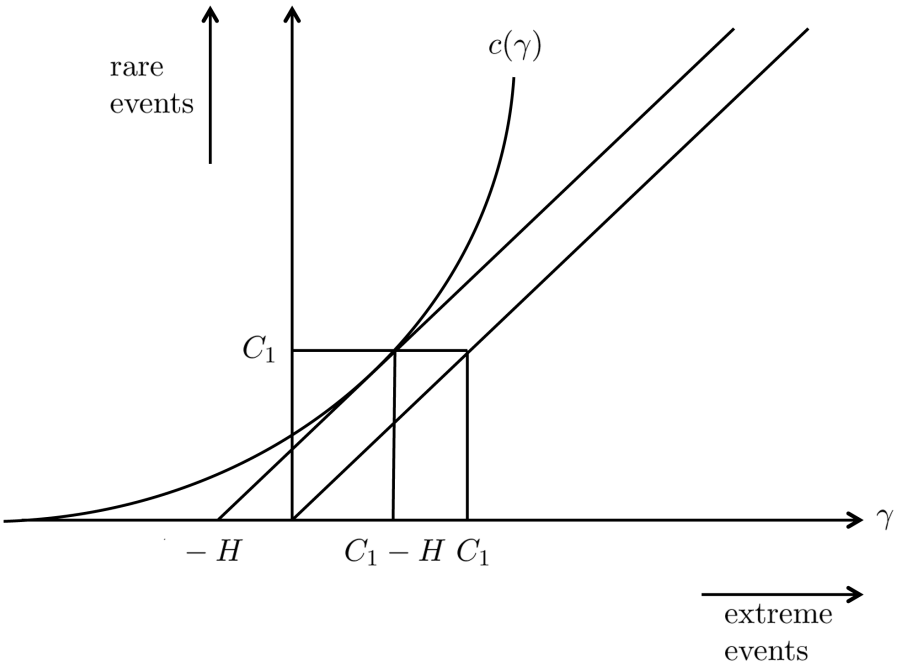

Figure 4.3: A schematic illustration showing the shift in $c(\gamma)$ of H for non-conservative processes.

Finally, for the universal model, the scaling moment function is written

$$K(q) = \begin{cases} \dfrac{C_1}{\alpha - 1}(q^\alpha - q) + Hq & \text{for} \quad \alpha \neq 1 \\ C_1 q \log(q) + Hq & \text{for} \quad \alpha = 1 \end{cases} \tag{4.4}$$

where α ($0 \leq \alpha \leq 2$) is the Lévy index, C_1 is the co-dimension of the mean singularity and H is the average deviation from the conservation field (see figure 4.3). The bijection between the orders of the moments and the singularities can be written in the case of $\alpha \neq 1$ as

$$q_\gamma = \left(\frac{\gamma_q}{C_1 \alpha'} + \frac{1}{\alpha} \right)^{1/\alpha}. \tag{4.5}$$

This leads to

$$c(\gamma + H) = \begin{cases} \left(\dfrac{\gamma}{C_1 \alpha'} + \dfrac{1}{\alpha} \right)^{\alpha'} & \text{for} \quad \alpha \neq 1 \\ C_1 e^{\gamma / C_1 - 1} & \text{for} \quad \alpha = 1 \end{cases} \tag{4.6}$$

In table 4.1, we summarise the turbulence models up to date and, their required number of parameters (n.o.p.) in comparison with universal multifractals.

n.o.p.	Date	References	Explanation	Parameters
1	1941	Kolmogorov, (Homogeneous Turbulence)	$\Delta u_\lambda \approx \varepsilon^{1/3}\lambda^{-1/3}$	$H = 1/3$
2	1962	Kolmogorov-Obukhov, (log-normal model)	$\langle \varepsilon_\lambda^q \rangle = \lambda^{K(q)}$ $K(q) = \frac{\Phi}{2}(q-1)q$	H, $\Phi = 2C_1$ $(\alpha = 2)$
2	1964	Novikov-Stewart, Mandelbrot, Frisch et. al, (β-model)	$K(q) = C_1(q-1)$	H, C_1 $(\alpha = 0)$
∞	1983-85	Grassberger, Hentschel-Procaccia, Schertzer-Lovejoy, Parisi-Frisch, (Multifractal model)	$K(q)$	$K(q)$
3	1987	Schertzer Lovejoy, (Universal Multifractals)	$K(q) = \frac{C_1}{\alpha - 1}(q^\alpha - q)$	H, C_1, α
1	1987	Meneveau and Sreenivasan, (p-model)	$K(q) = q - 1 \ldots$ $\ldots + \log_2 \left[p^q + (1-p)\right]^q$	p
2	1990	Yamazaki, (B-model)	$K(q) = q\xi + q^2\Theta/2$	ξ, Θ

Table 4.1: Summary of Turbulent Models

The parameters H, C_1 and α are thus the 'local' multifractal hierarchy around the average behaviour. Below we show that this characterisation will become global for the universal multifractal (up to the order q_D where the divergence of moments intervenes).

Universal attractors of additive processes can be used to deduce multiplying processes. This can be done by studying the 'generators' of the resulting field, ε_λ, resulting from the exponential of the generator. Multiplying fields, ε_λ, are equivalent to adding generators, Γ_λ (for fixed scale ratio). We are then led to seek 'generators' that are 'stable' and 'attractive' under 'addition'. With the help of the scaling moment function $K(q)$, which is the second Laplace characteristic function – also called the cumulant generating function – of the corresponding generator, we will show these stable and attractive generators are the stable extremal Lévy noises with $1/f$ (generalised spectra are characterised by the Lévy noise α ($P(-\Gamma_\lambda \geq s) \simeq s^{-\alpha}$ where $(s \gg 1)$) $\implies$ any $q > \alpha : \langle(-\Gamma_\lambda)^q\rangle = \infty$).

This index is the order of divergence of moments of the generator (except for the Gaussian $\alpha = 2$, where there is no divergence). These generators yield 'universal' expressions for the scaling function of the moments of the field $K(q)$ and of the co-dimension function $c(\gamma - H)$:

1. $\alpha = 0$:
   β-model mono-fractal case study

2. $0 < \alpha < 1$:
   Log-Lévy process with strong negative singularities, but bounded positive singularities

3. $\alpha = 1$:
   Multifractal Log-Cauchy

4. $1 < \alpha < 2$:
   Log-Lévy process with unbounded positive singularities

5. $\alpha = 2$:
   Multifractal Log-Normal[1]

[1] Log-Lévy or Log-Normal are misnames because of the difference in behaviour for $q \leq q_D$.

The Sampling Dimension

The co-dimension function is a measure of the fraction of the probability space formed by the total number of samples of dimension D occupied by the singularities of order equal to or superior to γ. If $c(\gamma)$ is an increasing function for positive values of γ, i.e. the largest singularities are the rarest, one will find that the maximum value of γ, denoted γ_s, observed on at least one sample in N_s independent samples of volume D is approximated by

$$N_s \lambda^D \lambda^{c(\gamma_s)} \sim 1. \tag{4.7}$$

Introducing the definition of the dimension of sampling D_s for N_s samples:

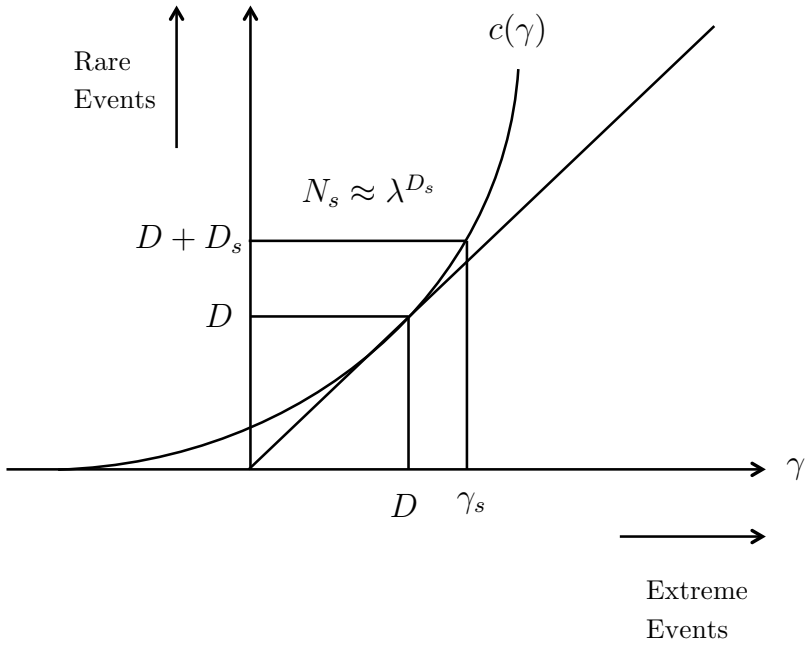

Figure 4.4: Schematic illustration of the sampling dimension and how it imposes a maximum order of singularities γ_s.

$$\lambda^{D_s} = N_s, \text{ and } D_s = \frac{\log N_s}{\log \lambda}. \tag{4.8}$$

Using equation 4.7 we obtain the following relation for γ_s:

$$c(\gamma_s) \approx D + D_s. \tag{4.9}$$

The last equation shows that the larger the sampling dimension the larger the spectrum of accessible values of γ (see figure 4.4). Although for universal multifractals the above relation can be solved for γ_s in practice it is more interesting to look to $q_s = c'(\gamma_s)$. The order q_s is therefore the highest order moment that can be reliably estimated with a finite samples size. This moment is given by the following formula:

$$q_s = \left[\frac{D + D_s}{C_1}\right]^{\frac{1}{\alpha}}. \tag{4.10}$$

4.2 Empirical Estimation Of UM Parameters

Linearity

As we saw in the previous chapter it is possible to have a number of scaling subranges with a variety of scaling exponents. This can cause problems when estimating the fits of our regressions on large datasets, especially if the position of a break is unknown, as is usually the case, thus biasing our estimates. To make life easier, therefore, we start by attempting to estimate the UM parameters on a single uniquely scaling sample i.e. there is no scaling break, as was commonly observed in the last chapter. Note, since the spectra is only a second-order statistic we cannot confirm the unique scaling will persist through higher order moments.

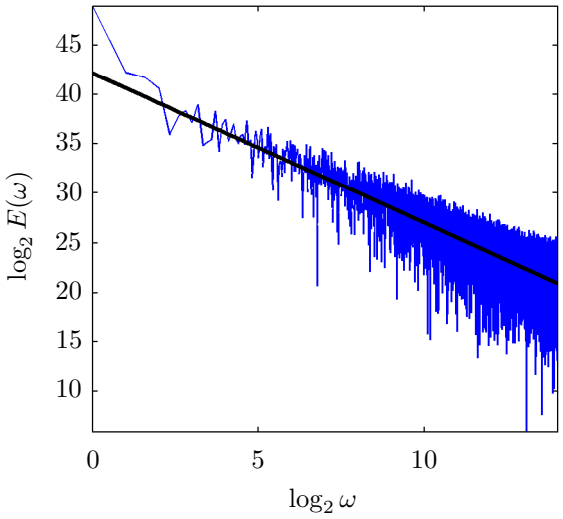

Figure 4.5: The energy spectra, $E(\omega)$, of a single sample of the horizontal velocity component $u(t)$. The sample is the velocity measured at 10Hz over one hour. This gives a maximum ratio of scale, $\lambda = 2^{15}$. In the plot the highest resolution $\log_2 = 14$ corresponds to 5Hz. This file was chosen as it (visually) showed little noise at the highest resolution. The slope of the solid black line corresponding to the scaling exponent β is 1.5.

To find a suitable file one would normally apply the following least-squares fitting method

$$R_i = y_i - f(x_i, \boldsymbol{m}), \tag{4.11}$$

where m_0 and m_1 are the intercept and slope in the function $\boldsymbol{m} = m_0 + m_1 x_i$ and x_i and y_i are the independent and dependent variables of a dataset consisting of $i = 1, \ldots, n$ data points. Figure 4.5 plots the function $f(x_i, \boldsymbol{m})$ estimated on the spectra of a file that has been visually chosen to be scaling.

Using a least-squares fitting method on noisy spectral data like those presented in figure 4.5 does not give a clear division between data with and without scaling breaks. One possibility for reducing the noise of a given sample when evaluating its scaling behaviour is to use the structure function,

$$\zeta(q) = \log(\langle|\Delta u(\tau)|^q\rangle)/\log(\tau), \tag{4.12}$$

where τ is the time separation between each velocity measurement. One of the issues associated with this method is that for the larger separations on a fixed length sample there are fewer statistics. This will typically correspond to a flattening at a scale that unfortunately corresponds approximately to the break in the data we are trying to avoid.

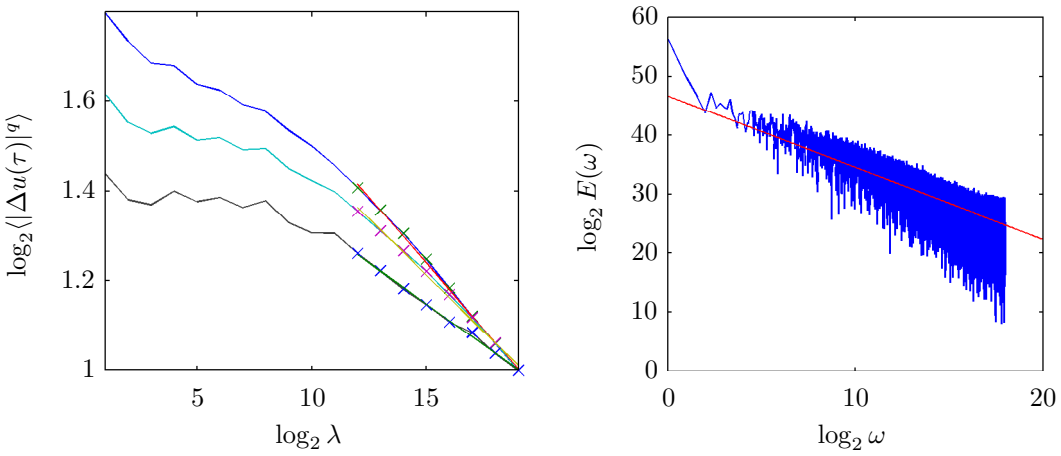

Figure 4.6: (a) Log-log plot of the u-component velocity time-increments for moments $q = 2$, 4 and 6 (from top to bottom); (b) energy spectra for the same sample, spectral exponent corresponding to the slope of the red line is 1.2.

Figure 4.6a is an example of the effects of poor statistics over larger scale separations; specifically $\log_2 \lambda > 10$. For the larger scale separations we find that for increasingly higher moments a spurious plateau occurs. When estimating the structure function by calculating the regression over the scale separations, the higher-order moments artificially decrease the value of $\zeta(q)$. Note this does not happen over the smaller separations due to the sufficient number of statistics. It is for this reason that the analyses that will involve the structure function hereafter are restricted strictly to the smallest separations. As a further comparison we have plotted the spectra from the same data (figure 4.6b). Unlike the moments of the increments the spectra have a unique scaling exponent through the scales.

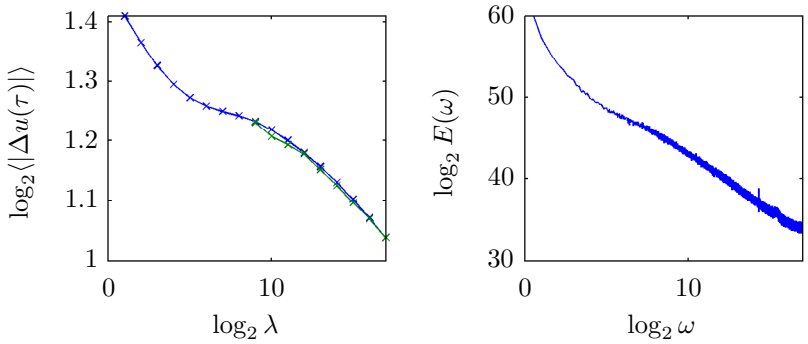

Figure 4.7: Left: blue crosses correspond to the ensemble-averaged first-order structure function (Corsica) obtained over the scales 0.1 seconds to approximately one-day. The superimposed green crosses are the structure function computed such that the statistics remain the same at all scale separations. This method requires $2N$ statistics. The r.h.s. plot shows the ensemble-averaged energy spectra over the same time-scales and for the same dataset.

In order to avoid the behaviour caused by the lack of statistics at larger separations we can take samples of length $2N$ in order to maintain the same statistics at all separations. Because the maximum length of each sample we have is 2^{19} the largest ranges of scales over which we can perform this sort of an analysis is therefore $\lambda = 2^9$, restricting us mainly to the highest frequencies. This is surprising that even for a very large, high resolution dataset (six-months at 10Hz), it is still difficult to obtain reasonable statistics at scales larger than a minute! It is for this reason alternative methods for analysing the scaling properties of higher order statistical moments were developed (see §4.2). Figure 4.7 compares the structure functions for decreasing and even statistics at larger

scales. We can see that maintaining even statistics across the scales doesn't bring any additional scaling information.

Empirical Estimates Of The Structure Function

To compute the structure function we require the moments of the increments of the velocity, either in space or time. In order to reduce the amount of time needed for the calculation of the moments at different spacings, τ, we have taken τ to be integer powers of two (in a similar way to the trace and double trace moment methods), meaning only $\log_2 N$ operations have to be performed per sample of length 2^N. We have also chosen to cut the daily samples of length 2^{19} into smaller sub-samples of length 2^{15} giving us a total of 2,576 sub-samples compared to the original 161 used for $\lambda = 2^{19}$. Increasing the statistics like this gives much smoother scaling behaviour over the higher frequencies.

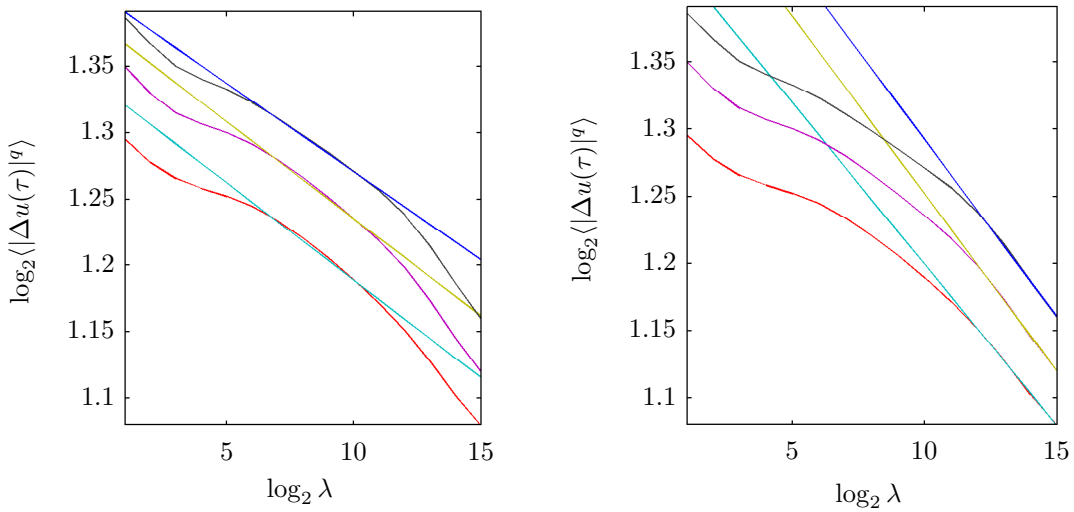

Figure 4.8: Ensemble average of the 2^{nd}, 3^{rd} and 4^{th} moments (bottom to top) of the increments of the horizontal velocity u versus λ in log-log plot.

Figure 4.8 is the ensemble average of the 2^{nd}, 3^{rd} and 4^{th} moments of the increments of the horizontal velocity u versus λ (i.e. $1/\tau$ so the orientation of the function is in the opposite direction to the standard plot) plotted with a log-log axis. The ensemble average is performed over all 2,576 files. In order to compare

the scaling of the increments of the structure functions we also computed the average spectra corresponding to the same data (figure 4.9).

Now, typically either the spectra or the first order structure function are used to estimate the parameter H. Estimating H from the spectra requires only the spectral exponent $\beta = 2H + 1$ omitting any intermittency correction. Starting first with the spectra we can see that there is an inertial range from $1\frac{1}{2}$ seconds to a minute with a spectral exponent $\beta = 1.27$ and therefore $H_\beta = 0.135$.

Calculating H from the increments of the velocity requires the log-log plot of the increments versus their scale separation. One would expect that the estimates from the two methods would not be vary to far from each other. However, this is not the case. For the first order moment of the increments the same smooth scaling behaviour observable in the spectra was instead curved. Furthermore, estimation and comparison of the parameter H showed a large discrepancy of the order 0.2.

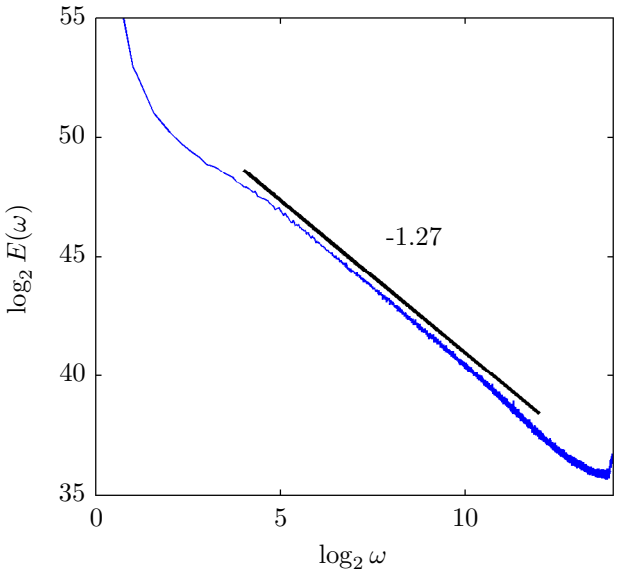

Figure 4.9: Ensemble averaged spectra of the same velocities used to calculate the moments of the increments in figure 4.8.

As a first order approximation we can estimate $H_{S(q)} = (S(q) + K(aq))/q$, for higher moment orders. We found that $H_{S(4)} \approx H_\beta$, gave the lowest R^2 over the same ranges of scaling as we had observed in the spectra (see top plot of figure

4.8a). Figure 4.8b shows regressions fitted over higher frequencies, the same curvature was less visible over lower order moments and the difference between the R^2 values was therefore indistinguishable due to the lower number of points the regression was estimated over.

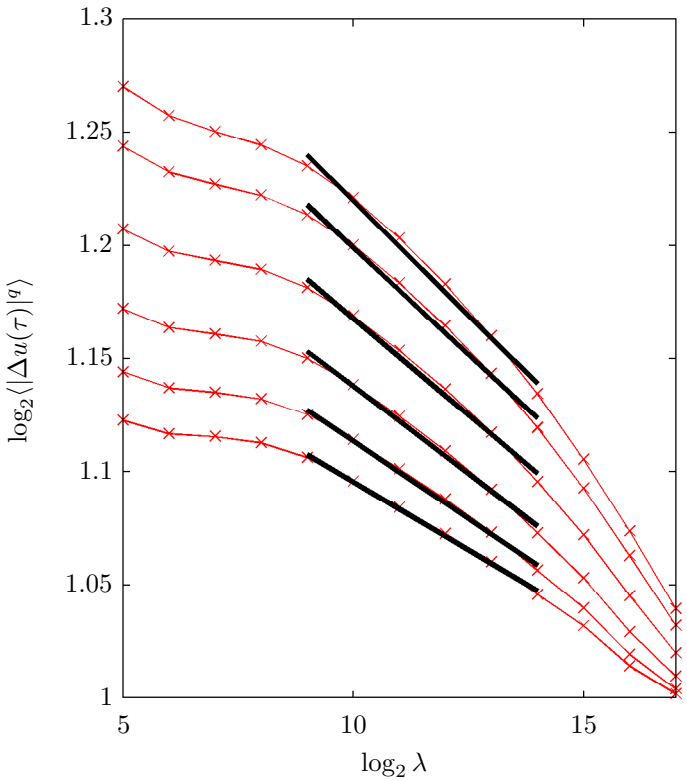

Figure 4.10: Plots of the moments of the velocity increments for $q = 1$ to 6 versus λ. The moments are averaged over the full Corsica dataset. The black lines correspond to the regressions used to estimate the structure function in figure 4.12.

Figure 4.10 plots the structure function for $q = 1$ to 6 for a larger $\lambda = 2^{18}$. The structure functions have been averaged over the full Corsica dataset therefore giving an average over 161 samples. As done previously we also compare the spectra (figure 4.11). The range of time-scales that are scaling are comparable; from one second to a minute ($\log_2 \lambda = 9$ to 14) with a similar scaling exponent ($\beta = 1.25$). The (absolute due to the use of λ on the horizontal axis) slopes of the black solid regression lines are the scaling exponent $\zeta(q)$. Figure 4.12 plots the function $\zeta(q)$.

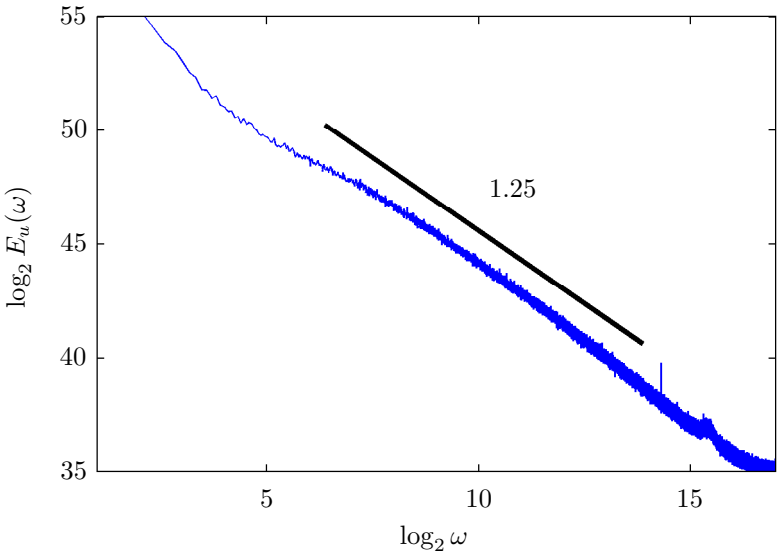

Figure 4.11: Average spectra of the velocities used in figure 4.10.

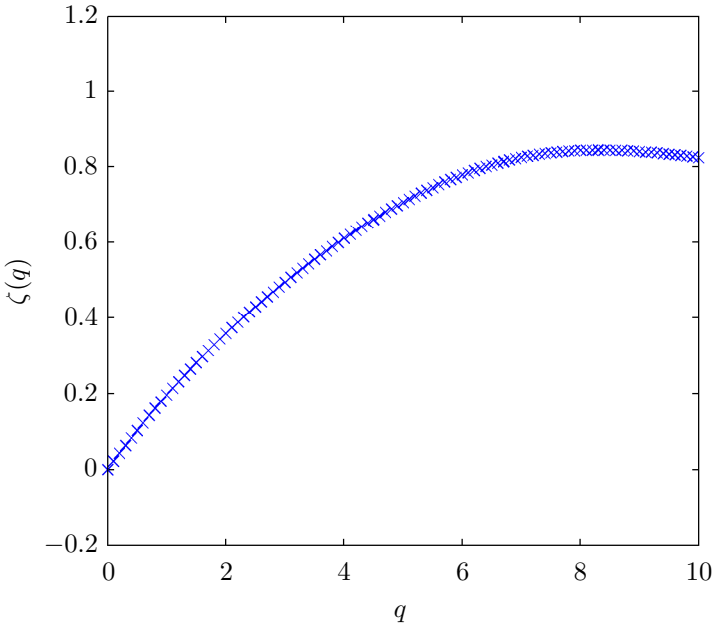

Figure 4.12: The scaling exponent of the structure function computed from the slopes of figure 4.10. The non-linear form of the scaling exponent corresponds to strong intermittency corrections. All of our previous discussions aim to determine this non-linearity ($K(aq)$).

Figure 4.12 shows the structure function computed from the slopes of figure 4.10. The non-linear form of the structure function corresponds to strong intermittency corrections. All of our future discussions aim to determine the non-linearity ($K(aq)$) of the function with the UM parameters α, C_1 and H. It is important to note while $\zeta(q)$ is non-linear there is no suggestion that for higher moments there is the effect of either q_s (equation 4.10) or q_D (equation 3.9); a linearity of $\zeta(q)$. This is an important result as shows that the structure function will smooth out the extremes of a process when ensemble averaged. This is consistent with our previous result showing that averaging over different anisotropies will result in something that appears isotropic. Whether this new isotropic field is in someway still representative of the sub-anisotropic fields is something we will discuss in more detail later on.

The Double Trace Moments (DTM)

We would like to estimate the universal multifractal (UM) parameters α, C_1 and H in order to reproduce the structure function of figure 4.12. The standard way to estimate the parameter α and therefore C_1 is to use the double trace moment (DTM) method. There are different means by which to do this however the usual way (see Lavallée [1991] and Schmitt et al. [1992]) is to define a normalised ηth power of the flux density ε

$$\varepsilon_\Lambda^{(\eta)} = \varepsilon_\Lambda^\eta / \langle \varepsilon_\Lambda^\eta \rangle \tag{4.13}$$

at the highest resolution $\Lambda = 1/\tau_0$, on which the trace moments (TM)s are then performed in the usual manner (this consists of taking the mean of the flux for different λ and q). In Schmitt et al. [1992] there is no mention of the use of the normalisation $\langle \varepsilon_\Lambda^{(\eta)} \rangle$, however, it is used in Veneziano and Furcolo [1999]. In Veneziano and Furcolo [1999] the normalised flux is defined instead as

$$\varepsilon_\lambda^{(\eta)} = \varepsilon_\lambda^\eta / \langle \varepsilon_\lambda^\eta \rangle. \tag{4.14}$$

Indeed for a scaling positive flux we can upscale $\varepsilon_\Lambda^{(\eta)}$ to the resolution λ to obtain the same result. The difference is however significant if instead of ε the non-positive velocity increments are used. This is discussed in more detail later on.

For DTM analyses we therefore use only equation 4.14.

Defining The Flux

In order to simulate a multifractal flux one requires the C_1 parameter of the conservative flux. It is for this reason that the DTMs are usually defined on ε_λ. This, however, isn't a necessary condition, merely a convenience since estimating the DTMs on the absolute velocity field requires an additional correction of the parameter $C_{1,\Delta u}$, i.e., $C_{1,\varepsilon} = C_{1,\Delta u} 3^\alpha$. It is usually easier therefore to simply calculate the parameters directly on a conservative field.

The flux is commonly defined as the third power of the velocity increments i.e. $\varepsilon_\lambda = |\Delta u_\lambda|^3 \lambda$. The DTM method is then applied to ε_λ (a positive quantity) in order to obtain the multifractality, α, and the mean co-dimension, C_1. When using this method we assume the linearly scaling part (λ^{-H}) is ignored. So what exactly does that mean? We showed in chapter one that the moments of the energy flux may scale as λ with exponent $K(q)$ (equation 1.14). From equation 4.13 we therefore have

$$\langle (\varepsilon_\lambda^{(\eta)})^q \rangle \propto \lambda^{K(q\eta) - qK(\eta)}. \tag{4.15}$$

Using the universality classes defined before i.e.,

$$K(q) = \frac{C_1}{\alpha - 1}\big(q^\alpha - q\big), \tag{4.16}$$

we obtain

$$K(q, \eta) = \eta^\alpha K(q). \tag{4.17}$$

This is a very important result as it gives an expression for the exponent α, independently of the resolution λ. This means we should be able to calculate the scaling non-linear part of the structure function ($K_\varepsilon(q)$) without the influence of λ^{qH}.

Figure 4.13 plots the DTMs computed on ε_λ for $q = 1.5$ and $\log \eta \in [-3 : 1]$ and the corresponding slopes estimated over the whole range of scales i.e. from 0.1 seconds to an hour. If we compare the scaling to that of the structure function it would seem that the curvature of the DTMs moments doesn't seem to be the result of a scaling break, more a problem with the assumption that $|\Delta u|^3 \lambda$ is not

a relevant proxy for the flux of energy flowing through the full range of scales and/or the Taylor hypothesis does not hold over this range.

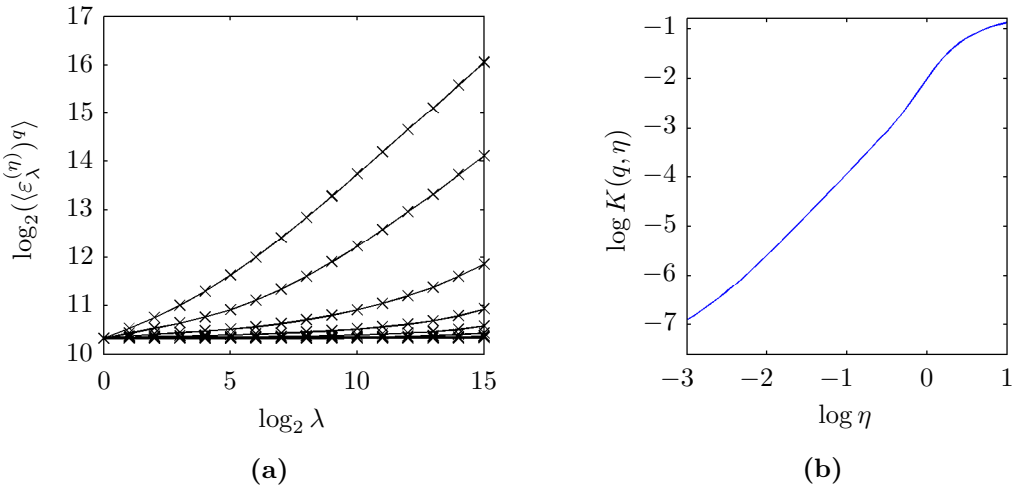

Figure 4.13: (a) plot of the DTMs estimated on the third power of the velocity increments for $q = 1.5$ and $\log \eta \in [-3 : 1]$. The slopes of these curves yield an estimate of $K(q, \eta)$ due to equation 4.14; (b) log-log plot of the slope $K(q, \eta)$ versus η for $q = 1.5$.

Local Estimates Of The DTMs

By equation 4.17 the multifractality is the slope of the log-log plot of the double trace moment $K(q, \eta)$ versus the moment order η (figure 4.14a). The slope (α) can be estimated using a number of methods (see Hoang [2011]), one of which counts a number of points about an inflection point should one exist. One method for determining the inflection point is to take the maximum local derivative, where the local estimator

$$\hat{\alpha}(q, \eta) = \frac{\partial \log(K(q, \eta))}{\partial \log(\eta)} = \frac{\eta}{K(q, \eta)} \frac{\partial K(q, \eta)}{\partial \eta} \text{ (again by equation 4.17)} \quad (4.18)$$

Figure 4.14 shows the standard s-shape versus the local estimate.

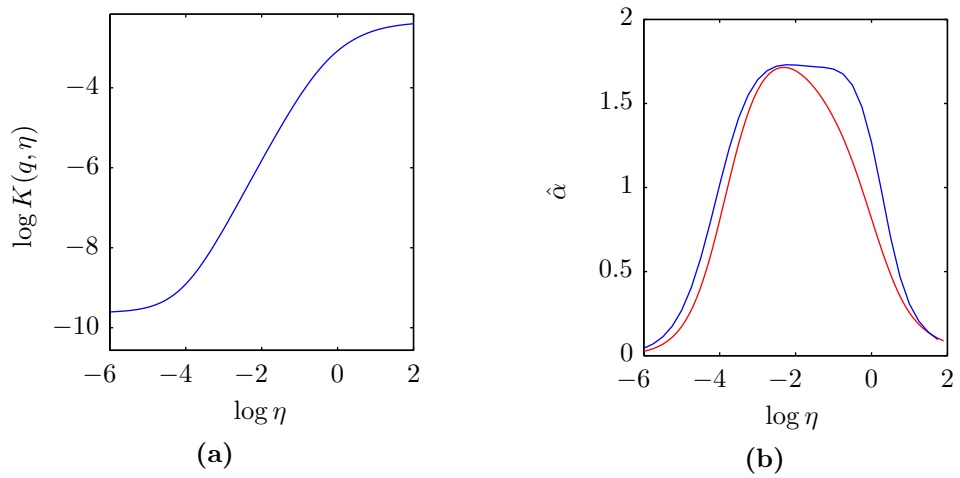

Figure 4.14: (a) Log-log plot of the $K(q,\eta)$ function versus $\log\eta \in [-6:2]$. The slope of the linear part gives the estimate of α; (b) the local derivative, $\hat{\alpha}$, of the curve given in (a) (blue) and the curve for a single measuring run (red).

The behaviour of the inflection point is a good indication of the quality of the estimate α; typically falling into one of three categories:

A wide range almost constant slope indicates the most stable estimate of α (blue curve in figure 4.14b). This is where the local derivative ($\hat{\alpha}$) exhibits a plateau like behaviour over a range of $\log\eta$. The length of the range over which $\hat{\alpha}$ remains constant can be used as a quantification of stability. Providing the field is scaling, ensemble averaging over a large number of samples with a small ratio of scales or having a small number of samples with a very large ratio scales, in general, resulted in a more stable estimate.

A unique inflection point indicates a reasonably stable estimate of α (red curve in figure 4.14b). Because the points either side of the inflection point decrease, the value of α will also decrease depending on how many points either side are included in the estimate. If the inflection point remains constant over a given range of $\log\eta$ the number of points taken either side doesn't matter since α remains the same.

A non-unique inflection point indicates an unstable estimate of α. If there is more than one or no inflection point in general we find a much higher

estimate of α. We discuss the possible reasons for instabilities in more detail later on.

One of the problems with looking to the DTMs over the full characteristic s-shaped range of the curve is, for the highest values of $\log \eta$ (in figure 4.13b this corresponds to $\log \eta \in [0 : 1]$) the flattening of the DTM curve corresponds to the highest moment, q_s, that can be reliably estimated by a finite sample size. The effect of q_s is a spurious linearity of the non-linear $K(q, \eta)$ function. The flattening at the smallest values of $\log \eta$ (from -6 to -4) is due to the number of zeros in the sample (see Hoang [2011] for details). Figure 4.15 illustrates this effect by adding and removing zeros from the sample. When all of the zeros are removed from the sample the estimator converges to two (the Lévy index for the log-normal model). When there are additional zeros added, the range over which the plateau exists is reduced up to the point where the original $\hat{\alpha}$ estimate becomes distorted from ~ 1.5 to 1.

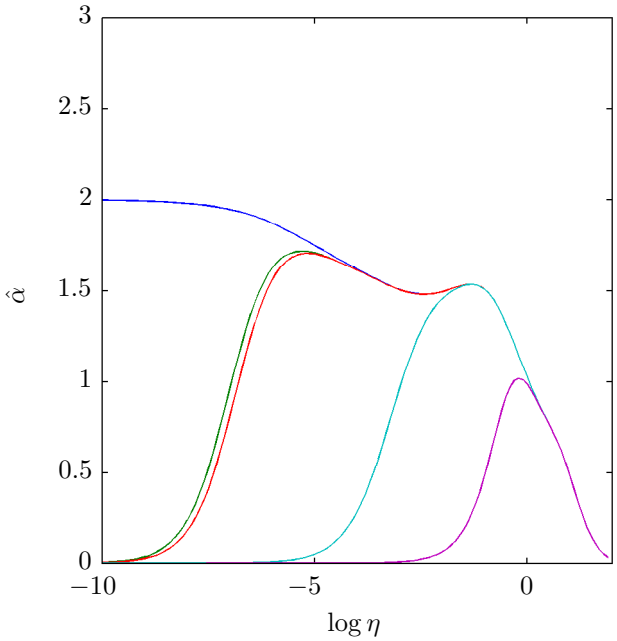

Figure 4.15: Plot of $\hat{\alpha}$ with zeros added and removed from a flux estimated on the third power of the velocity increments (red curve). Original estimated flux contained around 200 zeros. The green and blue curves correspond to 50 and 100% of those zeroes being removed. The turquoise and purple curves correspond to 50 and 100% of those zeros being added.

Coming back now to the DTMs of $|\Delta u|^3$, if one looks to the upper most curves of figure 4.13a (corresponding to the aforementioned high values of $\log \eta$, the q_s range) we may believe that the scaling is quite reasonable (possibly consisting of two or three scaling regions). However, if we look in a more objective manner using the normalised root mean squared error (NRMSE) as a function of $\log \eta$ (figure 4.16b) we find that for decreasing $\log \eta$ we have decreasing NRMSE.

In fact, over the very range where $\hat{\alpha}$ is constant ($\log \eta$ from -2 to -1), we have the worst possible scaling. The risk of basing the quality of scaling of the DTMs on this spurious linear scaling can be particularly misleading when the flux of the process is unknown (see Fitton et al. [a] for example). As discussed in the previous section, this is presumably the case in the surface-layer; due to impinging eddies and other anisotropic complexities. We may therefore consider a more general relation than K41 between the velocity increments Δu and the flux χ

$$\Delta u_\lambda \approx \chi_\lambda^a \lambda^{-h}, \tag{4.19}$$

where, χ_λ is a conservative process and a and h are given scaling exponents. If our process is unknown or the combination of different processes, the power we choose will change the range of the linearity of the DTMs such that $q_s' = aq_s$.

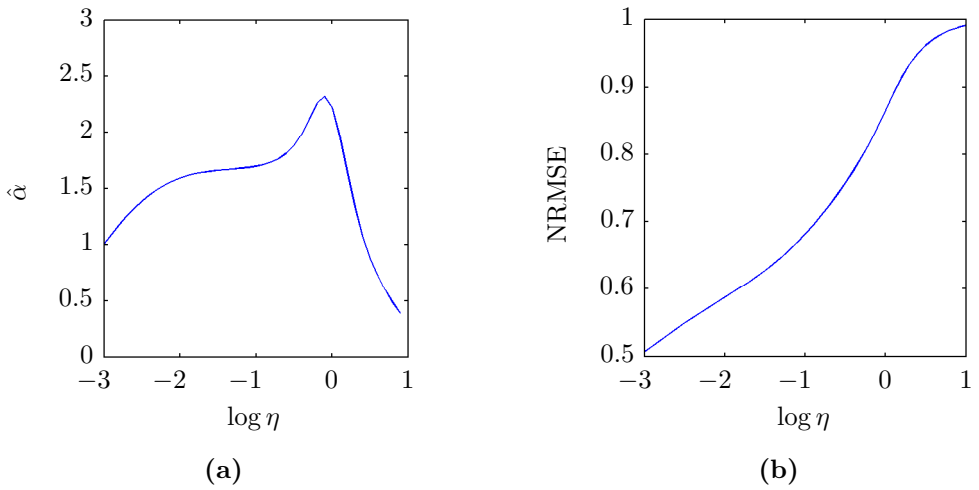

Figure 4.16: (a) the local derivative of the curve in figure 4.13b giving a local estimate of α, i.e. $\hat{\alpha} = \alpha(\eta)$; (b) plot of the corresponding NRMSE versus $\log(\eta)$.

We later show that the value of a simply translates the $\hat{\alpha}$ function, making it important to check and compare the scaling of the DTMs within the range of $\log \eta$ that α is estimated. For K41, $a = h = 1/3$ and $\chi_\lambda \equiv \varepsilon_\lambda$.

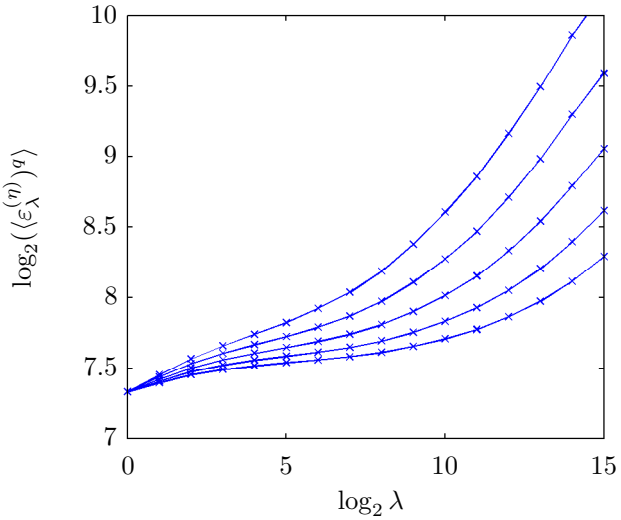

Figure 4.17: The DTMs estimated on the third power of the velocity increments ($\varepsilon = |\Delta u|^3$) for $q = 1.5$ (the same as in figure 4.13a) but for $\log \eta = 0.5$, 0, -0.5, -1, -1.5 and -2.

With this in mind we now look only to the DTMs for the values of $\log \eta$ where the plateau occurs. Figure 4.17 plots the DTMs at the points $\log \eta = 0.5$, 0, -0.5, -1, -1.5 and -2. The poor scaling of the DTMs over $\log \lambda$ is indeed in agreement with the low NRMSE values but in contradiction to the scaling observed in the spectra. The scaling is so bad that it implies that a fit over different λs would give UM parameters dependent on scale.

4.3 The Fractionally Integrated Flux (FIF)

Instead of simply taking the power of the increments of the velocity we can attempt to remove the linear part of the structure function by fractional integration. Exactly which field should be fractionally integrated i.e. the velocity field, u, itself or the increments, Δu, is not always clearly defined in the literature. Either way, we would expect the scaling exponents of each to be related by $h_{\Delta u} = h_u - 1$. To satisfy equation 4.19 it is sufficient to consider ($*$ denotes the convolution[1])

$$u_\lambda = \chi_\lambda^a * |t|^h. \tag{4.20}$$

In Fourier space this corresponds to

$$\hat{u}_\lambda \propto \hat{\chi}_\lambda^a \cdot |\omega|^{-(1+h)}. \tag{4.21}$$

As discussed above, our motivation is to find an order of fractional integration such that there exists a scale invariant flux χ_λ that satisfies equation 4.19. This is done by varying the order of fractional integration such that the DTMs become linear.

Figure 4.18 shows the effect of convoluting the u-component velocity for different values of h. For low h the DTM curve is concave in an inverse fashion to that observed in figure 4.16a. As h is increased the curved DTMs become more and more linear until at $h = 0.15$ we have our desired (linear in log-log plot) scaling as further highlighted by the solid black regression line. As we further increase h the convex curvature we found for the DTMs becomes apparent. If we were to further increase the value of h to $1/3$ we would find the same curved scaling that we observed in our previous plots since for $\varepsilon = \Delta u^3 \lambda$ we have hypothesised a scaling exponent $h = 1/3$. This result shows that over the time-scales 0.1 seconds to an hour the K41 scaling exponents aren't applicable.

[1] For the convolution to have a scaling exponent $-h$, you need to use a kernel X^{h-D}, where D is the dimension of the space (here 1). This is discussed in the appendix of Schertzer et al. [1997].

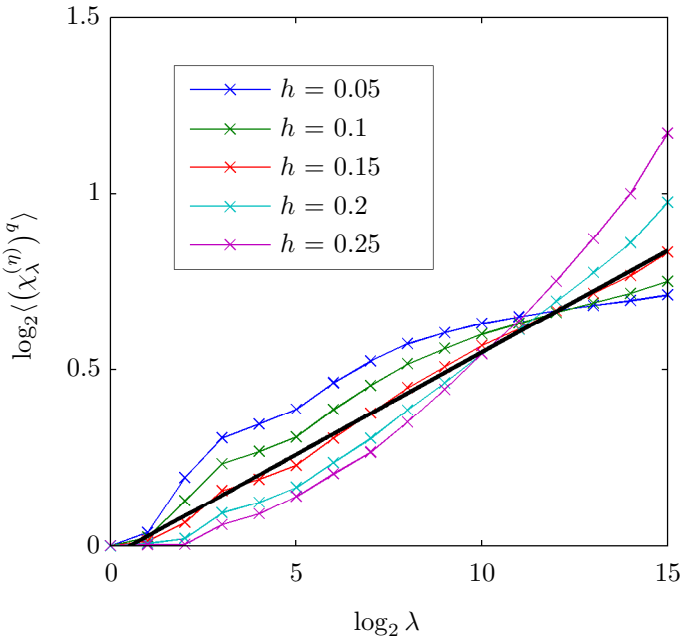

Figure 4.18: The DTMs calculated on the fractionally integrated velocities of our pre-selected, uniquely scaling, spectra in figure 4.5. The DTMs have been computed for $q = 1.5$ and $\log \eta = 0$ for $h \in [0.05 : 0.05 : 0.25]$. Here h corresponds to a de-convolution of χ_λ according to equation 4.20. The exponent $a = 1/3$.

We can manipulate the linear behaviour of the DTMs in order to determine the conservation parameter H for each sample. For each sample we calculate the DTMs on $\chi(h)$ (we used a larger set of the values of h to take into account as much of the variation as possible i.e. $h \in [0 : 1]$ for u and $h \in [-1 : 0]$ for Δu) and select the value of h with the highest NRMSE of the DTMs. We then assume this optimised value is the correct parameter of conservation, i.e. $H = h$.

Performing this operation on u over all scales (this meant including files with scaling breaks) gave a mean NRMSE of 0.86 compared to 0.65 for $h = 1/3$. Figure 4.19a is a histogram of h. The mean ($\overline{h} = 0.1$) is not far from the single sample value we used to test the method in figure 4.18. To ensure a high fidelity we have use samples with NRMSEs > 0.86. This filtering leaves a total of 1,052 out of the total 2,576 available samples. Figure 4.19b compares the local estimates of α for $h = 0.1$ and $h = 1/3$ for the 1,052 samples. It is clear that if the correct value of h is not applied the estimator will give unphysical estimates of $\hat{\alpha}$, i.e. $\hat{\alpha} = 4$!

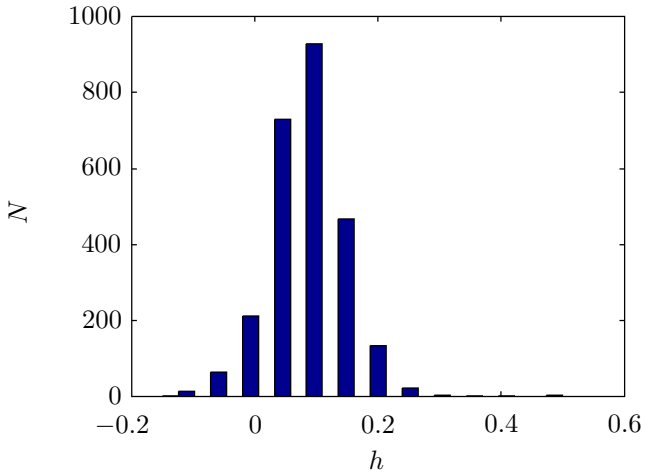

(a)

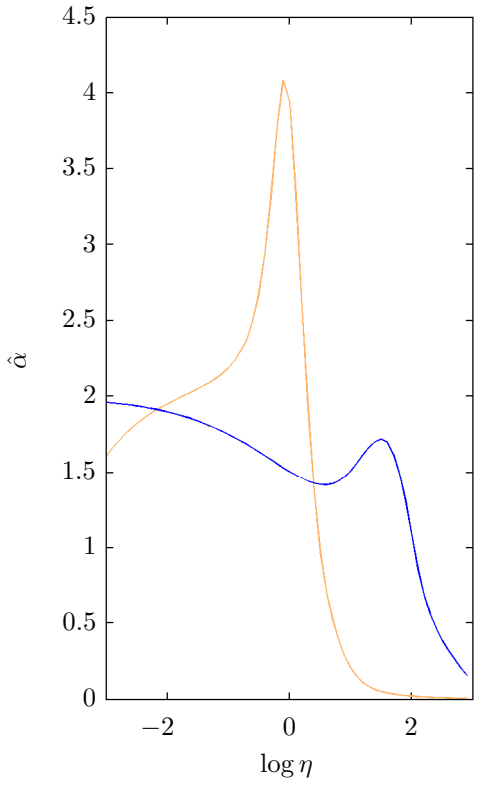

(b)

Figure 4.19: (a) Histogram of h calculated over the full Corsica dataset over the scales 0.1 seconds to an hour. The parameter h is optimised on the moments $q = 1.5$ and $\log \eta = 0$. The mean $\overline{h} = 0.09 \pm 0.1$. (b) plot of the local estimates of α for $h = 0.1$ and $h = 1/3$ for samples with NRMSEs > 0.86 (approximately 1,000 samples)

In our former results we defined the power of the flux density as the third power of the convoluted velocity and velocity increments as proposed by Kol-

mogorov. However, what we have seen is that h is in fact between 0.05 and 0.15 assuming the linearity of the DTMs is a good indication of the estimation of the parameter. What we haven't taken into account are the consequences of changing h without changing a. In figure 4.20 we have taken our uniformly scaling sample and performed the DTM technique on the data for *fixed* $a = 1/3$ and increasing h ($h \in [0.1 : 0.5]$) and *fixed* $h = 1/3$ and increasing a ($a \in [1/5 : 1]$).

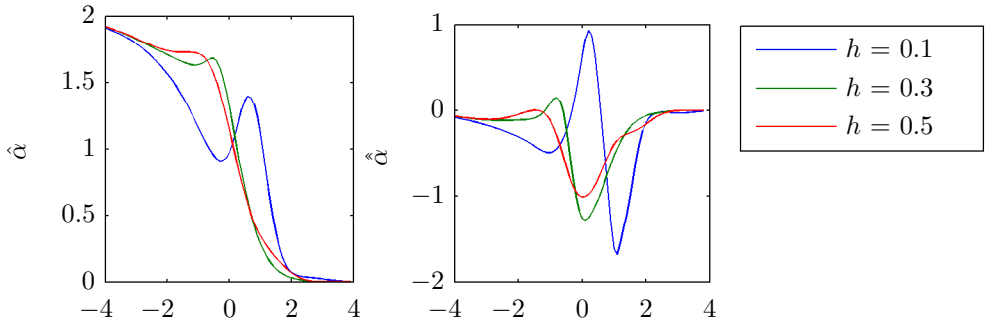

Figure 4.20: DTM analyses preformed for *fixed* $a = 1/3$ and increasing h: (left) local estimate, $\hat{\alpha}$, of the multifractality parameter α; (right) second order derivative of $K(q, \eta; a = 1/3)$.

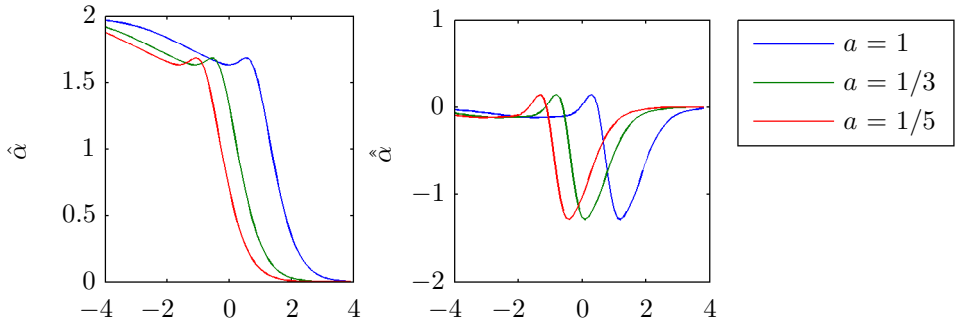

Figure 4.21: DTM analyses preformed for *fixed* $h = 1/3$ and increasing a: (left) local estimate, $\hat{\alpha}$, of the multifractality parameter α; (right) second order derivative of $K(q, \eta; a)$.

In figure 4.20 the effect of decreasing h causes a rightward shift in the position (roughly determined by $\max(\hat{\hat{\alpha}})$) of the plateau/spike where α is estimated. Inversely, in figure 4.21, the effect of increasing a causes a leftward shift in the position of the plateau/spike where α is estimated. We know that for $\log \eta = 0$ the flux is well defined. We can attempt to normalise either a or h by forcing the position of $\max(\hat{\hat{\alpha}})$ to be at $\log \eta = 0$ – compensating one with the other or vice versa. Figure 4.22 shows the correspondence between the two parameters.

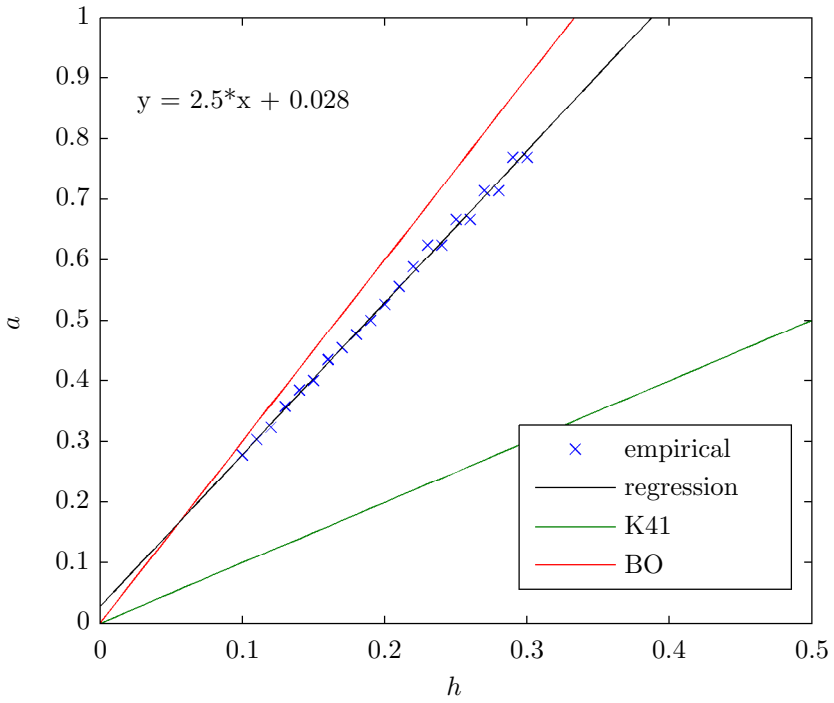

Figure 4.22: Plot of h versus a.

We can see that the relationship between the two parameters is linear as would be expected for K41. For a purely Kolmogorov process we expect H and a to have a one-to-one correspondence. Similarly for a Bolgiano-Obukhov process we expect H and a to be related by a factor 3. What we find is something in-between the two processes (a factor of 2.5) suggesting that there is a mixture of each of these processes. Moreover, in the classical definition of the structure function

$$\zeta(q) = Hq - K_{\varepsilon}(aq), \tag{4.22}$$

we find that for $q = 1/a$ and $\zeta(1/a) = H/a$. More generally

$$H(a) = \zeta(1/a)a. \tag{4.23}$$

Figure 4.22 clearly shows that equation 4.24 requires an intermittency correction

$$H(a) = \zeta(1/a)a + b \tag{4.24}$$

where $b \approx 0.04$. Figure 4.23 compares $\hat{\alpha}$ for $a = 0.5$ and $h \in [-1 : 0.01 : 1]$, a much larger range of values. Although complex on first appearance, what is of particular interest in this figure is the area under all of the sub-plots. It suggests that there is a stable estimator that can be determined through the ranges of η and h. Something we will come back to shortly.

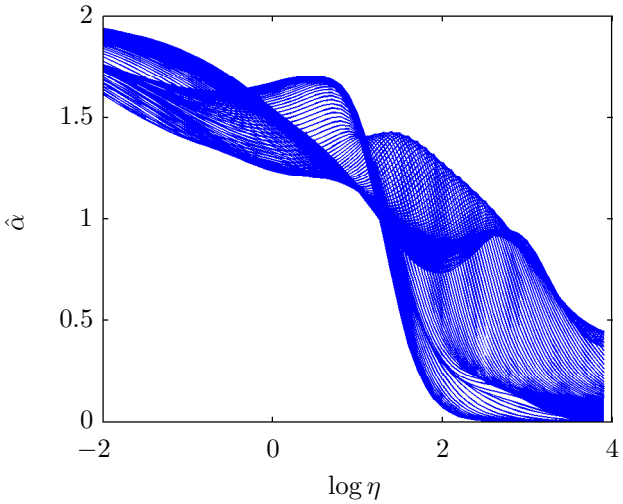

Figure 4.23: Comparison of $\hat{\alpha}$ for $a = 0.5$ and for $h \in [-1 : 0.01 : 1]$.

Local Surface Plots

When calculating the DTMs typically a single value of q is selected for a range of η or vice versa. Due to advances in computing power and vectorised functions we were instead able to calculate the DTMs over a large number of values of both q and η resulting in a surface plot. Figures 4.24 and 4.26 perform the same technique (i.e. optimising h at $q = 1.5$, $\log \eta = 0$) for Δu and u on the same sample. Optimal h corresponds to the solid black $\hat{\alpha}$ plot in figures 4.24a and 4.26a. We then compute the surface $\hat{\alpha}(q, \eta)$. To reiterate, we are optimising the DTMs of $\chi_\lambda(h)$ such that they are the most linear at $q = 1.5$ and $\log \eta = 0$. After $h = H$ is found we compute the DTMs for a range of q and η (specifically $q \in [0 : 4]$ and $\log \eta \in [-4 : 2]$) on the flux $\chi_\lambda(H)$. In the remaining analyses we do not raise $\chi_\lambda(H)$ to any power, i.e. $a = 1$. Figures 4.25 and 4.27 illustrate that

both u and Δu become more or less convex/concave with increasing or decreasing values of h.

As briefly discussed in the last section the relation between the exponents h_u and $h_{\Delta u}$ *should* be $h_{\Delta u} = h_u - 1$. For the same h values differing by a factor 1 i.e. -0.82 and 0.22, we obtain the most linear DTMs for both $\chi(h_u)$ and $\chi(h_{\Delta u})$ thus confirming this property. The corresponding estimates of the parameter C_1, however, are not the same. Since in both cases $\alpha = 1.6$ we can estimate the correction between the two as $C_1^* = C_1(a)^\alpha$ by equation 4.17. giving a to be approximately of the order two. This is further evidence that the power law λ^H isn't respected.

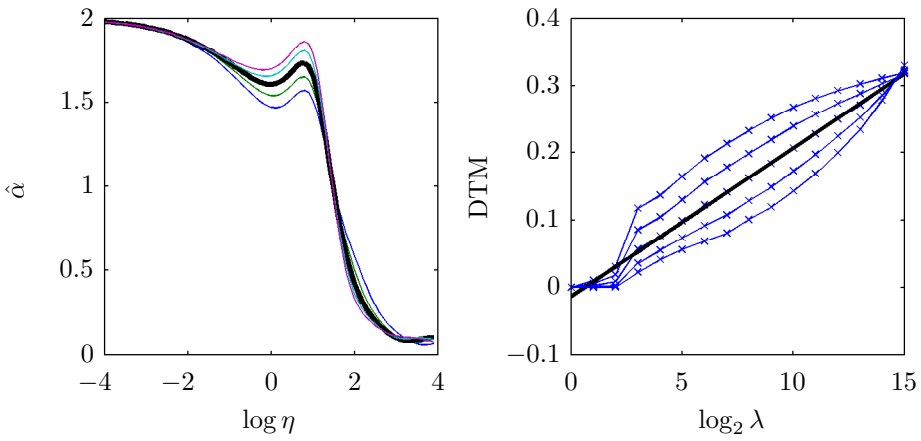

Figure 4.24: Plots of $\hat{\alpha}$ (left) corresponding to the DTMs (right) estimated on $\chi_\lambda(h) = |\Delta u * |t|^h|$ (from bottom to top) for $h_{\Delta u} = -0.92$, -0.87, -0.82, -0.77, -0.72. Corresponding UM parameters at $q = 1.5$ and $\log(\eta) = 0$ are $\alpha = 1.48$, 1.54, 1.60, 1.65, 1.69 and $C_1 = 0.033$, 0.033, 0.0320, 0.031, 0.030. Solid black lines in both plots correspond to $h = H = -0.82$.

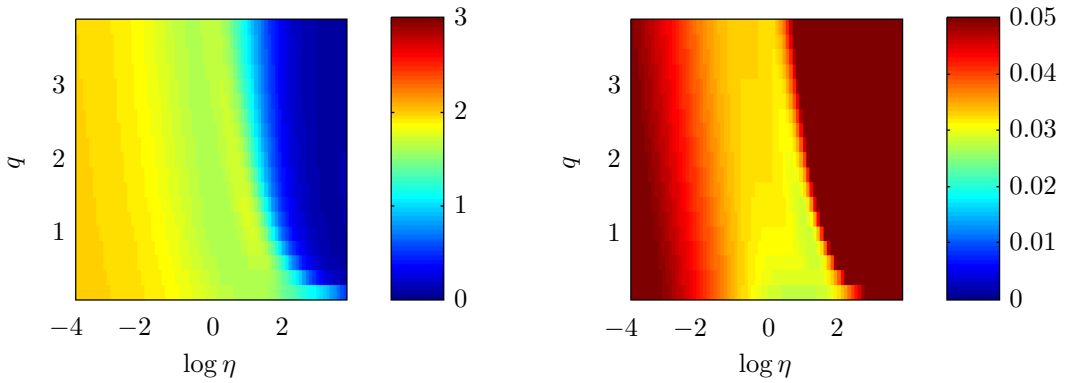

Figure 4.25: Surfaces $\hat{\alpha}(q,\eta)$ (a) and $\hat{C}_1(q,\eta)$ (b) for $q \in [0:4]$ and $\log\eta \in [-4:4]$, estimated on $\chi(0.82) = \Delta u * |t|^{-0.82}$.

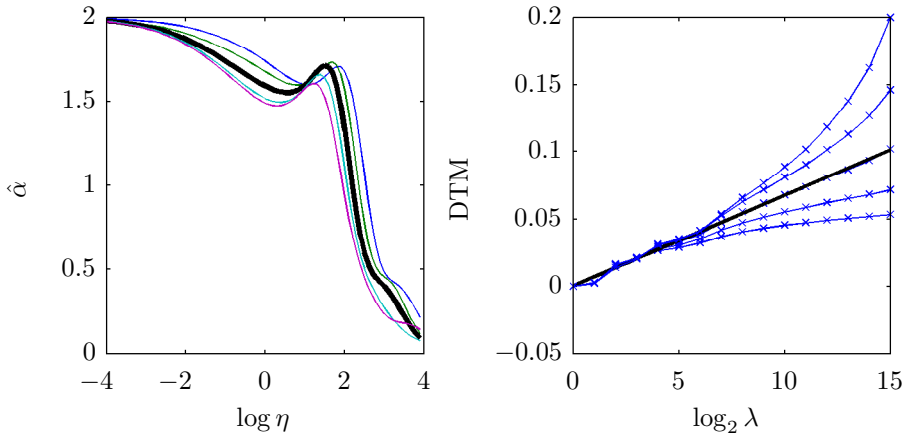

Figure 4.26: Plots of $\hat{\alpha}$ (left) corresponding to the DTMs (right) estimated on $\chi_\lambda(h) = |u*|t|^h|$ (from bottom to top) for $h = 0.12, 0.17, 0.22, 0.27, 0.32$. Corresponding UM parameters at $q = 1.5$ and $\log(\eta) = 0$ are $\alpha = 1.75, 1.70, 1.60, 1.53, 1.51$ and $C_1 = 0.005, 0.007, 0.01, 0.013, 0.018$. Solid black lines in both plots correspond to $h = H = 0.22$.

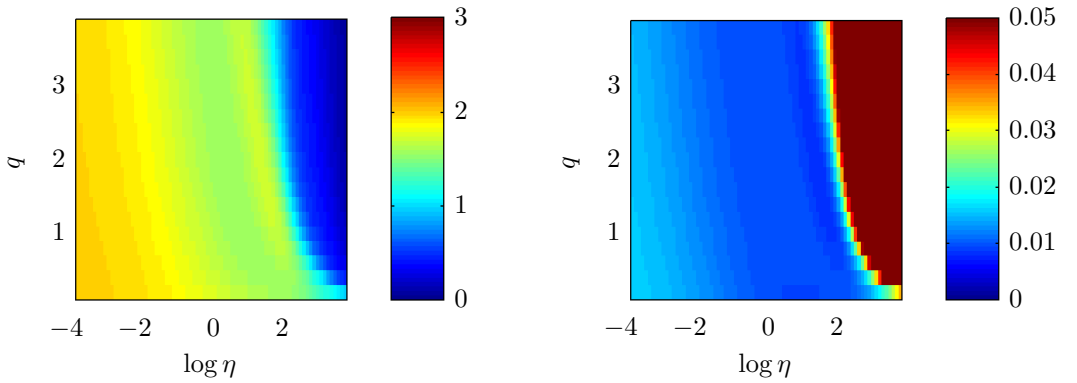

Figure 4.27: Surfaces $\hat{\alpha}(q, \eta)$ (a) and $\hat{C}_1(q, \eta)$ (b) for $q \in [0 : 4]$ and $\log \eta \in [-4 : 4]$, estimated on $\chi(0.22) = u * |t|^{0.22}$.

We may note that the seemingly inverse convex/concave behaviour we observe between $\chi(h) = u * |t|^h$ and $\chi(h) = \Delta u * |t|^h$ for this single sample are not representative of the general behaviour observed between the two fields. We found that the samples could curve as either of two plots shown here (figures 4.24 and 4.26).

4.4 h-Optimised UM Parameter Surfaces

We have seen that we can force the DTMs for a fixed value of q and η to be linear by fractionally integrating or differentiating either the velocity field or its increments respectively. The blue plot in figure 4.28 (superposed by the solid black regression line) shows the DTMs of the fractionally differentiated velocity increments with $h(q,\eta) = -0.84$, for $q = 1.5$ and $\eta = 1$. In figure 4.28 we plot the same curves but for $K(q \pm 1, \eta)$ (a) and $K(q, \eta \pm 1)$ (b). What this shows is that although we are forcing the DTMs to be linear at a given value of q and η, raising $\chi(h)$ to different moment orders changes the value of h needed to have linear DTMs.

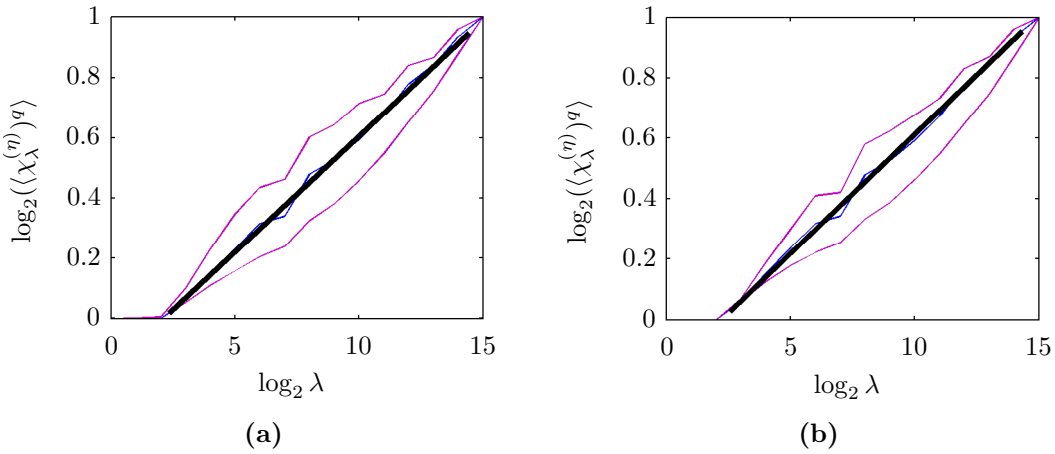

Figure 4.28: DTMs of the fractionally differentiated velocity increments with $h(q,\eta) = -0.84$, for $q = 1.5$ and $\log \eta = 0$ (blue plot superposed by black solid line). The purple curves either side show $K(q \pm 1, \eta)$ (a) and $K(q, \eta \pm 1)$ (b). The DTMs have been normalised by $K(q,\eta)$ at Λ.

In order to have a truly optimised-local estimate we must also optimise $\hat{\alpha}$. Since η is discretised we can optimise h at q_i and η_i and then estimate $\hat{\alpha}$ over η_{i-1} and η_{i+1}. The locally optimised parameter $C_{1,h}(q_i, \eta_i)$ is found by substituting $\alpha_h(q_i, \eta_i)$ and η_i into equation 4.16. Figures 4.29 and 4.30 show the surfaces $h(q,\eta)$, $\alpha_h(q,\eta)$ and $C_{1,h}(q,\eta)$.

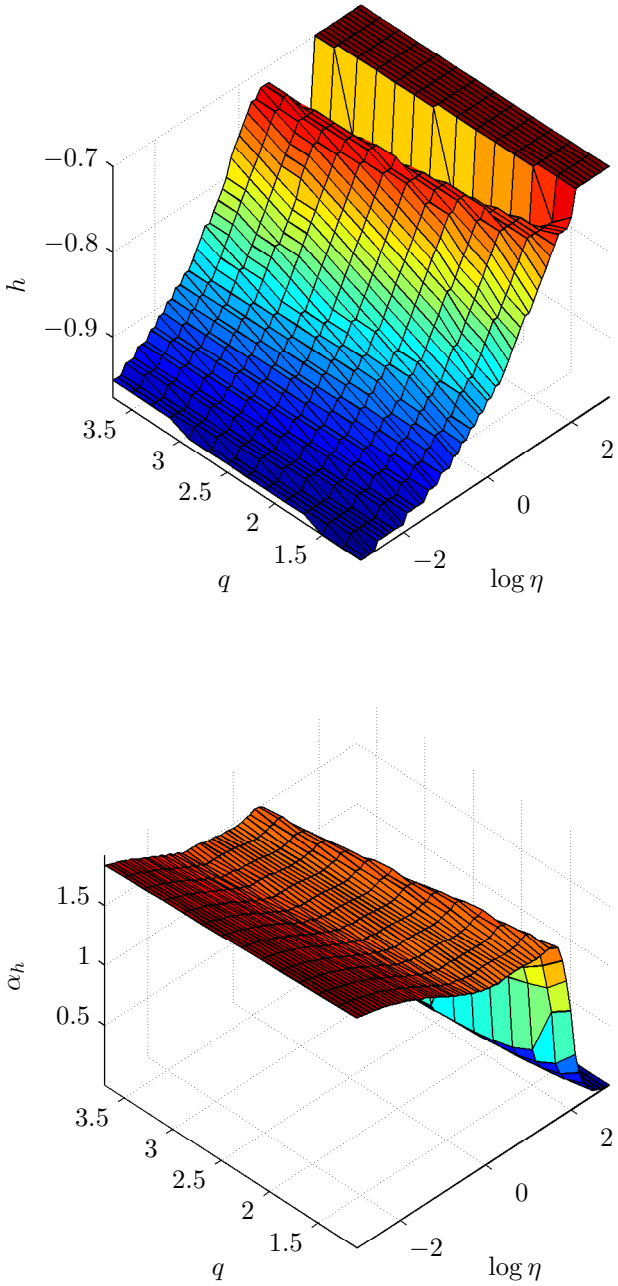

Figure 4.29: Surface plots of $h(q, \eta)$ (top) and $\alpha_h(q, \eta)$ (bottom) for $q \in [1 : 4]$ and $\log \eta \in [-3 : 3]$.

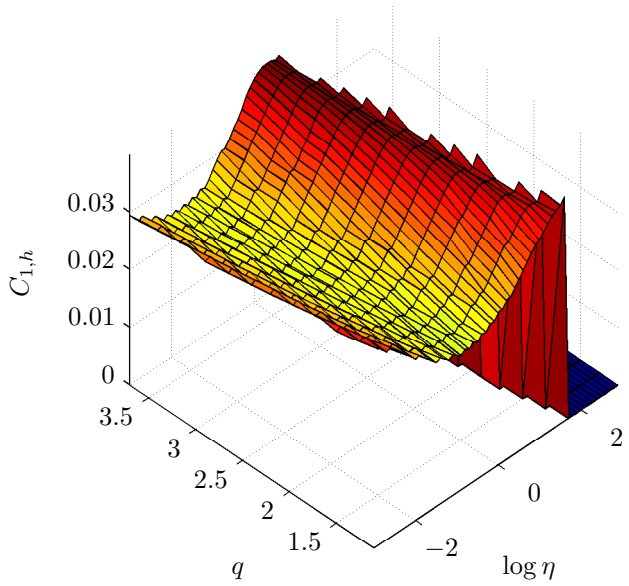

Figure 4.30: Surface plot of $C_{1,h}(q, \eta)$ for $q \in [1 : 4]$ and $\log \eta \in [-3 : 3]$.

We can see from figure 4.29 (top) that $h(q, \eta)$ shows significant variation across $\log \eta \in [-3 : 3]$ and $q \in [1 : 4]$. In particular across $\log \eta$ we see h varies from -1 to -0.7. The variation across q isn't so easily observed but is still there. We will come back to this later. Figure 4.29 (bottom) plots α_h. Although there is significant variation in h we are still able to observe a very well defined plateau in α_h suggesting that for this sample $\alpha = 1.5$. Unlike α_h, the surface of $C_{1,h}$ in figure 4.30 shows wave like behaviour across $\log \eta$. Something of a mixture between the two previous surfaces. Again the variation in $C_{1,h}$ through q is difficult to see in this format. There seems to be a singularity that occurs over larger values of $\log \eta$ in the function of $C_{1,h}(q, \eta)$. This is simply because $C_{1,h}(q, \eta)$ is estimated from $\alpha_h(q, \eta)$, and In figure 4.29 (top) $\alpha_h(q, \eta)$ tends to zero for large $\log \eta$ hence the occurrence of the singularity. The strong non-linearity in both $h(q, \eta)$ and $C_{1,h}(q, \eta)$ seems likely to be a triviality overlooked in the estimation of the parameters. However, as we will see in the remaining parts of the thesis, this triviality is much more complex to decipher than one might hope.

4.5 Multifractal Phase Transitions

When a first order multifractal phase transition occurs at a given critical moment order q_D (i.e. a divergence of statistical moments for orders $q \geq q_D$), the 'dressed' TM scaling function $K_D(q)$ has the following expression (G denotes the Heaviside step function) with respect to the 'bare' TM scaling function $K(q)$:

$$K_D(q) = G(q - q_D)(\gamma_{\Delta_s}(q - q_D) + K(q_D)) + (1 - G(q - q_D))K(q) \tag{4.25}$$

where the critical singularity γ_{Δ_s} is the largest singularity almost surely present in a sample of overall sampling dimension Δ_s. Δ_s can be estimated as:

$$\Delta_s = D + D_s;\ D_s \approx \log_\lambda(N_s) \tag{4.26}$$

where D is the dimension. The largest singularity, γ_{Δ_s}, is increasing with sample size from γ_s for a unique sample to infinity for an infinite sample. The order q_D is sample size independent, where $\gamma_D = K'(q_D)$ (prime denotes a Legendre transform), for a unique sample. The function $K(q_D)$ was defined in equation 3.9.

DTM Estimator Of The Index Of Multifractality

For UM's, the local log slope of the DTM scaling function $K(q, \eta)$ corresponds to the estimator $\hat{\alpha}$ defined in equation 4.18. The corresponding dressed DTM scaling function $K_D(q, \eta)$, has a similar expression to that of the bare DTM (equation 4.17) but with respect to the dressed $K_D(q)$ instead of the bare $K(q)$,

$$\begin{aligned} K_D(q, \eta) = K(q\eta) - qK(\eta) \ldots \\ \cdots + G(q\eta - q_D)(\gamma_{\Delta_s}(q\eta - q_D) + K(q_D) - K(q\eta)) \ldots \\ \cdots - q(G(\eta - q_D)(\gamma_{\Delta_s}(\eta - q_D) + K(q_D) - K(\eta)). \end{aligned} \tag{4.27}$$

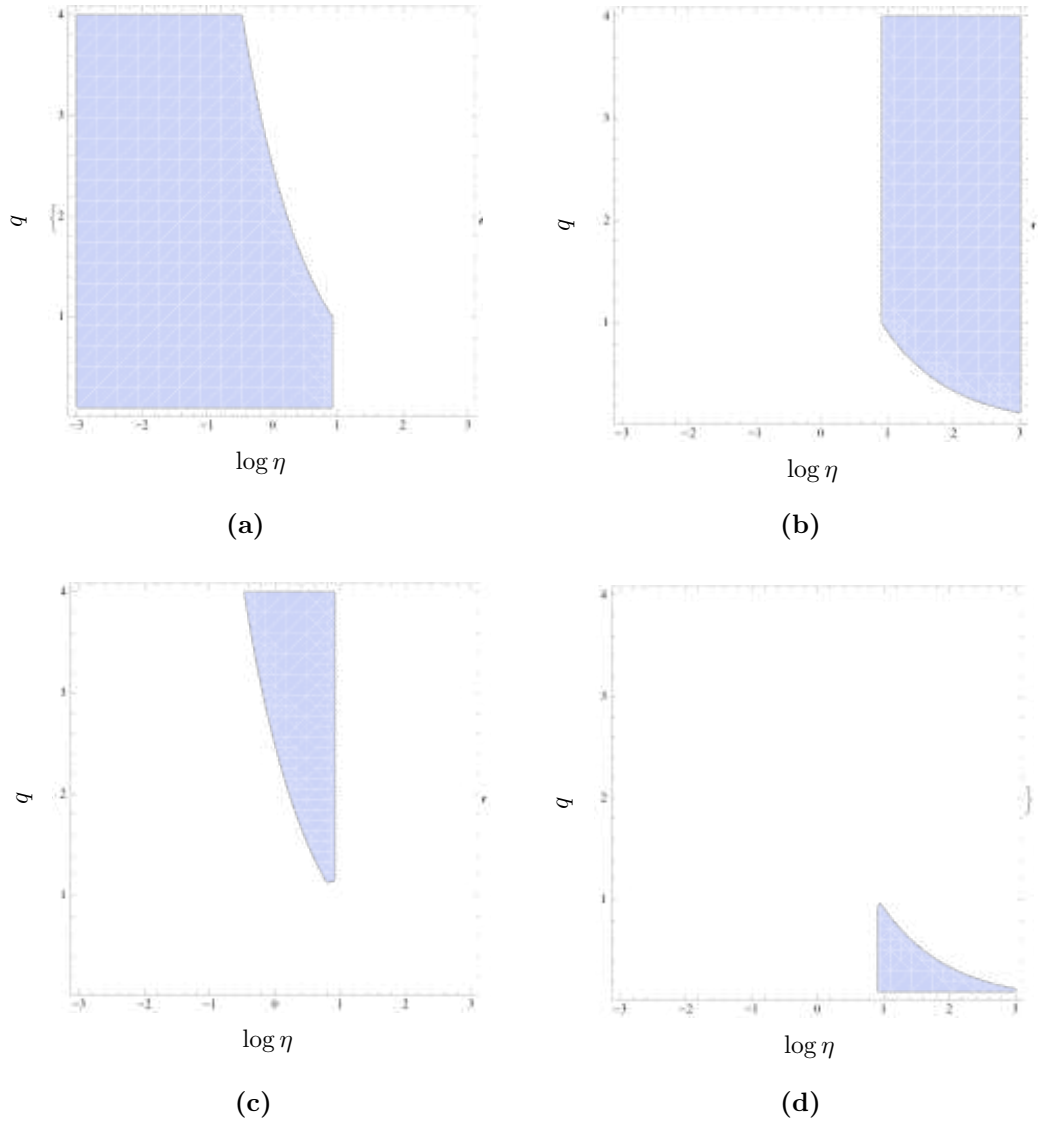

Figure 4.31: The four regions (s_1 to s_4) of the plan ($\log(\eta, q)$) delineated by the critical lines Δ ($\eta = q_D$) and E ($q = q_D e^{-\log(\eta)}$); (a): s_1 – no phase transition, (b): s_2 with both phase transitions, (c): s_3 with a unique phase transition at $q\eta = q_D$ and (d): s_4 for $\eta = q_D$.

As a consequence of this the effective local DTM estimator $\hat{\alpha}_D(q,\eta)$, estimates the local log slope of the DTM scaling function $K_D(q\eta)$ such that

$$\hat{\alpha}_D(q,\eta) = \partial \log(K_D(q,\eta))/\partial \log(\eta) = \eta \partial K_D(q,\eta)/K_D(q,\eta)\partial\eta \tag{4.28}$$

where

$$\begin{aligned} \partial K_D(q,\eta)/\partial\eta &= q(K'_D(q\eta) - K'_D(\eta)) \\ &= q(K'(q\eta) - K'(\eta))\dots \\ &\quad \cdots + q(G(q\eta - q_D)(\gamma_{\Delta_s} - K'(q\eta))\dots \\ &\quad \cdots - G(\eta - q_D)(\gamma_{\Delta_s} - K'(\eta))). \end{aligned} \tag{4.29}$$

This expression already points out that the phase transitions unfortunately yield spurious multifractality exponent estimates $\hat{\alpha}_D$, as confirmed in the next section. It is convenient to systematically introduce into the above equation the singularities $\gamma(q) = K'q)$. We find equation 4.29 is then

$$\begin{aligned} \partial K_D(q,\eta)/\partial\eta &= q(\gamma(q\eta) - \gamma(\eta)) \\ &\quad \cdots + G(q\eta - q_D)(\gamma_{\Delta_s} - \gamma(q\eta))\dots \\ &\quad \cdots - G(\eta - q_D)(\gamma_{\Delta_s} - (1 - G(\eta - q_D))\gamma(\eta))). \end{aligned} \tag{4.30}$$

Similarly the co-dimension $c(\gamma(q)) = q\gamma(q) - K(q)$ can be used in the expression of $K_D(q,\eta)$ (equation 4.27):

$$\begin{aligned} K_D(q,\eta) &= K(q\eta) - qK(\eta) \\ &\quad \cdots + G(q\eta - q_D)((\gamma_{\Delta_s} - \gamma_D)q\eta + c(\gamma(q\eta)) - c(\gamma_D)\dots \\ &\quad \cdots - q(G(\eta - q_D)(\gamma_{\Delta_s} - \gamma_D)\eta + c(\gamma(\eta)) - c(\gamma_D). \end{aligned} \tag{4.31}$$

Behaviour Of The Effective Estimator

Both the expressions of $K_D(q,\eta)$ and $\partial K_D(q,\eta)/\partial\eta$ (equations 4.27 and 4.29) show that there are four different behaviours of $\hat{\alpha}_D$ (equation 4.28, corresponding to the four sectors s_1 to s_2) of the the plane $(\log(\eta), q)$ delimited by the following critical lines Δ and E (respectively a straight line and exponential curve, see figure 4.31):

$$\Delta = \{(\log(\eta), q) \lfloor \eta = q_D\} \tag{4.32}$$

$$E = \{(\log(\eta), q) \lfloor q = q_D e^{-\log(\eta)}\} \tag{4.33}$$

where $\partial K_D(q,\eta)/\partial\eta$ is no longer point-wise defined, in particular in the quadruple critical point $(\log(q_D), q_D e^{q_D})$ corresponding to the the intersection of s_4 and E.

No Phase Transition

The absence of a phase transition means that $\hat{\alpha}_D(q,\eta) \equiv \hat{\alpha}(q,\eta)$, therefore yielding a non-spurious estimate of α. This corresponds to the area s_1 of the plane $(\log(\eta), q)$, to the l.h.s of the straight line Δ, the exponential curve E (figure 4.31), and the plateau $\hat{\alpha}_D(q,\eta) = \alpha$ of figure 4.31a:

$$\begin{aligned} \eta < q_D \text{ and } q\eta < q_D : & \\ \partial K_D(q,\eta)/\partial\eta &= q(\gamma(q\eta) - \gamma(\eta)) \\ K_D(q,\eta) &= K(q,\eta);\ \hat{\alpha}(q,\eta) = \alpha \end{aligned}$$

Two Phase Transitions

A double phase transition corresponds to the sector s_2 in figure 4.31b, i.e. on the l.h.s area of the straight line Δ and the exponential curve E as well as to the plateau $\hat{\alpha}_D(q,\eta) = 0$. In a rather straight forward manner, both phase transitions at $\eta = q_D$ and $q\eta = q_D\eta$ yield the same linear behaviour for $K_D(\eta)$ and $K_D(q\eta)$

and therefore both cancel in $\partial K_D(q,\eta)$ (equation 4.29). More precisely:

$$\begin{aligned} & \eta > q_D \text{ and } q\eta > q_D : \\ K_D(q,\eta) &= (q-1)(\gamma_{\Delta_s} q_D - K(q_D)) \\ \partial K_D(q,\eta)/\partial\eta = 0 &= \hat{\alpha}_D(q,\eta);\ \partial K_D(q,\eta)/\partial q = \gamma_{\Delta_s} q_D - K(q_D) \end{aligned}$$

It is worthwhile to note that the constant slope $\partial K_D(q,\eta)/\partial q$ of $K_D(q,\eta)$ with respect to q is positive, because:

$$\gamma_{\Delta_s} q_D - K(q_D) = (\gamma_{\Delta_s} - \gamma_D)\, q_D + c(\gamma_D) \tag{4.34}$$

where both terms are positive (the Legendre transform was used to obtain form $K(q_D)$ the co-dimension $c(\gamma_D)$ on the right-hand side of the equation). Consequently, in this sector of the plane $(\log(\eta), q)$, $K_D(q,\eta)$ is negative for $q \leq 1$ and positive for $q \geq 1$, as is in the sector s_1 .

A Unique Phase Transition

A unique phase transition yields spurious estimates of $\hat{\alpha}_D(q,\eta)$, corresponding to a transition between the two plateaux $\hat{\alpha}_D = \alpha$ (section 4.5) and $\hat{\alpha}_D = 0$ (section 4.5)

Phase Transition In $q\eta = q_D$

This phase transition corresponds to the section s_3 of figure 4.31, i.e. the uppermost sector defined by the curves Δ and E in the plane $(\log(\eta), q)$.

$$\begin{aligned} & \eta < q_D \text{ and } q\,\eta > q_D : \\ K_D(q,\eta) &= \gamma_{\Delta_s}(q\eta - q_D) + K(q_D) - qK(\eta) \\ \partial K_D(q,\eta)/\partial\eta &= q(\gamma_{\Delta_s} - \gamma(\eta));\ \partial K_D(q,\eta)/\partial q = \gamma_{\Delta_s}\eta - K(\eta) \\ \hat{\alpha}_D(q,\eta) &= q\eta(\gamma_{\Delta_s} - \gamma(\eta))/(\gamma_{\Delta_s}(q\,\eta - q_D) + K(q_D) - qK(\eta)) \end{aligned}$$

It is worthwhile to note that the slope $\partial K_D(q,\eta)/\partial\eta$ of $K_D(q,\eta)$ with respect to η is linear with respect to q and is positive. This is because the singularity $\gamma(\eta) = K'(\eta)$ is smaller than γ_D in the sector s_3 of the plane $(\log(\eta), q)$, whereas γ_{Δ_s} is larger.

Phase Transition In $\eta = q_D$

This corresponds to the sector s_4 of figure 4.31, i.e. the lower sector defined by the curves Δ and E in the plane $(\log(\eta), q)$.

$$\begin{aligned} & \eta > q_D \text{ and } q\,\eta < q_D : \\ K_D(q,\eta) &= K(q\eta) - q(\gamma_{\Delta_s}(\eta - q_D) + K(q_D)) \\ \partial K_D(q,\eta)/\partial\eta &= q(\gamma(q\eta) - \gamma_{\Delta_s});\ \partial K_D(q,\eta)/\partial q = \eta(K'(q\,\eta) - \gamma_{\Delta_s}) \\ \hat{\alpha}_D(q,\eta) &= q\eta(\gamma(q\eta) - \gamma_{\Delta_s})/(K(q\eta) - q(\gamma_{\Delta_s}(\eta - q_D) + K(q_D))) \end{aligned}$$

This time, the slope $\partial K_D(q,\eta)/\partial\eta$ of $K_D(q,\eta)$ with respect to η remains linear with respect to q, and negative. This is now because the singularity $\gamma(q\,\eta)$ is smaller than γ_D in the sector s_4 of the plane $(\log(\eta), q)$, whereas γ_{Δ_s} is larger.

Singular Behaviour Along The Critical Borderline Of The Sector s_1

This critical borderline corresponds to the union of $E^+ = E \cap \{q > 1\}$ and $\Delta^- = \Delta \cap \{q < 1\}$. The term $\partial K/\partial\eta$ has the jump $\Delta(\partial K/\partial\eta)$ across E^+ (from left to right, i.e. for increasing η's)

$$\Delta(\partial K/\partial\eta) = q(\gamma_{\Delta_s} - \gamma_D), \tag{4.35}$$

and an opposite jump across Δ^-

$$\Delta(\partial K/\partial\eta) = -q(\gamma_{\Delta_s} - \gamma_D). \tag{4.36}$$

The term $K(q,\eta)$ has no discontinuity. Putting the two expressions together we obtain the following jump $\Delta(\hat{\alpha}_D)$ for $\hat{\alpha}_D$ across E^+-

$$\Delta(\hat{\alpha}_D) = q_D(q/q_D)^{\alpha}(\gamma_{\Delta_s} - \gamma_D)/K(q), \tag{4.37}$$

and across Δ^-

$$\Delta(\hat{\alpha}_D) = (q/q_D^{\alpha-1})(\gamma_{\Delta_s} - \gamma_D)/\lfloor K(q)\rfloor. \tag{4.38}$$

Singular Behaviour Along The Critical Borderline Of The Sector s_2

This critical borderline corresponds to $E^- \cap \Delta^+$ with $E^- = E \cap \{q < 1\}$ and $\Delta^+ = \Delta \cap \{q > 1\}$. The term $\partial K/\partial\eta$ has the following jump across Δ^+

$$\Delta(\partial K/\partial\eta) = q(\gamma_D - \gamma_{\Delta_s}), \tag{4.39}$$

and again an opposite jump across E^-

$$\Delta(\partial K/\partial\eta) = -q(\gamma_D - \gamma_{\Delta_s}). \tag{4.40}$$

Again, using the fact that $K(q,\eta)$ has no discontinuity, we obtain the following jump $\Delta(\hat{\alpha}_D)$ across

$$\Delta(\hat{\alpha}_D) = (\gamma_{\Delta_s} - \gamma_D)/(\lfloor q-1\rfloor(\gamma_{\Delta_s} q_D - K(q_D)) \tag{4.41}$$

Empirical Evidence Of q_D

Figures 4.32 and 4.33 use a fixed h approach; h is optimised at $q = 1.5$, $\log \eta = 0$, and the DTMs are computed for the remaining values of q and η. Figures 4.34, 4.35 and 4.36 use the $h(q, \eta)$ approach. We were also interested in whether or not the same behaviour occurred for the velocity field itself not just for the increments. Figures 4.33 and 4.35 analyse Δu while 4.32 and 4.34 analyse u.

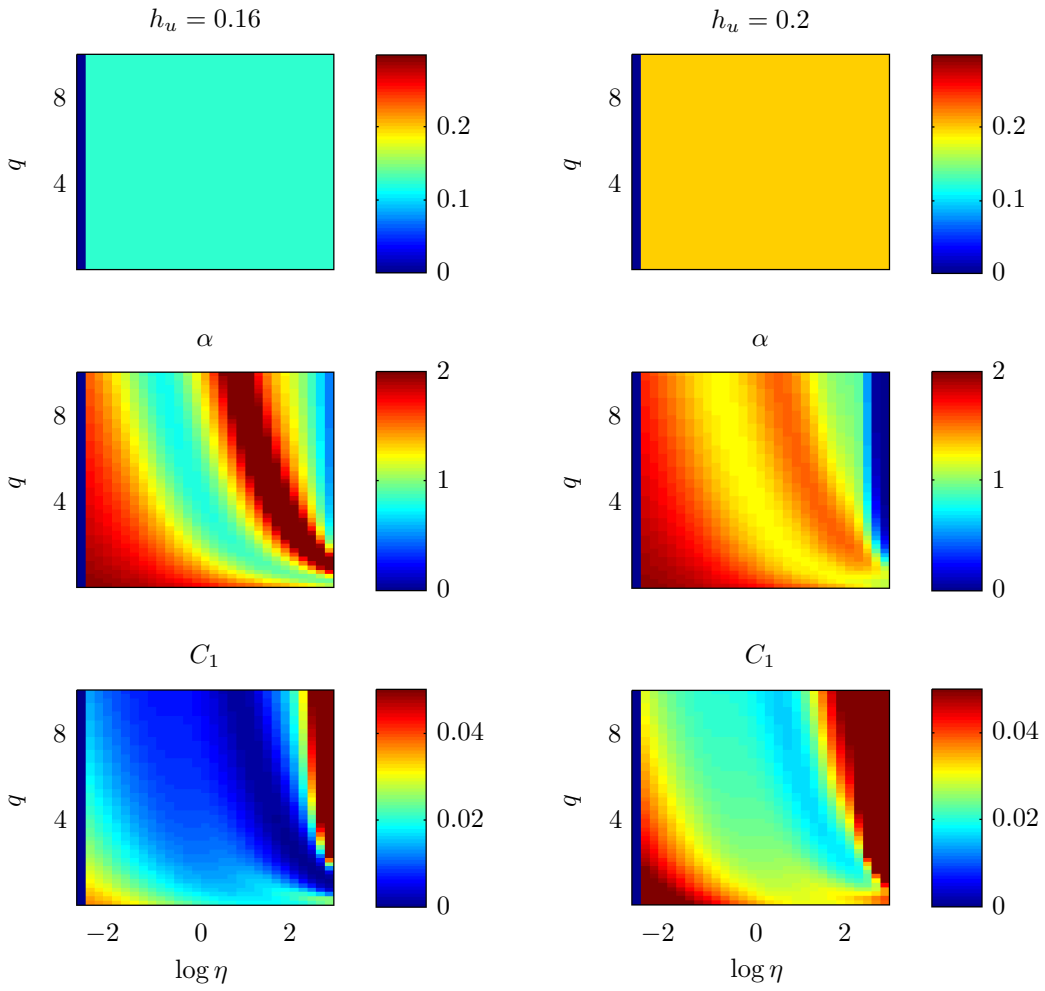

Figure 4.32: Fixed h approach with $h_u = 0.16$ in (a) and $h_u = 0.2$ in (b); estimated at $q = 1.5$, $\log \eta = 0$ on the fractionally differentiated u-component velocity. L.h.s plots corresponds to the sample attributed to q_D and the r.h.s plots are attributed to q_s.

Looking to figure 4.32 (fixed point on u), the first obvious difference between the two samples is the value of h_u. The q_s attributed sample has $h_u = 0.2$ and for the q_D attributed sample $h_u = 0.16$. It is not clear whether the difference in h_u is the result or the consequence of higher (1.5) and lower (< 1) bands of α over $\log \eta \in [-1 : 0]$. Nonetheless, the contrast between adjacent bands is clearly stronger in the case of q_D, varying from 1 to 2 from $\log \eta = 0$ to 1.

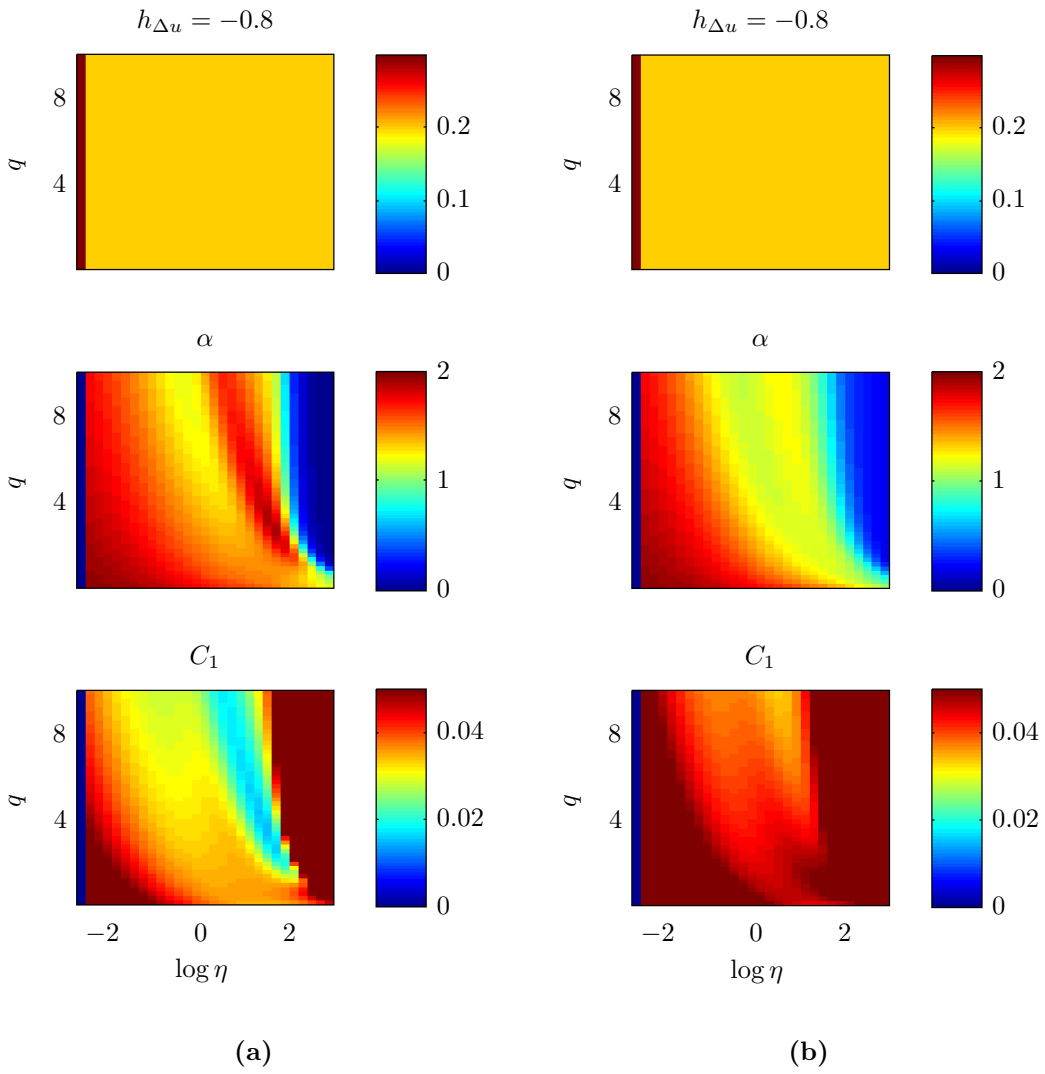

Figure 4.33: Fixed h approach with $h_{\Delta u} = -0.8$ ($h_u = 0.2$) estimated at $q = 1.5$, $\log \eta = 0$ on the fractionally differentiated u-component velocity increments Δu. L.h.s plots corresponds to the sample attributed to q_D and r.h.s plots attributed to q_s.

In figure 4.33 (fixed point on Δu) we see now that $h_{\Delta u}$ remains the same for both sample types. The largest difference now is in the surface plot of $\hat{\alpha}$. As with figure 4.32, $\hat{\alpha}$ remains similar in value (1.7) across lower values of $\log \eta$ (from 0 to -3). Over values of $\log \eta > 0$ the sample attributed to q_s exhibits a low band of $\alpha \approx 1.5$ whereas the sample attributed to q_D has the characteristic discontinuity show to occur in the previous section; consistent at least with the plots for u.

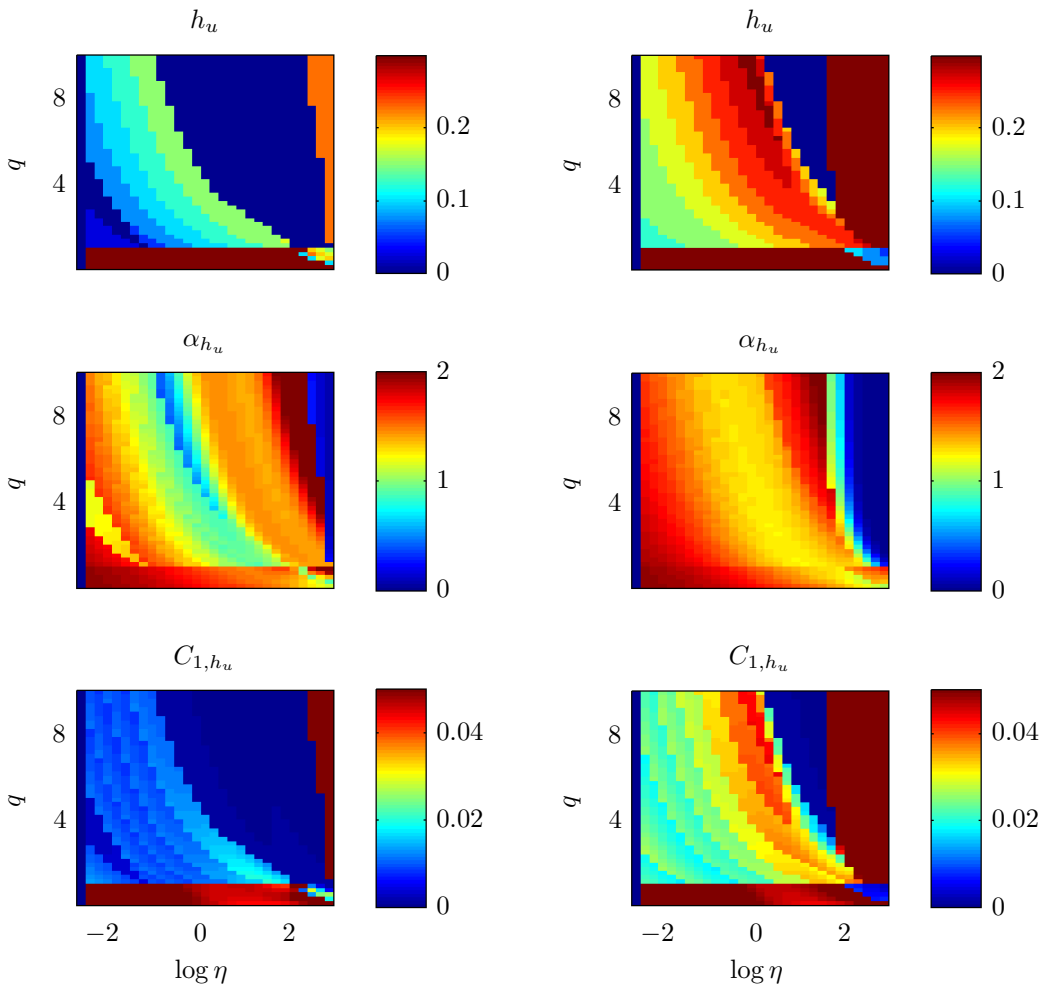

Figure 4.34: Optimised $h_u(q, \eta)$ estimated on the fractionally differentiated u-component velocity. L.h.s plots correspond to the sample attributed to q_D and r.h.s plots attributed to q_s.

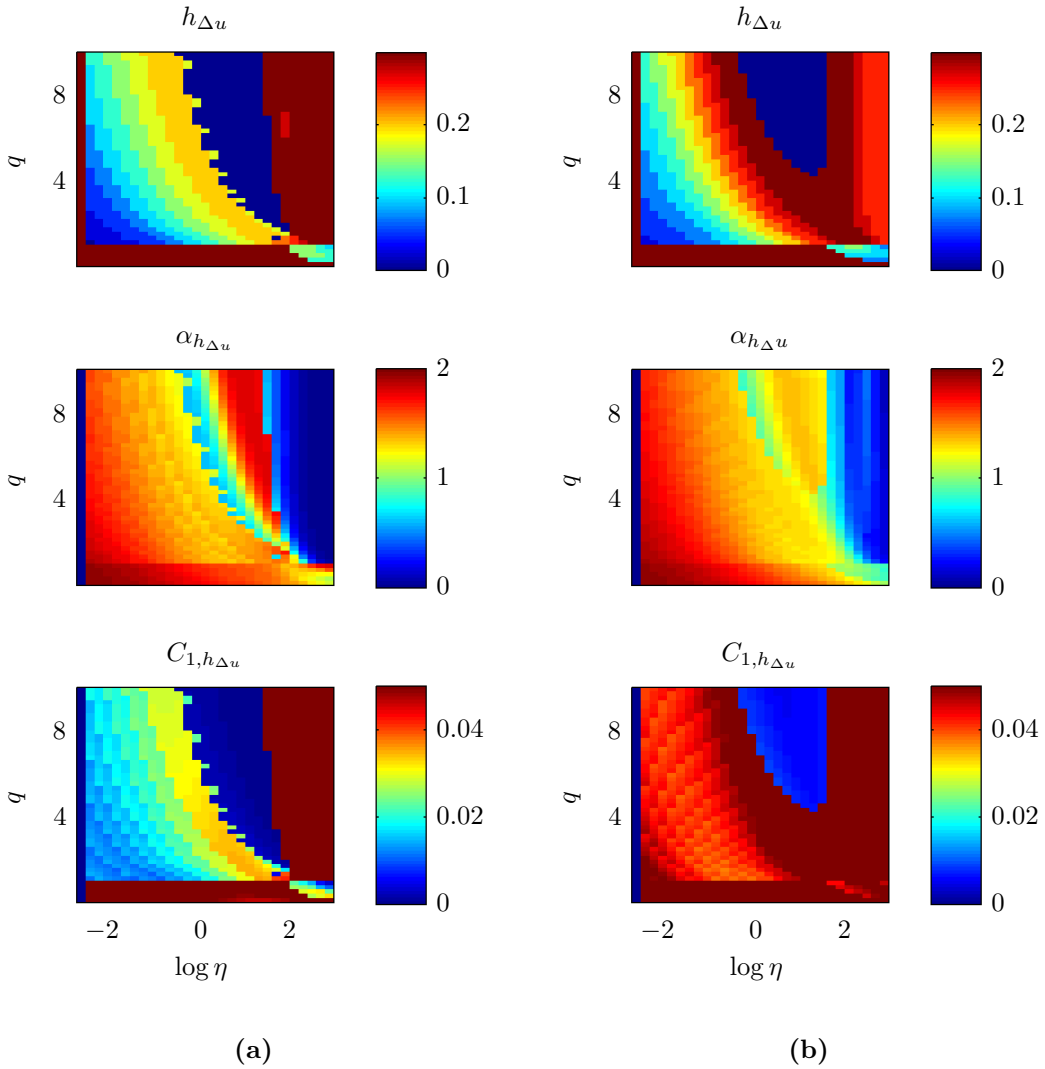

Figure 4.35: Order-Dependent optimisation method $h_{\Delta u}(q, \eta)$ estimated on the fractionally differentiated u-component velocity increments Δu. L.h.s plots corresponds to the sample attributed to q_D and r.h.s plots attributed to q_s.

In figure 4.34 the discrete nature of the optimisation method now becomes visible. We can see that (for u) the occurrence of the phase transition range $q\eta = q_D$ (range s_3 from §4.5) is now marked by a 0 estimation of $h_u(q, \eta)$. This is because we are unable to optimise h on the DTMs because they are already linear. This results in the minimum value being selected ($h = 0$). The difference between the two samples is now much clearer. The lower order occurrence of linearity in

$\zeta(q)$ for q_D is reproduced in the surface plots corresponding to a much larger s_3 section. For q_s this range is much smaller resulting in a stable band of $\hat{\alpha}$ that gives $\alpha \approx 1.5$. As with the fixed h method we find α to be much smaller for q_D of u (≈ 1).

In figure 4.35, as in the h point method, we find that $\hat{\alpha}$ is similar in value for both samples, across q and η. It isn't clear why α varies so much when calculated on u. One explantation may be that the range of estimation across $\log \eta$ is shifted rather than the exponent itself changing. Differentiating the field in real space (Δu) and then fractionally integrating by $H + 1$ will not give the same result as simply fractionally integrating by h particularly if λ does not follow a power law. We have seen in the previous section that the $K(q, \eta)$ function will shift from left to right depending on the value of h. Depending on which operation is performed we may shift the function in or out of the good range of $\log \eta$ for estimation.

Finally, we may note that in all of the above figures one main consistency remains in that h and C_1 are either lower or higher depending on if there is q_s or q_D. When there is q_D both h and C_1 are low, $h = 0.1$ and $C_1 = 0.01$. When there is q_s, $h = 0.2$ and $C_1 = 0.03$. Although this seems counter intuitive it is indeed in agreement with a reduction in dimension due anisotropy.

Figure 4.36 plots the surfaces $h_{\Delta u}$, $\alpha_{h_{\Delta u}}$ and $C_{1,h_{\Delta u}}$ averaged over the full dataset. The strong discontinuities have been somewhat smoothed, however, it is clear q_D still exists. This is a very important result as it is suggests that the structure function cannot reproduce the same behaviour i.e. a divergence of moments, when ensemble averaged over the dataset as discussed briefly in §4.2. Finally, the order-dependent optimisation method does not bring a great deal of additional information to that of the fixed-h method when used over a large number of statistics. Its main use is to be found on the individual statistics of the sample. Something we discuss in the next section.

In the remaining sections we focus our attention solely on the UM parameters estimations based on Δu. This seemed to make more sense as the field is directly comparable with the statistics of the structure function. For brevity of notation we drop the Δu suffix from $h_{\Delta u}$.

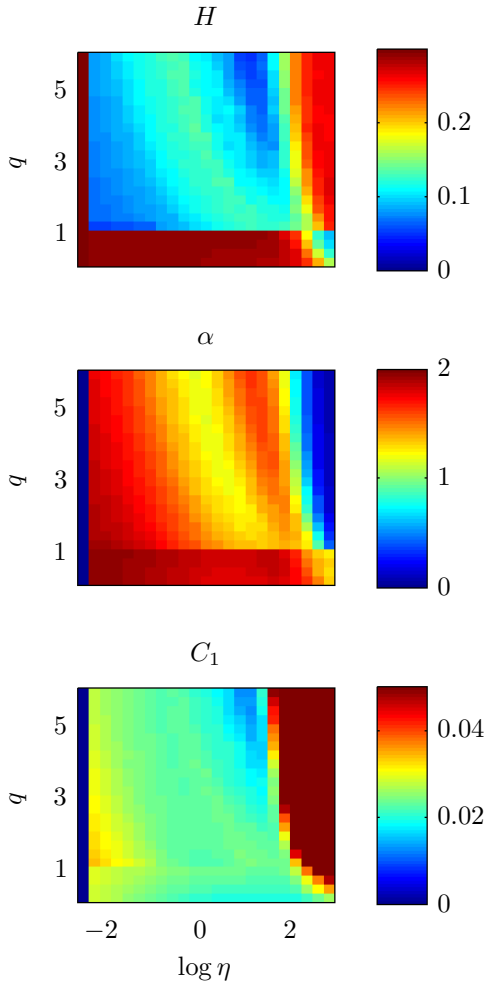

Figure 4.36: Order-dependent optimisation method $h_{\Delta u}(q, \eta)$ estimated on the fractionally differentiated u-component velocity increments Δu; ensemble averaged across the entire Corsica dataset.

4.6 Reconstruction Of The Structure Function

There is a particular inconsistency that has arisen between the structure function and the extreme behaviour we are trying to understand. We recall that, from the very beginning, our aim has been to reproduce the highly intermittent velocity wind increments for use in applied wind energy related areas. We showed through empirical estimation of the power-law tails of the increments that q_D-compatible behaviour was observable on almost every sample; averaging a value of around 4 a the highest resolution and 5 at larger time-scales. The inconsistency that has arisen is therefore the lack of the prediction of the linearity of the higher-order moments due to the effect of q_D.

We have shown theoretically that the spike seen in the surface plots of $\hat{\alpha}$ estimated from the DTMs is due to q_D. We have also shown that the occurrence of q_D is easily possible for even slightly component-wise anisotropic fields. What is incompatible with the empirical data is the lack of linearity of $\zeta(q)$ that should occur over the moments $q > q_D \approx 4$, assuming our 'empirical' estimations of q_D are meaningful. Note for a power estimated on the cube of the velocity increments, it is not clear that even the mean will be well defined. It seems that by ensemble averaging the structure function this behaviour becomes obscured.

The $K_h(q)$ Function

Figure 4.37 takes two samples, a sample that exhibits a particularly large spike and a sample that exhibits a plateau-like behaviour, i.e. the effect of q_s and q_D a first and second-order phase transition. We then compute the following scaling moment function (the sub-index-h refers simply to the function parameters optimisation on h),

$$K_h(q) = \frac{C_{1,h}}{\alpha_h - 1}\left(q^{\alpha_h} - q\right). \tag{4.42}$$

The semi-analytical structure function is then

$$\zeta_h(q) = qh - K_h(q). \tag{4.43}$$

This is then compared to the structure function, $\zeta(q)$, computed in the classical way, i.e. on the velocity increments by equation 4.12. In both methods we have restricted ourselves to the smallest scales in order to avoid the problems associated with the larger scale separations (see figure 4.38). In order to estimate the parameter α_h we require η_{i+1} and η_{i-1}. So that it is the scaling moment function of the TMs we are calculating we set $\eta = 1$; this gives the now only q-dependent UM parameters: $h(q)$, $C_{1,h}(q)$ and $\alpha_h(q)$. Note, due to the adverse effects of q_D that we previously described this may not always be the best method. This is discussed later.

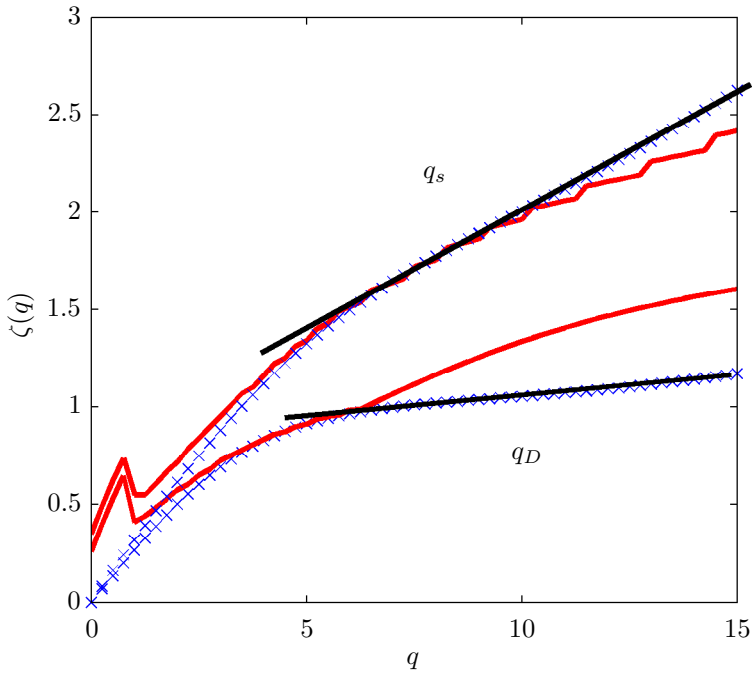

Figure 4.37: Plot of $\zeta(q)$ (blue crosses) and $\zeta_h(q)$ (red solid) for samples assumed to be influenced by q_s (top) and q_D. The black solid lines highlight the ranges where $\zeta(q)$ becomes linear.

The first thing to notice is that the function $K_h(q)$ is in good agreement with the structure function for $q < q_s$ and q_D and for $q > 3$. The discrepancy over the smaller moments is likely due to the optimisation procedure. As discussed in the previous section, the optimisation procedure will fail for $q < 1$ and when $K(q)$ is linear. Secondly, we see that it is indeed possible to reproduce the linear

behaviour associated with a divergence of moments, but only on a unique sample, thus confirming our previous hypothesis that smoothing occurs when averaging the structure function. The orders of q where $\zeta(q)$ becomes linear are marked with a solid black line. We may briefly note now that the observation of q_D on a single infers, if we are to remain within the UM framework, that $D < 1$. This is in agreement with our results on the anisotropic function $\rho(\phi)$.

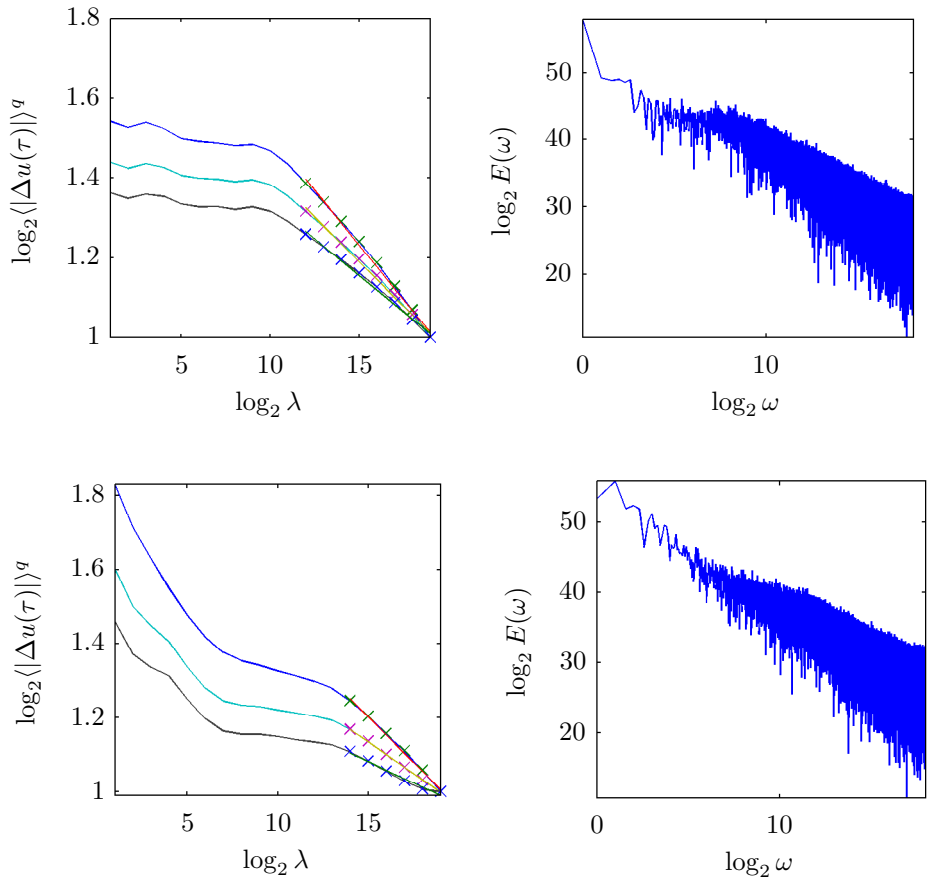

Figure 4.38: Scaling analyses for samples assumed to be influenced by q_s (top) and q_D (bottom). Left: plot of the second, fourth and sixth moments of the velocity increments. The crosses corresponds to the range of scales over which the structure function is estimated; right: corresponding velocity spectra.

Figure 4.38 plots the probabilities of exceedance for the two samples at the highest resolution $\Lambda = 0.1$ seconds for comparison. The tail exponents for q_s and q_D are 6 and 4 respectively. A visual comparison with the structure functions in figure 4.37 give q_s to be approximately 10 and $q_D = 7$. The difference between

the orders is in agreement but the actual departure is somewhat overestimated. Our aim now is to be able to predict either q_s or q_D within the UM framework.

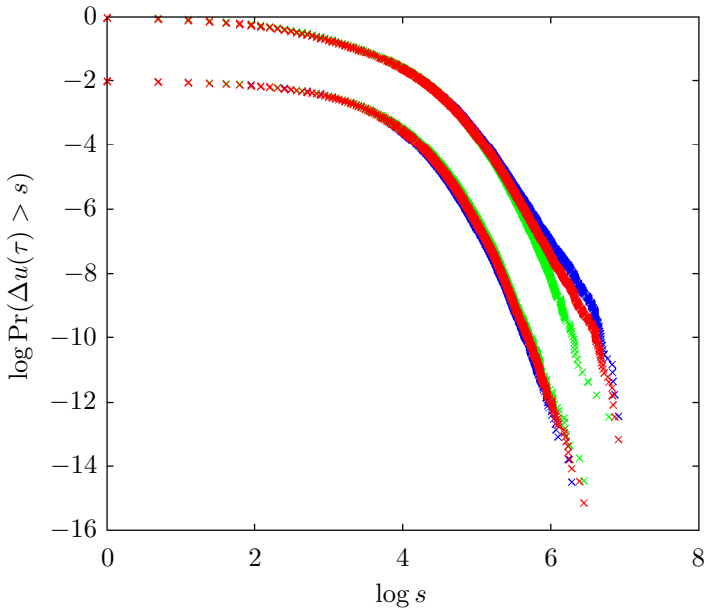

Figure 4.39: Plots of the exceedance probabilities of $|\Delta u(\tau)|$ (red), $\Delta u(\tau) < 0$ (blue) and $\Delta u(\tau) > 0$ (green) for a sample with q_s (lower plot) and q_D (upper plot). The lower plot has been shifted for clarity. The slopes correspond to q_s and q_D are 6 and 4.

Coming back now to the function $\zeta_h(q)$ we see that when the structure function becomes linear, $\zeta_h(q)$ departs from $\zeta(q)$. When the assumed case of q_s occurs we underestimate the structure function. When the assumed case of q_D occurs the structure function is over estimated. To try to understand this we have plotted the UM parameters as functions of q (figures 4.40 and 4.41).

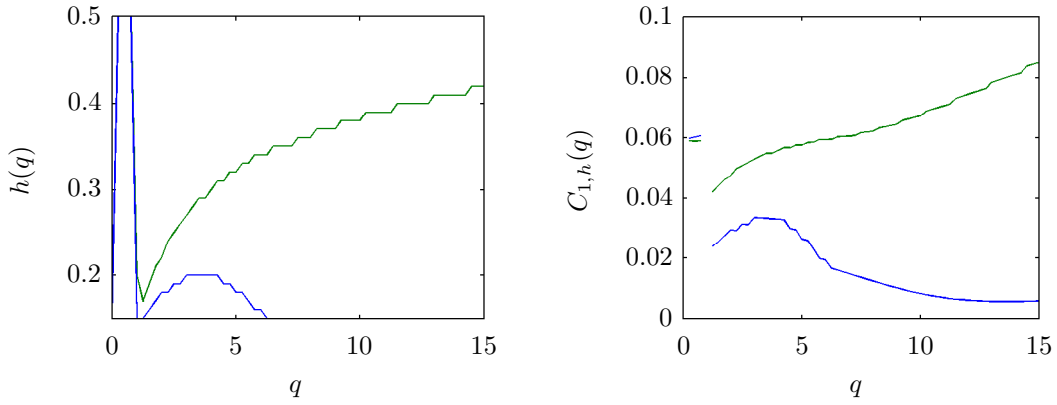

Figure 4.40: Plots of $h(q)$ (left) and $C_{1,h}(q)$ (right) for q_s (green) and q_D (blue)associated files.

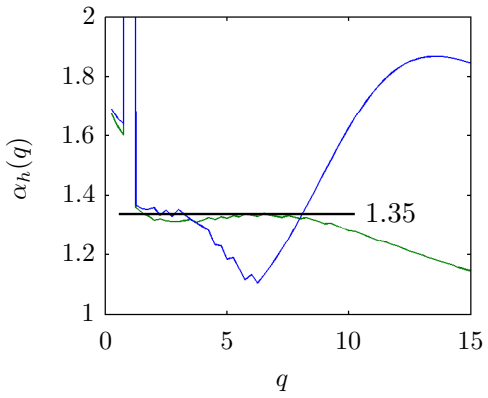

Figure 4.41: Plot of α_h for q_s and q_D (green and blue).

From figure 4.40 we can see that both h and $C_{1,h}(q)$ are non-linear in q for both of the samples. Figure 4.41 shows that on the contrary $\alpha_h(q)$ remains constant at $\alpha \approx 1.4$ in both cases; up to $q = 7$ for q_s and $q = 3$ for q_D. For the case of q_D we see that we loose the stability of the parameter α over $q > 3$. This may be due to the fact we are in an unstable region (i.e. s_2), interestingly we are still able to reproduce $\zeta(q)$. Using $\alpha_h(q)$ and $C_{1,h}(q)$ we can estimate $q_{s,h}(q)$ (figure 4.42).

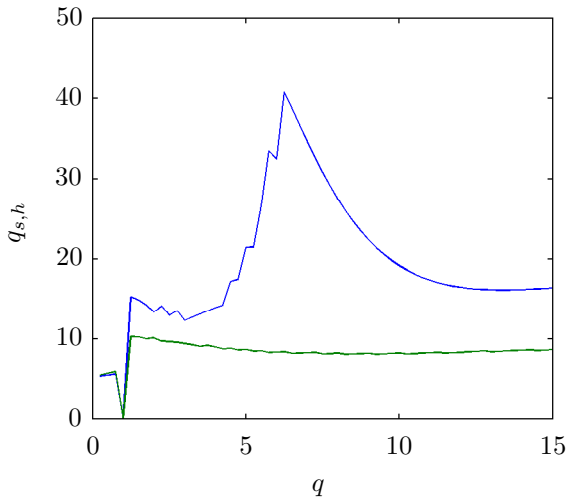

Figure 4.42: Plot of $q_{s,h}(q)$ for sample assumed to be influenced by q_s and q_D (green and blue).

For the sample with assumed q_s behaviour we can see that q_s is in agreement with the linear departure of figure 4.37 ($q = 10$). We would like to also estimate q_D, however, for these parameters and for $D = 1$ the values are greater than 20. We mentioned before that for q_D to be observed on a single sample we must have $D < 1$. For $C_1 = 0.03$, $\alpha = 1.4$ and $q_D = 7$ we find $D = 0.07$. Moreover, $C_{1,\Delta u}/D \approx 0.4$ implies that $a^{-\alpha} \cdot C_{1,\Delta u} = C_{1,\varepsilon}$. This gives $a = 1/6$!

It is not unexpected that $C_{1,h}(q)$ is consequently non-linear in q since a fractional convolution of order h will shift the singularities γ by $\gamma + h$. Therefore if $h(q)$ is non-linear in q the mean of the singularities C_1 will also be non-linear in q. Figure 4.43 plots $C_{1,h}(q)$ verses $h(q)$. As with the DTMs, figure 4.43 plots $C_{1,h}(q)$ versus $h(q)$ such that the non-linearity of the functions becomes independent of the scale λ. It isn't clear exactly what the slopes of the function correspond to. We can hypothesise though that it corresponds to an additional correctional term in the $K(q)$ function. The correction is quantified by the slope of the ratio of $C_{1,h}(q)$ and $h(q)$, M say.

We calculate M only over the moments $q \in [1 : 4]$. This is because for $q < 1$ the optimisation of h results in spurious estimates. For the sample attributed to q_s we find $M = 9.5$ and for q_D, $M = 5$. Figure 4.44 plots the histogram of M over the full dataset. We attempted to correlate M with the empirical estimates

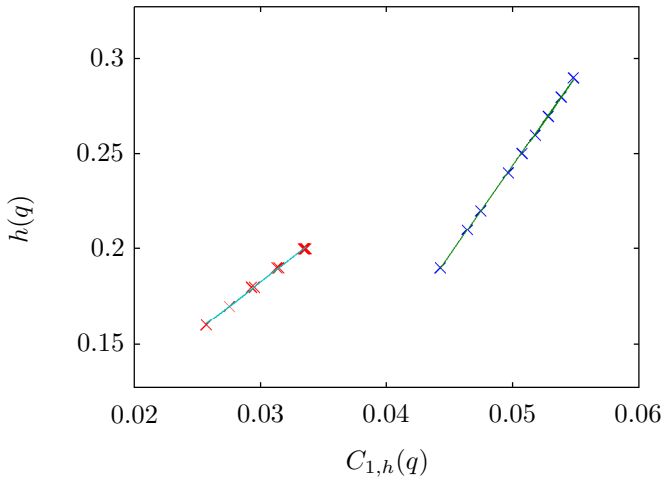

Figure 4.43: Plots of $C_{1,h}(q)$ versus $h(q)$ for the moments $q \in [1:4]$. The slopes M for the two samples are 9.5 (q_s) and 5 (q_D).

of q_D finding $R = 0.1$. This is not unexpected as there is no reason a correction for $\zeta(q < q_D)$ would be influenced by q_D.

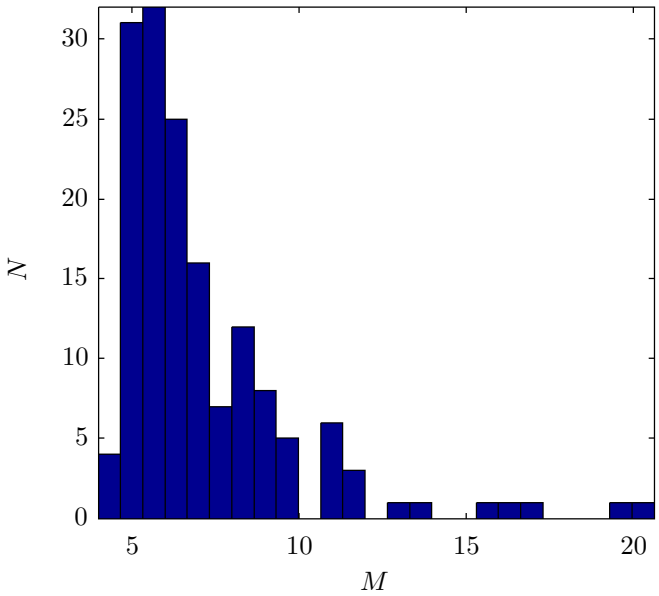

Figure 4.44: Histogram of the slopes (M) of $C_{1,h}(q)$ plotted against $h(q)$; taken over the full Corsica dataset. The slopes are estimated over the moments $q \in [1:4]$.

Although we are beginning to understand how to quantify this additional cor-

rection we are still unable to retrieve the parameter that predicts the divergence of moments. In the next we attempt to better understand this problem.

4.7 Summary Of Chapter 4

Universal multifractals provide a framework in which anisotropic, scaling, and correlated fields have power law statistics. The parameters of the framework α, C_1 and H, describe the extremeness, intermittency and correlation of the field. However, estimating the multifractality and co-dimension of a given process requires not only that the process itself is scaling but also that its positive flux proxies. It turns out that in both of the datasets we had available to us, obtaining a scaling flux from either the velocity or temperature increments, is much more complicated a task than one would expect.

While analysing this data we found that flux proxies based on the modulus of the wind velocity increments yield non-scaling statistical moments and therefore spurious multifractal parameter estimates. Furthermore, it can be difficult to initially identify the non-scaling behaviour of the data. If we are to remain within the framework of universal multifractals the algebraic fall-off observed in the probability distributions of the velocity increments corresponds to a divergence of moments in both the scaling moment function and the structure function; the point at which they both become linear. In terms of the (double) trace moments, a spurious linearity occurs giving a false impression of scaling. This can be particularly misleading when the energy flux is defined through the third power of the velocity. The larger the power the closer the trace moments (TMs and DTMs) are to the spurious linear range. To deal with this we suggested the use of a best fit versus $\hat{\alpha}$ plot. When an $\hat{\alpha}$ plateau occurs, corresponding to a stable α, subject to a high regression. However, it is precisely the non-scaling behaviour of statistical moments with spurious multifractal parameter estimates that we have spent most of our time studying; attempting to either remove or quantify its effects.

We have shown that the the non-scaling behaviour (or a trace moment curvature) that appears when using the flux proxies can be linearised with a fractional integration, i.e., with the h-optimisation method. The extensive application of this method confirms that the atmospheric surface-layer *is scaling* (aniso -tropically), and that it *is multifractal*, i.e. it has a unique multifractality index $\alpha = 1.4$. The downside is that both the co-dimension and the Hurst exponent

become q-dependent. This is outside of the linear scale invariance framework.

As the curvature of the trace moments varies with q (and η) we have developed a series of methods that equally optimises the UM parameters at each value of q and η. So much so that we are still unable to find a unique co-dimension and Hurst exponent for the atmospheric surface-layer. We are however able to show that it takes very little to destroy the scaling properties of the flux of a given process and that it is possible to locally (for each order q) reconstruct the scaling moments and therefore structure function of the velocity with a fractionally integrated flux.

In the majority of files we found that although the (double) trace moments could be linearised through fractional integration the much required stable parameter α remained elusive. Instead a strong spike would occur in the $\hat{\alpha}$ function. Using the notion of multifractal phase transition, theoretical developments on the local estimate of α revealed that for q_D four sectors would occur in the surface of $\hat{\alpha}$; one of which gives the good parameter and the singular boundary separating the sectors explained our spike. We put forward an analytical expression for these four sectors. Then the instability of the $\hat{\alpha}$ function on individual samples meant that the dimension of the measurements must be less than unity if to remain in the UM framework. Due to the increasing evidence of very strong anisotropies in the surface-layer it has become increasingly clear that this is the cause of the behaviour.

Comparisons of the spectra of the time-series velocities differentiated in time and in space showed that it is not possible to obtain a spectral exponent $\beta > 0$ for the spatial derivative of the velocity time-series as predicted by dimensional analysis. This suggests that spatial derivatives will insufficiently de-correlate time-series wind velocities. Although a space-time anisotropy causes problems for a homogeneous isotropic assumption, provided it is scaling and multifractal it can be modelled. Although we have had spatial scale separations available to us we have remained mainly dependent on the time-series statistics of the data, i.e. the presumption that the observable inertial ranges are Kolmogorov requires Taylor's frozen turbulence hypothesis. If we merely assume that they are scaling we can still attempt to quantify the temporal statistics of the process. For this we require universal multifractals. If we are to truly understand the relation between time and space correlations a more rigorous measurement campaign is needed.

References: Chapter 4

R. Benzi, G. Paladin, G. Parisi, and A. Vulpiani. On the multifractal nature of fully developed turbulence and chaotic systems. *Journal of Physics A: Mathematical and General*, 17(18):3521, 1984. URL http://www.google.fr/search?client=safari&rls=10_7_4&q=On+the+multifractal+nature+of+fully+developed+turbulence+and+chaotic+systems&ie=UTF-8&oe=UTF-8&redir_esc=&ei=urbnUduNCMO7O8rXgcAC.

G. Fitton, I. Tchiguirinskaia, D. Schertzer, and S. Lovejoy. Multifractal Statistical Methods And Space-Time Scaling Laws For Turbulent Winds (submitted). In *Euromech 2012*.

A. S. Gurvich and A. M. Yaglom. Breakdown of eddies and probability distributions for smallscale turbulence. *Phys. Fluids*, 10:S59, 1967.

C. T. Hoang. Prise en compte des fluctuations spatio-temporelles pluies-débits pour une meilleure gestion de la ressource en eau et une meilleure évaluation des risques. 2011. URL http://www.google.fr/search?client=safari&rls=10_7_4&q=Prise+en+compte+des+fluctuations+spatio+temporelles+pluies+debits+pour+une+meilleure+gestion+de+la+ressource+en+eau+et+une+meilleure+evaluation+des+risques&ie=UTF-8&oe=UTF-8&redir_esc=&ei=LnyfUeLyB_KY1AWltoG4CQ.

D. Lavallée. *Multifractal techniques: analysis and simulation of turbulent fields*. PhD thesis, McGill University at Montréal, 1991. URL http://scholar.google.com/scholar?q=related:VAofCH6iUAUJ:scholar.google.com/&hl=en&num=20&as_sdt=0,5.

C. Meneveau and K. R. Sreenivasan. Simple multifractal cascade model for fully developed turbulence. *Physical review letters*, 59(13):1424, 1987. URL http://www.google.fr/search?client=safari&rls=10_7_4&q=Simple+multifractal+cascade+model+for+fully+developed+turbulence&ie=UTF-8&oe=UTF-8&redir_esc=&ei=-7bnUaWRIIHMPYH3gLAB.

E. A. Novikov and R. W. Stewart. The intermittency of turbulence and the spectrum of energy dissipation fluctuations. *Izv. Geophys. Ser*, 3:408–413, 1964.

D. Schertzer. Physical modeling and analysis of rain and clouds by anisotropic scaling multiplicative processes. *J. Geophys. Res.*, January 1987. URL http://www.physics.mcgill.ca/~gang/eprints/eprintLovejoy/neweprint/JGR.SL.1987.good.pdf.

D. Schertzer, S. Lovejoy, F. Schmitt, Y. Chigirinskaya, and D. Marsan. Multifractal cascade dynamics and turbulent intermittency. *Fractals*, 5(3):427–471, 1997. doi:10.1142/S0218348X97000371. URL http://dx.doi.org/10.1142/S0218348X97000371.

F. Schmitt, D. La Vallée, D. Schertzer, and S. Lovejoy. Empirical determination of universal multifractal exponents in turbulent velocity fields. 68(3):305–308, January 1992. URL http://www.google.fr/search?client=safari&rls=10_7_4&q=Empirical+determination+of+universal+multifractal+exponents+in+turbulent+velocity+fields&ie=UTF-8&oe=UTF-8&redir_esc=&ei=N8oPUf7YFqmH0AWFhYBg.

Y. Tessier, S. Lovejoy, and D. Schertzer. Universal multrifractals: Theory and observations for rain and clouds. *Journal of Applied Meteorology;(United States)*, 32(2), January 1993. URL http://www.google.fr/search?client=safari&rls=10_7_4&q=Universal+multrifractals+Theory+and+observations+for+rain+and+clouds&ie=UTF-8&oe=UTF-8&redir_esc=&ei=yDWJUJ74LpGLhQe-nYDgCA.

D. Veneziano and P. Furcolo. A modified double trace moment method of multifractal analysis. *Fractals*, 7(02):181–195, 1999. URL http://www.google.fr/search?client=safari&rls=10_7_4&q=A+

modified+double+trace+moment+method+of+multifractal+analysis&ie=UTF-8&oe=UTF-8&redir_esc=&ei=AMoPUdeoD8mc0QXgyYDgBg.

H. Yamazaki. Breakage models: Lognormality and intermittency. *Journal of Fluid Mechanics*, 219:181–193, 1990. URL http://www.google.fr/search?client=safari&rls=10_7_4&q=Breakage+models+Lognormality+and+intermittency&ie=UTF-8&oe=UTF-8&redir_esc=&ei=ZbfnUeaFK4LdOsLOgcgL.

Chapter 5

5.1 Comparison Of Methods

In this chapter we discuss whether or not it is possible to reproduce the structure function with stable parameters. In appendix B.4 we see that the addition of a non-scaling process to that of a scaling process can cause the TMs and DTMs to become convex, i.e. the total process becomes non-scaling. We fractionally integrated or differentiated either the velocity or its increments in order to obtain linear TMs and DTMs. The result of the local linearisation of the DTMs is q and η dependency for the parameters C_1 and H. If we take the dependency of the parameters on q into account when calculating the scaling moment function $(K_h(q))$ we are able to reproduce the empirical structure function. However, if we wish to simulate a given field we require unique parameters. We therefore endeavour in this chapter to compare different methods in order to see if there if there is any convergence to stable parameter estimates. As a basis for testing our parameters we will use the structure function of figure 4.12 of the previous chapter. Note this is the ensemble averaged structure function calculated over the full Corsica dataset.

The DTMs On A FiF

We start off with the DTMs calculated on the fractionally integrated flux for a fixed value of h; avoiding therefore the q dependency. Figure 5.1 shows the DTMs for $q = 1.5$ and $\log \eta \in [-3 : 3]$ computed on $\chi = \Delta u * |t|^{-0.9}$. Using $h = -0.9$ proved to be the best value for the range of scales shown by the black

solid lines. We have included the DTMs for $h = -1$ as a comparison. We can see that when the correct value is used the same scaling region as the spectra becomes visible (i.e. from $\log_2 \lambda = 9$ to 14). Note although the DTMs appear scaling, the logarithmic axis masks the curvature that we described in §4.4.

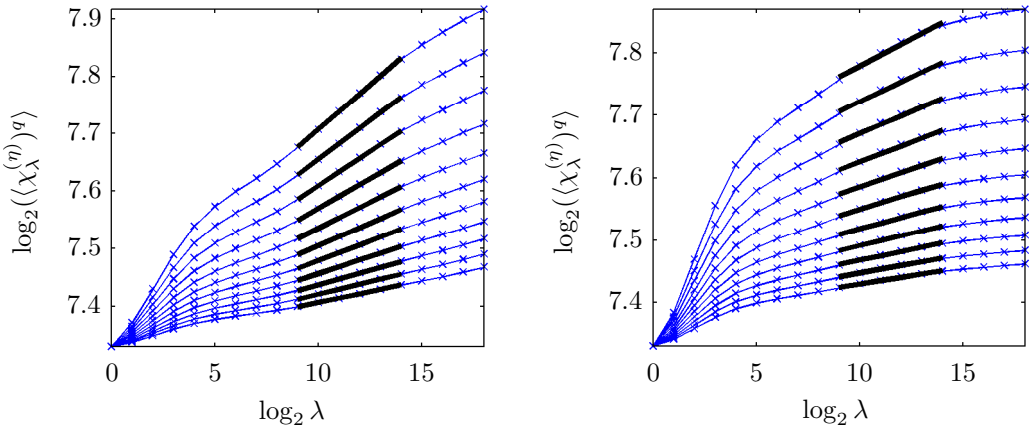

Figure 5.1: Plots of the DTMs estimated on χ for $h = -0.9$ (a) and $h = -1$ (b).

The Double Structure Function (DSF)

The double structure function $S_\lambda(q, \eta)$ corresponds to a modification of the structure function inspired by the DTM method, i.e. it shares with DTMs the property of being defined by two exponents q and η, having the same role as for DTM, but with an algebraic aggregation of the fluctuations Δu_λ like for the classical structure function:

$$S_\lambda(q, \eta) = \langle (\Delta u_\lambda^{(\eta)})^q \rangle \text{ where } |\Delta u_\lambda^{(\eta)}| = |\Delta u_\lambda|^\eta / \langle |\Delta u_\lambda|^\eta \rangle$$

This equation is indeed similar to equation 4.14 with similar properties, e.g. its scaling exponent. Nevertheless, it has the advantage to deal directly with the velocity fluctuations of the velocity instead of algebraically aggregating an energy flux proxy. Figure 5.2 plots $S_\lambda(q, \eta)$ for $q = 1.5$ and $\log \eta \in [-3 : 3]$.

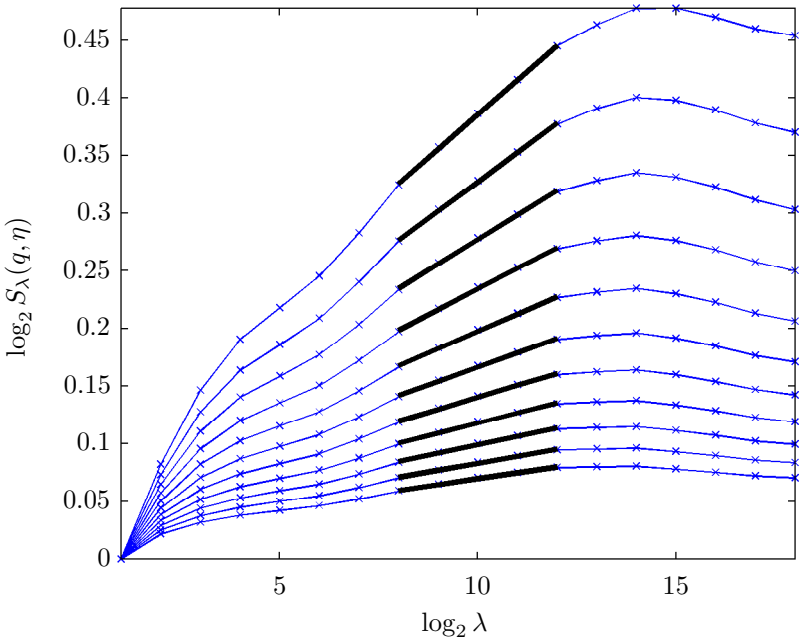

Figure 5.2: The DSF for $q = 1.5$ and $\log \eta \in [-3 : 3]$.

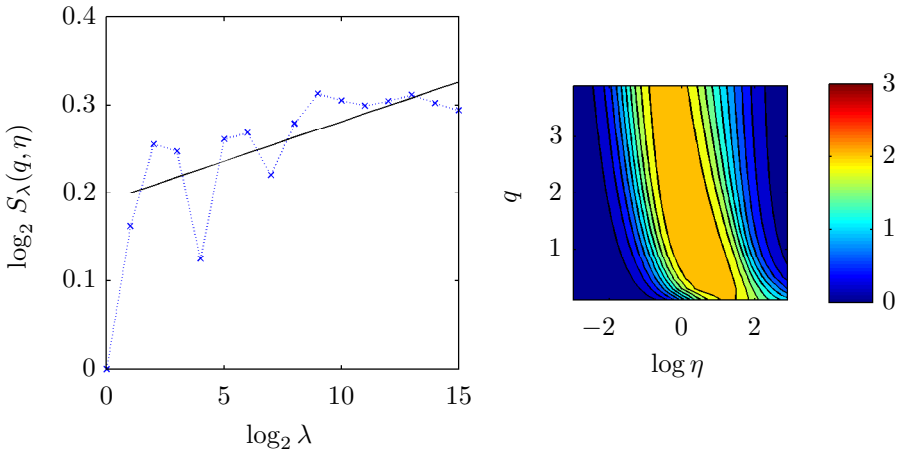

Figure 5.3: Plot of the DSF method (left) computed on a single sample for $q = 1.5$ and $\log \eta = 0$. The corresponding surface of $\hat{\alpha}$ is plotted to the right. At $q = 1.5$ and $\log \eta = 0$, $\alpha = 2.2$ and $C_1 = 0.014$.

We can see that the range of scales (from $\log_2 \lambda = 8$ to 12) that are scaling are not quite the same as those in the spectra. When using the DSF method a positive slope appears over the highest frequencies. This corresponds to negative H and

may be associated to a non-scaling process. The discrepancy in scaling ranges therefore may be because of the aggregation of this noise through increasing scales; although this doesn't explain why there is a disagreement with the spectra. Instead of estimating over exactly the same range, we have adjusted the range slightly in DSF such that it is over the range of scales that appears to scale the best.

Contrary to the DTM method, it is not possible to use the DSF on individual samples due to its highly variable nature. Figure 5.3 shows the DSF estimated on a single sample with one of the highest NRMSE values in the whole of the Corsica dataset. Although there appears to be some scaling the quality of the estimate is unreliable. This is further confirmed by the estimation of the parameter $\alpha > 2$.

Comparison Of Local Multifractality Functions

Figure 5.4 plots $\hat{\alpha}$ for the two DTMs (i.e. for $h = -1$ and $h = -0.9$) and the DSF.

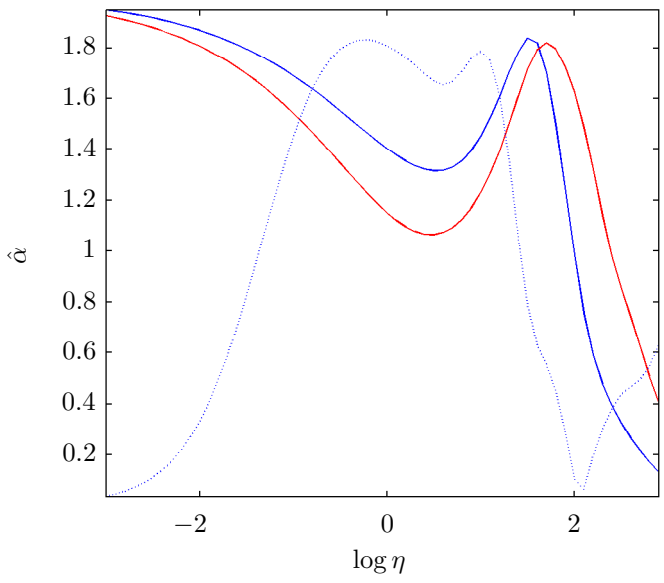

Figure 5.4: Comparison of $\hat{\alpha}$ estimated over $\log \eta \in [-3 : 3]$ for $q = 1.5$, from the DTMs of figure 5.1 (red and blue solid lines for $h = -1$ and -0.9 respectively) and the DSF of figure 5.3 (dotted blue line).

We can see that the maximum spikes give estimates that are comparable however the estimations around $\log \eta = 0$ differ by a factor of 0.4 to 0.8 depending on which h is chosen. Since the 'spikes' have been shown to be spurious estimates of the parameter α we are left with a large discrepancy between the two parameters.

Because there is no clear range over which $\hat{\alpha}$ is constant it isn't clear which estimate should be used. This is less the case with the DSF method. To combat this we will use a range of estimates across $\log \eta$ and see which gives the best fit versus the structure function. In order to reproduce the structure function we must choose a unique value of h to match our unique parameters. Since our DTMs are integrated by $h = 0.1$ we will also use $H = 0.1$ for the DSF. This is because we cannot directly estimate H from the DSF.

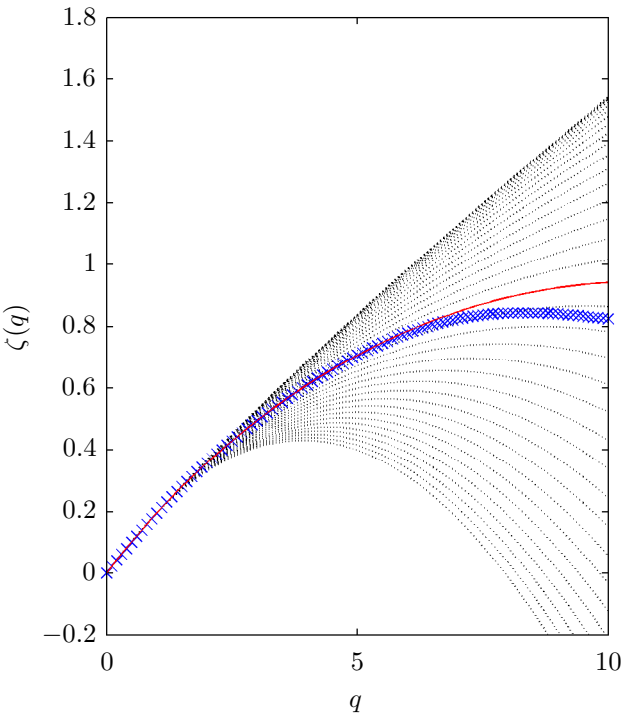

Figure 5.5: Plot of the empirical structure function $\zeta(q)$ (blue crosses) compared to the semi-analytical structure function estimated from the DTMs of the fractionally integrated flux. The dotted line curves correspond to the variation in parameters $\hat{\alpha}$ and $\hat{C}_1$ (from the solid blue curve in figure 5.4) across $\log(\eta) \in [-3 : 0.1 : 1]$. The red curve corresponds to the best fitting of those parameters, i.e., $\alpha = 1.64$ and $C_1 = 0.019$ at $\log(\eta) = -1.3$.

Figure 5.5 plots the structure function and the semi-analytical structure function for the range of parameters across $\log \eta$. Similarly figure 5.6 does the same for the estimates from the DSF method. The red curves in both figures correspond to the semi-empirical curve with the best fit. Comparing the two methods we can see that DSF gives the best overall fit. Both methods estimate similar values of C_1 with DSF giving a slightly higher estimate of α that results in a better overall fit.

Although both methods do well to fit the lower order moments (up to $q = 7$ in both cases) it is more important to be able to estimate q_s and q_D.

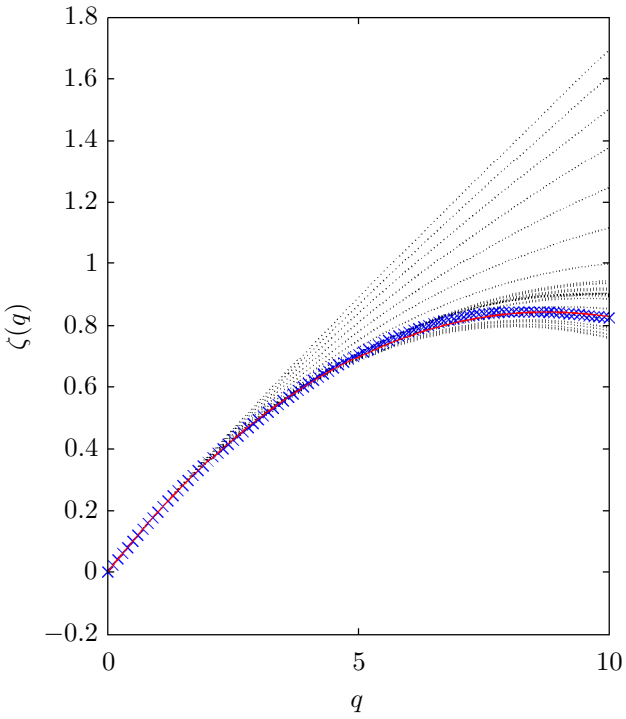

Figure 5.6: Plot of the empirical structure function $\zeta(q)$ (blue crosses) compared to the semi-analytical structure function estimated from the DSF of the velocity increments. The dotted line curves correspond to the variation in parameters $\hat{\alpha}$ and $\hat{C}_1$ (from the dotted blue curve in figure 5.4) across $\log(\eta) \in [-3 : 0.1 : 1]$. The red curve corresponds to the best fitting of those parameters, i.e., $\alpha = 1.79$ and $C_1 = 0.0172$ at $\log(\eta) = -0.5$.

Figures 5.7 and 5.8 show the estimation of q_s for the variation in parameters across η. For such low values of C_1 we would not expect to see q_D and therefore haven't computed it. For DSF we can see that q_s is fairly well estimated, for the

DTM method however q_s is much larger than the observed divergence from the empirical curve.

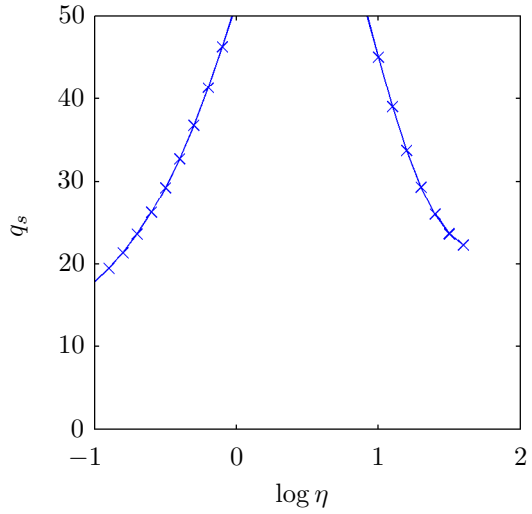

Figure 5.7: Plot of q_s estimated from the $\hat{\alpha}(\eta)$s and $\hat{C}_1(\eta)$s of the DTMs of the fractionally differentiated velocity.

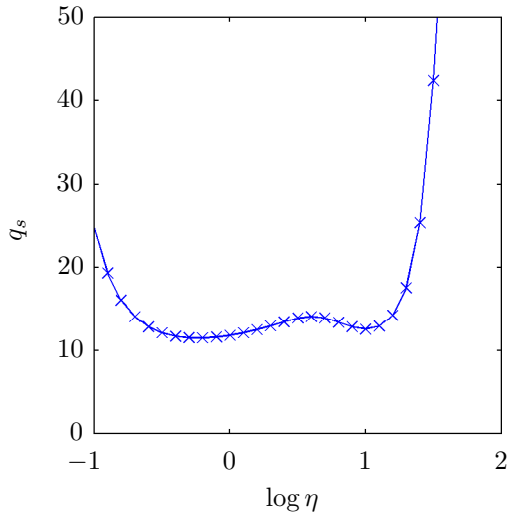

Figure 5.8: Plot of q_s estimated from the $\hat{\alpha}(\eta)$s and $\hat{C}_1(\eta)$s of the DSF of the velocity increments.

We have shown that although there are parameters that come from both the DTMs and DSF methods that can be selected within a (large) margin of error that will fit the lower order moments of the structure function. Moreover, these parameters 'predict' to some extent the order at which the functions become linear. We need to ask though, is this really the right approach? We have seen that due to the instability in the estimates of the parameters it becomes a very precarious procedure selecting which parameters we should use. Furthermore, a very common justification for the correct estimation of the UM parameters is the correct 'prediction' of q_s.

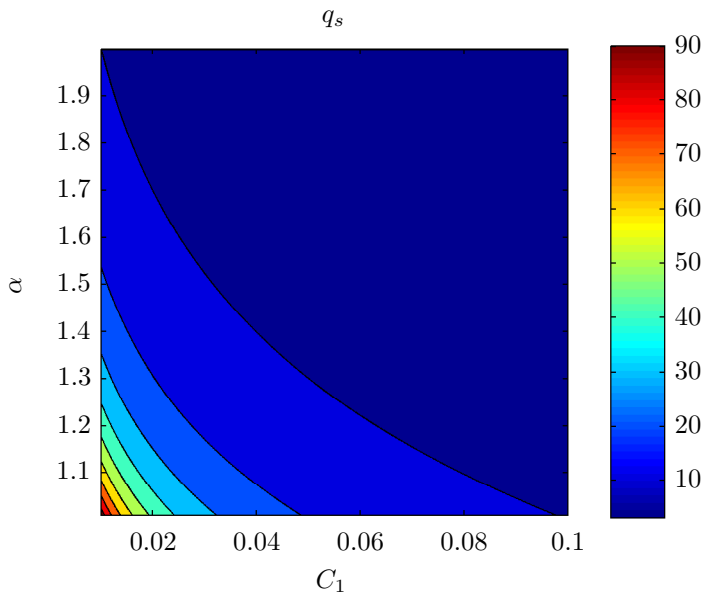

Figure 5.9: Surface of q_s for a range of values of α and C_1; $D = 1$.

Figure 5.9 shows the ranges of the parameters α and C_1 for which q_s is estimated. We see that the lower the value of q_s (specifically less than 10) the larger the possible range of values for the parameters. It is therefore unsurprising that q_s is quite often predicted. If we are to truly justify that it is q_s we are predicting we should find that there is an increase in the estimation of q_s with increasing D_s. This however is not the case, as we have clearly shown (due to the spikes in the surfaces of $\hat{\alpha}$) that for individual samples we are observing q_D.

So what exactly is happening? We have shown from very early on that the velocity wind increments exhibit a divergence of moments on each individual sample of the order 4 to 6 with increasing resolution. We have been able to show that because the velocity field is highly component-wise anisotropic the occurrence of q_D on a single sample is possible. Moreover, we have shown that the addition of a non-scaling white noise can produce the spurious convex curvature of the DTMs.

In which of these situations is the classical UM model applicable and in which other situations must we modify the model? When we ensemble average the structure functions of the Corsica dataset we loose the characteristic divergence of moments that we are so desperate to predict. Is the UM model therefore more applicable? Although the linearity over higher orders is lost we have shown that the ensemble averaged DTMs are still more convex. This convexity requires local fractional integration to be removed. What happens when the linearity over higher order of the structure functions persists? Can we predict this behaviour? Figure 5.10 plots the ensemble averaged structure functions of the high-frequency scaling ranges of the Growian dataset.

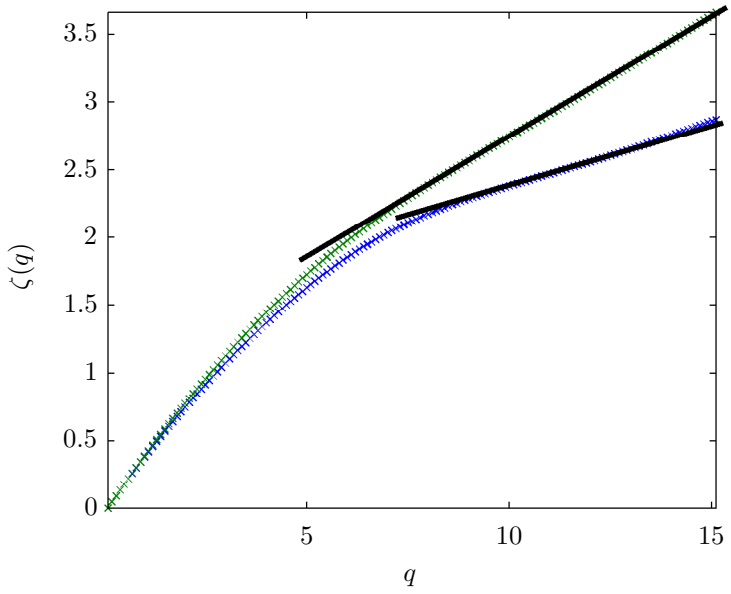

Figure 5.10: Ensemble averaged structure functions computed on the Growian dataset over the time-scales 0.4 to 6.4 seconds at 50 (blue) and 100m (green).

We can see that we are approximately able to recover $\zeta(3) = 1$[1] corresponding to K41, unlike for the structure functions of the Corsica dataset. The reason for this is simply the higher value of β (≈ 1.7) as opposed to 1.3 found in the spectra. We can simply say, therefore, that the Growian dataset over smaller scales is closer to a Kolmogorov-like energy. In the next section we will look at exactly which parts of these functions we can predict within the standard UM framework.

[1] This was pointed out by Annick Pouquet in a private communication.

5.2 Multifractality Estimation From The Structure Function

The structure function exponent $\zeta(q)$ defines the function $f(q)$ in the following way:

$$f(q) = \zeta(q)/q = H - K_\varepsilon(qa)/q \tag{5.1}$$

where $K_\varepsilon(q)$ is the scaling moment function of the conservative flux ε. With the help of:

$$K_\varepsilon(q, a) = K_\varepsilon(qa) - qK_\varepsilon(a) \tag{5.2}$$

we find that for universal multifractals

$$K_\varepsilon(q, a) = a^\alpha K_\varepsilon(q). \tag{5.3}$$

The function $f(q)$ then becomes

$$f(q) = H + aC_{1,\varepsilon}/(\alpha - 1) - a^\alpha C_{1,\varepsilon} q^{\alpha-1}/(\alpha - 1). \tag{5.4}$$

Differentiating $f(q)$ yields the following estimate for α:

$$\alpha \propto \frac{\log[-df(q)/dq]}{\log q} + 2. \tag{5.5}$$

If the structure function can be fit by UM parameters, i.e. the process can be defined by unique parameters α, C_1 and H, equation 5.5 is linear over $\log q$. Figure 5.11 plots $f'(q)$ computed on the ensemble averaged structure function of the Corsica dataset used in the previous section. Note, since $f'(q)$ is negative we must subtract the absolute slope!

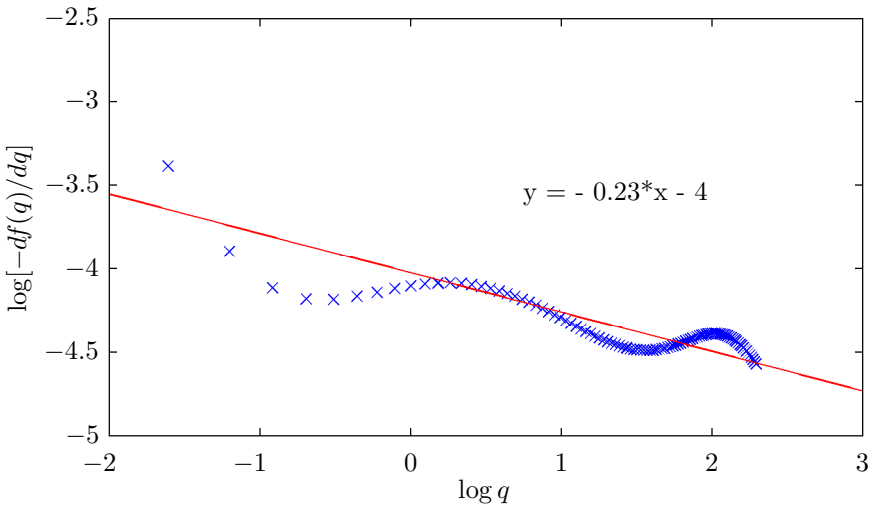

Figure 5.11: Plot of $f'(q)$ computed on the ensemble averaged structure function of the Corsica dataset used in the previous section. Slope of the red line of best fit is -0.23 ($\alpha = 1.77$ and $C_1 = 0.018$). Estimating α requires the subtraction of the absolute slope.

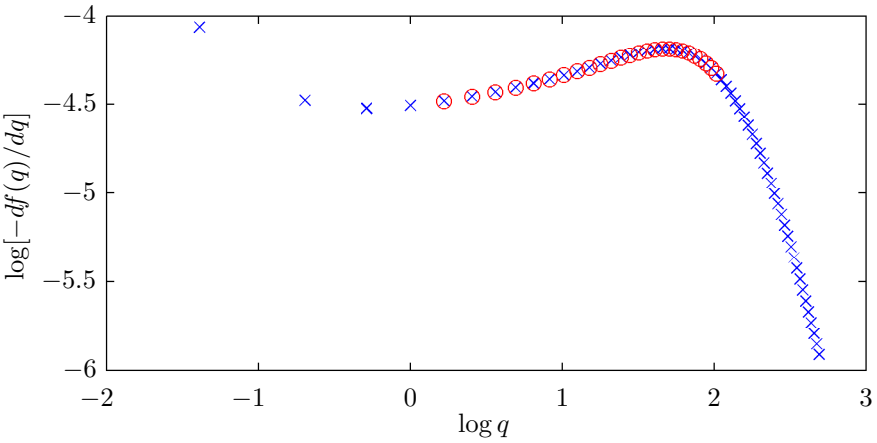

Figure 5.12: Plot of $f'(q)$ computed on the structure function of a single (q_s-like) sample from the Corsica dataset. The red circles correspond to the range of q over which the $K_h(q)$ function had the best fit.

Figure 5.11 is clearly far from linear in form. However, as a rough approximation of α we may calculate the slope of the function over the full range of q giving $\alpha \approx 1.8$ and $C_1 \approx 0.02$. Surprisingly these estimates are in fairly good agreement with those of the DSF. Although the estimates are within the standard

UM framework it is clear from the non-linearity of the function (this suggests a possible dependence on q) that the standard model is not a good approximation. On the other hand this behaviour could also be due to the poor approximation of the discrete derivative of the function $f(q)$.

Figure 5.12 plots the same function, $f'(q)$, for the individual sample we ascribed to the behaviour of q_s. In particular we have marked out the values of q of the function that have the closest fit to the $K_h(q)$ function. It is in fact *the* most non-linear part of the function that is best reproduced by $K_h(q)$.

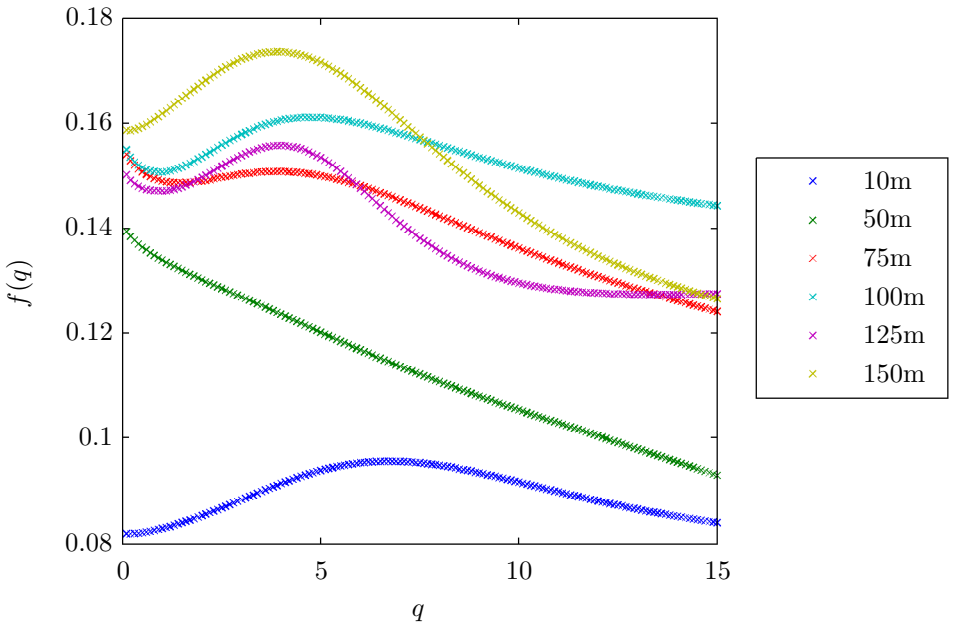

Figure 5.13: Plots of $f(q)$ for the Growian dataset at 10, 50, 75, 100, 125 and 150m in height over the time-scales half a minute to five minutes.

By equation 5.4 we can quickly identify if a function can be fitted by the UM model since it should correspond to the sum of a power law with a constant. If the function is more complex then we are out of the framework of UMs. Figure 5.13 plots the $f(q)$ functions at six heights taken from the Growian dataset. The $f(q)$ functions were computed on structure functions estimated over the time-scales of half a minute to five minutes. The clear non-power law behaviour exhibited in $f(q)$ at most of the heights in figure 5.13 further suggests that a more complex model is required. It is only the data 50m that is compatible with equation 5.5.

In figure 5.14 we plot the $f(q)$ function for a simulated velocity with an added Gaussian white noise. The velocities are computed by convoluting a simulated conservative flux, i.e., $u_N(t) = \varepsilon_N^{1/3} * |t|^{1/3}$. The conservative flux, ε_N, is simulated using the discrete α-model with UM parameters $\alpha = 1.3$ and $C_1 = 0.15$. We then add a Gaussian white noise, $X(t)$, to u_N in a similar way to that done in appendix B.4; in appendix B.4 the noise is added only to the simulated conservative flux to show that curving DTMs will occur. We require the approximation to the velocity field so that the structure function can be computed.

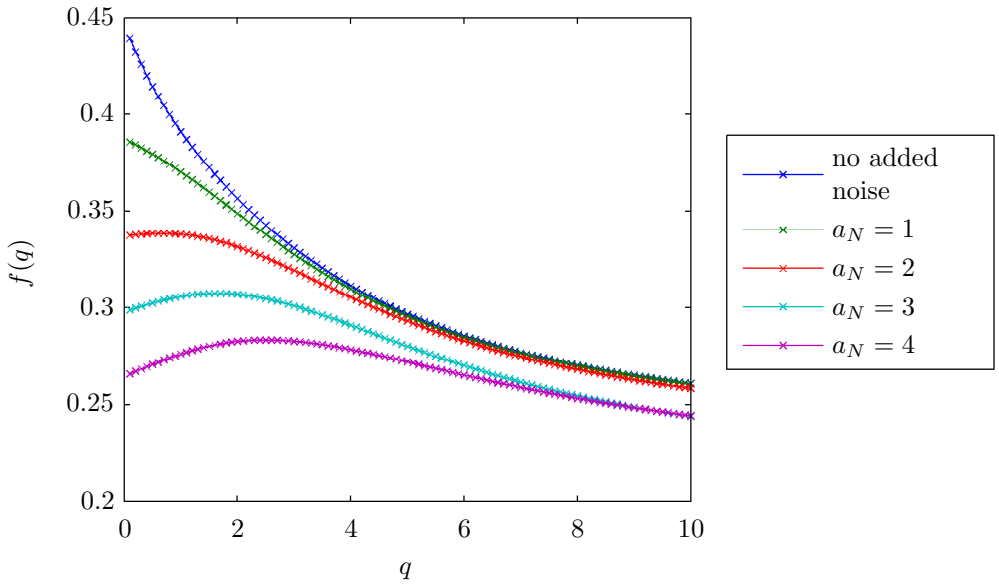

Figure 5.14: Plots of $f(q)$ of $u_N(t) + X(t) = (\varepsilon_N^{1/3} * |t|^{1/3}) + X(t)$ for an increasing power of noise a_N. The conservative flux, ε_N, is simulated using the discrete α-model with UM parameters $\alpha = 1.3$ and $C_1 = 0.15$.

The power with a constant form of $f(q)$ that we are looking for in order to apply the UM framework is well reproduced when u_N has no noise added (the upper most blue plot of figure 5.14). As an increasingly dominating noise is added to the process we begin to observe the same wave-like behaviour apparent in the empirical $f(q)$ functions of the Growian dataset. It seems that there is an additional contribution to the process that determines the function $f(q)$s vertical position.

We add the white noise to the simulated field we are not de-colouring the high-frequencies of the process in a way that would mimic the instrumental noise of an anemometer say. If we therefore look at the spectrum of $u_N(t) + X(t)$, for increasing powers, the scaling of the process seems almost unaffected. The scaling exponent however becomes lower and lower. Note, the slope of the spectra estimated in both the Corsica and Growian datasets is 1.3. This subtle behaviour suggests it would be very difficult to distinguish a mixture of the two processes simply by looking at their spectrum.

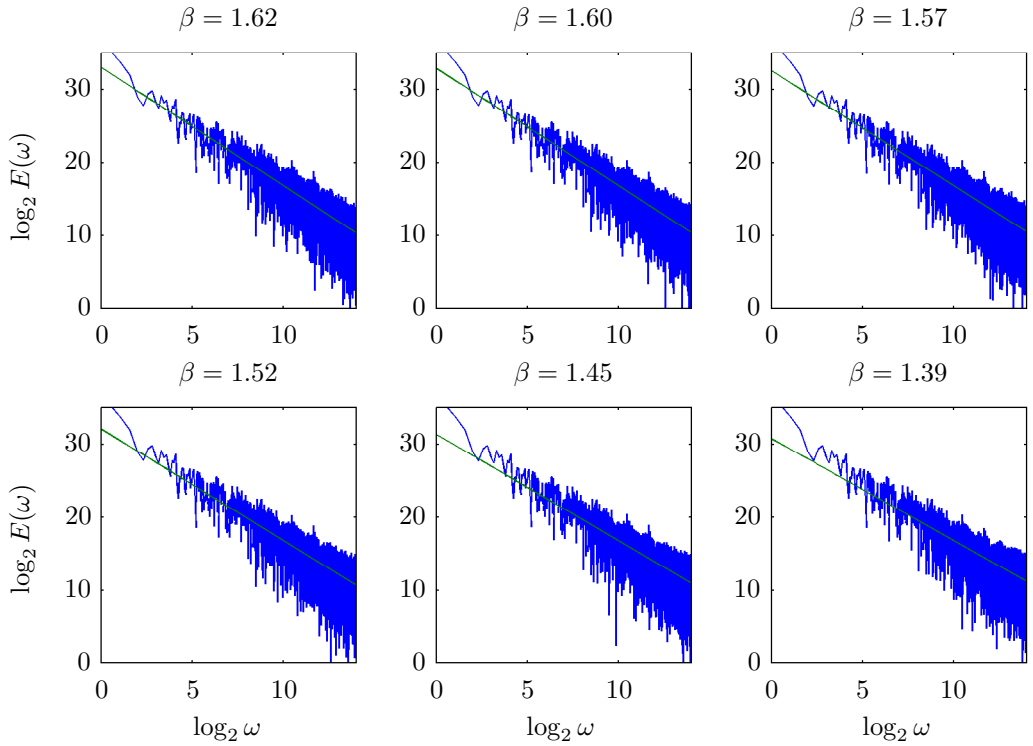

Figure 5.15: Plots of the energy spectra of $u_N(t) + X(t)$ for increasing powers of the added noise $X(t)$: $a_N \in [0 : 4]$.

Although we have been able to show that adding a non-scaling noise to the scaling velocity can result in adverse effects when approximating the flux from its absolute increments $|\Delta u|$, it still isn't clear why Δu scale differently. It is likely that the aggregation of the non-scaling noise accumulates through the scales thus amplifying the effect. The question we instead aim to answer is whether or not the q dependence of the UM parameters is the consequence of forcing non-scaling data

to scale through fractional differentiation/integration or whether it is inherent in the process. In the previous section we showed that the model is indeed required to be more complex but whether or not that could be a simple modification of the standard model is another question. The extreme curvature we have observed in $|\Delta u|$ and therefore any power of the field thereafter is not observed to the same extent in either the structure function or the double structure function. We have shown that there are ranges of q and η where the TMs and DTMs scale and the optimisation method ceases to work.

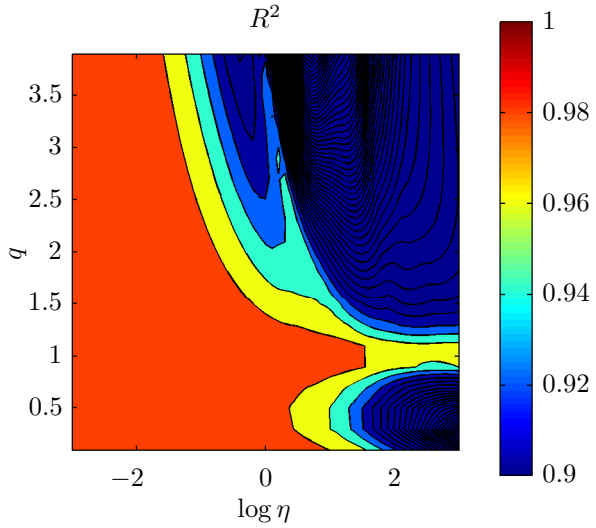

Figure 5.16: Surface plot of $R^2(q, \eta)$ for the double structure function.

If we are to believe the non-linearity of the DTMs is solely the product of the fractionally integrated flux model we would expect that the DSF, calculated only on the velocity increments, would be uniform in h across the surface q and η. Because we cannot directly measure h we must instead use R^2 – the quality of the linear fit of the DSF. If h remains constant across q and η we would expect R^2 to be constant except for large q in which either q_s or q_D intervene.

Figure 5.16 shows the surface contour plot of R^2 of the DSF of the previous section. Although the variation seems rather negligible it is still present. Moreover, R^2 decreases with q proving that there is q dependence on Δu without the use of the FiF model.

5.3 Five Parameter Fitting Model

We already saw that the FIF model yields the following scaling exponent $\zeta(q)$ for the structure function:

$$\zeta_{\Delta u}(q) = qH - K_\varepsilon(aq), \tag{5.6}$$

where $K_\varepsilon(q)$ is the scaling moment function of the conservative flux ε and corresponds to the (non-linear) contribution of intermittency. The energy flux density can be estimated with the help of $\hat{\varepsilon} \approx (\Delta u_\lambda \lambda^H)^{1/a}$.

For a universal multifractal flux ε:

$$K_\varepsilon(q) = \frac{C_{1,\varepsilon}}{\alpha - 1}\left(q^\alpha - q\right). \tag{5.7}$$

We can define a scaling moment function for the velocity fluctuations by:

$$K_{\Delta u} = K_\varepsilon(qa) = K_\varepsilon(q; a) + qK_\varepsilon(a). \tag{5.8}$$

In the case of a universal multifractal flux, this could be rewritten as:

$$K_{\Delta u}(qa) = a^\alpha K_\varepsilon(q) + qK_\varepsilon(a). \tag{5.9}$$

Therefore, the co-dimension $C_{1,\Delta u}$ of the mean intermittency of the velocity fluctuations is given by:

$$C_{1,\Delta u} = a^\alpha C_{1,\varepsilon}. \tag{5.10}$$

In order to obtain α and we must fractionally integrate the velocity increments so that h is optimised. Once a stable value of α is found we can then optimise the function $K_{\Delta u}(qa)$ on a in order to find the optimum value of a (and therefore C_1) that best fits the function $\zeta(q)$. Because a unique value of h is required for the structure function we used a different number of methods to estimate H: taking the mean across q, using the slope of the spectral exponent and also $H \approx \zeta(1)$. We found that each method would led to biases that would be compensated by either a or C_1 in the iterative process, thus it wasn't of great importance which value we chose provided it was within a given margin of error of the spectral exponent.

In order to begin the optimisation of the function we require an initial C_1 value. We attempted to use $C_{1,h}$ at $q = 1.5$ but found that we could not fit the structure function in this way for the majority of the files. Instead we needed to separate the two terms of equation 5.9, i.e.,

$$K_{\Delta u}(qa_1; a_2) = a_1^{\alpha} K_{\varepsilon}(q) + qK_{\varepsilon}(a_2). \tag{5.11}$$

The separation corresponds to a weighting of C_1 for the non-linear term or a weighting with respect to the power of the flux for the linear conservation term. It allows us to effectively choose any C_1 we require to fit the structure function but only as a function of the initial $C_{1,h}$, a_1 and most importantly α_h. Under this separation of operations we find that when $a_1 = a_2$ the value C_1 of the velocity increments has been correctly initially estimated using the FiF model.

Figure 5.17 plots the histograms of the denominators $1/a_1$ and $1/a_2$ of the parameters a_1 and a_2. We are interested in the denominators as they correspond to the power that the velocity increments are raised to in order for us to obtain our conservative quantity. Figure 5.17b shows that $1/a_2$ is of the order 20 on average with isolated cases reaching up to 50! This is clearly unphysical since for powers of this value we obtain $C_1 > 2$ for the flux. For $1/a_1$ (figure 5.17a) we find values that are lower (11) but are still 8 orders more than those predicted by K41.

Figure 5.17c plots the ratio of a_1 and a_2 in order to find samples where $a_1 = a_2$. Out of the total 161 samples we find 10 with $a_1 = a_2$. The majority of the samples require that a_1 be smaller to a_2. This corresponds to χ being raised to a larger power than the normalisation required for the structure function suggesting that $C_{1,h} < C_{1,\Delta u}$ for the majority of samples.

Figure 5.18 plots the structure functions of two samples that have $a_1 = a_2$. In both cases it is necessary to have an extremely large value of $C_{1,\varepsilon}$ and a in order to fit the functions. In Gires et al. [2013], a toy model is proposed where the normal multifractal model is multiplied by a binary β-model. This has the effect of reducing the support of the mixed-process, as may be the case here. If we consider that the contribution from the non-scaling part of the process reduces the support of the dimension and that this contribution is proportional to the

q-dependence of the parameters, it may be that we can quantity the non-scaling effect with the artificial increase in the parameter $C_{1,\varepsilon}$.

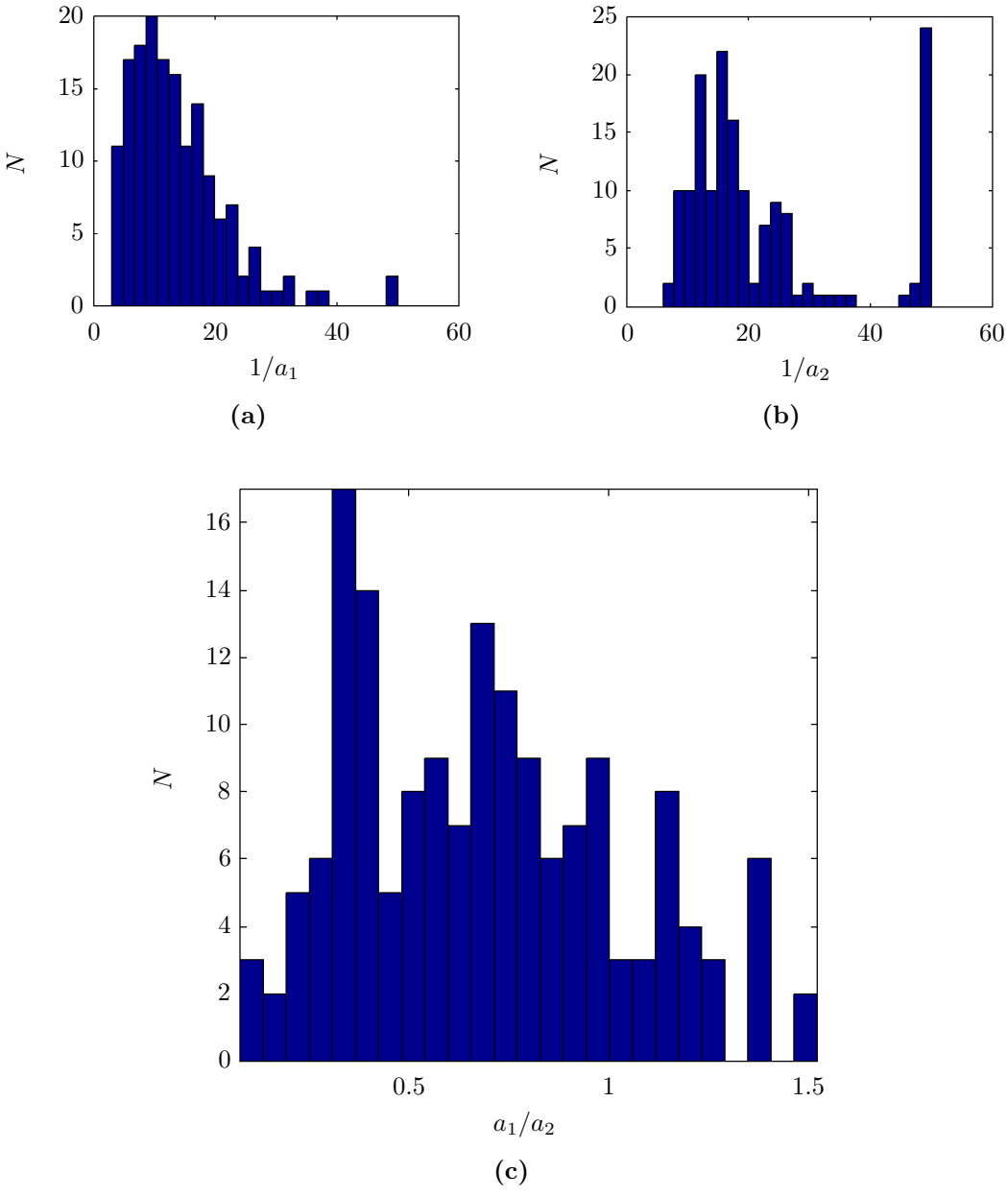

Figure 5.17: Histograms of the denominators $1/a_1$ (a) and $1/a_2$ (b). The averages over the whole sample are 11 and 19 for $1/a_1$ and $1/a_2$ respectively; (c) histogram of a_1/a_2

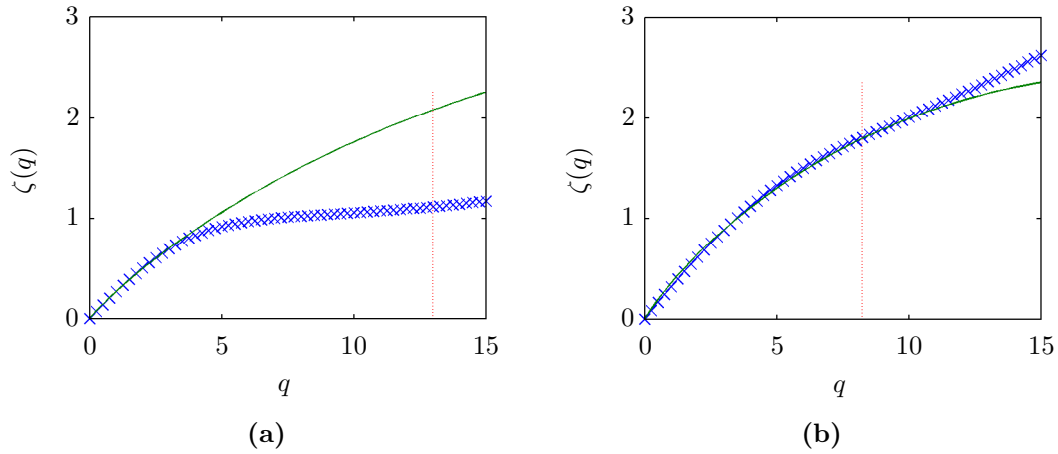

Figure 5.18: Structure functions estimated on the velocities of the Corsica dataset, for files that can be fitted with parameters $a_1 = a_2$. The parameters used to fit the left plot are: $C_1 = 0.83$, $\alpha_h = 1.36$ and $a = 13$; right: $C_1 = 1.1$, $\alpha_h = 1.34$ and $a = 11$.

5.4 Prospects: From Analysis To Modelling

A worst case study?

All of the preceding chapters have been devoted to understanding the fundamental phenomenon of turbulence intermittency within the surface-layer. This has been done with the help of a thorough multifractal analysis of two rather large data bases from two very different test sites. Before discussing how these insights can help to model the turbulent velocity field, it is indispensable to emphasise that the surface-layer is presumably the most challenging problem in fluid dynamics; loosely speaking a possible worst case scenario that has frightened many theoreticians. Indeed, turbulence intermittency is already such a difficult problem that the most achieved tools to understand, analyse and simulate this phenomenon have been developed in the most simplified, ideal cases, i.e. where many symmetries, other than scale invariance have been hypothesised.

These pre-suppositions can be traced back at least to Kolmorogov's hypothesis of 'local isotropy' Kolmogorov [1941a]. A hypothesis that has become so widely used that it has become a pre-requisite for scaling – a flow is required to be first translation invariant (in time and space) and isotropic before discussing its scaling properties. Loosely speaking, scale invariance should not be one of the first symmetries to be considered, but rather the last one. One may note that this was not always the case for Sedov [1972], who in spite of the fact that his book title only mentions self-similarity, he somewhat considered self-affinity. This wasn't by chance; it was, as discussed below, related to wall turbulence.

A hierarchy of symmetries

The strong anisotropy of geophysical flows due to gravity and related phenomena (buoyancy forces, stratification/convection) brought into question whether or not there exists a hierarchy of symmetries, leading eventually to generalised scale invariance (GSI, Schertzer and Lovejoy [1985a]). The radical paradigm shift that GSI introduced requires that scaling first be posit, before then studying the remaining symmetries. These symmetries are then no longer as trivial as

rotation invariance, a compatible (generalised) scale is no longer equivalent to a Euclidean distance.

As noted by Schertzer and Lovejoy [2006], it is rather ironic that fractal geometry Mandelbrot [1982], a mathematical construct that claimed the irrelevance of Euclidean geometry to natural phenomena, still remained based on a Euclidean metric! The GSI paradigm shift was already required for the 'free atmosphere' because of its anisotropy, but some space translation invariance was nevertheless expected to be an acceptable approximation.

This is no longer the case with wall-bounded turbulence such as that of the surface-layer, i.e., the system's properties drastically change with altitude. A considerable amount of research has been invested into deciphering these changes using so-called 'mean' profiles. These efforts have been without a general consent as to which law is truly valid, e.g., are they logarithmic, power-law, or do they result from a mixture of both laws?

One basic problem is the difficulty, not to say impossibility, to establish a clean Reynolds decomposition between the mean and the fluctuations when the mean defined over a given time scale is embedded into larger scale fluctuations. As a consequence, the aforementioned definitions can easily be sample dependent. This is the main reason we have not attempted to proceed with Reynolds decomposition methods as they would not have been supported by the performed spectral analyses. Indeed, the spectral analyses do not point out a spectral energy gap.

One may note that the spectral techniques, that have been mostly pioneered by the Russian school of turbulence, already require a given type of a statistical translation invariance and if possible a statistical rotation invariance to be easily handled. Various researchers therefore, have tried to adapt this technique to both anisotropy and non-translation invariance, e.g. using horizontal spectra depending on the altitude and looking for relations between them, etc. There is therefore no surprise that we were compelled to also adapt the multifractal analysis tools to the complexity of the surface-layer. This adaptation pre-figures for a large part that of the simulation tools.

What kind of complexity?

The main complexity of the surface-layer with respect to the free atmosphere, is the obvious fact that the hierarchy of eddies cannot be freely expanded to all sizes because of the complex interactions with the surface. This problem has led to the decomposition of the surface-layers into several sub-layers Pouquet et al. [1976], Korotkov [1976], Chashechkin [1989], **?** and Drobinski et al. [2004].

In a very general manner, larger-sized eddies, often called impinging eddies, are not only compelled to be strongly anisotropic (smaller ones are presumably anisotropic due to buoyancy forces, like in the free atmosphere), but also their interaction with other eddies are no longer dominated by interactions with eddies of a similar size. This can be seen as interactions bypassing the usual cascade steps Korotkov [1976], Kader and Yaglom [1989] and Yaglom [1993]. These types of interactions are called 'non-local' because they correspond, in Fourier space, to a convolution of Fourier components that have very different wave numbers. This is in opposition to the classical interactions that are 'local', i.e. that result in a convolution of components with similar wavenumbers.

The energy transfer time for non-local interaction can no longer be 'locally' estimated with the help of the usual eddy turn-over-time $\tau(\ell) \approx \ell/\Delta u(\ell)$. This drastically changes the relationship between the energy flux, ε, and the energy co-variance (and spectrum). This explains the failures of the DTMs when using the usual energy flux density proxy based on the third-order structure function, i.e. $\varepsilon(\ell) \approx (\Delta u(\ell))^3/\ell$. It also implies that other proxies, for example, those used in rainfall, radiance, finance and even complex free-atmosphere measurements, will likely have encountered similar problems; problems that might have been over-sighted.

Indeed the goodness of this proxy strongly depends on the approximation $\varepsilon(\ell) \approx (\Delta u(\ell))^2/\tau(\ell)$, i.e. that eddy turn-over-time $\tau(\ell)$ is the effective energy transfer time. This explains why we have invested a great deal of effort into looking for other energy flux proxies (i.e. by modifying the exponent a and the fractional integration order h, see section 4.3), as well as looking to whether or not it is possible to find a relevant generalised scale.

Which (generalised) scale invariance?

In a very general manner Schertzer and Lovejoy [2011], we are looking to characterise the transformation of either a function f (e.g. the velocity field) or a measure μ (e.g. the flux of energy) in response to a (possibly generalised) contraction/dilation T_λ (respectively for $\lambda \geq 1$ and $\lambda \leq 1$) of their definition domain E. The simplest case, corresponds to an isotropic, contraction/dilation, i.e., $\forall x \in E : T_\lambda = x/\lambda$. This could already be generalised to a non-isotropic contraction/dilation, T_λ, by introducing a non-scalar generator $G \neq sI$, where I is the identity matrix and s is a scalar.

$$T_\lambda = \lambda^G \equiv \exp(\log(\lambda)G). \tag{5.12}$$

The change from scalar to non-scalar generators introduces the important question of non-commutativity (i.e. $A \cdot B \neq B \cdot A$), which may have important consequences. The resulting transformation of a function f of a measure μ corresponds respectively to their 'pullback' transform T^*_λ:

$$\forall x : T^*_\lambda(f)(x) = f(T_\lambda x) \tag{5.13}$$

and 'push forward' transform $T_{*\lambda}$:

$$\forall f : \int f T_{*\lambda}(d\mu) = \int T^*_\lambda(f) d\mu. \tag{5.14}$$

The name pullback evokes the fact that this transform acts in the opposite direction ('contravariantly') to that of the original transform T_λ. This general notion is particularly useful when dealing with differential equations Schertzer et al. [2011]. The dual push-forward transform $T_{*\lambda}$ is particularly useful when mathematically dealing with singular measures such as rain accumulation Schertzer et al. [2010]. It is rather easy to check that the (trivial) multiplicative group property of the original transform, T_λ, extends to both the pullback and push-forward transforms, and that both are linear respectively on vector spaces of functions and their dual spaces of measures.

For a non-scalar generator G, T_λ is no longer an isometric contraction/dilation due to the non-commutativity of its generator with that of rotation. There are, however, generalised scales $\|\cdot\|$, that are linear with respect to the contraction parameter $1/\lambda$:

$$\forall x \in E,\, \forall \lambda \in R^+ :\ \|T_\lambda x\| = \|x\|/\lambda, \tag{5.15}$$

and are non-degenerate ($\|x\| = 0 \Rightarrow x = 0$); balls defined by these scales are strictly decreasing with the contraction T_λ. These three properties define a generalised scale associated to a generalised contraction/dilation.

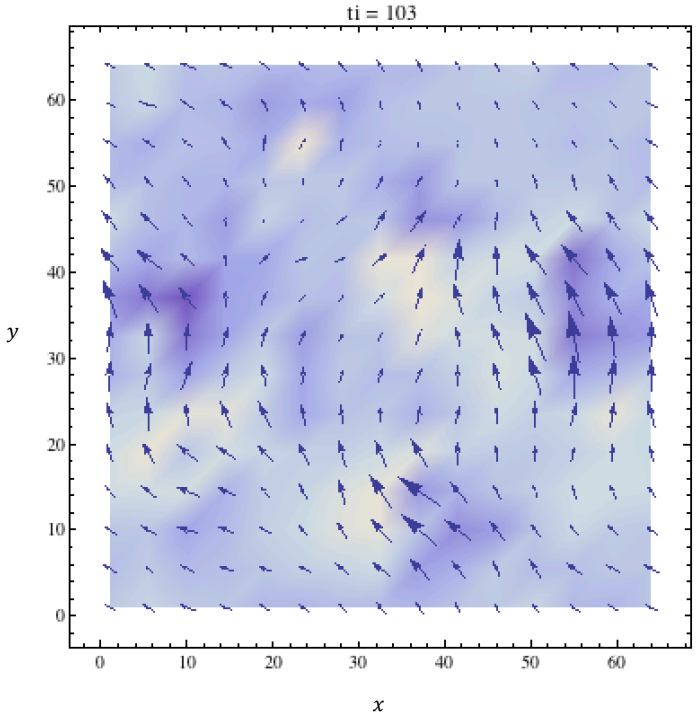

Figure 5.19: A $2D$ cut of a multifractal simulation of a vector field defined over a $2D+1$ domain with a resolution $\lambda = 64$. The coloured background corresponds to the vorticity component perpendicular to the cut.

Not only the simplistic, isotropic scale invariance ($G = I$) is irrelevant for the boundary layer, but also the simplest GSI case, where the generator G (and therefore T_λ) is diagonal, in particular in the usual reference frame (x, y, z, t).

It corresponds to self-similarity – the components scale differently and independently. Indeed, the general description of the surface-layer (section 5.4), as well our previously detailed results show that the space and time components of the velocity field do not scale independently. This is because there is a more complex interrelation between the size and life-time of the structures than previously believed. This result is in agreement with the apparent non-scaling behaviour we observed on time-series and rather again may be opposite to what is observed in the free atmosphere where the life time-scales like the eddy turn-over-time $\tau(\ell) \approx \ell^{2/3}$ over a wide range of scales Schertzer et al. [1997].

Which multifractal modelling?

Multifractal techniques have been rather extensively developed to deal with non-scalar generators (Gs) for scalar valued fields, and more recently progressed to vector valued fields, e.g. to define a multifractal alternative to quasi-geostrophic turbulence Schertzer et al. [2011]. This corresponds to one introducing into the co-domain, i.e. the vector space where the field is valued, a (possibly generalised) contraction/dilation $\tilde{T}_\lambda$. For instance, a multifractal measure μ will then be an invariant measure of the symmetry S_λ[1] resulting from the composition of T_λ and $\tilde{T}_\lambda$:

$$S_\lambda(\mu) = \mu; \;\; S_\lambda = \tilde{T}_\lambda \circ T_{*,\lambda} \tag{5.16}$$

Generally, the invariance involves an equality in distribution (denoted by $\stackrel{d}{=}$). This is precisely the case for the definition of simple scaling given by Lamperti [1962], where:

$$\tilde{T}_\lambda = \lambda^{-H}. \tag{5.17}$$

For multifractals $\tilde{T}_\lambda$ is no longer defined by a unique scaling exponent H, but by a full set of singularities (γs) that correspond to realisations of a given random

[1]The notation, S_λ, for symmetry should not be confused with the DSF used in the previous sections.

generator Γ_λ:

$$\tilde{T_\lambda} \stackrel{d}{=} \lambda^{-\gamma} = \exp(-\Gamma_\lambda). \tag{5.18}$$

To illustrate, figure 5.19 displays an image extracted from a stochastic multifractal simulation of a $2D$-valued vector field defined on a $2D+1$ time-space domain.

Our empirical results point out new challenges for modelling as they show that:

1. at each altitude, there are cross-correlations between the horizontal velocity components,

2. and that there is no translation invariance of the fluctuations along the vertical (e.g. the amplitude of H is very sensitive to the altitude).

None of the above are insurmountable obstacles simply because we remain in the very general framework of Lie cascades Schertzer and Lovejoy [1995], where the one parameter groups of transforms T_λ and $\tilde{T_\lambda}$ result from the exponentiation of their generators. These belong to a given Lie algebra.

Like a Monsieur Jourdain, who, speaking prose all his life, did so without knowing it, we also have been dealing with scalar cascades that are in fact the simplest case Lie cascades. With respect to the two aforementioned properties that we have already (partial answers:

1. We are required to introduce this property into the generator Γ_λ. This is particularly simple when the generator is a multivariate normal field, but, is a bit more tricky for Lévy generators because multivariate Lévy variables are non-parametric. Indeed, the direction dependence is defined by a measure which is nonetheless manageable, although rather demanding (e.g. Schertzer et al. [2001]).

2. Proceeding differentially rather than in an integrated manner, as is usually done for translation invariant multifractal fields, is not as subtle. It requires us to deal with infinitesimal generators g_γ of T_λ and $\tilde{T_\lambda}$ instead of $G\log(\lambda)$ and Γ_λ that correspond to an integration over a given finite resolution λ.

I can only regret that the difficulties faced during the data analysis did not leave me enough time to explore these challenging questions.

5.5 Summary Of Chapter 5

In this section we inter-compare the results from the standard methods of empirical estimation of the UM parameters with a range of newly developed alternative methods: the double structure function (DSF), the $K_h(q)$ function, the five-parameter model and the $f'(q)$ function, that has aided us in the search for stable parameters. Although the results from all of the different techniques are consistent, the most powerful tool and also the most simple is the $f'(q)$ function. The $f'(q)$ function allows one to quickly determine whether the UM framework is applicable. Having said this, with a combination of the DSF and the $f'(q)$ function (α estimated over the full range of q) showed that a rough approximation could be used to reproduce the structure function up to the order $q = 9$. The isolated case where this approximation was the most applicable was the range of scales of the Corsica dataset that was the most isotropic. The corresponding divergence of moments was therefore much larger than that predicted empirically from the probability distributions, $q_D > 9$ rather than 5, thus highlighting the trade-off required in order to fit the standard model.

If we are to fully understand the process we must first understand whether or not we can separate the scaling multifractal process from the non-scaling process (with the linear scaling framework) and if yes how do we quantify each of the two and what are the consequences in terms of extremes if we neglect the non-scaling part. Adding varying degrees of white Gaussian noise at the highest resolutions of the simulated UM data produces the same non-scaling behaviour as observed in the empirical data. We arrived to the conclusion that the aggregation of the flux proxies may amplify the non-scaling contribution and should be considered within the non-linear generalised scaling invariance (GSI) framework.

References: Chapter 5

Y. D. Chashechkin. Hydrodynamics of a sphere in a stratified fluid. *Fluid Dynamics*, 24(1):1–7, 1989. URL http://www.google.fr/search?client=safari&rls=10_7_4&q=Hydrodynamics+of+a+sphere+in+a+stratified+fluid&ie=UTF-8&oe=UTF-8&redir_esc=&ei=2ZznUcubCKi30QWCxYDYAQ.

P. Drobinski, P. Carlotti, R. K. Newsom, R. M. Banta, R. C. Foster, and J. L. Redelsperger. The structure of the near-neutral atmospheric surface layer. *Journal of the atmospheric sciences*, 61(6):699–714, 2004. doi:10.1175/1520-0469(2004)061¡0699:TSOTNA¿2.0.CO;2. URL http://dx.doi.org/10.1175/1520-0469(2004)061<0699:TSOTNA>2.0.CO;2.

A. Gires, I. Tchiguirinskaia, D. Schertzer, and S. Lovejoy. Development and analysis of a simple model to represent the zero rainfall in a universal multifractal framework. *Nonlinear Processes in Geophysics*, 20(3):343–356, 2013. doi:10.5194/npg-20-343-2013. URL http://www.nonlin-processes-geophys.net/20/343/2013/.

B. A. Kader and A. M. Yaglom. Spatial correlation functions of surface-layer atmospheric turbulence in neutral stratification. *Boundary-Layer Meteorol*, pages 1–17, 1989. URL http://www.springerlink.com/index/R23468231254223N.pdf.

A. Kolmogorov. The local structure of turbulence in incompressible viscous fluid for very large Reynolds numbers. In *Dokl. Akad. Nauk SSSR*, pages 9–13, January 1941. URL http://www.google.fr/search?client=safari&rls=10_7_4&q=The+local+structure+of+turbulence+in+incompressible+viscous+

fluid+for+very+large+Reynolds+numbers&ie=UTF-8&oe=UTF-8&redir_esc=&ei=XiiJUOr5CaKI0AXmxoGoDA.

B. N. Korotkov. Kinds of local self-similarity of the velocity field of prewall turbulent flows. *Fluid Dynamics*, 11(6):850–856, 1976. URL http://link.springer.com/article/10.1007/BF01026403.

J. Lamperti. Semi-stable stochastic processes. *Transactions of the American Mathematical Society*, 104(1):62–78, 1962. URL http://www.google.fr/search?client=safari&rls=10_7_4&q=Semi+stable+stochastic+processes&ie=UTF-8&oe=UTF-8&gws_rd=cr&redir_esc=&ei=pkrpUZqiNsW3hAfd04HYBw.

B. B. Mandelbrot. *The fractal geometry of nature*. W. H. Freeman and Co., San Francisco, Calif., 1982. ISBN 0-7167-1186-9. URL http://www.ams.org/mathscinet-getitem?mr=MR665254.

A. Pouquet, U. Frisch, and J. Léorat. Strong MHD helical turbulence and the nonlinear dynamo effect. *Journal of Fluid Mechanics*, 77(321-354):44, 1976. URL http://www.google.fr/search?client=safari&rls=10_7_4&q=Strong+MHD+helical+turbulence+and+the+nonlinear+dynamo+effect&ie=UTF-8&oe=UTF-8&redir_esc=&ei=oJznUeLjN4mX1AWGzICIBg.

D. Schertzer and S. Lovejoy. Generalised scale invariance in turbulent phenomena. *PhysicoChemical Hydrodynamics*, 6:623–635, January 1985. URL http://www.google.fr/search?client=safari&rls=10_7_4&q=Generalised+scale+invariance+in+turbulent+phenomena&ie=UTF-8&oe=UTF-8&redir_esc=&ei=4jSJUMnJA4jIhAfYwoCoCw.

D. Schertzer and S. Lovejoy. From scalar cascades to Lie cascades: joint multifractal analysis of rain and cloud processes. *Space/time variability and interdependence for various hydrological processes, edited by: Feddes, RA, Cambridge University Press*, pages 153–173, 1995. URL http://www.google.fr/search?client=safari&rls=10_7_4&q=From+scalar+cascades+to+Lie+cascades+joint+multifractal+analysis+of+

rain+and+cloud+processes&ie=UTF-8&oe=UTF-8&gws_rd=cr&redir_esc=&ei=mkzpUYBW7d7sBtmigIgB.

D. Schertzer, S. Lovejoy, F. Schmitt, Y. Chigirinskaya, and D. Marsan. Multifractal cascade dynamics and turbulent intermittency. *Fractals*, 5(3):427–471, 1997. doi:10.1142/S0218348X97000371. URL http://dx.doi.org/10.1142/S0218348X97000371.

D. Schertzer, M. Larcheveque, J. Duan, V. V. Yanovsky, and S. Lovejoy. Fractional Fokker–Planck equation for nonlinear stochastic differential equations driven by non-Gaussian Lévy stable noises. *Journal of Mathematical Physics*, 42:200, 2001. URL http://www.google.fr/search?client=safari&rls=10_7_4&q=Fractional+Fokker+Planck+equation+for+nonlinear+stochastic+differential+equations+driven+by+non+Gaussian+Levy+stable+noises&ie=UTF-8&oe=UTF-8&gws_rd=cr&redir_esc=&ei=RU3pUfizIMXb7Ab3l4C4Cw.

D. Schertzer, I. Tchiguirinskaia, S. Lovejoy, and P. Hubert. No monsters, no miracles: in nonlinear sciences hydrology is not an outlier! *Hydrological Sciences Journal–Journal des Sciences Hydrologiques*, 55(6):965–979, 2010. URL http://www.google.fr/search?client=safari&rls=10_7_4&q=No+monsters+no+miracles+in+nonlinear+sciences+hydrology+is+not+an+outlier&ie=UTF-8&oe=UTF-8&gws_rd=cr&redir_esc=&ei=MkLpUZz4Kaby7AaygYGACQ.

D. Schertzer, I. Tchiguirinskaia, S. Lovejoy, and A. Tuck. Quasi-geostrophic turbulence and generalized scale invariance, a theoretical reply. *Atmos. Chem. Phys. Discuss*, 11(1):3301–3320, 2011. doi:10.5194/acpd-11-3301-2011. URL http://www.google.fr/search?client=safari&rls=10_7_4&q=Quasi+geostrophic+turbulence+and+generalized+scale+invariance+a+theoretical+reply&ie=UTF-8&oe=UTF-8&redir_esc=&ei=Ru6HUIyfEanA0QWG1YCwBQ.

D. Schertzer and S. Lovejoy. Multifractals en Turbulence et Gèophysique. *Irruption des Géométries Fractales dans la Sciences. G. Belaubre and F.*

Begon. Paris, Académie Européeene Interdisciplinaire des Sciences, pages 189–209, 2006. URL http://www.google.fr/search?client=safari&rls=10_7_4&q=Multifractals+en+Turbulence+et+Geophysique&ie=UTF-8&oe=UTF-8&gws_rd=cr&redir_esc=&ei=Xy3pUcrBLsa5hAfWoIGQAg.

D. Schertzer and S. Lovejoy. Multifractals, Generalized Scale Invariance And Complexity In Geophysics. *Int. J. Bifurcation Chaos*, 21(12):3417–3456, December 2011. doi:10.1142/S0218127411030647. URL http://www.physics.mcgill.ca/~gang/eprints/eprintLovejoy/neweprint/IJBC.2012.S0218127411030647.pdf.

L. I. Sedov. Methods of similitude and dimensionality in mechanics. 1972.

A. M. Yaglom. Similarity laws for wall turbulent flows: their limitations and generalizations. In *New Approaches and Concepts in Turbulence*, pages 7–27. Springer, 1993. ISBN 3764329246. URL http://www.google.fr/search?client=safari&rls=10_7_4&q=Similarity+laws+for+wall+turbulent+flows+their+limitations+and+generalizations&ie=UTF-8&oe=UTF-8&gws_rd=cr&redir_esc=&ei=fmrpUdr5BoiChQeM4oHgCQ.

Conclusions

Our goal from the start has been to reduce uncertainties in wind resource assessment. We claim that, based on the state of art in wind energy, poor approximations to the high-number of degrees of freedom that arise in a bounded, turbulent, atmosphere are the main cause of uncertainty. Numerical attempts to model these complex and highly non-linear processes typically require a truncation of scales and more often than not complex parameterisations. We argue that due to the symmetries of the governing equations of fluid motion for a high-Reynolds number flow, the statistics of the wind are scaling and multifractal. It is therefore unnecessary to truncate the scales of the process.

Our results confirm that the atmospheric surface-layer *is scaling* and *is multifractal*, however, they also show that this scaling and multifractality are not only strongly anisotropic, a feature that already requires the framework of (linear) generalised scale invariance,(GSI), but there is a strong lack of translation invariance that requires *non-linear* GSI.

We have developed several new techniques to estimate the *multifractality index* α, in particular to take care of the extremes present in a sample that easily introduce statistical biases in classical estimation methods, such as the trace-Moments (TM) and Double Trace Moments (DTM). Let us recall that this index α has several important properties: it measures the multifractality our field: $\alpha = 0$ corresponds to a mono-fractal field, whose intermittency is independent of the considered activity of the field, i.e. the extremes are not that much different from the mean. Its maximal value $\alpha = 2$ corresponds to the misnamed 'log-normal' cascade model, whose extremes are much larger than those of a log-normal distribution. It also characterises the generator of the cascade process;

more precisely it corresponds to the Lévy stable index of the generator in the framework of universal multifractals (UM).

We believe that it is particularly significant that we constantly estimate this multifractality index $\alpha \approx 1.4$. This not only confirms a significant multifractality, but also confirms that, despite the complexity of the surface-layer, a given universality of the generator of the cascade exists. Furthermore, this generator is significantly different from a normal generator, i.e. the log-normal model is not applicable. We found that the estimates of two other fundamental scaling exponents were much less stable and difficult to obtain although their interpretations are much simpler. Indeed, they are only fractal exponents (contrary to α) – the scaling exponent H of the mean field ($H = 0$ for a strictly scale invariant mean field) and the co-dimension C_1 of its support that measures the mean intermittency ($C_1 = 0$ for a homogeneous field). This difficulty, surprising at first glance, is rather typical of non-linear GSI.

We developed several methods to better estimate the parameters – in particular making detailed studies of the sensitivity of parameter estimation methods to instrumental noises: structure functions (SF), TMs and DTMs. This led us to introduce a hybrid method somewhere between the SF and the DTM method; the double structure function (DSF), that rather combines both of the other methods advantages for large statistics. Developments in the structure function led to analyses based on the q-normalised method: $f(q) = \zeta(q)/q$, where $\zeta(q)$ is the scaling exponent of the structure function.

We also highlight several important features:

- The scaling anisotropy of the samples: to avoid shadow effects from masts, we are compelled to deal with samples whose 'mean' velocity is near-perpendicular to the masts. The anisotropy of these samples turns out to be beyond a trivial component-wise anisotropy corresponding to prefactors depending on the direction, i.e., the scaling exponents themselves (in particular H) depend on the direction.

- We derive an analytical expression for the direction dependence of H and plot the corresponding 'potatoid' shapes of the isolines of the exponent

values. The expression is based on the cross-correlation between orthogonal components of the singularities.

- We show that this scaling anisotropy has important consequences for first-order multifractal phase transitions; it decreases the critical order q_D (the analog of the inverse of a critical temperature) at which the transitions occur. This decrease is so significant that these transitions may occur on a unique sample whereas usually they are expected only a very large number of samples since they correspond to a divergence of moments for an infinite number of samples.

- Not taking care of these phase transitions leads to spurious estimates of the multifractal exponent α.

- The lack of translation invariance of the fluctuations along the vertical space axis forces us to deal with non-linear GSI as opposed to simple GSI in order to avoid inconsistencies.

As briefly discussed in the last section we believe that these features must not only to be taken into account to develop adequate modelling but, are manageable in the framework on non-linear GSI.

The aim of this thesis has not been to show whether a deterministic or statistical approach is better. Its aim, although changing, has finally been to clarify what needs to be done next and with which tools. By very carefully applying a range of statistical methods we have shown that turbulence is far more complex than its face value shows. Nonetheless, it is multifractal and scaling, although only in a non-linear and generalised manner. We pointed out how to go from multifractal analysis to a multifractal surface-to-boundary-layer model. A model like this would provide not only very accurate energy predictions but also meaningful nowcasts. This is an exciting concept as it will not only drive competitiveness in the market but also give wind energy the ability to dominate the energy market.

Bibliography

R. Baïle. *Analyse et modélisation multifractales de vitesses de vent. Application à la prévision de la ressource éolienne.* PhD thesis, Université Pascal Paoli, 2010. URL http://tel.archives-ouvertes.fr/tel-00604139/.

M. Barnsley. *Fractals everywhere.* Academic Press Inc., Boston, MA, 1988. ISBN 0-12-079062-9. URL http://www.ams.org/mathscinet-getitem?mr=MR977274.

R. Benzi, G. Paladin, G. Parisi, and A. Vulpiani. On the multifractal nature of fully developed turbulence and chaotic systems. *Journal of Physics A: Mathematical and General*, 17(18):3521, 1984. URL http://www.google.fr/search?client=safari&rls=10_7_4&q=On+the+multifractal+nature+of+fully+developed+turbulence+and+chaotic+systems&ie=UTF-8&oe=UTF-8&redir_esc=&ei=urbnUduNCMO7O8rXgcAC.

P. Bernardara, D. Schertzer, E. Sauquet, I. Tchiguirinskaia, and M. Lang. The flood probability distribution tail: how heavy is it? *Stochastic Environmental Research and Risk Assessment*, 22(1):107–122, 2008. URL http://link.springer.com/article/10.1007/s00477-006-0101-2.

N. Bleistein and R. A. Handelsman. Asymptotic Expansions of Integrals. 1986.

R. Bolgiano Jr. Turbulent spectra in a stably stratified atmosphere. *J. Geophys. Res.*, 64(12):2226–2229, January 1959. URL http://www.google.fr/search?client=safari&rls=10_7_4&q=Turbulent+spectra+in+a+stably+stratified+atmosphere&ie=UTF-8&oe=UTF-8&redir_esc=&ei=qiyJUP_kK4HL0QWil4CgBQ.

T. Burton, D. Sharpe, and N. Jenkins. *Wind energy*. John Wiley&Sons, 2001. URL https://cdp.pageplace.de/cdp/public/publications/DT0154/9781119992721/PREVIEW/9781119992721_preview.pdf.

N. Busch and L. Kristensen. Cup anemometer overspeeding. *Journal of Applied Meteorology*, 15:1328–1332, 1976. URL http://www.google.fr/search?client=safari&rls=en-us&q=Cup+anemometer+overspeeding&ie=UTF-8&oe=UTF-8&redir_esc=&ei=ZHUiUPe5BqaW0QWFkYCYDQ.

L. P. Chamorro and F. Porté-Agel. Effects of Thermal Stability and Incoming Boundary-Layer Flow Characteristics on Wind-Turbine Wakes: A Wind-Tunnel Study. *Boundary-Layer Meteorol*, 136(3):515–533, June 2010. doi:10.1007/s10546-010-9512-1. URL http://www.springerlink.com/index/10.1007/s10546-010-9512-1.

F. H. Champagne. The fine-scale structure of the turbulent velocity field. *Journal of Fluid Mechanics*, 86(1):67–108, 1978.

Y. D. Chashechkin. Hydrodynamics of a sphere in a stratified fluid. *Fluid Dynamics*, 24(1):1–7, 1989. URL http://www.google.fr/search?client=safari&rls=10_7_4&q=Hydrodynamics+of+a+sphere+in+a+stratified+fluid&ie=UTF-8&oe=UTF-8&redir_esc=&ei=2ZznUcubCKi30QWCxYDYAQ.

Y. Chigirinskaya, D. Schertzer, S. Lovejoy, A. Lazarev, and A. Ordanovich. Unified multifractal atmospheric dynamics tested in the tropics: part I, horizontal scaling and self criticality. *Nonlinear Processes in Geophysics*, 1(2):105–114, January 1994. URL http://adsabs.harvard.edu/cgi-bin/nph-data_query?bibcode=1994NPGeo...1..105C&link_type=ABSTRACT.

Y. Chigirinskaya, D. Schertzer, and S. Lovejoy. An alternative to shell-models: More complete and yet simple models of intermittency. pages 263–266, 1998. URL http://link.springer.com/chapter/10.1007/978-94-011-5118-4_65.

A. Clauset, C. R. Shalizi, and M. E. Newman. Power-law distributions in empirical data. *SIAM review*, 51(4):661–703, 2009. URL

http://www.google.fr/search?client=safari&rls=10_7_4&q=Power+law+distributions+in+empirical+data&ie=UTF-8&oe=UTF-8&redir_esc=&ei=xIt_UcHBD4KIhQeS8oHgCw.

P. A. Davidson, Y. Kaneda, K. Moffatt, and K. R. Sreenivasan. A voyage through turbulence. 2011. doi:10.1017/CBO9781139018241. URL http://books.google.com/books?hl=en&lr=&id=04QIthkkPf0C&oi=fnd&pg=PR11&dq=a+voyage+through+turbulence&ots=Jc7udrSjYE&sig=67Q8bJJrZcm7G0Y-6oEBP6eA0xI.

P. Drobinski, P. Carlotti, R. K. Newsom, R. M. Banta, R. C. Foster, and J. L. Redelsperger. The structure of the near-neutral atmospheric surface layer. *Journal of the atmospheric sciences*, 61(6):699–714, 2004. doi:10.1175/1520-0469(2004)061¡0699:TSOTNA¿2.0.CO;2. URL http://dx.doi.org/10.1175/1520-0469(2004)061<0699:TSOTNA>2.0.CO;2.

K. J. Falconer. *The geometry of fractal sets*, volume 85 of *Cambridge Tracts in Mathematics*. Cambridge University Press, Cambridge, 1986. ISBN 0-521-25694-1; 0-521-33705-4. URL http://www.ams.org/mathscinet-getitem?mr=MR867284.

J. Feder and P. Bak. Fractals. *Physics Today*, 42:90, 1989.

W. Feller. *An introduction to probability theory and its applications. Vol. II.* Second edition. John Wiley & Sons Inc., New York, 1971. URL http://www.ams.org/mathscinet-getitem?mr=MR0270403.

G. Fitton, I. Tchiguirinskaia, D. Schertzer, and S. Lovejoy. Multifractal Statistical Methods And Space-Time Scaling Laws For Turbulent Winds (submitted). In *Euromech 2012*, a.

G. Fitton, I. Tchiguirinskaia, D. Schertzer, and S. Lovejoy. The Anisotropic Multifractal Model and Wind Turbine Wakes. *7th PhD Seminar on Wind Energy in Europe*, pages 115–118, 2011a. URL http://hal.archives-ouvertes.fr/hal-00696108/.

G. Fitton, I. Tchiguirinskaia, D. Schertzer, and S. Lovejoy. Scaling Of Turbulence In The Atmospheric Surface-Layer: Which Anisotropy? *Journal of Physics: Conference Series*, 318(7):072008, January 2011b. doi:10.1088/1742-6596/318/7/072008. URL http://www.google.fr/search?client=safari&rls=en-us&q=Scaling+Of+Turbulence+In+The+Atmospheric+Surface+Layer+Which+Anisotropy&ie=UTF-8&oe=UTF-8&redir_esc=&ei=b5hUT8DlGsOF8gO5kJTwBQ.

G. Fitton, I. Tchiguirinskaia, D. Schertzer, and S. Lovejoy. Torque Fluctuations In The Framework Of A Multifractal 23/9-Dimensional Turbulence Model. In *EUROMECH Colloquium 528*, 2012. URL http://www.google.fr/search?client=safari&rls=10_7_4&q=Torque+Fluctuations+In+The+Framework+Of+A+Multifractal+23+9+Dimensional+Turbulence+Model&ie=UTF-8&oe=UTF-8&gws_rd=cr&ei=WWI4UqfLIIeN7Qbao4DQCQ.

G. F. Fitton. Multifractal Analysis And Simulation Of Wind Energy Fluctuations. URL http://www.google.fr/search?client=safari&rls=10_7_4&q=MULTIFRACTAL+ANALYSIS+AND+SIMULATION+OF+WIND+ENERGY+FLUCTUATIONS&ie=UTF-8&oe=UTF-8&gws_rd=cr&ei=o2E4UuuUHtSN7Abi8IH4DQ.

G. F. Fitton, I. Tchiguirinskaia, D. Schertzer, and S. Lovejoy. Scaling Anisotropy And Extremes In The Wake Of A Turbine (submitted). In *21eme Congres Francais de Mecanique: Journal of Mechanics and Industry*, b.

S. T. Frandsen. Turbulence and turbulence-generated structural loading in wind turbine clusters, 1994. URL http://www.google.fr/search?client=safari&rls=10_7_4&q=Turbulence+and+turbulence+generated+structural+loading+in+wind+turbine+clusters&ie=UTF-8&oe=UTF-8&redir_esc=&ei=fiOJUeL9LNOa0AXB24CYDQ.

I. Fredholm. Sur une classe d'équations fonctionnelles. *Acta Mathematica*, 27(1):365–390, 1903. URL http://www.springerlink.com/index/c41371137837p252.pdf.

U. Frisch. Fully developed turbulence and intermittency. *Annals of the New York Academy of Sciences*, 357(1):359–367, 1980. URL http://onlinelibrary.wiley.com/doi/10.1111/j.1749-6632.1980.tb29703.x/abstract.

U. Frisch, P. Sulem, and M. Nelkin. A simple dynamical model of intermittent fully developed turbulence. *Journal of Fluid Mechanics*, 87(04): 719–736, January 1978. URL http://www.google.fr/search?client=safari&rls=10_7_4&q=A+simple+dynamical+model+of+intermittent+fully+developed+turbulence&ie=UTF-8&oe=UTF-8&redir_esc=&ei=E9eHUK2mMeSp0QWJnIDYBA.

K. Fuchs. *Multifractal Analysis of the wind in the wind park ERSA*. PhD thesis, Carl von Ossietzky Universitat Oldenburg, 2008.

C. Garrett and W. Munk. Oceanic mixing by breaking internal waves. In *Deep Sea Research and Oceanographic Abstracts*, pages 823–832. Elsevier, 1972. URL http://www.google.fr/search?client=safari&rls=10_7_4&q=Oceanic+mixing+by+breaking+internal+waves&ie=UTF-8&oe=UTF-8&gws_rd=cr&ei=jUErUoquO6en0wWFzYCIBg.

A. Gires, I. Tchiguirinskaia, D. Schertzer, and S. Lovejoy. A toy model to deal with zero rainfall in a Universal Multifractal framework. In *EGU General Assembly Conference Abstracts*, page 13292, 2012.

A. Gires, I. Tchiguirinskaia, D. Schertzer, and S. Lovejoy. Development and analysis of a simple model to represent the zero rainfall in a universal multifractal framework. *Nonlinear Processes in Geophysics*, 20(3):343–356, 2013. doi:10.5194/npg-20-343-2013. URL http://www.nonlin-processes-geophys.net/20/343/2013/.

S. Gsänger. World Wind Energy Report 2010, in. *World Wind Energy Association*, 2010. URL http://scholar.google.com/scholar?q=related:ubi-3xEiyMQJ:scholar.google.com/&hl=en&num=20&as_sdt=0,5&as_ylo=2010&as_yhi=2010.

H. Günther and B. Hennemuth. Erste Aufbereitung von flächenhaften Windmessdaten in Höhen bis 150m. *Deutscher Wetter Dienst, BMBF-Projekt A*, 329372: 1998, 1988.

A. S. Gurvich and A. M. Yaglom. Breakdown of eddies and probability distributions for smallscale turbulence. *Phys. Fluids*, 10:S59, 1967a.

A. Gurvich and A. Yaglom. Breakdown of eddies and probability distributions for small-scale turbulence. *Phys. Fluids*, 10:S59, January 1967b. URL http://www.google.fr/search?client=safari&rls=10_7_4&q=Breakdown+of+eddies+and+probability+distributions+for+small+scale+turbulence&ie=UTF-8&oe=UTF-8&redir_esc=&ei=HzKJUI6hLZOQhQes7ICwAg.

F. Hausdorff. Dimension und äußeres Maß. *Mathematische Annalen*, 79 (1-2):157–179, 1918. URL http://link.springer.com/article/10.1007/BF01457179.

J. R. Herring, J. P. Chollet, G. R. Newman, M. Lesieur, D. Schertzer, and M. Larcheveque. Comparative assessment of spectral closures as applied to passive scalar diffusion. *Journal of Fluid Mechanics*, 124(235):411–437, 1982. URL http://journals.cambridge.org/production/action/cjoGetFulltext?fulltextid=390001.

C. T. Hoang. Prise en compte des fluctuations spatio-temporelles pluies-débits pour une meilleure gestion de la ressource en eau et une meilleure évaluation des risques. 2011. URL http://www.google.fr/search?client=safari&rls=10_7_4&q=Prise+en+compte+des+fluctuations+spatio+temporelles+pluies+debits+pour+une+meilleure+gestion+de+la+ressource+en+eau+et+une+meilleure+evaluation+des+risques&ie=UTF-8&oe=UTF-8&redir_esc=&ei=LnyfUeLyB_KY1AWltoG4CQ.

H. Holmes. WAUDIT Guidance Report - WP6 Deliverable D24. *Public*, pages 1–30, October 2011. URL http://www.waudit-itn.eu/newsAndEventsDetail.php?idn=47.

S. J. Hovde, A. F. Tuck, S. Lovejoy, and D. Schertzer. Vertical scaling of temperature, wind and humidity fluctuations: dropsondes from 13 km to the surface of the Pacific Ocean. *International Journal of Remote Sensing*, 32(20):5891–5918, October 2011. doi:10.1080/01431161.2011.602652. URL http://www.tandfonline.com/doi/abs/10.1080/01431161.2011.602652.

T. Ishihara, T. Gotoh, and Y. Kaneda. Study of high-Reynolds number isotropic turbulence by direct numerical simulation. *Annual review of fluid mechanics*, 41:165–180, 2009. URL http://www.google.fr/search?client=safari&rls=10_7_4&q=Study+of+high+Reynolds+number+isotropic+turbulence+by+direct+numerical+simulation&ie=UTF-8&oe=UTF-8&gws_rd=cr&ei=0sspUuKpDfDb7Aa65YGYCw.

B. A. Kader and A. M. Yaglom. Spatial correlation functions of surface-layer atmospheric turbulence in neutral stratification. *Boundary-Layer Meteorol*, pages 1–17, 1989. URL http://www.springerlink.com/index/R234682312542223N.pdf.

A. Kolmogorov. The local structure of turbulence in incompressible viscous fluid for very large Reynolds numbers. In *Dokl. Akad. Nauk SSSR*, pages 9–13, January 1941a. URL http://www.google.fr/search?client=safari&rls=10_7_4&q=The+local+structure+of+turbulence+in+incompressible+viscous+fluid+for+very+large+Reynolds+numbers&ie=UTF-8&oe=UTF-8&redir_esc=&ei=XiiJUOr5CaKI0AXmxoGoDA.

A. Kolmogorov. Dissipation of energy in the locally isotropic turbulence. reprinted 1991. In *Proc R Soc Lond A*, pages 15–17, January 1941b.

A. Kolmogorov. A refinement of previous hypothesis concerning the local structure of turbulence in a viscous incompressible fluid at high Reynolds number. *J. Fluid Mech*, 13:S2, 1962. URL http://scholar.google.com/scholar?q=related:TrvmATypJ4gJ:scholar.google.com/&hl=en&num=30&as_sdt=0,5.

B. M. Koprov, V. M. Koprov, V. M. Ponomarev, and O. G. Chkhetiani. Experimental studies of turbulent helicity and its spectrum in the atmospheric bound-

ary layer. *Dokl. Phys.*, 50(8):419–422, August 2005. doi:10.1134/1.2039983. URL http://link.springer.com/10.1134/1.2039983.

F. Körber, G. Besel, and H. Reinhold. *Meßprogramm an der 3 MW-Windkraftanlage GROWIAN: Förderkennzeichen 03E-4512-A*. Große Windenergieanlage Bau-u. Betriebsges., 1988.

B. N. Korotkov. Kinds of local self-similarity of the velocity field of prewall turbulent flows. *Fluid Dynamics*, 11(6):850–856, 1976. URL http://link.springer.com/article/10.1007/BF01026403.

L. Kristensen. *Cups, props and vanes*. Risø National Laboratory, August 1994. URL http://orbit.dtu.dk/fedora/objects/orbit:87767/datastreams/file_7767071/content.

J. Lamperti. Semi-stable stochastic processes. *Transactions of the American Mathematical Society*, 104(1):62–78, 1962. URL http://www.google.fr/search?client=safari&rls=10_7_4&q=Semi+stable+stochastic+processes&ie=UTF-8&oe=UTF-8&gws_rd=cr&redir_esc=&ei=pkrpUZqiNsW3hAfd04HYBw.

L. Laporte, É. Dupont, B. Carissimo, L. Musson-Genon, and C. Sécolier. Atmospheric CFD simulations coupled to mesoscale analyses for wind resource assessment in complex terrain. In *Proceedings of the European wind energy conference, Marseille, France*, 2009. URL http://www.google.fr/search?client=safari&rls=10_7_4&q=Atmospheric+CFD+simulations+coupled+to+mesoscale+analyses+for+wind+resource+assessment+in+complex+terrain&ie=UTF-8&oe=UTF-8&redir_esc=&ei=BHF-Ue3hNdHB7AaH3ICQAg.

J. P. Laval, J. McWilliams, and B. Dubrulle. Forced stratified turbulence: Successive transitions with Reynolds number. *Phys. Rev. E*, 68(3):036308, September 2003. doi:10.1103/PhysRevE.68.036308. URL http://link.aps.org/doi/10.1103/PhysRevE.68.036308.

D. Lavallée. *Multifractal techniques: analysis and simulation of turbulent fields*. PhD thesis, McGill University at Montréal, 1991. URL

http://scholar.google.com/scholar?q=related:VAofCH6iUAUJ:scholar.google.com/&hl=en&num=20&as_sdt=0,5.

A. Lazarev, D. Schertzer, S. Lovejoy, and Y. Chigirinskaya. Unified multifractal atmospheric dynamics tested in the tropics: part II, vertical scaling and generalized scale invariance. *Nonlinear Processes in Geophysics*, 1(2):115–123, January 1994. URL http://adsabs.harvard.edu/cgi-bin/nph-data_query?bibcode=1994NPGeo...1..115L&link_type=ABSTRACT.

Y. Levi, E. Shilo, and I. Setter. Climatology of a summer coastal boundary layer with 1290-MHz wind profiler radar and a WRF simulation. *Journal of Applied Meteorology and Climatology*, 50(9):1815–1826, 2011. URL http://www.google.fr/search?client=safari&rls=10_7_4&q=Climatology+of+a+summer+coastal+boundary+layer+with+1290+MHz+wind+profiler+radar+and+a+WRF+simulation&ie=UTF-8&oe=UTF-8&redir_esc=&ei=5beDUZqrIaSh7AbOjoHgCw.

M. Lilley, S. Lovejoy, K. Strawbridge, and D. Schertzer. 23/9 dimensional anisotropic scaling of passive admixtures using lidar aerosol data. *Phys. Rev. E*, 70(3):036307, January 2004. URL http://www.google.fr/search?client=safari&rls=10_7_4&q=23+9+dimensional+anisotropic+scaling+of+passive+admixtures+using+lidar+aerosol+data&ie=UTF-8&oe=UTF-8&redir_esc=&ei=8ymJUInPBsqb0QWLzYGgBQ.

S. Lovejoy and D. Schertzer. Scale invariance, symmetries, fractals, and stochastic simulations of atmospheric phenomena. *Bulletin of the American meteorological society*, 67(1):21–32, 1986. URL http://www.google.fr/search?client=safari&rls=10_7_4&q=Scale+invariance+symmetries+fractals+and+stochastic+simulations+of+atmospheric+phenomena&ie=UTF-8&oe=UTF-8&redir_esc=&ei=YW8aUZXIF8uS0QWN6YGoBA.

S. Lovejoy and D. Schertzer. Scale, scaling and multifractals in geophysics: twenty years on. *Nonlinear dynamics in geosciences*, pages 311–337, January 2007. URL http://www.google.fr/search?client=safari&rls=10_7_4&q=Scale+scaling+and+multifractals+in+geophysics+twenty+years+on&ie=UTF-8&oe=UTF-8&redir_esc=&ei=xCqJUOj-MMOj0QWi-oCgBQ.

S. Lovejoy, D. Schertzer, M. Lilley, K. B. Strawbridge, and A. Radkevich. Scaling turbulent atmospheric stratification. I: Turbulence and waves. *Q.J.R. Meteorol. Soc.*, 134(631):277–300, 2008. doi:10.1002/qj.201. URL http://doi.wiley.com/10.1002/qj.201.

S. Lovejoy, A. F. Tuck, S. J. Hovde, and D. Schertzer. Vertical cascade structure of the atmosphere and multifractal dropsonde outages. *Journal of Geophysical Research: Atmospheres (1984–2012)*, 114(D7), 2009. doi:10.1029/2008JD010651. URL http://onlinelibrary.wiley.com/doi/10.1029/2008JD010651/full.

S. Lovejoy and D. Schertzer. *The weather and Climate: emergent laws and multifractal cascades*. Cambridge University Press, 2013a.

S. Lovejoy and D. Schertzer. The climate is not what you expect. *Bull. Amer. Meteor. Soc*, 2013b.

P. Lynch. *The emergence of numerical weather prediction: Richardson's dream*. Cambridge University Press, 2006.

B. Mandelbrot. How long is the coast of Britain? Statistical self-similarity and fractional dimension. *Science*, 156(3775):636, January 1967. URL http://www.google.fr/search?client=safari&rls=10_7_4&q=How+long+is+the+coast+of+Britain+Statistical+self+similarity+and+fractional+dimension&ie=UTF-8&oe=UTF-8&redir_esc=&ei=-SqJUO2EJcHS0QXl8IHYAw.

B. Mandelbrot. Fractals, Chance and Dimension. 1977.

B. B. Mandelbrot. Intermittent turbulence in self-similar cascades- Divergence of high moments and dimension of the carrier. *Journal of Fluid Mechanics*, 62(2):331–358, 1974. doi:10.1017/S0022112074000711. URL http://journals.cambridge.org/production/action/cjoGetFulltext?fulltextid=385759.

B. B. Mandelbrot. *The fractal geometry of nature*. W. H. Freeman and Co., San Francisco, Calif., 1982. ISBN 0-7167-1186-9. URL http://www.ams.org/mathscinet-getitem?mr=MR665254.

I. Marusic, B. J. McKeon, P. A. Monkewitz, H. M. Nagib, A. J. Smits, and K. R. Sreenivasan. Wall-bounded turbulent flows at high Reynolds numbers: Recent advances and key issues. *Phys. Fluids*, 22(6):065103, 2010. doi:10.1063/1.3453711. URL http://link.aip.org/link/PHFLE6/v22/i6/p065103/s1&Agg=doi.

C. Meneveau and K. R. Sreenivasan. Simple multifractal cascade model for fully developed turbulence. *Physical review letters*, 59(13):1424, 1987. URL http://www.google.fr/search?client=safari&rls=10_7_4&q=Simple+multifractal+cascade+model+for+fully+developed+turbulence&ie=UTF-8&oe=UTF-8&redir_esc=&ei=-7bnUaWRIIHMPYH3gLAB.

A. Monin and A. M. Yaglom. Statistical Fluid Mechanics: Mechanics of Turbulence, vol. 2, 874 pp. 1975.

T. Mücke, D. Kleinhans, and J. Peinke. Atmospheric turbulence and its influence on the alternating loads on wind turbines. *Wind Energ.*, 14(2):301–316, March 2011. doi:10.1002/we.422. URL http://onlinelibrary.wiley.com/doi/10.1002/we.422/full.

E. A. Novikov and R. W. Stewart. The intermittency of turbulence and the spectrum of energy dissipation fluctuations. *Izv. Geophys. Ser*, 3:408–413, 1964.

A. Obukhov. Effect of Archimedean forces on the structure of the temperature field in a turbulent flow. In *Dokl. Akad. Nauk SSSR*, page 1246, 1959.

A. Obukhov. Some specific features of atmospheric turbulence. *J. Geophys. Res.*, 67(8):3011–3014, 1962.

G. Parisi and U. Frisch. On the singularity structure of fully developed turbulence. *Turbulence and predictability in geophysical fluid dynamics*, pages 84–87, 1985.

J. Peinke, P. Schaumann, and S. Barth. *Wind energy: proceedings of the euromech colloquium*. Springer, 2006.

J. Pinel, S. Lovejoy, and D. Schertzer. The horizontal space-time scaling and cascade structure of the atmosphere and satellite radiances. *Atmos. Res.(submitted)*, 2013. URL http://www.physics.mcgill.ca/~gang/eprints/eprintLovejoy/neweprint/AtmosRes_15.2.13.final.pdf.

A. Pouquet, U. Frisch, and J. Léorat. Strong MHD helical turbulence and the nonlinear dynamo effect. *Journal of Fluid Mechanics*, 77(321-354): 44, 1976. URL http://www.google.fr/search?client=safari&rls=10_7_4&q=Strong+MHD+helical+turbulence+and+the+nonlinear+dynamo+effect&ie=UTF-8&oe=UTF-8&redir_esc=&ei=oJznUeLjN4mX1AWGzICIBg.

L. F. Richardson. Weather prediction by numerical process. 2007. URL http://books.google.com/books?hl=en&lr=&id=D52d3_bbgg8C&oi=fnd&pg=PA3&dq=weather+prediction+by+numerical+process&ots=6_OwhW5IZp&sig=_iwiOtMACeMce0k_Ixrd7aIjJ0E.

J. S. Rodrigo. State-of-the-Art of Wind Resource Assessment. *N/A*, pages 1–25, January 2011. URL http://www.waudit-itn.eu/download.php?id=103&parent=79.

D. Schertzer. Physical modeling and analysis of rain and clouds by anisotropic scaling multiplicative processes. *J. Geophys. Res.*, January 1987. URL http://www.physics.mcgill.ca/~gang/eprints/eprintLovejoy/neweprint/JGR.SL.1987.good.pdf.

D. Schertzer and S. Lovejoy. Elliptical turbulence in the atmosphere. In *Symposium on Turbulent Shear Flows, 4 th, Karlsruhe, West Germany*, page 11, January 1984a. URL http://www.google.fr/search?client=safari&rls=10_7_4&q=Elliptical+turbulence+in+the+atmosphere&ie=UTF-8&oe=UTF-8&redir_esc=&ei=4jSJUNnnA4-GhQe62YGQBg.

D. Schertzer and S. Lovejoy. On the dimension of atmospheric motions. *Turbulence and Chaotic phenomena in Fluids*, pages 505–512, 1984b. URL http://scholar.google.com/scholar?q=related:JvT9pIKaPsgJ:scholar.google.com/&hl=en&num=20&as_sdt=0,5&as_ylo=1983&as_yhi=1983.

D. Schertzer and S. Lovejoy. Generalised scale invariance in turbulent phenomena. *PhysicoChemical Hydrodynamics*, 6:623–635, January 1985a. URL http://www.google.fr/search?client=safari&rls=10_7_4&q=Generalised+scale+invariance+in+turbulent+phenomena&ie=UTF-8&oe=UTF-8&redir_esc=&ei=4jSJUMnJA4jIhAfYwoCoCw.

D. Schertzer and S. Lovejoy. The dimension and intermittency of atmospheric dynamics. *Turbulent shear flow*, 4(7):7–33, January 1985b. URL http://www.google.fr/search?client=safari&rls=10_7_4&q=The+dimension+and+intermittency+of+atmospheric+dynamics&ie=UTF-8&oe=UTF-8&redir_esc=&ei=4jSJUOzlA4exhAfks4HwAQ.

D. Schertzer and S. Lovejoy. Scaling nonlinear variability in geodynamics: multiple singularities, observables and universality classes. *Nonlinear Variability and Geophysics: Scaling and Fractals. Kluwer, Dordrecht*, pages 41–92, 1991.

D. Schertzer and S. Lovejoy. Hard and soft multifractal processes. *Physica A: Statistical Mechanics and its Applications*, 185(1-4):187–194, January 1992. URL http://www.google.fr/search?client=safari&rls=10_7_4&q=Hard+and+soft+multifractal+processes&ie=UTF-8&oe=UTF-8&redir_esc=&ei=zTSJUOHNF86RhQe9wYG4CQ.

D. Schertzer and S. Lovejoy. Multifractal Generation of Self-Organized Criticality. *Fractals In the natural and applied ...*, 1993. URL http://www.physics.mcgill.ca/~gang/eprints/eprintLovejoy/neweprint/Novak.all.pdf.

D. Schertzer and S. Lovejoy. EGS Richardson AGU Chapman NVAG3 Conference: Nonlinear variability in geophysics: scaling and multifractal processes. *Nonlinear Processes in Geophysics*, 1(2/3):77–79, 1994.

D. Schertzer and S. Lovejoy. From scalar cascades to Lie cascades: joint multifractal analysis of rain and cloud processes. *Space/time variability and interdependence for various hydrological processes, edited by: Feddes, RA, Cambridge University Press*, pages 153–173, 1995. URL http://www.google.fr/search?client=safari&rls=10_7_4&q=From+scalar+cascades+to+Lie+cascades+joint+multifractal+analysis+of+

rain+and+cloud+processes&ie=UTF-8&oe=UTF-8&gws_rd=cr&redir_esc=&ei=mkzpUYBW7d7sBtmigIgB.

D. Schertzer, S. Lovejoy, and D. Lavallée. Generic multifractal phase transitions and self-organized criticality. *Cellular Automata: prospects in ...*, 1993. URL http://132.206.6.11/~gang/eprints/eprintLovejoy/neweprint/Schert93.all.pdf.

D. Schertzer, S. Lovejoy, F. Schmitt, Y. Chigirinskaya, and D. Marsan. Multifractal cascade dynamics and turbulent intermittency. *Fractals*, 5(3):427–471, 1997. doi:10.1142/S0218348X97000371. URL http://dx.doi.org/10.1142/S0218348X97000371.

D. Schertzer, M. Larcheveque, J. Duan, V. V. Yanovsky, and S. Lovejoy. Fractional Fokker–Planck equation for nonlinear stochastic differential equations driven by non-Gaussian Lévy stable noises. *Journal of Mathematical Physics*, 42:200, 2001. URL http://www.google.fr/search?client=safari&rls=10_7_4&q=Fractional+Fokker+Planck+equation+for+nonlinear+stochastic+differential+equations+driven+by+non+Gaussian+Levy+stable+noises&ie=UTF-8&oe=UTF-8&gws_rd=cr&redir_esc=&ei=RU3pUfizIMXb7Ab3l4C4Cw.

D. Schertzer, P. Bernardara, A. Biaou, I. Tchiguirinskaia, M. Lang, E. Sauquet, H. Bendjoudi, P. Hubert, S. Lovejoy, and J. M. Veysseire. Extrêmes et multifractals en hydrologie: résultats, validations et perspectives. *La Houille Blanche*, (5):112–119, 2006. doi:10.1051/lhb. URL http://www.shf-lhb.org/articles/lhb/abs/2006/05/lhb2006095/lhb2006095.html.

D. Schertzer, I. Tchiguirinskaia, S. Lovejoy, and P. Hubert. No monsters, no miracles: in nonlinear sciences hydrology is not an outlier! *Hydrological Sciences Journal–Journal des Sciences Hydrologiques*, 55(6):965–979, 2010. URL http://www.google.fr/search?client=safari&rls=10_7_4&q=No+monsters+no+miracles+in+nonlinear+sciences+hydrology+is+not+an+outlier&ie=UTF-8&oe=UTF-8&gws_rd=cr&redir_esc=&ei=MkLpUZz4Kaby7AaygYGACQ.

D. Schertzer, I. Tchiguirinskaia, S. Lovejoy, and A. Tuck. Quasi-geostrophic turbulence and generalized scale invariance, a theoretical reply. *Atmos. Chem. Phys. Discuss*, 11(1):3301–3320, 2011. doi:10.5194/acpd-11-3301-2011. URL http://www.google.fr/search?client=safari&rls=10_7_4&q=Quasi+geostrophic+turbulence+and+generalized+scale+invariance+a+theoretical+reply&ie=UTF-8&oe=UTF-8&redir_esc=&ei=Ru6HUIyfEanA0QWG1YCwBQ.

D. Schertzer and S. Lovejoy. Multifractals en Turbulence et Gèophysique. *Irruption des Géométries Fractales dans la Sciences. G. Belaubre and F. Begon. Paris, Académie Européeene Interdisciplinaire des Sciences*, pages 189–209, 2006. URL http://www.google.fr/search?client=safari&rls=10_7_4&q=Multifractals+en+Turbulence+et+Geophysique&ie=UTF-8&oe=UTF-8&gws_rd=cr&redir_esc=&ei=Xy3pUcrBLsa5hAfWoIGQAg.

D. Schertzer and S. Lovejoy. Multifractals, Generalized Scale Invariance And Complexity In Geophysics. *Int. J. Bifurcation Chaos*, 21(12):3417–3456, December 2011. doi:10.1142/S0218127411030647. URL http://www.physics.mcgill.ca/~gang/eprints/eprintLovejoy/neweprint/IJBC.2012.S0218127411030647.pdf.

F. Schmitt, D. La Vallée, D. Schertzer, and S. Lovejoy. Empirical determination of universal multifractal exponents in turbulent velocity fields. 68(3):305–308, January 1992. URL http://www.google.fr/search?client=safari&rls=10_7_4&q=Empirical+determination+of+universal+multifractal+exponents+in+turbulent+velocity+fields&ie=UTF-8&oe=UTF-8&redir_esc=&ei=N8oPUf7YFqmH0AWFhYBg.

F. Schmitt, D. Schertzer, S. Lovejoy, and Y. Brunet. Empirical study of multifractal phase transitions in atmospheric turbulence. *Nonlinear Processes in Geophysics*, 1(2/3):95–104, 1994. URL http://www.google.fr/search?client=safari&rls=10_7_4&q=Empirical+study+of+multifractal+phase+transitions+in+atmospheric+turbulence&ie=UTF-8&oe=UTF-8&redir_esc=&ei=yROKUdWoJsGg0QXAl4D4CQ.

L. I. Sedov. Methods of similitude and dimensionality in mechanics. 1972.

J. E. Simpson. *Sea breeze and local winds*. Cambridge University Press, 1994.

R. B. Smith. The influence of mountains on the atmosphere. *Advances in geophysics.*, 21:87–230, 1979.

C. G. Speziale. Analytical Methods for the Development of Reynolds-Stress Closures in Turbulence. *Annu. Rev. Fluid Mech.*, 23(1):107–157, January 2011. doi:doi: 10.1146/annurev.fl.23.010191.000543. URL http://dx.doi.org/10.1146/annurev.fl.23.010191.000543.

Y. Tessier, S. Lovejoy, and D. Schertzer. Universal multrifractals: Theory and observations for rain and clouds. *Journal of Applied Meteorology;(United States)*, 32(2), January 1993. URL http://www.google.fr/search?client=safari&rls=10_7_4&q=Universal+multrifractals+Theory+and+observations+for+rain+and+clouds&ie=UTF-8&oe=UTF-8&redir_esc=&ei=yDWJUJ74LpGLhQe-nYDgCA.

K. Thomsen, H. A. Madsen, G. C. Larsen, and T. J. Larsen. Comparison of methods for load simulation for wind turbines operating in wake. *Journal of Physics: Conference Series*, 75(1):012072, August 2007. doi:10.1088/1742-6596/75/1/012072. URL http://stacks.iop.org/1742-6596/75/i=1/a=012072?key=crossref.360ec517d13216b4510cd56436b59dd2.

K. Thomsen and H. A. Madsen. A new simulation method for turbines in wake?applied to extreme response during operation. *Wind Energ.*, 8(1):35–47, 2004. doi:10.1002/we.130. URL http://doi.wiley.com/10.1002/we.130.

A. Tsinober. New approaches and concepts in turbulence. 1993. doi:10.1007/978-3-0348-8585-0. URL http://books.google.com/books?hl=en&lr=&id=E5YPi4GhhEMC&oi=fnd&pg=PP13&dq=New+approaches+and+concepts+in+turbulence&ots=RqCWdOMsHv&sig=tmCr_jgFjFApGYBhv3s1qrkMzds.

D. Veneziano and P. Furcolo. A modified double trace moment method of multifractal analysis. *Fractals*, 7(02):181–195, 1999. URL http://www.google.fr/search?client=safari&rls=10_7_4&q=A+modified+double+trace+moment+method+of+multifractal+analysis&ie=UTF-8&oe=UTF-8&redir_esc=&ei=AMoPUdeoD8mc0QXgyYDgBg.

M. Wächter, H. Heißelmann, M. Hölling, A. Morales, P. Milan, T. Mücke, J. Peinke, N. Reinke, and P. Rinn. Wind Energy and the Turbulent Nature of the Atmospheric Boundary Layer. *arXiv*, February 2012. doi:10.1080/14685248.2012.696118. URL http://arxiv.org/abs/1202.2245v2.

T. Wallbank. WindSim Validation Study. *CFD validation in Complex terrain*, January 2008. URL http://www.google.fr/search?client=safari&rls=10_7_4&q=WindSim+Validation+Study&ie=UTF-8&oe=UTF-8&redir_esc=&ei=DzaJUMCEG4Wi0QXQi4CYBA.

J. Wilson, D. Schertzer, and S. Lovejoy. Nonlinear variability in geophysics: multifractal simulations and analysis. *Fractals: physical origin and consequences*, pages 185–208, 1990. URL http://books.google.com/books?hl=en&lr=&id=ks49t6QcfY8C&oi=fnd&pg=PA49&dq=non+linear+variability+in+geophysics&ots=KnYZAykFVt&sig=NO59b4f6pwvGh0ovT7T9vgpT76s.

R. Wu. The influences of orography upon the flow within Ekman boundary layer under the approximation of geostrophic momentum. *Advances in Atmospheric Sciences*, 2(1):1–7, 1985. URL http://link.springer.com/article/10.1007/BF03179731.

J. C. Wyngaard and O. R. Cote. Cospectral similarity in the atmospheric surface layer. *Q.J.R. Meteorol. Soc.*, 98(417):590–603, 1972.

B. I. Xue-yan, L. Feng, and W. Dui. Comparison of Some Limits for Stability Classification. *Journal Of Tropical Meteorology*, 11(2), 2005. URL http://d.wanfangdata.com.cn/periodical_rdqxxb-e200502006.aspx.

A. M. Yaglom. The influence of fluctuations in energy dissipation on the shape of turbulence characteristics in the inertial interval. In *Soviet Physics Doklady*, page 26, 1966.

A. M. Yaglom. Similarity laws for wall turbulent flows: their limitations and generalizations. In *New Approaches and Concepts in Turbulence*, pages 7–27. Springer, 1993. ISBN 3764329246. URL http://www.

google.fr/search?client=safari&rls=10_7_4&q=Similarity+laws+for+wall+turbulent+flows+their+limitations+and+generalizations&ie=UTF-8&oe=UTF-8&gws_rd=cr&redir_esc=&ei=fmrpUdr5BoiChQeM4oHgCQ.

H. Yamazaki. Breakage models: Lognormality and intermittency. *Journal of Fluid Mechanics*, 219:181–193, 1990. URL http://www.google.fr/search?client=safari&rls=10_7_4&q=Breakage+models+Lognormality+and+intermittency&ie=UTF-8&oe=UTF-8&redir_esc=&ei=ZbfnUeaFK4LdOsLOgcgL.

P. K. Yeung and Y. Zhou. Universality of the Kolmogorov constant in numerical simulations of turbulence. *Phys. Rev. E*, 56(2):1746–1752, August 1997. doi:10.1103/PhysRevE.56.1746. URL http://link.aps.org/doi/10.1103/PhysRevE.56.1746.

M. Yokokawa, K. Itakura, A. Uno, T. Ishihara, and Y. Kaneda. 16.4-Tflops direct numerical simulation of turbulence by a Fourier spectral method on the Earth Simulator. pages 50–50, 2002. URL http://ieeexplore.ieee.org/xpls/abs_all.jsp?arnumber=1592886.

R. K. P. Zia, E. F. Redish, and S. R. McKay. Making Sense of the Legendre Transform. *arXiv*, June 2008. URL http://arxiv.org/abs/0806.1147.

Appendix A

A.1 Conservation

Under certain conditions of mathematical regularity, the integral of the energy rate density ε of a fluid parcel is conserved by the non-linear terms of the Navier-Stokes equation. Starting with the equation of an inviscid fluid (i.e., $\nu = 0$; Euler equation) with no forcing term at constant density:

$$\frac{\partial \boldsymbol{u}}{\partial t} = -(\boldsymbol{u} \cdot \nabla)\boldsymbol{u} - \nabla p, \tag{A.1}$$

Multiplying both sides by $\boldsymbol{u}$:

$$\varepsilon = -\frac{1}{2}\frac{\partial}{\partial t}(\boldsymbol{u} \cdot \boldsymbol{u}) = -\boldsymbol{u} \cdot (\boldsymbol{u} \cdot \nabla)\boldsymbol{u} - (\boldsymbol{u} \cdot \nabla)p, \tag{A.2}$$

Because of incompressibility (i.e., $\boldsymbol{u} \cdot \nabla = 0$), equation A.2 becomes

$$\varepsilon = -\nabla \cdot \left[\left(\frac{1}{2}(\boldsymbol{u} \cdot \boldsymbol{u}) + p\right)\boldsymbol{u}\right] \tag{A.3}$$

Integrating over a volume of space V, it yields (due to Gauss' divergence theorem):

$$\int_V \varepsilon dV = -\int_V \nabla \cdot \left[\left(\frac{1}{2}(\boldsymbol{u} \cdot \boldsymbol{u}) + p\right)\boldsymbol{u}\right] dV = -\oint_S \left(\frac{1}{2}(\boldsymbol{u} \cdot \boldsymbol{u}) + p\right)\boldsymbol{u} \cdot \boldsymbol{dS} \tag{A.4}$$

where the right hand integral is over the surface only. The first term represents the transfer of kinetic energy across the surface, the second is the work done by

pressure forces; there is no net source or sink of ε inside the volume. We now consider the dissipation term $\nu\nabla^2\boldsymbol{u}$; multiplying by $\boldsymbol{u}$, ignoring the surface term just discussed, we obtain:

$$\int_V \varepsilon dV = \nu\boldsymbol{u} \cdot \int_V \nabla^2\boldsymbol{u} dV \tag{A.5}$$

Now, using vector identities, we have:

$$\boldsymbol{u} \cdot \nabla^2\boldsymbol{u} = -|\nabla \wedge \boldsymbol{u}|^2 - \nabla \cdot [(\nabla \wedge \boldsymbol{u}) \wedge \boldsymbol{u}] \tag{A.6}$$

The second term an the right hand side is a divergence, when integrated over a volume it can be rewritten as a surface integral (Gauss' theorem):

$$\int_V \varepsilon dV = -\nu \int_V |\nabla \wedge \boldsymbol{u}|^2 dV - \nu \oint_S [(\nabla \wedge \boldsymbol{u}) \wedge \boldsymbol{u}] \cdot \boldsymbol{dS} \tag{A.7}$$

Since the surface integral is null if S is a current surface ($\boldsymbol{dS} \perp \boldsymbol{u}$) or a rigid boundary $\boldsymbol{u} = 0$ the right hand side integrand is a positive definite quantity, $\nu > 0$, and hence the viscosity is always dissipative (decreases the total energy).

A.2 The Kolmogorov Hypotheses

H1 *In the limit of infinite Reynolds numbers, all possible symmetries of the Navier-Stokes equation, usually broken by the mechanisms producing turbulent flow, are restored in a statistical sense at small scales and away from boundaries.*

By small scale we understand scales $\ell \ll L$ where L, the integral scale, is characteristic of the production of turbulence. Small-scale homogeneity is defined as the property of having homogeneous increments i.e. in terms of velocity increments we have:

$$\Delta \boldsymbol{u}(\ell) \equiv \boldsymbol{u}(\boldsymbol{r} + \ell) - \boldsymbol{u}(\boldsymbol{r}). \tag{A.8}$$

Specifically, it is assumed that

$$\Delta \boldsymbol{u}(\boldsymbol{r} + \rho, \ell) \stackrel{d}{=} \Delta \boldsymbol{u}(\boldsymbol{r}, \ell). \tag{A.9}$$

for all increments ℓ and all displacements ρ which are small compared to the integral scale.

Similarly, *isotropy* means, in the present context, that the statistical properties of velocity increments are invariant under simultaneous rotations of ℓ and $\Delta \boldsymbol{u}$ and are likewise simultaneously reversed for parity.

H2 *Under the same assumptions as in H1, the turbulent flow is self-similar at small scales, i.e. it possesses a unique scaling exponent H.*

Thus, there exists a scaling exponent $H \in \mathbb{R}$ such that symmetry 6 in §1.1 is satisfied.

H3 *Under the same assumptions as in H1, the turbulent flow has a finite non-vanishing mean rate of dissipation $\langle \varepsilon \rangle$ per unit mass.*

For H3, we must keep the integral scale L and the r.m.s. velocity fluctuations, u_δ, fixed, and let $u \to 0$. Otherwise, $\langle \varepsilon \rangle$ must be non-dimensionalised through division by u_δ^3/ℓ_0.

A.3 Fractal Dimensions

If we take an object with linear size equal to 1 (or any object with a normalised outer scale, L, as is generally the case) residing in a Euclidean dimension D, and reduce its linear size n times by the factor $\ell_n = 1/\lambda^n$ in each spatial direction, it takes $N_n = \ell_n^{-D}$ number of self similar objects to cover the original object as illustrated in figures A.2a, A.2b and A.2c. We define λ as the *ratio of scales* and λ^n as the *magnification factor*.

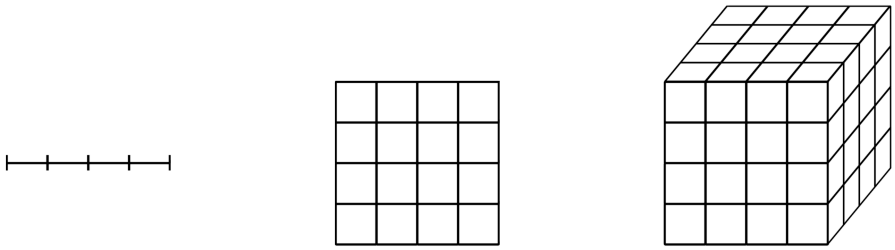

(a) $N_1 = 4^1$. **(b)** $N_1 = 4^2$. **(c)** $N_1 = 4^3$.

Figure A.1: A line, square and cube broken into $\lambda = 4$ self similar parts with the smallest segments of length $\ell_1 = 1/4$.

We can express the dimension of the self-similar object simply through the exponent of the number of self-similar pieces (with scale ratio λ) into which the figure may be broken.

Using logarithms we obtain

$$\text{dimension} = \frac{\log(\text{number of self-similar pieces})}{\log(\text{magnification factor})}. \tag{A.10}$$

For a square with dimension 2 there are ℓ_n^{-2} self-similar pieces each with a mag-

nification factor λ^n. equation A.10 thus becomes

$$D = \frac{\log(N_n)}{\log(\lambda^n)} = \frac{\log(\ell_n^{-2})}{\log(\ell_n^{-1})} \tag{A.11}$$

$$= \frac{-2\log(\ell_n)}{-1\log(\ell_n)} = 2. \tag{A.12}$$

We can see from equation A.12 that the (integer) dimension is independent of scale factor, ℓ_n, and also therefore n. Similarly if we take equation A.10 as the same definition for the fractal dimension, D_F, of a self-similar object such that the

$$\text{fractal dimension} = \frac{\log(\text{number of self-similar pieces})}{\log(\text{magnification factor})} \tag{A.13}$$

and the number of self-similar pieces is chosen to be some 'fraction' of the the total space i.e. 3 out of the 4 segments is occupied $\implies N_n = 3^n$ for scale ratio $\lambda = 4$

$$D_F = \frac{\log(N_n)}{\log(\lambda^n)} = \frac{n\log(3)}{n\log(\lambda)} \implies \frac{\log(N_n/N_{n-1})}{\log(\lambda)} \tag{A.14}$$

$$= \frac{\log(3)}{\log(4)} = 0.75.$$

Again we see that the fractal dimension does not depend on the finite scale n but on the ratio between each scale and the number of counted objects at that scale ratio.

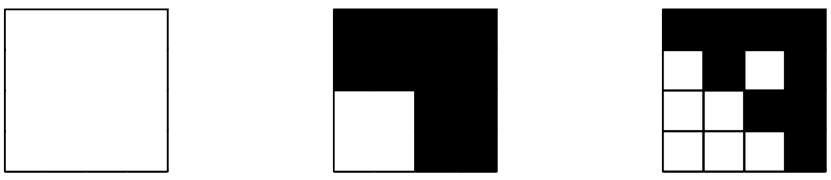

(a) $N_0 = 3^0$. **(b)** $N_1 = 3^1$. **(c)** $N_2 = 3^2$.

Figure A.2: Three iterations of a fractal process on a square with ratio of scales, $\lambda = 2$, and fractal dimension, $D_F = 0.75$.

Being able to determine the number of 'active' countable objects at any scale ℓ simply through the dimension, fractal dimension (or fractal co-dimension as we will see in the next section) and the ratio of the largest scale and the scale of interest is a very desirable property since they are all (D, D_F and λ) easily obtainable from empirical data. Thus we find equations. A.11 and A.14 are typically written in the form

$$N_\lambda = \lambda^D \text{ and } N_\lambda(A) = \lambda^{D_F(A)} \tag{A.15}$$

where A is the space and/or time set in which the 'activity' is occurring.

Types Of Fractal Dimension

Box-counting dimension D_0: $N_\lambda(A) = \lambda^{D_0(A)}$ is the typical number of disjoint balls or cubes of resolution λ covering A.

Hausdorff dimension D_H: It is often considered as the rigorously defined fractal dimension. It has indeed a precise mathematical definition, going back to (Hausdorff [1918]) i.e. for any compact set A: $D(A)$ is the critical dimension of the of the D-dimensional Haussdorff measure $m_D(A)$ such that: $D < D(A) = m_D(A) = \infty$; $D > D(A) : m_D(A) = 0$. However, it has only limited practical applications, since the Hausdorff dimension requires us to consider coverings with balls of various sizes, not of a characteristic size.

A.4 Fractal Co-dimensions

The notion of fractal co-dimension, c, can be defined both statistically and geometrically. While the latter is much more popular, we will demonstrate that the former is much more useful and general since it applies also to stochastic processes and not only to deterministic ones.

Geometric Definition Of A Fractal Dimension

Let $A \subset E$ (the embedding space) with $\dim(E) = D$ and $\dim(A) = D_F(A)$. Then the co-dimension $c(A)$ is defined as

$$c(A) = D - D_F(A). \tag{A.16}$$

This definition corresponds merely to an extension of the (integer) co-dimension definition for vector subspaces.

The co-dimension can be considered to be more fundamental than the notion of the fractal dimension and should be introduced directly. Indeed, this is the case if we consider the scaling behaviour of the probability, P, that a ball B_λ (of size $\ell = L/\lambda$) intersects A.

Probabilistic Definition Of A Fractal Dimension

Let B_λ be a ball of size $\ell = L/\lambda$, then from equations A.15 and A.16 we find

$$P(B_\lambda \cap A) \simeq \lambda^{-c(A)} \tag{A.17}$$

where '$\simeq$' means equality within slowly varying and constant factors. We can see that c is directly defined as an exponent measure of the fraction of the space occupied by the fractal set A in an embedding space E which can even be an infinite dimensional space (again see Fredholm theory).

Relating The Two Definitions

Since the probability of the event, $B_\lambda \cap A$, is defined as

$$P(B_\lambda \cap A) \simeq \frac{N(B_\lambda \cap A)}{N(B_\lambda \supset E)} \simeq \frac{\lambda^{-D_F(A)}}{\lambda^{-D}}. \tag{A.18}$$

It is easy to check that when $c < D_F = \dim(E) < \infty$ the two definitions are equivalent

$$(\text{Definition A.4}: \ c(A) \leq D < \infty) \Leftrightarrow (\text{Definition A.4}: \ D_F(A) \geq 0) \tag{A.19}$$

Rather obviously the statistical definition does not imply any limitation on c. However, the equivalence between the two does not hold as soon as $c(A) > D$. This is the so-called 'latent' dimension 'paradox'... corresponding to the fact that a deterministic geometric definition is no longer possible. This is not surprising since the definition A.4 overcomes many limitations of the Hausdorff dimension which is defined for compact sets (hence bounded sets): the co-dimension measures the *relative sparsity* of a phenomena (the relative frequency of occurrence), whereas the dimension measures its *absolute sparsity* (the absolute frequency of occurrence).

A.5 Divergence Of Moments And The α-Model

From the α-model we have

$$\langle \varepsilon_\lambda^q \rangle = \lambda^{\gamma+q}\lambda^{-c} + \lambda^{\gamma-q}(1-\lambda^{-c}). \tag{A.20}$$

When $q \to \infty$, $q = q_D$. As such

$$\langle \varepsilon_\lambda^{q_D} \rangle = \lambda^{\gamma+q_D}\lambda^{-c}. \tag{A.21}$$

We can see the r.h.s of the above equation is analogous to $\lambda^{K(q_D(c/\gamma_+ - c))}$, thus equating 3.9 and A.21 we obtain

$$q_D = \frac{c-D}{\gamma_+ - D}. \tag{A.22}$$

This implies for q_D to be greater than 1, c must be greater than the maximum singularity γ_+.

A.6 Renormalising Discrete Cascades

The singularities γ_+ and γ_- create a step by step infinite hierarchy of mixed singularities ($\gamma_- \leq \gamma \leq \gamma_+$) such that at the n^{th} step we have

$$\gamma_n = \frac{n^+\gamma^+ + n^-\gamma^-}{n^+ + n^-} \quad \text{where} \quad n = n^+ + n^-. \tag{A.23}$$

and therefore also

$$P(\mu_\varepsilon = \lambda^{\gamma_{n^+},\gamma_{n^-}}) = \binom{n}{n^+} \lambda^{-cn^+}(1-\lambda^{-c})^{n^-}, \tag{A.24}$$

where $\binom{n}{k}$ is the number of combinations of n objects taken k at a time. This implies that we may write:

$$P(\varepsilon_{\lambda^n} \geq (\lambda^n)^{\gamma_i}) = \sum_j m_{ij}(\lambda^n)^{-c_{ij}}. \tag{A.25}$$

The m_{ij}s are the 'sub-multiplicities', c_{ij} are the corresponding exponents ('sub-co-dimensions') and λ^n is the total ratio of scales from the outer scale to the smallest scale. Notice that the requirement that $\langle \mu_\varepsilon \rangle = 1$ implies that some of the λ^{γ_i} are greater than one (increases) and some are less than one (decreases), that is, some $\gamma_i > 0$ and some $\gamma_i < 0$. Note also that the α-model will have bounded singularities

$$-\gamma_- \leq \gamma_i \leq \gamma_+, \tag{A.26}$$

i.e. the maximum attainable singularity $\gamma_{\max}$ is equal to γ_+. The final step in re-normalising is to replace the above n step, 2 state cascade by a single λ^n step cascade with $n+1$ states. Finally doing this and making the replacement $\lambda^n \to \lambda$, in the limit $\lambda \to \infty$, means one of the terms in the sum will dominate (that with the smallest c_{ij}). Hence defining

$$c_i = \min\{c_{ij}\} = c(\gamma_i) \tag{A.27}$$

this yields for $\lambda \to \infty$

$$P(\varepsilon_\lambda \geq \lambda^{\gamma_i}) = m_i \lambda^{-c_i} \tag{A.28}$$

where c_i is the co-dimension and m_i is the multiplicity. If we now drop the subscripts 'i' (this allows for the possibility of a continuum state, e.g. the process being defined by a uniform or other continuous distribution) then we obtain:

$$P(\varepsilon_\lambda \geq \lambda^\gamma) \simeq \lambda^{-c(\gamma)} \cdot m(\gamma);\ \frac{dc}{d\gamma} > 0. \tag{A.29}$$

Thus, the multifractal field, ε_λ, at the ratio of scale λ can be written:

$$P(\varepsilon_\lambda \geq \lambda^\gamma) \simeq \lambda^{-c(\gamma)}. \tag{A.30}$$

where $\simeq$ absorbs the multiplicative p_{ij}. Each value of ε_λ corresponds to a singularity (where strictly speaking 'singularity' applies only to $\gamma > 0$ i.e. when $\varepsilon \to \infty$ for $\lambda \to \infty$, when $\gamma < 0$ it is a 'regularity') of order γ and co-dimension $c(\gamma)$.

A.7 Legendre Transformation

We now derive the basic connection between $c(\gamma)$ and the moment scaling exponent $K(q)$. To relate the two; we first write the expression for the moments in terms of the probability density of the singularities:

$$p(\gamma) = \left|P'(\gamma)\right| \approx c'(\gamma) \cdot \log(\lambda) \cdot \lambda^{-c(\gamma)} \simeq \lambda^{-c(\gamma)} \tag{A.31}$$

(where we have absorbed the $c'(\gamma) \cdot \log(\lambda)$ factor into the $\simeq$ symbol since it is slowly varying, sub-exponential). This yields:

$$\langle \varepsilon_\lambda^q \rangle = \int dP(\varepsilon_\lambda) \cdot \varepsilon_\lambda^q \simeq \int \lambda^{-c(\gamma)} \lambda^{q\gamma} d\gamma \tag{A.32}$$

where we have used $\varepsilon_\lambda = \lambda^\gamma$ on the r.h.s. which is justified for the change in variable ε_λ for γ when λ is a fixed parameter. Hence:

$$\langle \varepsilon_\lambda^q \rangle = \lambda^{K(q)} = e^{K(q)\log(\lambda)} = \int_{-\infty}^{\infty} e^{\xi f(\gamma)} d\gamma; \;\; \xi = \log(\lambda); \;\; f(\gamma) = q\gamma - c(\gamma); \;\; \lambda \gg 1; \tag{A.33}$$

We see that our problem is to obtain an asymptotic expansion of an integral with integrand of the form $\exp(\xi f(\gamma))$ where $\xi = \log(\lambda)$ is a large parameter and $f(\gamma) = q\gamma - c(\gamma)$. These expansions can be conveniently performed using the mathematical technique of 'steepest descents' e.g. which shows that the dominant term in the expansion for the integral is

$$\exp\left[\xi \max_\gamma(f(\gamma))\right] \tag{A.34}$$

i.e. the integral is dominated by the singularity γ which yields the maximum value of the exponent so that as long as $\xi = \log(\lambda) \gg 1$:

$$K(q) = \max_\gamma \left\{q\gamma - c(\gamma)\right\} \tag{A.35}$$

This relation between $K(q)$ and $c(\gamma)$ is called a 'Legendre transform'; see figure A.3). We can also invert the relation to obtain $c(\gamma)$ from $K(q)$; just as the inverse Laplace transform used to obtain $K(q)$ from $c(\gamma)$ is another Laplace transform

so the inverse Legendre transform is just another Legendre transform. To show this, consider the twice iterated Legendre transform $L(q)$ of $K(q)$:

$$L(q) = \max_{\gamma} \left\{ q\gamma - (\max_{q} \left\{ q^*\gamma - K(q^*) \right\}) \right\} = \max_{\gamma;q^*} \left\{ \gamma(q - q^*) + K(q^*) \right\} \quad \text{(A.36)}$$

Taking $L' = 0 \implies q = q^*$ we see that $L(q) = K(q)$; this shows that a Legendre transform is equal to its inverse (see Zia et al. [2008] for further details on all of the above), hence we conclude:

$$c(\gamma) = \max_{q}(q\gamma - K(q)). \quad \text{(A.37)}$$

The γ for which a given q maximises $q\gamma - c(\gamma)$ is γ_q and it is the solution of $c'(\gamma q) = q$ (figure A.4). Similarly, the value of q for which a given γ maximises $q\gamma - K(q)$ is q_γ so that:

$$q_\gamma = c'(\gamma), \quad \text{(A.38)}$$

$$\gamma_q = K'(q). \quad \text{(A.39)}$$

This is a one-to-one correspondence between moments and orders of singularities (see figures A.3 and A.4).

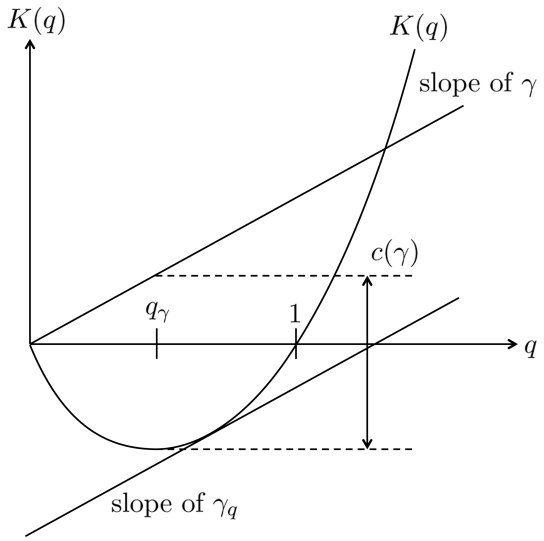

Figure A.3: $K(q)$ versus q showing the tangent line $K'(q_\gamma) = \gamma$ with the corresponding chord γ_q. Reproduced from (Tessier et al. [1993]).

Note that if γ is bounded by $\gamma_{\max}$ (for example in the α-model; $\gamma \leq \gamma_+$) there is a $q_{\max} = c'(\gamma_{max})$ such that for $q > q_{\max}$, $K(q) = q\gamma_{\max} - c(\gamma_{\max})$, i.e. $K(q)$ becomes linear in q (see figure A.5).

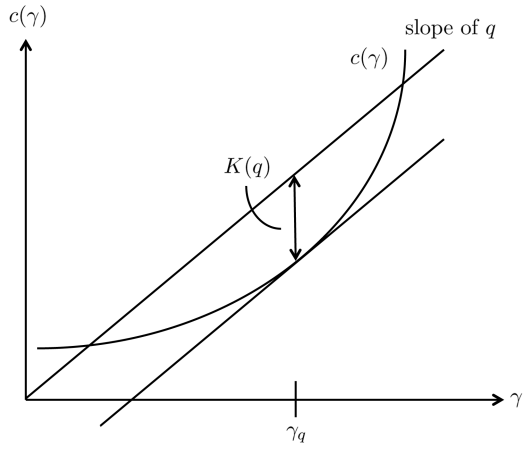

Figure A.4: $c(\gamma)$ vs. γ showing where the tangent $c'(\gamma_q) = q$ with the corresponding chord γ_q.

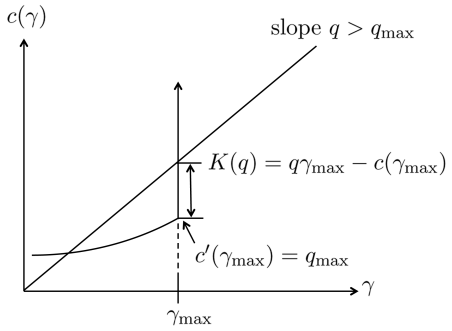

Figure A.5: Using the Legendre transformation of $K(q)$ to derive the maximum order of singularity present ($\gamma_{\max}$; corresponding moment $q_{\max} = c'(\gamma_{\max})$ When $q > q_{\max}$ the Legendre transform will have a maximum value $\gamma = \gamma_{\max}$ as shown. This implies $K(q)$ is linear for $q > q_{\max}$. Reproduced from course notes, 1996 (Schertzer and Lovejoy [1994]).

Appendix B

B.1 Vorticity Scaling

The three-dimensional vorticity in Cartesian co-ordinates is

$$\Omega = \nabla \times \boldsymbol{u} = \left(\frac{\partial w}{\partial y} - \frac{\partial v}{\partial z}, \frac{\partial u}{\partial z} - \frac{\partial w}{\partial x}, \frac{\partial v}{\partial x} - \frac{\partial u}{\partial y} \right). \tag{B.1}$$

We start first with the vorticity of the Corsica dataset. For the Corsica dataset we have the three-dimensional wind in time at two heights. This means we can calculate only one component of the vorticity, the y-component Ω_y, using the following terms $\Delta u/\Delta z$ and $\Delta w/\Delta x$ provided Taylor's approximation is valid for space separations in x, i.e. where $\Delta x = U\Delta t$.

Figure B.1: Illustrative diagram of the two different methods for obtaining the differences of the velocity.

In an attempt to match the two separations $\Delta x \approx \Delta z$ there are two manipulations that can be performed. The first and most physically representative method is to increase/decrease the time-scale separation. If our mean $U \approx 1.5$m/s

is representative, we require Δt to be about 30 seconds to match a vertical space-separation of 50m. We found that increasing Δt for $\Delta u(\Delta t)$, $\Delta v(\Delta t)$ and $\Delta w(\Delta t)$ to anything larger than the smallest separation possible (0.1 seconds) led to spurious spectral oscillations. Note this happened only if the differences were taken using a windowing method (see figure B.1). Figures B.2 and B.3 plot the spectra of the velocity increments for increasing Δt using the two different methods.

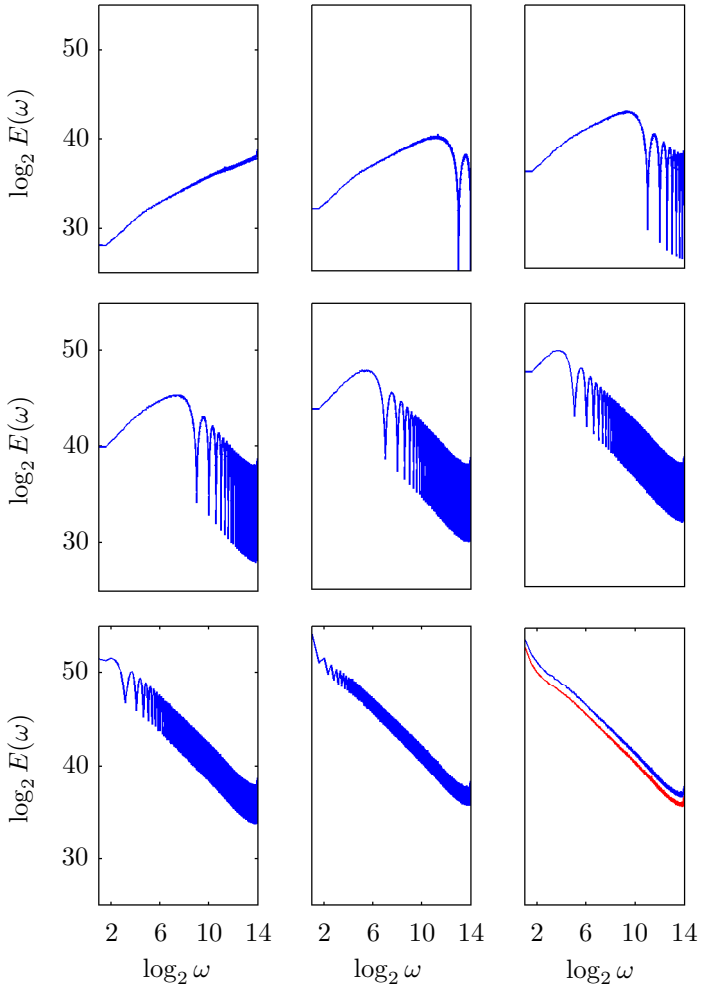

Figure B.2: Plots of the energy spectra of $\Delta u(\Delta t)$ for $\Delta t = 0.1 \times 2^n$ seconds, where $n \in [0 : 2 : 16]$ (left to right and from top to bottom). The velocity increments are calculated using the windowing method. In the final plot the red plot corresponds to the spectra of $u(t)$.

When the windowing method is used the smallest time-scale separation yields a spectrum with the scaling exponent of the derivative $\partial u/\partial t$, i.e., approximately $\omega^2 E_u$. For increasing time-scale separations a de-correlation occurs until we find $E_{\Delta u} \approx 2E_u$. When the non-windowing method is used we find that the scaling exponent (2/3) remains stable with increasing Δt, i.e. no de-correlation occurs.

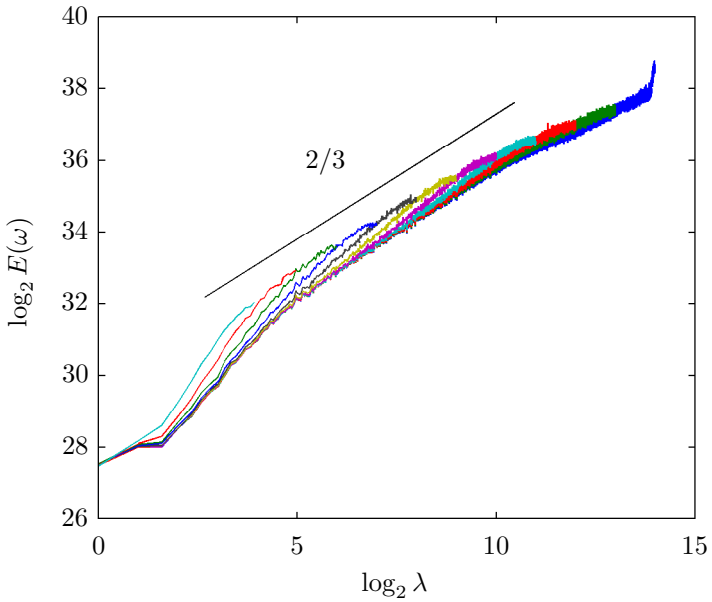

Figure B.3: Plots of the energy spectra of $\Delta u(\Delta t)$ for $\Delta t = 0.1 \times 2^n$ seconds, where $n \in [0 : 2 : 16]$. For increasing Δt the number of values of $\Delta u(\Delta t)$ decreases hence the leftward reduction in the sample size.

If we are unable to increase Δt using the windowing method we can alternatively manipulate the mean wind U. Since the spectra discussed in previous sections have multiple scaling regions (corresponding to multiple means over different scales), estimations could be biased and therefore the manipulations are justified. Figure B.4 plots the vorticity component Ω_y for fixed $\Delta t = 0.1$s and for increasing $U = 2^n$m/s, for $n \in [8 : 15]$ (from top to bottom). When we change U we are in fact simply changing the weighting of the term $\Delta w/\Delta x$. The larger U the more we decrease the weighting of the term. Therefore, figure B.4 corresponds simply to the transition between the spectra of Δu and Δw.

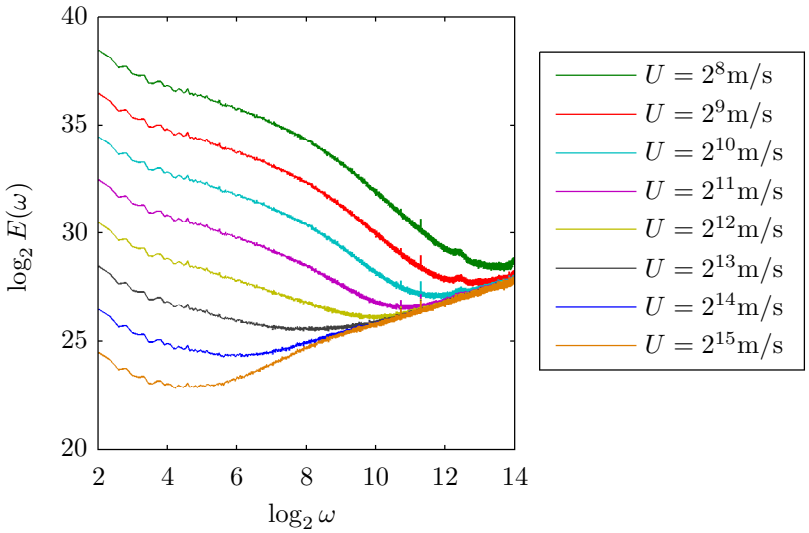

Figure B.4: Energy spectrum of the vorticity component Ω_y for $U = 2^n$m/s, for $n \in [8 : 15]$ (see legend).

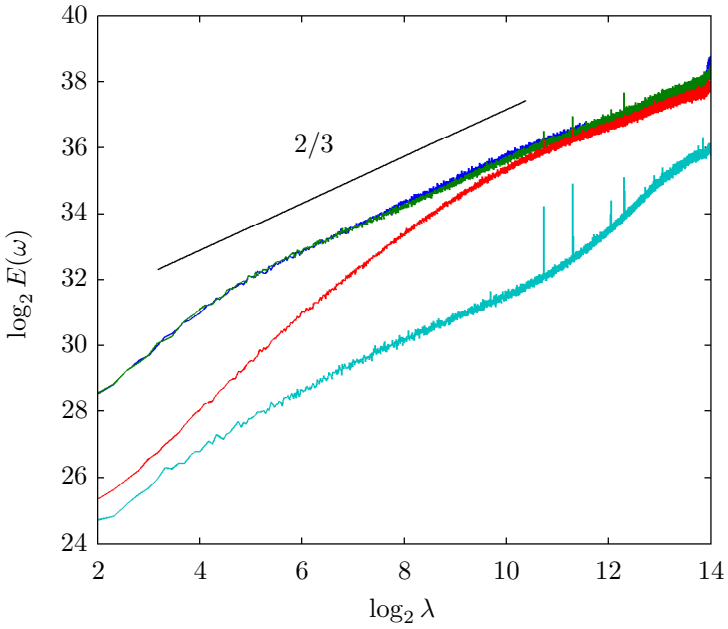

Figure B.5: Plots of the energy spectrum of the time-increments ($\Delta t = 0.1$s) of the three-dimensional velocity: $\Delta u(\Delta t)$ (blue), $\Delta v(\Delta t)$ (red), and $\Delta w(\Delta t)$ (green), and the temperature increments $\Delta T(\Delta t)$ (turquoise).

Figure B.5 plots energy spectrum of the time-increments of the three-dimensional velocity and temperature. Dimensional analysis of the velocity increments yields a positive scaling exponent of 1/3. The increments of three velocity components exhibit a scaling exponent of 1/2 from 0.2 seconds to 5 seconds. This is then diminished to 2/3 for the horizontal components from 5 seconds to a minute ($\log_2 \omega = 10$ to 6). These exponents are indeed not far from their expected scaling exponent. For the spectra of the temperature increments a much higher scaling exponent (4/3s) is observed. This is due to high frequency white noise.

Figure B.6 plots the y-compoent vorticity but for a much longer sample so that the previously observable -2 scaling ranges of the velocity are included. Indeed we find that, as with the other measured quantities, a -2 scaling range occurs even for the vorticity.

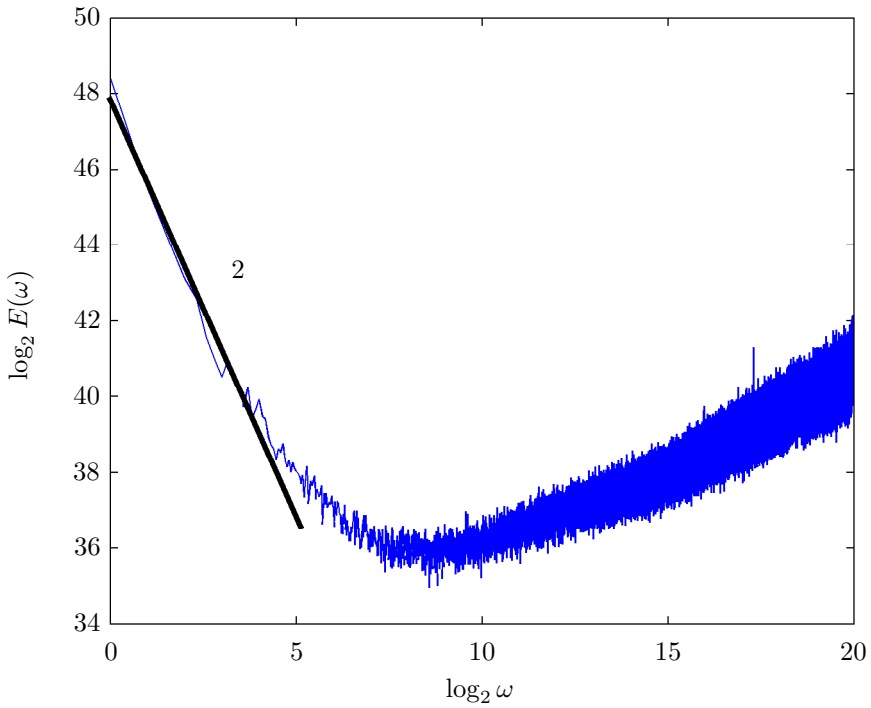

Figure B.6: Plot of the energy spectrum of the $\Delta u(\Delta t)$ for a concatenated time-series with $\lambda = 2^{21}$.

In figure B.7 we compare the time-averaged energy spectrums of the time-series' velocities u and w and their respective increments in space i.e. $\Delta u(\Delta z)$ and $\Delta w(\Delta z)$. It seems that the taking the differences of the velocities in space extends the adjoining -1 scaling range up to much higher frequencies. If we go by the same argument that is typically applied to the vertical velocity component i.e. that the fluctuations observable at any given distance above the ground are restricted to structures that are smaller than the height of measurements, we can infer that the vertical velocity increments of the horizontal wind will also be subject to this condition. Because this effect occurs at different time-scales for either the horizontal or vertical components it may be possible to directly estimate the space-time anisotropies.

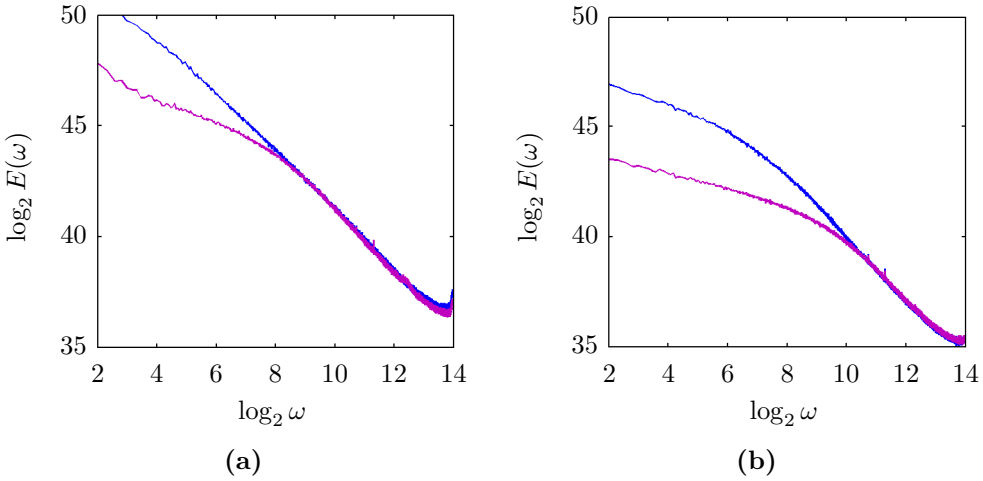

Figure B.7: Comparison of the energy spectra of the velocities (blue) $u(t,z)$ (a) and $w(t,z)$ (b) and their respective spatial derivatives (purple) $\Delta u(t,\Delta z)$ (a) and $\Delta w(t,\Delta z)$ (b) where $\Delta z = 20$m. The velocities corresponds to the Corsica dataset.

In fact we show in figure B.8, using the Growian dataset, that the frequency that the -1 adjoining range begins at does not significantly depend on the size of the space-separation. This suggests that the anisotropy is in fact universal across space-time. Because there are no observable scales in which a vorticity spectrum ensues when the derivative is taken in space it may be that the spatial derivative does not sufficiently remove the correlation of the velocities in time. This may be because of the complexities that arise when taking spatial derivatives of a time-

series. If there is a space-time anisotropy one could believe that the time-series data are more correlated than the spatial derivatives (at a fixed 50m scale) allow us to remove.

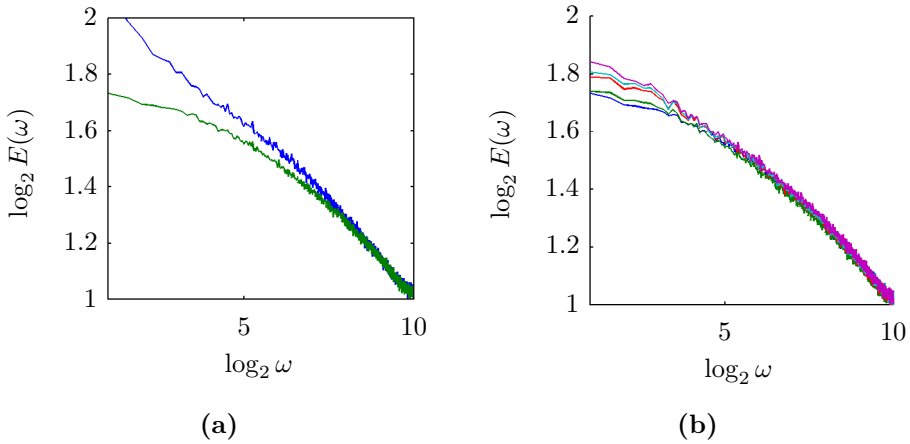

Figure B.8: (a) Comparison of the energy spectra of the velocities (blue) $u(t, z)$ and their respective spatial derivatives (green) $\Delta u(t, \Delta z)$ where $\Delta z = 40$m; (b) Comparison of $\Delta u(t, \Delta z)$ for $\Delta z = 40$, 65, 90, 115 and 140m (blue, red, green, turquoise and purple).

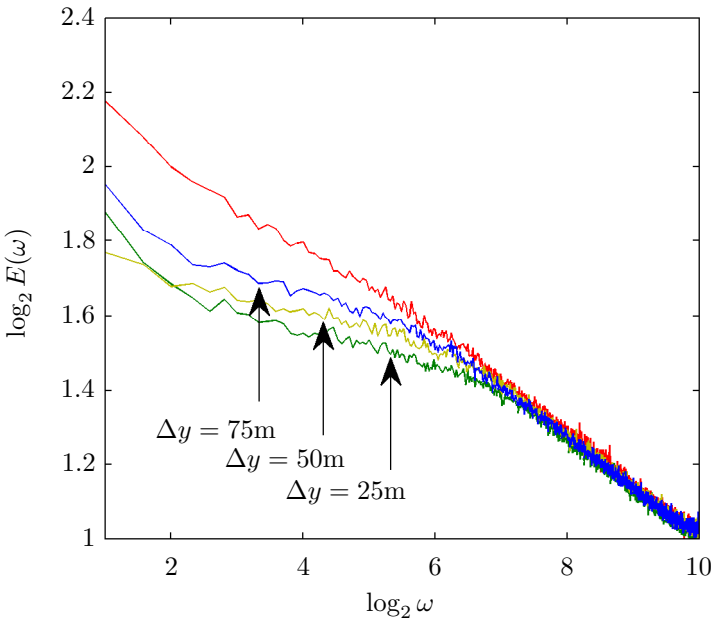

Figure B.9: Comparison of the energy spectra of the horizontal velocity (red) $u(t, y)$ and its respective spatial derivatives $\Delta u(t, \Delta y)$ for $\Delta y = 25$, 50 and 75m.

As was done with the vertical spatial increments, figure B.9 compares the energy spectra of the horizontal velocity $u(t, y)$ and its respective horizontal spatial derivatives $\Delta u(t, \Delta y)$. Unlike the vertical spatial increments however, increasing Δy has an effect on the scaling of the spectra of $\Delta u(t, \Delta y)$. It seems the larger the increment Δy the further the Kolmogorov range extends. This is somewhat contradictory to our previous results but could be explained by a strong horizontal anisotropy instead. This would be consistent with our other analyses on component-wise anisotropy.

B.2 Quantifying The Effects Of Phase Transitions

We have shown that the non-scaling TM and DTMs can be corrected by a fractional integration/differentiation however, we haven't yet discussed the scaling properties of the singularities of the flux. If the scaling moment functions aren't scaling we can expect that the singularities also won't scale. Unlike the TMs and DTMs we expect the singularities γ to change linearly i.e. $\gamma + h$. To analyse the scaling properties of γ we estimate $\gamma_s \approx \gamma_{\max}$ at different λ. Indeed, analysing this quantity at different resolutions confirmed that it too, as with the TM and DTMs wasn't scaling. Figure B.10 plots $\gamma_{\max}$ at decreasing resolutions $\lambda = 2^{15}$, 2^{13}, 2^{11}, 2^9, 2^7 and 2^5. We can see that the decrease from 0.059 to -0.41 is significant enough to say there is no conservation.

Because we cannot manipulate the curvature of the singularities with a convolution as we did with the TMs and DTMs we attempted to find other means by which to force the singularities to behave as conservative process. One interesting observation was the apparent dependence on the initial time-separation of the velocity increments used to approximate the flux; an idea that we originally developed when looking to the scaling properties of the vorticity. More formally we define our flux as

$$\varepsilon(\tau_0) = |\Delta u(\tau_0)|^3 \tag{B.2}$$

where τ_0 is the initial separation between the velocity increments. The positive flux field $\varepsilon(\tau_0)$ is then upscaled in the usual way to obtain either the TMs or the DTMs. We emphasise that for different τ_0 our total ratio of scales, λ, remains the same. Figure B.11 plots $\gamma = \log_\lambda(\varepsilon(\tau_0))$ through λ and for different values of τ_0.

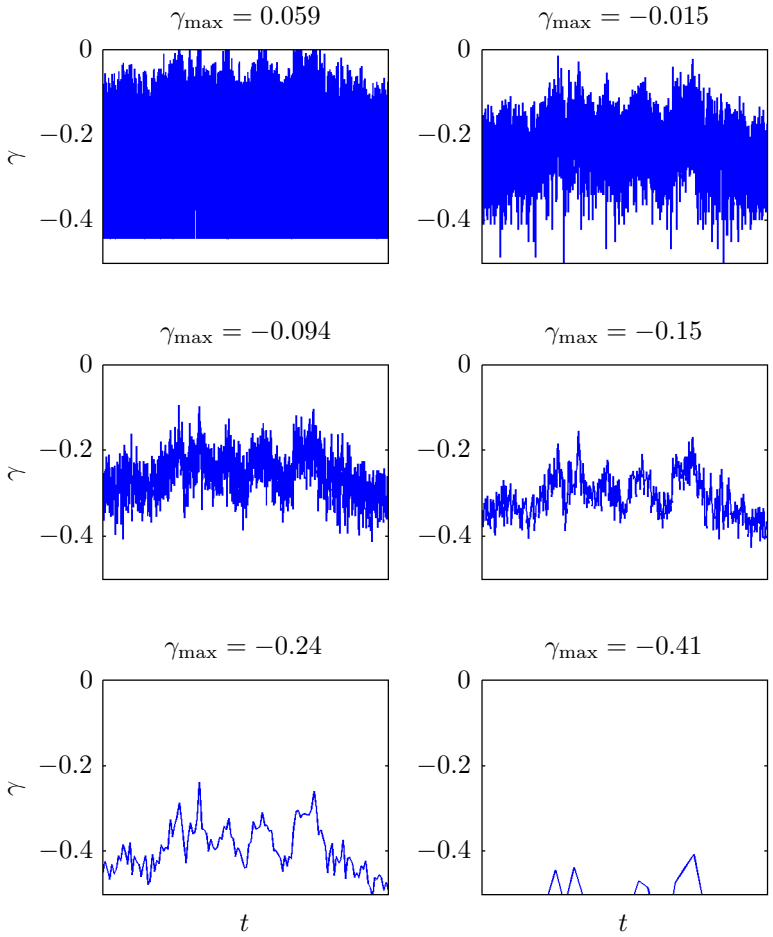

Figure B.10: Plots of the time-series of $\gamma = \log_\lambda(\varepsilon_\lambda)$ at decreasing resolutions $\lambda = 2^{15}$, 2^{13}, 2^{11}, 2^9, 2^7 and 2^5.

We can see that for $\tau_0 = 0.1$s a similar but not the same curving, non-scaling, behaviour occurs as has been the case with our TMs and DTMs estimated on the same quantity. For increasing τ_0 we are changing the curvature of the singularities with respect to λ, as was done with h for the DTMs. In fact, when we change τ_0 we are also indirectly changing H since over larger time-scales, due to scaling changes observed in the structure functions, the correlation between u_n and u_{n+1} is different. We show in figure B.12 that, unfortunately the change in H for increasing τ_0 is unrelated the linearity/non-linearity of the TMs and DTMs, i.e, the TMs are still curving. It is possible to manipulate the curvature of the TMs and DTMs through τ_0 as was done with fractional integration however the same

result is obtained in that $\tau_0(q, \eta)$ is required to fully optimise the functions.

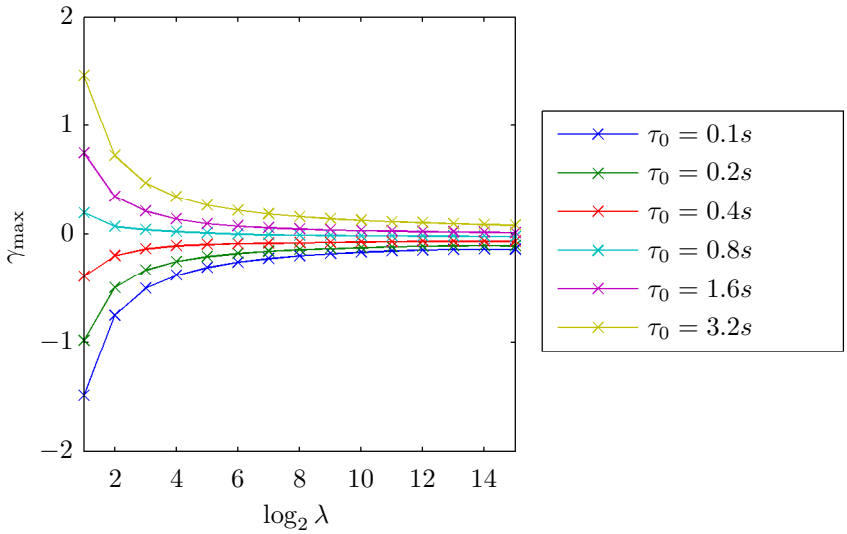

Figure B.11: Plot of $\gamma_{\max}(\lambda)$ for different τ_0 (see legend).

What is of particular interest is that we seem to be able to obtain a linear scaling for τ_0 somewhere between 0.4 and 0.8s. We showed in chapter two that the one-dimensional projection of an anisotropic two or three-dimensional process will result in a reduction in dimension. It may be that as we increase τ_0 the deformation of the space – that has resulted from component-wise anisotropy and therefore an uneven distribution of the one-dimensional singularities – is reduced. We can hypothesis therefore that the τ_0 that results in the most linear distribution of singularities across λ is the so called 'iso-scale' predicted by GSI. Figure B.13 plots the histogram of the τ_0s that produce the most linear distribution of $\gamma_{\max}$s across λ over the whole dataset. The distribution seems to have two more frequent values of τ_0, $\tau_0 = 3.2$s and $\tau_0 = 1$hr. Whether these time-scales truly corresponds to an iso-scale is open for discussion. What can be shown however, is that q_D is the result of the uneven distribution of the singularities.

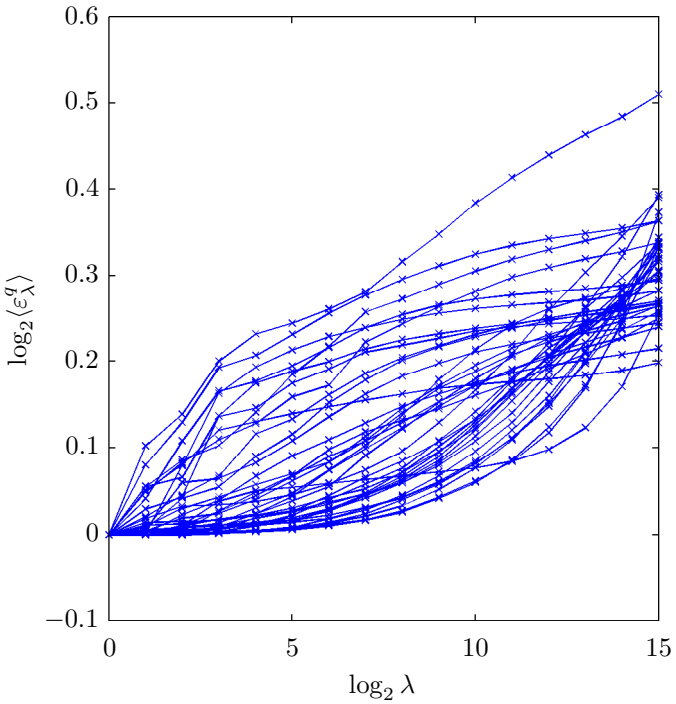

Figure B.12: Plots of the TMs for optimal τ_0 for the first 30 samples.

Figure B.14 plots the surfaces h, α_h and $C_{1,h}$ calculated on $\chi = \varepsilon(\tau_0)$ where τ_0 is the optimal value as shown in figure B.13. When we use a τ_0 that is linear in λ (note this usually corresponds to a constant $\gamma_{\max}$) the singular behaviour that we have shown is due to the linearity of the function $K(q_D)$ is completely lost. Note the dependence on h is still maintained further confirming that the occurrence of q_D and the curvature observed in the TMs and DTMs are unrelated. In the next section we discuss what may be the causes of the non-scaling behaviour of the TMs and DTMs.

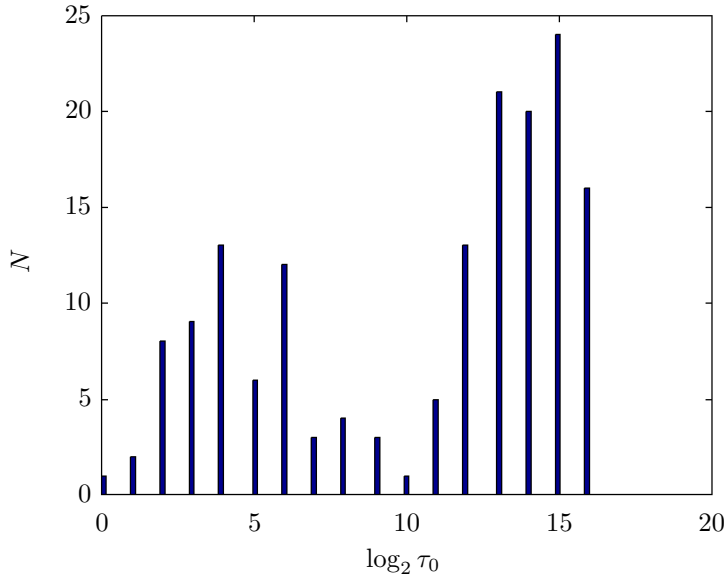

Figure B.13: Histogram of the optimal τ_0 that satisfies the most linear distribution of $\gamma_{\max}$ across λ.

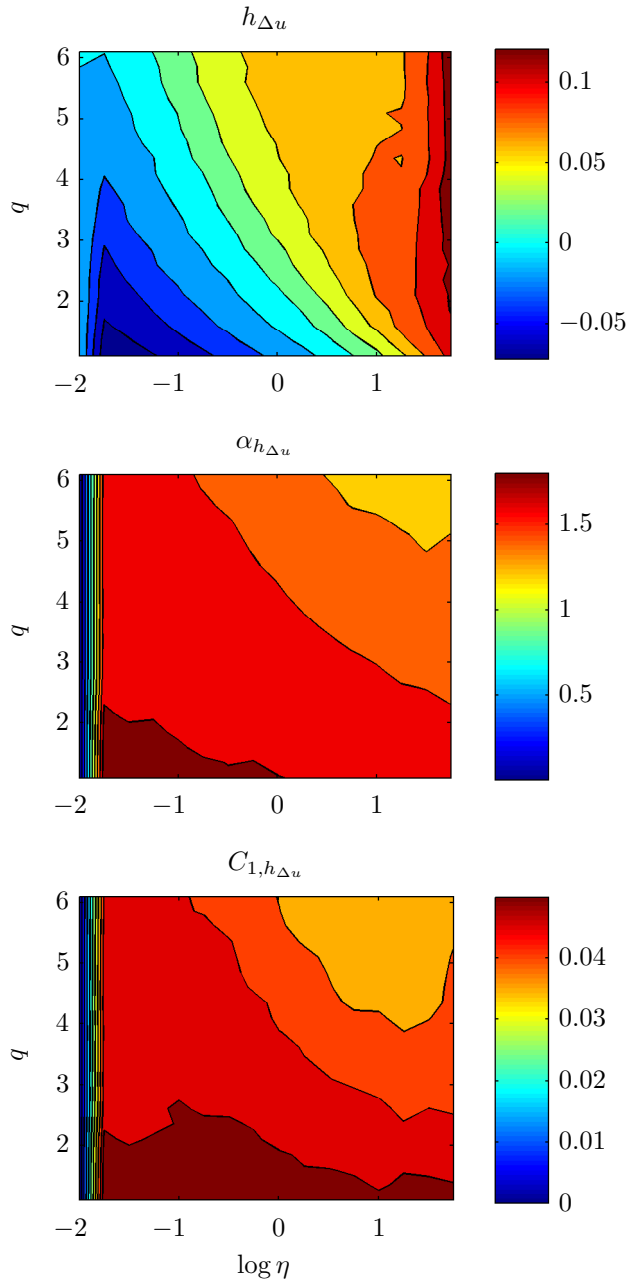

Figure B.14: Surfaces plots of h, α_h and $C_{1,h}$ calculated on $\chi = \varepsilon(\tau_0)$ where τ_0 is the optimal values shown in the histogram of figure B.13

B.3 Empirical Co-Dimension Functions

Due to the aforementioned complexities involved in the estimation of the parameters for the scaling moment function, it can sometimes be easier to estimate the parameters directly from the co-dimension function. There are typically two standard methods used to calculate the $c(\gamma)$, the probability distribution-multiple scaling (PDMS) method and the Weibull plotting position. Note is also possible to compute the Laplace transform of the $K(q)$ function however this wouldn't solve any of the previous problems we had encountered. We attempted to apply the PDMS method to the data, however, the non-scaling of the singularities meant the estimation of the slopes was unreliable. This left the Weibull plotting position.

There are two clear problems when using Weibull plotting position. The first is that we define our probability $\Pr = i/(N+1) \approx i/\lambda$, because the index $i \in [1 : \lambda]$ is positive, the maximum co-dimension we can obtain is 1 since $c(\gamma_i) = 1 - \log_\lambda i$. The second problem is that because we are calculating our Weibull plotting positions on one sample the sampling dimension, $D_s = 0$. Thus, because $c(D) = \gamma_s$ and the dimension of the sample $D = 1$, the maximum obtainable co-dimension should correspond to γ_s. If in each sample the maximum observed singularity is more or less than γ_s, due to the even spacing enforced by the Weibull plotting position, the remaining singularities will be incorrectly distributed. We can simulate this problem by defining

$$c(\gamma_i) = C_1\big(\frac{\gamma_i}{C_1\alpha'} + \frac{1}{\alpha}\big)^{\alpha'}, \tag{B.3}$$

where $\gamma_i = \log_\lambda(i/\lambda)$ and i is positive and evenly spaced as defined early. In figure B.15 we use a spacing of $i \in [1 : 10 : \lambda]$. To simulate the effect of our maximum singularity deviating from γ_s we shifted the singularities for the corresponding co-dimensions by a factor of i_0 i.e.

$$\Pr(\varepsilon_\lambda \geq \lambda^{\gamma_{i+i_0}}) \propto \lambda^{-c^*(\gamma_i)}. \tag{B.4}$$

The yellow and purples plots in B.15 correspond to $i_0 = -6$ ($\max(\gamma) < \gamma_s$) and

6 ($\max(\gamma) > \gamma_s$) respectively. The control plot is the solid blue curve where $i_0 = 0$ or $\max(\gamma) = \gamma_s$. The corresponding difference $\gamma' = \max(\gamma) - \gamma_s$ caused by shifting the index by six places is approximately ± 0.15. The effect of having $\gamma_{\max} \neq \gamma_s$ is that the $c(\gamma)$ function is either more or less curved than it should be making it difficult to estimate the true values of the parameters that fit the curve.

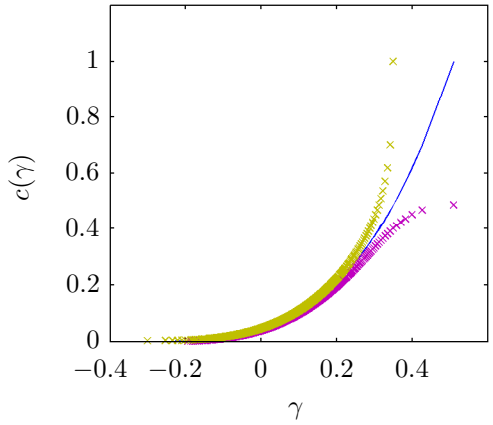

Figure B.15: (a) Plot of $c^*(\gamma_i)$ for $i_0 = 0$ (solid blue line), $i_0 = -6$ (yellow crosses) and $i_0 = +6$ (purple crosses).

B.4 Approximating The Non-Scaling Behaviour Of The Trace Moments

A large part of the third chapter of this thesis has been devoted to linearising the DTMs through fractional differentiation/integration. The result of this manipulation has been the non-unique estimation of the parameters H and C_1 (i.e. a dependence on q of the estimates). This situation is not within the UM framework as unique parameters are required in order to simulate the velocities.

A possible solution to this problem is to find a $\log \lambda'$ say in which the TMs and DTMs are linear. If, as with $C_{1,h}$ and h, the change in λ' or moreover $\log \lambda'$ is proportional to the change in either $C_{1,h}$ or h – where $C_{1,h}$ and h are related by M – through q and η there then exists a universal function $f : \lambda \mapsto \lambda'$ that can be used to simulate the fields. Figure B.16 attempts to illustrate this function or transformation.

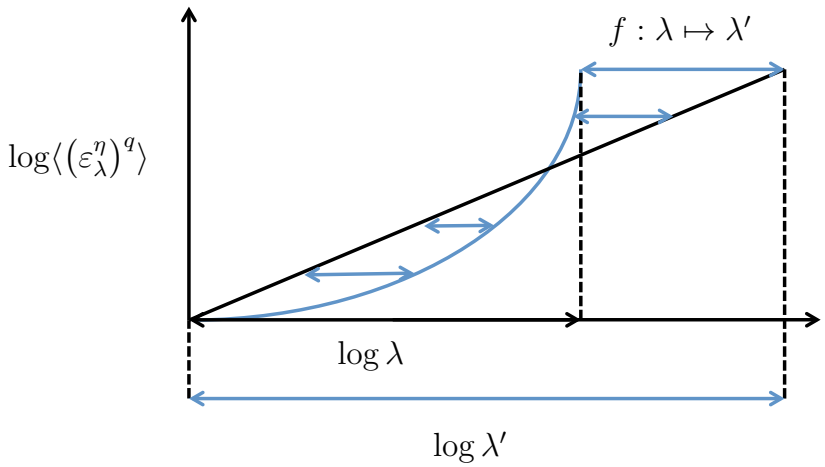

Figure B.16: Diagram of the transform of the non-linear $\log \lambda$ to the linear $\log \lambda'$.

The plots of both the TMs and DTMs of $\varepsilon_\lambda = |\Delta u|^3$ have shown that there is a strong curvature that one might attempt to fit with a power law. As an example therefore figure B.17 plots the TM of ε_λ at $q = 1.5$ versus $(\log_2 \lambda)^\mu$ for

$\mu \in [1:10]$. This means we are looking for

$$\log_2 \lambda' = (\log_2 \lambda)^\mu. \tag{B.5}$$

We can see that a power law works to some extent. Indeed over a given range of λ for $\mu = 7$ we are able to approach a scaling behaviour in these new coordinates. One clear problem is the poor normalisation at $\log_2 \lambda = 0$. The function we are using in this case however is just an example.

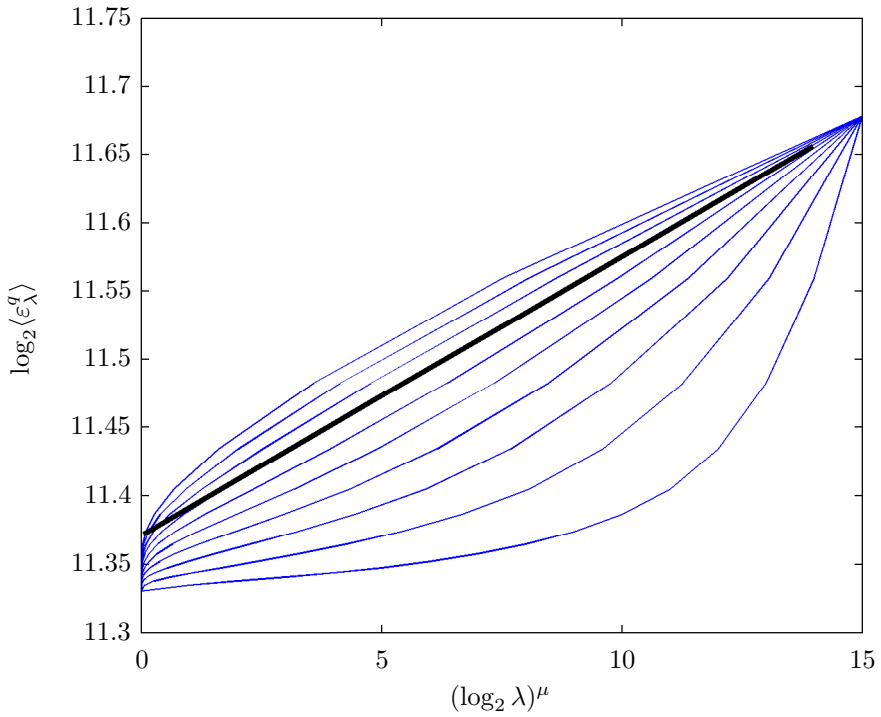

Figure B.17: Plots of the TM of $\varepsilon = |\Delta u|^3$ at $q = 1.5$ versus $(\log_2 \lambda)^\mu$ for $\mu \in [1:10]$ (from bottom to top).

Nonetheless, comparing the change in the parameter $\mu(q, \eta)$ with that of (for instance) the change in $C_1(q, \eta)$ (figure B.18) we find that the two surfaces cancel to (approximately) form a universal constant (figure B.19) of 0.4. Note the transform $f : \lambda \mapsto \lambda'$ can be any function provided the parameter or parameters of the function change proportionally to $C_{1,h}$ and h.

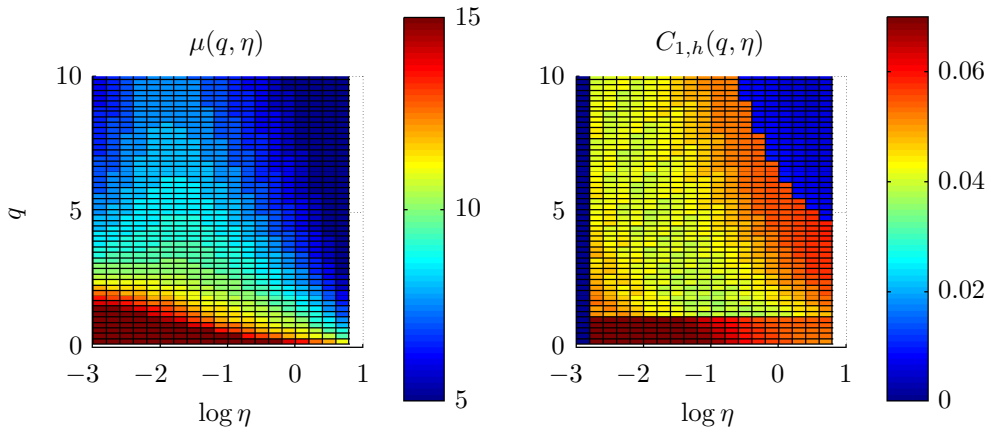

Figure B.18: Surface plots of $\mu(q,\eta)$ (left) and $C_{1,h}(q,\eta)$ (right).

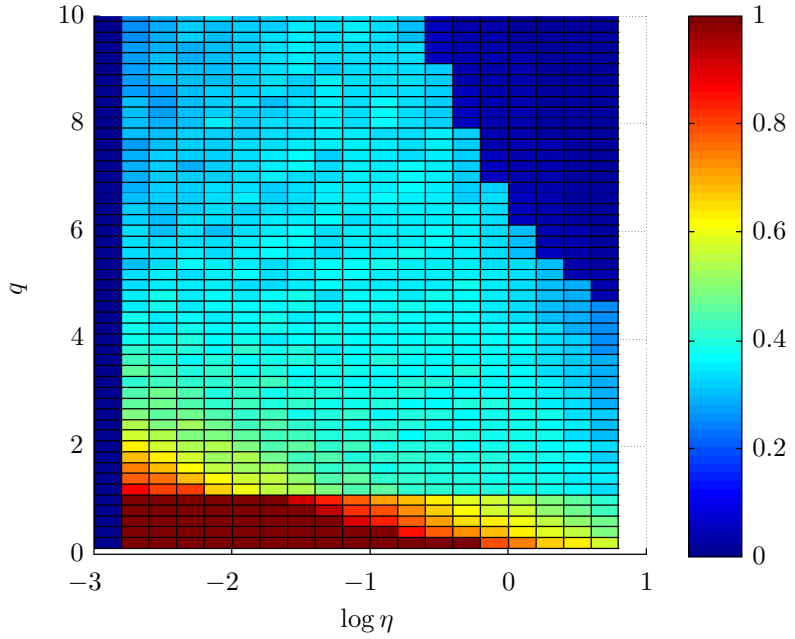

Figure B.19: The surface $\mu(q,\eta)\cdot C_{1,h}(q,\eta)$.

For practical applications we can now use this constant to reconstruct so that our flux will have parameters of the form

$$\mu C_1 = 0.4, \tag{B.6}$$

where C_1 is related to H through M, i.e. for this (q_s-like case) $H = 9.5C_1$. For the simplest solution to the equation B.6 we can use $\mu = 1$ so that $\lambda' = \lambda$. This means we must simulate a field with $C_1 = 0.4$ and $H = 4$! This is an unphysically large value showing there is something we aren't quite understanding. We can attempt to reduce this value by increasing μ but due to the double exponential form of the equation increasing μ to even 2 means simulating a field with resolution $\lambda = 2^{11}$ would require $\lambda' = 2^{83}$. One reason we are obtaining such large values could be we are not using the correct function $f(\lambda)$. We have chosen a power law function as an approximation. A more reasonable approach will be to determine a physical reason why the positive energy flux requires a different metric and how that can be used to determine $f(\lambda)$.

As discussed in chapter three, Novikov Novikov and Stewart [1964] predicts a length-scale that depends on the friction velocity. If our surface-layer friction velocity follows a logarithmic profile (i.e. equation 2.1) we have

$$\lambda' = \log(\lambda). \tag{B.7}$$

Indeed this also gives a non-linear function $f(\lambda)$ however with a logarithmic function we are not able to find a q and η dependent parameter that we can use to find a universal constant in C_1 as changing the base of the logarithm gives only a linear shift.

Coming back now to our solution to equation B.6. If we are indeed able to find an $f(\lambda)$ that sufficiently satisfies the curvature of the TMs and DTMs a simple fractional integration of the field will not return the same curvature. In figure B.20 we have taken a simulated flux with parameters $\alpha = 1.2$ and $C_1 = 0.15$. The flux has then been fractionally differentiated/integrated for $h \in [-1 : 1]$. We can see that for negative h we are able to manipulate the scaling such that it becomes curved however for positive h there is no amount of correlation that changes the TMs curvature in an opposite convex fashion. We must therefore look to other 'manipulations' of the data in order to obtain this characteristic convexity.

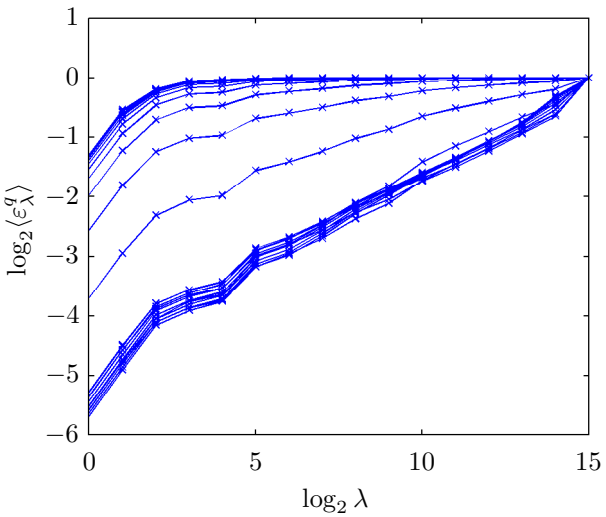

Figure B.20: The trace moment at $q = 1.5$ of the convoluted, simulated, energy flux $\varepsilon_c = \varepsilon * \lambda^h$ for $h \in [-1 : 0.1 : 1]$ from top to bottom.

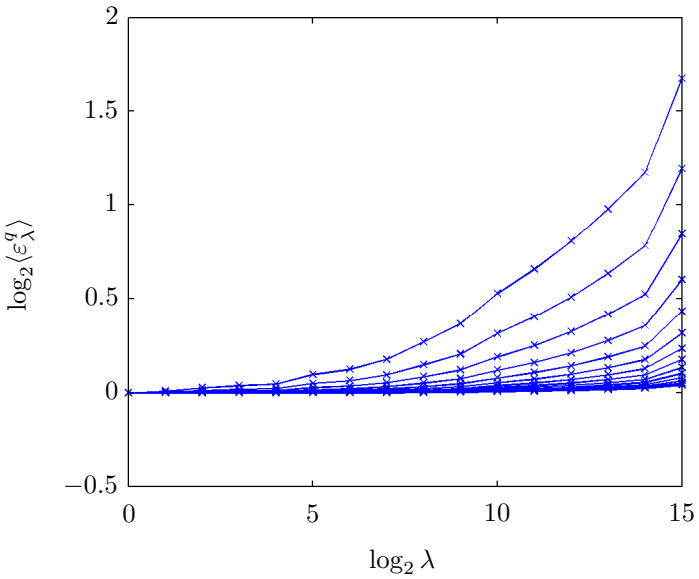

Figure B.21: The trace moment at $q = 1.5$ of $\varepsilon + c$ for $c \in [5 : 10]$ from top to bottom.

The multiplication of two scaling processes will sum the C_1s of the processes. It is therefore not the influence of a scaling process that is causing this behaviour. A simple result that shows how easily the scaling of a process can be destroyed is the addition of a constant to the scaling flux i.e. $\varepsilon(t) + c$, which is a way to increase the mean of the process without increasing the singularities – the non-scaling way to smooth the singularities (figure B.24).

Indeed, the addition of a constant results in the convex curving of the TMs and DTMs as it appears in the data. But, the corresponding homogeneous function $h(q, \eta)$ (figure B.22) isn't what we find in the empirical data.

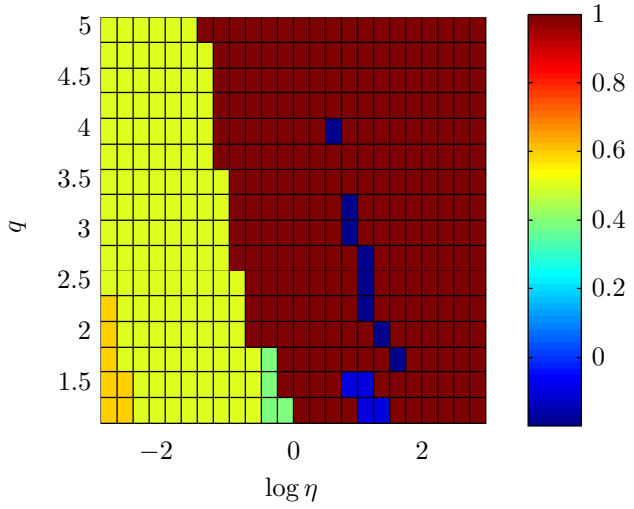

Figure B.22: Surface plot of $h(q, \eta)$ estimated on $\varepsilon + 5$.

Instead of simply adding a constant (that should be vanishing with Δu), a more realistic approach is to add a Gaussian noise, $X(t)$, to the simulated flux: $\varepsilon_N(t) = \varepsilon(t) + X(t)$. Figures B.23 and B.24 plot ε_N for Gaussian noises with increasing power and their corresponding TMs. As with the addition of a constant we can see that the addition of a non-scaling white-noise will also result in a convexity (proportional to the power) in the TMs estimated on ε_N. If we look to the corresponding figure B.25 of $h(q, \eta)$ estimated on ε_N, the characteristic non-linear surface observed in the empirical data now becomes apparent. In the next section we will discuss the consequences of the mixing of processes and whether or not the UM framework needs to be adapted.

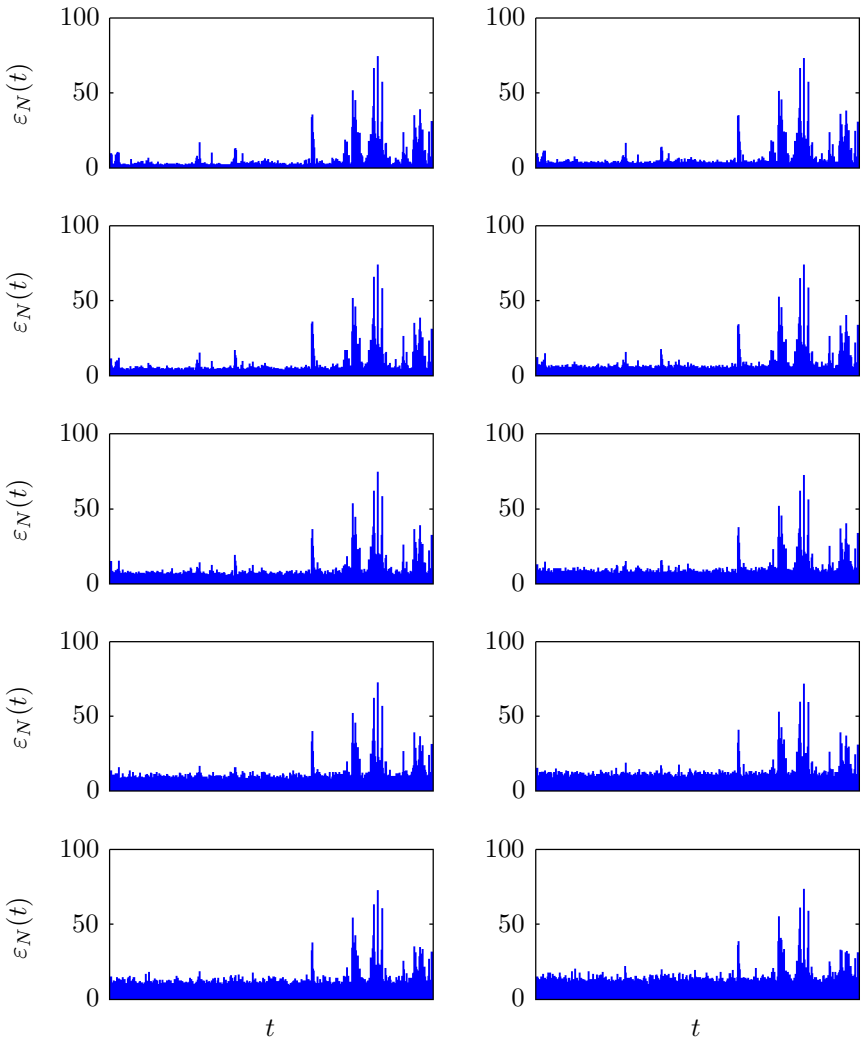

Figure B.23: Plots of the simulated velocity field, $\varepsilon_N(t)$, i.e. the simulated flux, with an added white-noise, $X(t)$, where $X(t)$ has increasing power 10^{a_N} for $a_N \in [0:9]$ (from left to right and from top to bottom).

By increasing the power of the white noise we are increasing the range of the (non-scaling) singularities of $X(t)$. The scale that will be influenced by $X(t)$ therefore increases with the increase in the power of $X(t)$.

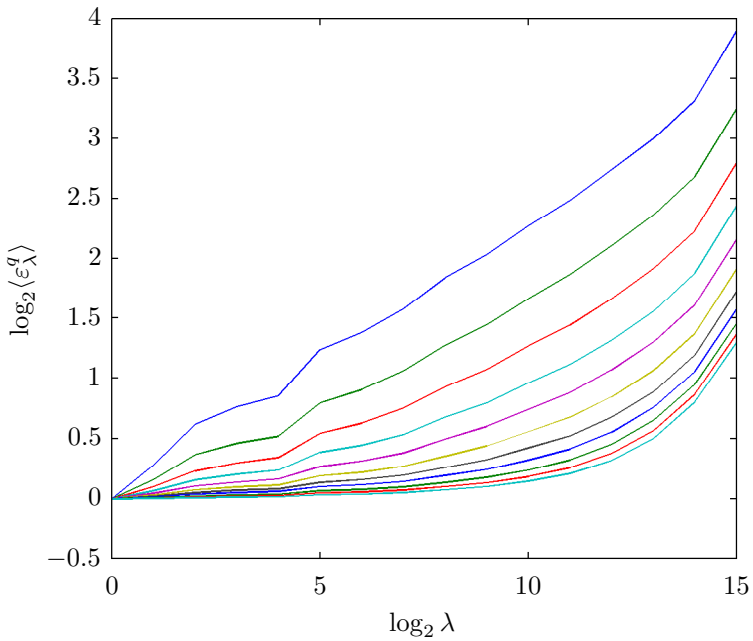

Figure B.24: Trace moment at $q = 1.5$ calculated on ε_N for the increasing (from top to bottom) powers of added white noise of figure B.23.

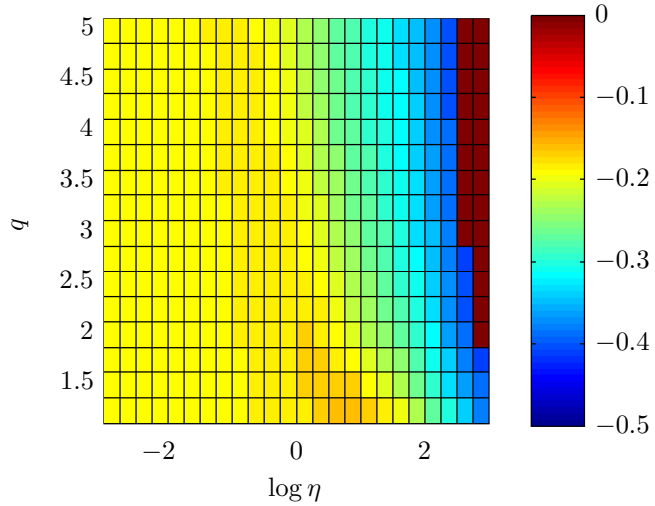

Figure B.25: Surface plot of $h(q, \eta)$ estimated on ε_N for $a_N = 5$.

Publications

MULTIFRACTAL ANALYSIS AND SIMULATION OF WIND ENERGY FLUCTUATIONS

G. F. Fitton

Université Paris Est, Ecole des Ponts ParisTech, LEESU
6-8 Av. Blaise Pascal - Cité Descartes
Champs sur Marne, 77455 Marne la Vallée Cedex 2, France
George_Fitton@Yahoo.co.uk

Abstract

One of the key thematic areas for the development of future research in wind energy is wind conditions. To better understand this topic requires the development of new numerical methods and measuring techniques capable of reaching micro scale effects. My PhD thesis will focus on advanced characterisation of micro-scale wind turbulence with respect to non-Gaussian heavy tailed statistics and short term extreme events (gusts) on the scales of 1 to 1000 m and/or 1 to 100 sec. Based on experimental data, multifractal wind field models with high frequency turbulent dynamics will be developed. Such models are promising candidates for providing initial flow conditions for turbulent dynamic CFD calculations. A combination of multifractals with other more classical models can open new perspectives for many industrial applications.

Introduction

Over the last twelve months I have studied mathematical and numerical methods for modelling atmospheres and oceans; specifically fluid dynamics, atmospheric physics, conservation laws and numerical techniques. The outcome, an ability to model fluid and gas flow based on an understanding of governing equations and their physical properties. I am now looking to apply this knowledge to a new and exciting area of research, multifractals.

Traditional numerical approaches are forced to transform partial differential equations (PDE's) into ordinary differential equations (ODE's) by implicitly imposing the regularity and homogeneity assumptions. The problem encountered with these assumptions is a violation of the fundamental symmetry of the non-linear PDE's which can lead to a reduction in variability. This then questions the relevance of the resulting numerical codes because their scales are different from those of the observations. Using multifractals on the other hand allows us to understand and to model extremely variable space-time fields thus accounting for extreme events (gusts). If properly applied, I believe a multifractal wind analysis and model will be a greatly beneficial contribution to weather/wind prediction.

Atmospheric dynamics and the cascade paradigm

In 1922, the meteorologist Lewis Richardson in his book "Weather Prediction by Numerical Processes" expressed the idea of atmospheric dynamics. In poetic form, he suggested that the turbulence in the atmosphere produced by an outer force, giving rise to kinetic energy at big scales, is transferred to smaller scales

without dissipation until the terms of viscosity can not be neglected anymore. The theory of turbulence went on with the work of [3] about homogeneous turbulence. With the help of the so-called refined self-similar hypothesis [4], the velocity increment singularities were linearly related to the singularities of the energy flux whose energy spectrum obeys the famous -5/3 law over the scaling range (Fig.1). However, it required some time and various developments before providing well-defined cascade models ([8]; [5]; [2]).

Simple cascade models were developed to explain how geophysical variability occurs over a very large range of scales supposing that the same elementary process act at each scale. In the pedagogical case of "discrete" in scale cascade models "eddies" are defined by the hierarchical and iterative division of a D-dimensional cube into smaller sub-cubes (see Fig. 2), with a constant ratio of scales $\lambda = L/l$, where l is the scale of observation, L the outer scale. The energy flux is modulated in a multiplicative way from one scale to the next smaller scale. Thus, after a big number of cascade steps, the energy is concentrated in small areas. Since we simply follow how the turbulent energy flux becomes more and more inhomogeneous as large structures break up into smaller and smaller scales, cascades are a very general paradigm. After 1983 multiplicative cascades evolved to a multifractal theory [6], allowing a statistic evaluation of the variability for all scales.

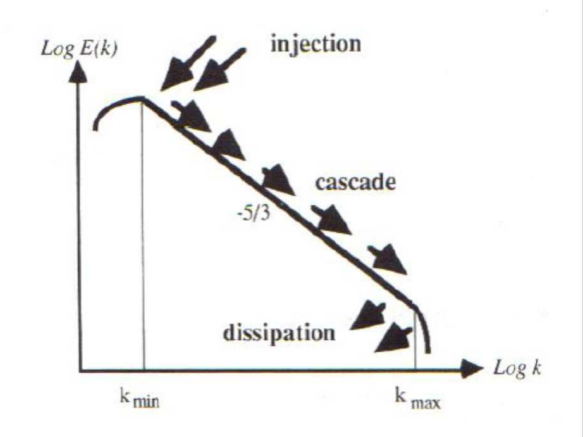

Figure 1: Schematic illustration of the Kolmogorov-Obukhov spectrum that follows the power law with the exponent -5/3, developing Richardson's idea

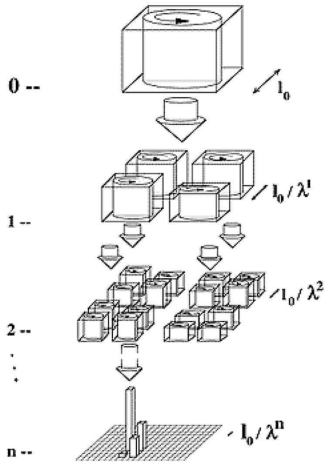

Figure 2: Schematic illustration of "discrete" in scale cascade model. The energy is concentrated in small areas after a big number of cascade steps

In a very general manner, multifractals are space or space-time fields that have structures at all scales. The wind velocity field is strongly turbulent and variable over a wide range of scales in space and time. Figures 3 and 4 display examples of numerical simulations for the city of Marseille (France) performed with the mesoscale model MESO-NH (developed by Meteo-France and the Laboratoire d'aérologie) to illustrate such a variability. Multifractal analyses of simulations can be used to get better incite on a performance of numerical models. For instance, [7] analysed a variability of these data by estimating statistical moments at various scales. He concluded that for the horizontal wind velocity field the results agree with earlier empirical and theoretical results within the realms of statistical variability. On the contrary, the vertical wind velocity field does not coincide with a scaling theory.

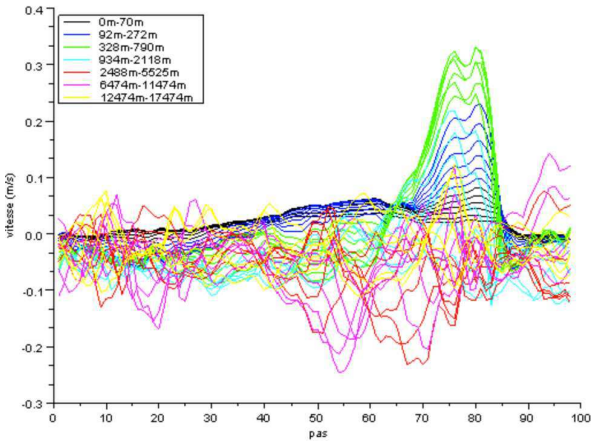

Figure 3: Time fluctuations of a vertical component of wind velocity at city of Marseille (France) simulated by the MESO-NH model.

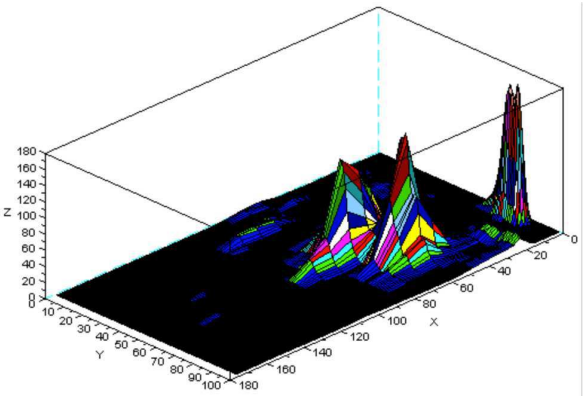

Figure 4: Space-time intermittency of the energy fluxes (z-axis) simulated during 100 time steps of MESO-NH model with Buoyancy forces.

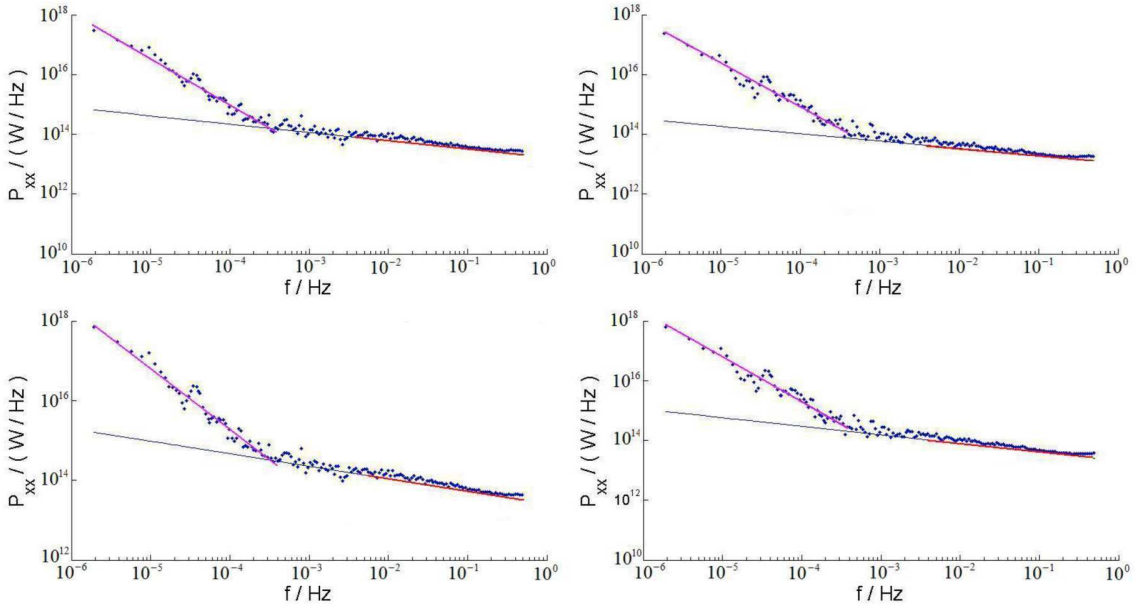

Figure 5: (from Fuchs (2008): The spectra calculated from the energy fluxes of the wind data measured at the altitude of 23m (left) and 43m (right). The spectra correspond to a horizontal component of the wind measurements (top) and to three dimensional wind data (bottom).

Intermittency and multifractal wind gusts

Multiplicative models produce hierarchies of self-organised random structures that yield not so trivial consequence. As already mentioned, higher and higher levels of 'activity' of the field are concentrated on smaller and smaller fractions of space. That is the intermittency, also referred to as micro scale effects that appear in the range of 1 to 1000m or 1 to 100sec. Fluctuations on these scales are known to show extremely non-Gaussian statistics, i.e. with probabilities of extreme events (wind gusts) much higher than for quasi-

Gaussian fields. These more frequent intermittent bursts may cause additional mechanical loads, deviations in the expected power production and large short time power fluctuations. Our current understanding of multifractal extremes points out the necessity - as well as the possibility - of developing a new extreme value theory that could deal with processes having long-range dependences. At the same time, there remains the fundamental question of establishing a more direct connection between multifractals and the deterministic-like nonlinear equations that are supposed to generate them, in particular the Navier-Stokes equations. This would have many fundamental consequences such as opening the road to new renormalisation techniques able to grasp intermittency as well as to a better knowledge of the mathematical properties of the solutions of these equations.

Acknowledgments

The organisers of the EAWE 6th PhD Seminar on Wind Energy for allowing me to take part.
The European Wind Energy Academy (EAWE) for the training opportunity.
Marie Curie Initial Training Network (EU-FP7-ITN-WAUDIT) for financial support during my PhD.

References

[1] Fuchs K. 2008, Multifractal Analysis of the wind in the wind park ERSA, Mémoire de Projet de fin d'Etude, Ecole des Ponts ParisTech, 74p

[2] Frisch, U., P. L. Sulem, et al. (1978). "A simple dynamical model of intermittency in fully develop turbulence." Journal of Fluid Mechanics 87: 719-724.

[3] Kolmogorov A. N., 1941, A local structure of turbulence in an incompressible viscous fluid for very large Raynolds numbers. Proc. Acad. Sci. URSS.,Geochem. Sect. 30, 299-303

[4] Kolmogorov A. N., 1962, A refinement of previous hypotheses concerning the local structure of turbulence in a viscous incompressible fluid at high Raynolds number. J. Fluid Mech. 83, 349

[5] Mandelbrot, B. B. (1974). "Intermittent turbulence in self-similar cascades: divergence of high moments and dimension of the carrier." Journal of Fluid Mechanics 62: 331-350.

[6] Menyah K. 2009, Dynamique dans le modéle MESO-NH, une analyse multifractale, Mémoire de Projet de fin d'Etude, Ecole des Ponts ParisTech, 44p.

[7] Schertzer, D. and S. Lovejoy (1983). On the dimension of atmospheric motions. Turbulence and Chaotic phenomena in Fluids, IUTAM, Kyoto, IUTAM.

[8] Yaglom A. M., The influence on fluctuaion in energy dissipation on the shape of turbulent characteristics in the inertial interval. Sov. Phys. Dokl. 2,26

Scaling Of Turbulence In The Atmospheric Surface-Layer: Which Anisotropy? for publication in *Journal of Physics: Conference Series*

G. Fitton[1], **I. Tchiguirinskaia**[1], **D. Schertzer**[1] **and S. Lovejoy**[2]

[1]Universitè Paris Est, Ecole des Ponts ParisTech, LEESU, 6-8 avenue B. Pascal, Citè Descartes, 77455, Marne-la-Vallèe, France; tel. : +33 1 6415 3607, fax: +33 1 6415 3764

[2]McGill University, Physics department, 3600 University street, Montreal, Quebec, Canada

E-mail: fittong@cereve.enpc.fr

Abstract. This paper aims to provide an insight into the fundamental relationships between large and small scale wind velocity fluctuations within the boundary layer through careful analysis of measuring mast wind velocities. The measuring mast was in a wind farm on top of a mountain (with steep inclines of about 30°) on an island surrounded by the sea which meant the horizontal mean flow fluctuations were dominated by buoyancy forces and vertical shears at large scales (above 500m). Thus using a variety of methods including spectral, integrated spectral, integrated cospectral and multifractal analysis we were able to clearly dispel the relevance of 2D turbulence and give on the contrary some credence to the multifractal anisotropic model.

1. Introduction

The topic of wall-bounded turbulent flows has received continuous attention since the formulation of the boundary layer concept. Although significant experimental work has been carried out over the past decade on wall-bounded turbulence, many of the outstanding issues remain open. New experiments, driven by the desire to generate data at high Reynolds numbers, have led to new questions related to scaling and the role of the largest scale motions. A recent paper (1) combines the outputs of international cooperative research on high Reynolds number wall-bounded turbulence and highlights the key issues that need to be resolved, e.g. the existence of a logarithmic sublayer, validity of the locally isotropic turbulence hypothesis and the relations between inner and outer scaling. The authors particularly promote the idea that "extracting a theory by sifting through the data more carefully is the missing element". In response to this, our paper discusses a possibility to explain the observable scaling behaviour of atmospheric turbulence at low altitudes with the help of an anisotropic multifractal model (2).

2. Data Description and Pre-processing

We had available to us six-months (from 16/11/2002 to 15/05/03) of wind velocity and temperature measurements from a wind farm test site subject to wake turbulence effects. The wind farm was in the North of Corsica (France), 3km from the sea on the East and West and 4km on the North. The site has an annual mean wind velocity of about 7.6m/s at 40m. There

are 20 turbines in total with 13 (Ersa site) situated along the crest of Torricella and 7 (Rogliano site) along the crest of Petraggine. The altitudes of the crests range from 480 to 520m with a 30° incline across most of the distance. All of the turbines have a hub height of 60m and are positioned 117m apart at the Ersa site and 136m apart at the Rogliano site.
The measurements came from three 3D sonic anemometers with a 10Hz data output rate. The anemometers were positioned at 22, 23 and 43m on a mast in the centre of three concentric turbines at the Ersa site. The first anemometer at 22m was positioned directly on the mast. The second, at 23m, was positioned at the end of a horizontal pole with length 2.5m and azimuth 134°. The highest mast at 43m was positioned on a 3m pole on top of the mast.
When using data from devices not positioned directly on top of the mast (those at 22 and 23m), it was necessary to take into account the possibility of the interaction of the wind with the mast, thus destroying the quality of the measurements. To check for this problem we took data with daily mean wind passing directly through the mast (48 of the 102 days) and did a cross comparison at different heights. We observed large numbers of anomalous small fluctuations in the vertical component (high frequency noise through spectral representation) being measured at 22m. This is likely due to the vertical fluctuations being much smaller in magnitude making the measurements increasingly sensitive to disturbances at small scales. It is important to note that this was not observed at 23 and 43m thus aiding our confidence in the quality of data at these heights and our observations thus from.
Although confident our data was free of physical interference, corrupt and missing data files made it difficult to have long runs of continuous error free (*clean*) data. Out of the 181 days of data only 10 of the days were time continuously clean. For non-time continuous data (independent samples) there were 161 days of clean data. Note that the requirement for clean data at all three heights reduced the number of independent samples, at for example 43m, from 161 to 102 days.

3. Spectral Analysis

3.1. Overview

A spectral representation was used to determine the overall scaling behaviour of our data. This is because a random field is *scaling* when its spectrum follows a power law of the form $E(\omega) \propto \omega^{-\beta}$ (see (3)) where E is a function of frequency, ω, in Fourier space and β is the often called "spectral slope" estimated by plotting the spectra on a log-log graph (see section 3.2 for distributions of β for the data). The (co) spectrum of two fields (which are identical for the spectrum) is the real part of the scalar product of their Fourier transforms. The Fourier transforms were computed using the fast Fourier transform (FFT) algorithm (see sections 3.3 and 3.4).
With the use of the FFT algorithm we were restricted to data of sizes 2^n where $n \leq \log_2(N_s)$ and N_s is the sample size. Thus, given the longest time continuous sample was 10 days, the maximum range of scales achievable was of about 6 orders of magnitude. While a spectral representation of long runs of data is indispensable to evaluate the overall scaling behaviour and its limitations, sample averaged estimates are used to define the spectral exponents more precisely (see section 3.3). Since averaging requires more than one sample, given such a large discontinuous dataset, it was important to choose a suitable subsample size, N_{ss}, to obtain the most amount of information from the data. For the majority of this study we focused on analyses with $N_{ss} = 2^{19}$ (section 3) with a brief discussion on the benefits of a larger subsample ($N_{ss} = 2^{22}$) in section 4.

3.2. Probability Distributions of Spectral Slopes β

The spectral analyses showed similar scaling behaviour, consisting of three subranges divided by two breaks, for all three velocity components u, v, w and temperature θ. The first two subranges, R_{HF} and R_{MF}, over high and mid frequencies respectively, were partially in agreement with

Kolmogorov's -5/3 law of locally isotropic turbulence. As described in (3), the exponent will define an inertial subrange for all three velocity components adjoined by a -1 power law (at sufficiently high Reynolds numbers as discussed in (1)), obtained from dimensional analysis of the logarithmic sublayer, over smaller wave numbers and frequencies. A 3D inertial range was observed but only up to between 1 and 100 seconds at which the vertical component diverged from the scaling of the horizontal components and temperature and remained dissimilar until the third subrange, R_{LF}, at low frequencies. The adjoining -1 power law was observed for all three components and temperature but as mentioned before the length and position varied depending not only on the component but on the day.

More specifically for the positions of high to mid frequency breaks, X, we observed variations between 5 and 100 seconds and for the positions of mid to low frequency changes in subrange scaling, Y, we observed variations between 10 minutes and 2 hours. The change in position of the breaks in scaling are likely due to the changes in wind direction however it was difficult to see correlation because of reasons later discussed in section 3.4.

Because the position and length of each subrange varied greatly for each sample, it was necessary to also calculate β over varying positions and lengths and not simply over the whole range. A simple algorithm determined the position of the breaks based on the minimum and maximum of $\Delta\beta = \beta_{n+1} - \beta_n$ over the range i of $E(\omega_i) \approx \omega_i^{\beta_n}$ where $i = 2^n, ..., 2^{n+\Delta n}$ and $n = 1, ..., \log_2(N_s - \Delta n)$. The value $\Delta n = 5$ was found to be the most appropriate compromise between the best fit, R^2, and the loss of information at the sample bounds.

The following probability density functions (PDF)s of β consist of two types of plot. Those where the distributions do not differ significantly for horizontal and vertical (Figures 1 and 2, one plot per figure in blue) and those that do (Figure 3, two plots compared per figure with horizontal in red and vertical blue).

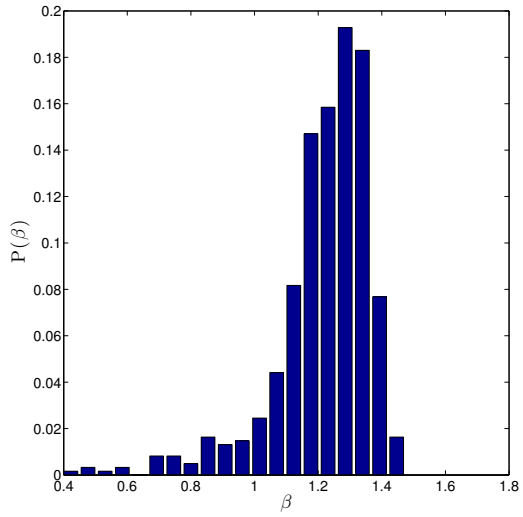

Figure 1. PDF of spectral slopes for high frequency subrange $R_{HF} = [0.2\text{s} : X]$ with X varying between 5 and 100 secs. Mean $\beta = 1.21$ (u, v and w at 23 and 43m).

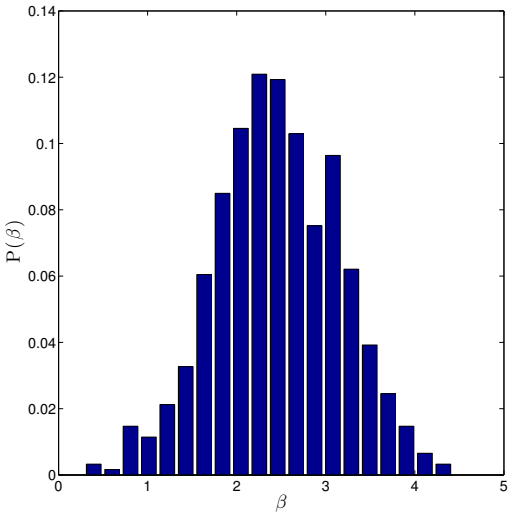

Figure 2. PDF of spectral slopes for low frequency subrange $R_{LF} = [Y : 0.1 \times 2^{19}\text{s}]$ with Y varying between 10 mins and 2 hrs. Mean $\beta = 2.45$ (u, v and w at 23 and 43m).

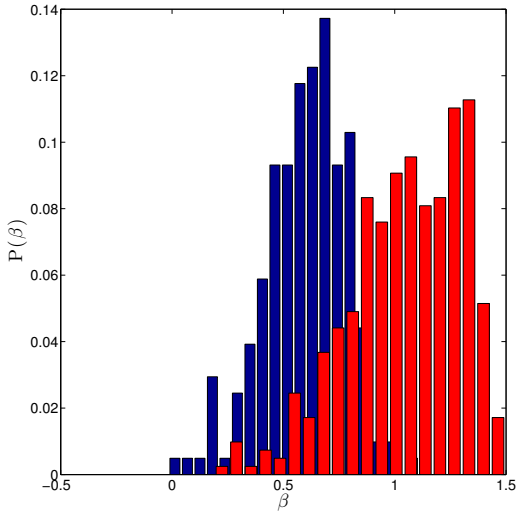

Figure 3. PDF of spectral slopes for mid frequency subrange $R_{MF} = [X : Y]$. Mean $\beta = 1.05$ for horizontal components in red and mean $\beta = 0.59$ for vertical component in blue (u, v and w at 23 and 43m).

Some of the spectral exponents for the horizontal components in Figure 3 (over 10% of the values) were comparable with those of the high frequency subrange in Figure 1. This suggested there were days where the scaling was observable up to longer time scales. Thus following this observation the data was filtered based on β for the mid frequency range, R_{MF}, as discussed in the next section.

3.3. Averaged Spectra

We averaged the spectra of the extreme case mid frequency scaling behaviour to obtain better estimates of the spectral exponent. For a fair comparison we needed an equal number of

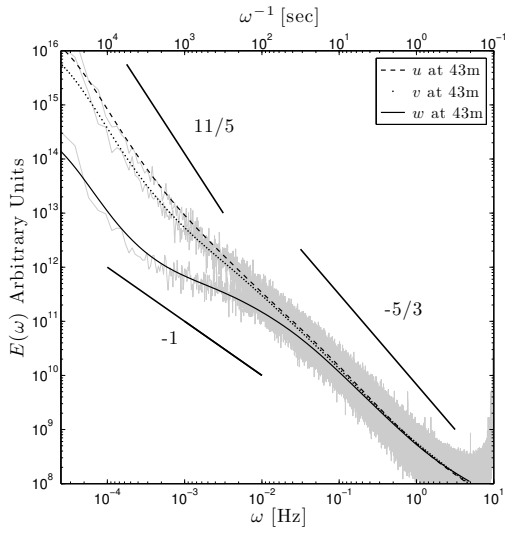

Figure 4. Energy spectra of u, v and w at 43m averaged over 11 unperturbed days. The dashed, dotted and solid lines are the smoothed interpolation (using three-point moving average method) of the spectra.

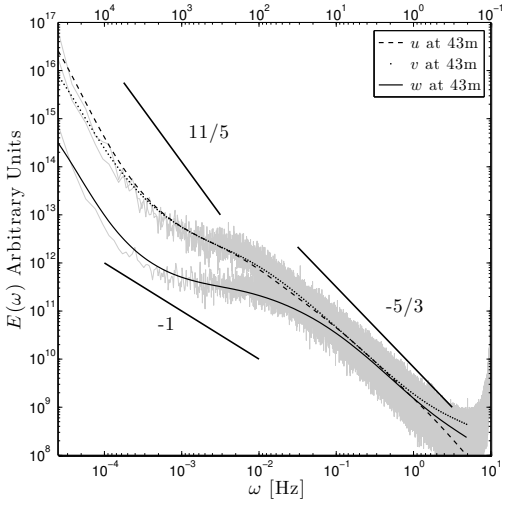

Figure 5. Energy spectra of u, v and w at 43m averaged over 11 perturbed days. As in Figure 4 the dashed, dotted and solid lines are the smoothed interpolation of the spectra.

subsamples for each case. We found the bounds $\beta \geq 1.20$ and $\beta \leq 0.80$, which we define simply as *unperturbed* and *perturbed* scaling respectively (see Figures 4 and 5 for the reasoning behind this), gave a suitable representation of the extreme case behaviour (11 days for each case). Note the filtering of the spectral exponent to select these days was only applied to the horizontal u-component at 43m.

Our results confirmed unique scaling over small scales with $1.21 \leq \beta \leq 1.34$ for all three velocity components up to between 15 and 50 seconds at which the scaling of the vertical w-component changes to an adjoining -1 power law subrange with $0.34 \leq \beta \leq 0.65$ in agreement with wall-bounded theory. Spectral slopes being lower than 5/3 and 1 could be understood with the intermittency correction (see section 4). Such high intermittency corrections were particularly relevant for our case study due to the increased likelihood of small fluctuations from the wind turbines and complex terrain.

The horizontal velocity components u and v continued to scale, almost identically, up to between 10^2 and 10^3 seconds before a departure from the scaling regime was seen. Figure 4 shows a spectral exponent (mean $\beta = 2.28$ over R_{LF}) consistent with Bolgiano-Obukhov theory (7; 8) that predicts a power law of -11/5 for a buoyancy force subrange i.e. $\beta = 2H + 1$ with $H = 5/3$ for vertical shears. This is not the case for the perturbed days whose spectral exponent (mean $\beta = 2.99$ over R_{LF}) is closer to that of the Lumley-Shur law or 2D turbulence spectral exponent of -3 (see section 5 for a more in depth discussion on this topic).

3.4. Integrated Spectra

Figures 6 and 7 display the integrated spectra of all three velocity components for perturbed and unperturbed days. The main interest in presenting the data this way was the clarity with which the positions of the breaks in the scaling (defined by the positions of the peaks and troughs in energy) could be seen and compared with the positions of the breaks in Figures 4 and 5. Such clear separations in the scaling allowed us to obtain estimates of the integral length scales using the empirically derived formulae

$$L_u = 10.3z, \;\; L_v = 7.5z \;\; \& \;\; L_w = 0.5z, \tag{1}$$

as suggested in (4). Tables 1 and 2 show the estimates of the characteristic velocity U_w and the relative frequencies $\Delta t'_u$ and $\Delta t'_v$ derived from Δt_w.

Table 1. Table of estimates derived from length scale coefficients of (4) using Δt_w at 43m.

43m	L_w [m]	Δt_w [s]	U_w [m/s]	$\Delta t'_u$	$\Delta t'_v$
unperturbed	21.5	50	0.43	1,050	750
perturbed	21.5	15	1.43	316	226

Table 2. Table of estimates derived from length scale coefficients of (4) using Δt_w at 23m.

23m	L_w [m]	Δt_w [s]	U_w [m/s]	$\Delta t'_u$	$\Delta t'_v$
unperturbed	11.5	30	0.38	636	454
perturbed	11.5	8	1.44	168	120

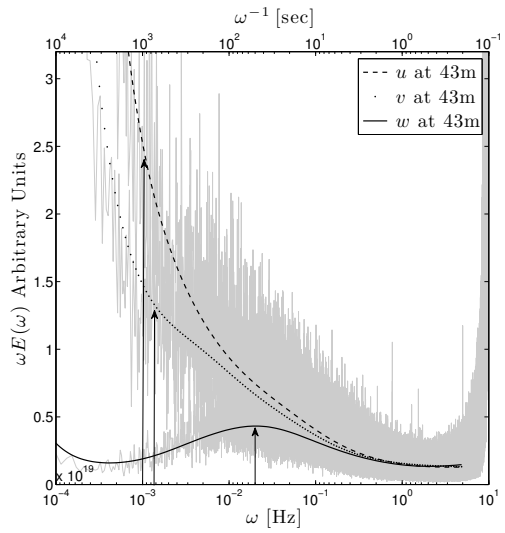

Figure 6. Integrated energy spectra of u, v and w at 43m averaged over 11 unperturbed days. The dashed, dotted and solid lines are the same interpolation as for Figures 4 and 5. The arrows correspond to $\Delta t'_{u,v}$ calculated from the length scales derived in (4) (see Table 1).

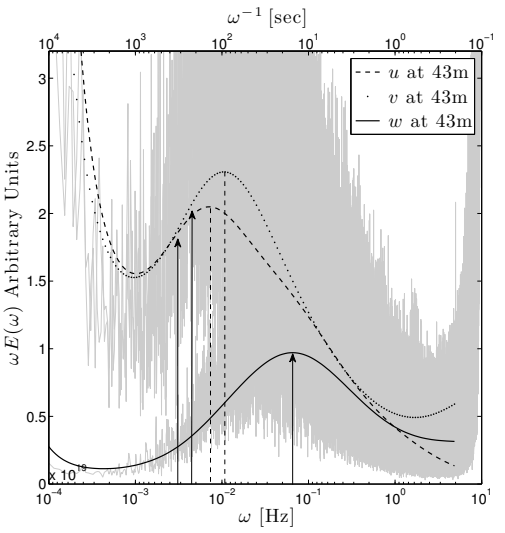

Figure 7. Integrated energy spectra of u, v and w at 43m averaged over 11 perturbed days. The dashed vertical lines correspond to the integrated spectral peaks over the mid frequency subrange.

In addition, given we have the characteristic length scales and velocity we can estimate a Reynolds number of about $10/1.5 \times 10^{-5} \sim 10^6$. This estimate confirms that the investigated wind field exhibits fully developed turbulence and remains consistent with the Reynolds numbers of the boundary layer experiments summarised in (1).

We can see from Figure 6 that the change in scale of the horizontal and vertical wind components seems to be in good agreement with the semi-theoretical results of (4) obtained for the atmospheric surface layer. On the contrary, Figure 7 demonstrates that the -1 power law appears much earlier than the predicted values defined by Eq. (1). A possible explanation for this could be the wake turbulence effects attributed to the turbines. As underlined in (5) large fluctuations in the wind during the trial period of the wind farm often led to interruptions in the functioning of the turbines during days when either strong or weak winds were being registered. Two examples of contrasting wind speed and direction occurred on October 26$^{\text{th}}$, 2002 and April 26$^{\text{th}}$, 2003 where very strong Westerly winds meant every turbine was operating and very weak South-Easterly winds meant every turbine had to be stopped for each of the days respectively. Both events took place at the Ersa site. Given the very low characteristic velocities $U_w \sim 0.4$ (see Tables 1 and 2) coincide with the better scaling of the horizontal velocity components u and v it is possible this may have been due to the stopping of the turbines in events similar to those aforementioned.

Given this result one would expect to see strong correlation between mean wind speeds, direction and scaling. This however is not the case (correlation coefficient less than 0.5). One possible explanation is that although we have 11 days of extreme behaviour at each end of the spectrum the other 80 days consist of "mixed" periods of functioning. What this means is that by example on April 28$^{\text{th}}$, 2003 all of the turbines on the site were shut down up to 9h30 due to very weak South-Easterly winds. Then at 12h20 due to a much stronger South-Easterly wind 10 of the 20 turbines began to function. This goes some way into explaining why there is no clear correlation.

3.5. Integrated Cospectra

A condition of the applicability of the coefficients derived in (4) is that the structures of the surface-layer turbulence respect the statistical mirror symmetry with respect to the (x, z) plane i.e. when the direction of the horizontal u-component coincides with the direction of the mean wind $E(\omega) = \{E_{uv}; E_{vw}; E_{v\theta}\} = 0$

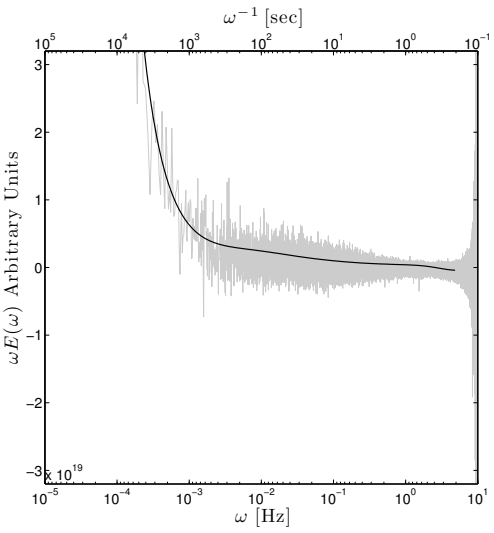

Figure 8. Energy cospectra of u and v and w at 43m averaged over 11 unperturbed days.

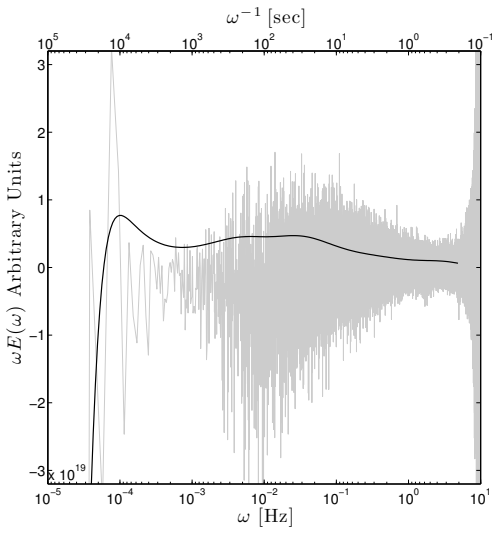

Figure 9. Energy cospectra of u and v and w at 43m averaged over 11 perturbed days.

Although some of our data and analyses agreed with the length scales of (4) our cospectra are not compatible with the classical theory. As illustrated by Figure 8, we found that the cospectrum, E_{uv}, returned values that were of the same order as the previously calculated spectra over the inertial range and were therefore not neglectable. Furthermore scaling was present the cospectra E_{uv} similar to the scaling of the integrated spectra (see Figures 6 and 8 for comparison). This demonstrated that the direction of the horizontal u-component of velocity did not coincide with the direction of the mean wind. In fact the mean wind was seemingly directed in the South-East or North-West directions explaining the strong correlation between u and v components. Winds in this direction have the least influence from wake effects on the mast. In comparison, Figure 7 displays very strong fluctuations of the cospectrum over the same frequencies that combined with the characteristic velocity $U_w \sim 1.5$m/s for perturbed days (see Tables 1 and 2), gave a range of scales comparable with the height of the turbines and the associated scales of wake-created coherent structures.

In addition to the cospectrum of the horizontal components we looked at the correlation of the other velocity components and temperature. Figures 10 and 11 display the behaviour of the corresponding covariance, which is the buoyancy flux, $E_{w\theta}$, in Fourier space. The inverse FFT of $E_{w\theta}$ from the data in these figures was positive. This meant we were observing buoyancy forces thus confirming the presence of anisotropic scaling i.e. that we have vertically dominating shears at large scales and horizontally dominating shears at smaller scales (up to the scales of a few centimetres).

The physical reasoning for this lies in the topographical features of the wind farm. Because the wind farm is close to the sea, strong convective forces drive atmospheric structures vertically. Large structures intercept with the mountain and are pushed by prevailing winds upwards against the side of the mountain and across the face of the mast. Since the mountain is surrounded by such a steep slope we would expect this feature to be prevalent throughout

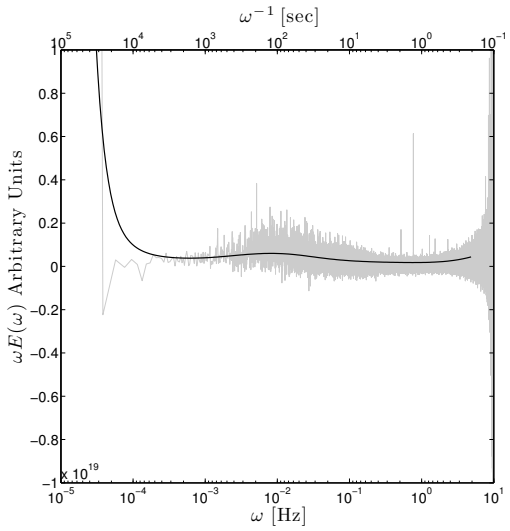

Figure 10. Energy cospectra of w and θ and w at 43m averaged over 11 unperturbed days.

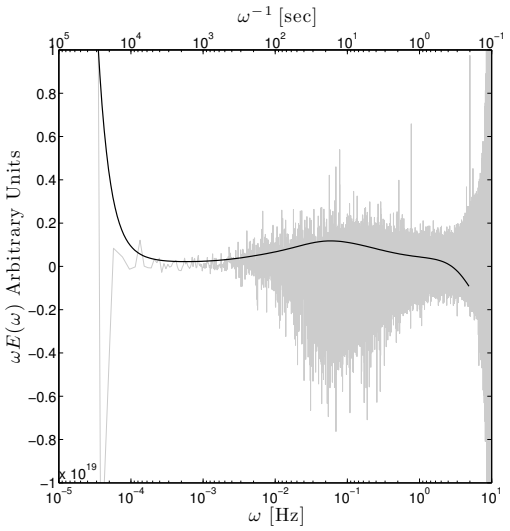

Figure 11. Energy cospectra of w and θ and w at 43m averaged over 11 perturbed days.

all of our data at large scales. With a characteristic velocity $U_w \sim 0.5$ for unperturbed days (Tables 1 and 2) the departure from Kolmogorovs scaling gave a rough estimate of 500m. This is a large scale that is indeed compatible with the dominating height of the area.

4. Multifractal Analysis

We have seen from Figures 1 and 2 that we have unique scaling defining an inertial range for small scales where the spectral exponent, β, varies between 1.21 and 1.34 and is thus lower than the expected spectral exponent 5/3 predicted by Kolmogorov. The difference corresponds to the intermittency correction (3) that, as discussed below, is due to very high heterogeneity of the mean field for atmospheric turbulence. Its increase implies an increase of wind extremes which is expected for a wind farm. Thus one may consider a spectral exponent $\beta = 2H + 1 - K(2)$ to account for this, where $K(2)$ is the second order scaling moment function. For R_{HF} $0.34 \leq K(2) \leq 0.55$, for R_{MF} $0.33 \leq K(2) \leq 0.42$ and for R_{LF} $0.16 \leq K(2) \leq 0.32$. For universal multifractals (2), the function $K(q)$ is given by:

$$K(q) = \frac{C_{1,\varepsilon}}{\alpha - 1}\left(q^{\alpha} - q\right) \tag{2}$$

where q is the order of moment and α and C_1 are the multifractal parameters defining the degree of multifractality and the inhomogeneity of the mean field respectively. They are estimated with the use of the double trace moment (DTM) method based on the following relation

$$K(q, \eta) = K(q\eta) - qK(\eta) = \eta^{\alpha} K(q, 1). \tag{3}$$

Normally α is obtained by fixing q and obtaining the slope of $|K(q, \eta)|$ as a function of η on a log-log graph. Alternatively, given we know the power law relation between the flux and the velocity i.e. $\varepsilon \propto \Delta V^3$, we can inversely fix $\eta = 1, 3$ for ε and ΔV respectively and obtain α as the slope of $K_{\Delta V}$ and K_{ε} as a function of q also on a log-log graph where

$$K_{\varepsilon}(q, 1) = \frac{C_{1,\varepsilon}}{\alpha - 1}\left(q^{\alpha} - q\right), \;\; K_{\Delta u}(q, 3) = 3^{-\alpha}\frac{C_{1,\Delta V}}{\alpha - 1}\left(q^{\alpha} - q\right). \tag{4}$$

It is then elementary to derive the following relation

$$\alpha = \log_3(K_\varepsilon / K_{\Delta V}). \tag{5}$$

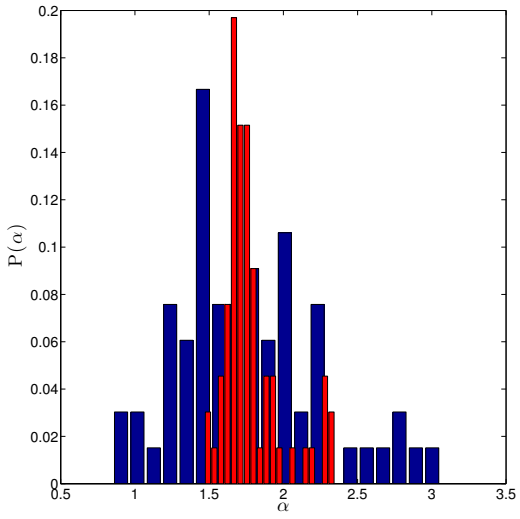

Figure 12. PDF of parameter α over high frequencies in red and low frequencies in blue for unperturbed days. Mean $\alpha = 1.78$ and 1.75 for high and low frequencies respectively (u and v at 22, 23 and 43m).

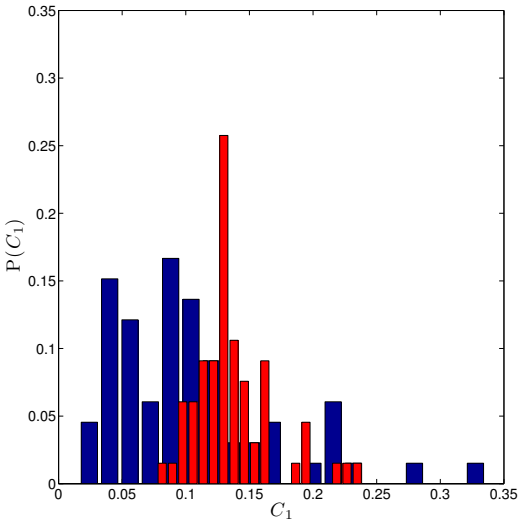

Figure 13. PDF of parameter C_1 over high frequencies in red and low frequencies in blue for unperturbed days. Mean $C_1 = 0.14$ and 0.1 for high and low frequencies respectively (u and v at 22, 23 and 43m).

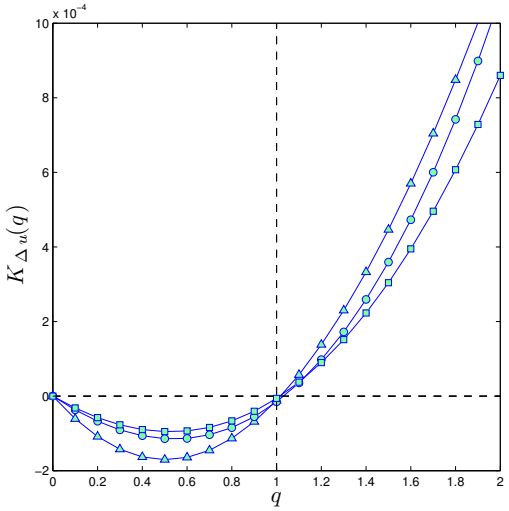

Figure 14. Scaling moment function over high frequency subrange for Δu where $\triangle$, $\circledcirc$ and $\square$ are the function at 22, 23 and 43m respectively.

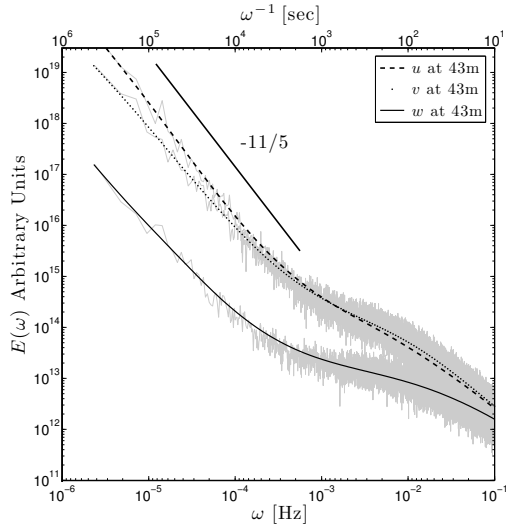

Figure 15. Plot of lower frequency scaling for $N_{ss} = 2^{22}$. Mean $\beta = 2.03$ with intermittency correction $K(2) = 0.22$ for u, v and w at 43m.

Figures 12 and 13 display PDFs of the multifractal parameters α and C_1 of the energy flux estimated on the data. Note that the distributions were only for the horizontal components since the vertical component did not scale up to large scales. For high frequency ranges the mean multifractality index of $\alpha = 1.78$ and the mean inhomogeneity of the mean field $C_1 = 0.14$. For low frequency ranges $\alpha = 1.75$ and $C_1 = 0.10$.
The strong multifractality of the data results in the strong non-linearity of the scaling moment function, as illustrated by Figure 14 for the horizontal u-component of the wind velocity at each of the three height measurements. For the large scale range R_{LF} in Figure 12 there were values of α that exceed the maximum of 2. These high values could be explained by either bad or limited scaling. Another explanation could be an inappropriate flux as discussed in section 5. In fact the two issues are closely related.
The PDF of the spectral exponents estimated over large scales (Figure 2) illustrates the difficulty in distinguishing the type of scaling law. In particular the Bolgiano-Obukhov -11/5 and Lumley-Shur -3 laws. Since the integrated spectra (Figures 6 and 7) clearly dismissed the idea of 2D turbulence, the spectral estimates could have been producing values in and around -3 simply because they were too sensitive to the limited length of data. This is confirmed in Figure 15 which displays a much clearer scaling behaviour over the large scales due to the use of longer data samples which results in a much better agreement with Bolgiano-Obukhov -11/5 law (mean $\beta = 2.03$ with intermittency correction $K(2) = 0.22$ for u, v and w at 43m).

5. The Multifractal Anisotropic Model

To take into account the dominant role of the vertical motion of large scale atmospheric structures, one may consider that the buoyancy force variance flux, ϕ, plays the same role as the energy flux, ε, in 3D turbulence but only along the vertical (2). This is contrary to the classical "buoyancy subrange" that postulates an isotropic turbulence (7; 8) with two different (horizontal and vertical) scaling regimes. This corresponds to the coupled sets of scaling equations (2; 6):

$$\left.\begin{array}{l} \Delta V(\Delta x) \stackrel{d}{=} (\varepsilon(\Delta x))^{1/3}\Delta x^{1/3} \\ \Delta V(\Delta z) \stackrel{d}{=} (\phi(\Delta z))^{1/5}\Delta x^{3/5} \end{array}\right\} \implies (\varepsilon(\Delta x))^{1/3} \approx (\phi(\Delta z))^{1/5} \text{ when } \Delta x^{1/3} \approx \Delta z^{3/5} \quad (6)$$

where $\Delta V(\Delta x)$ and $\Delta V(\Delta z)$ denote the horizontal and vertical shears of the horizontal wind respectively and the symbol $\stackrel{d}{=}$ means equality in probability distribution.
Because the scaling fluctuations of both fluxes are not neglected (due to their explicit scale dependency) we can define anisotropic scaling (as defined by the anisotropic multifractal model (2)) at all significant scales instead of two isotropic regimes, separated by a scaling break. This means the iso-shear surfaces will be ellipsoids rather than spheres and that the horizontal and vertical extents of the atmospheric structures will be equal only at the sphero-scale which is generally of the order of 10-20 centimetres. If the multifractality of two fluxes remain the same, the multifractal anisotropic model predicts that both weak and mean events will have codimensions that are in the same ratio as the corresponding degrees of non-conservation of the mean field:

$$\frac{C_{1,\varepsilon}}{C_{1,\phi}} = \frac{H_{1,\varepsilon}}{H_{1,\phi}} = \frac{5}{9}, \quad (7)$$

where $C_{1,\varepsilon}$ is the codimension for the energy flux over high frequency ranges, R_{HF}, and $C_{1,\phi}$ is the codimension for the buoyancy force variance flux over low frequency ranges, R_{LF}. Remember that the codimensions are for the horizontal components on unperturbed days only. In analogy to Eq. 4 , Eq. 6 implies $C_{1,\phi} = (5/3)^{\alpha}C_1 \approx 0.25$ when using the mean values $\alpha \approx 1.8$ and $C_1 = 0.1$ estimated for the energy flux over large scales (Figures 12 and 13). The ratio $C_{1,\epsilon}/C_{1,\phi} = 0.14/0.25 = 0.56$ which remains close to the predicted value $0.555\ldots$. This fully validates the multifractal anisotropic model.

6. Conclusion

The aim of this study was to explore the scaling behaviour of atmospheric velocity and temperature measurements in a wind farm test site subject to wake turbulence effects. Two or three scaling subranges were identified depending on the direction of the mean wind. We started from the investigation of possible relations between wind velocity scaling breaks and associated theories of turbulence in the atmospheric surface-layer. Once we verified that the investigated wind field exhibited fully developed turbulence it was possible to use multifractal methods to deal with the strong intermittency. For days with no interaction with the turbines the multifractal anisotropic model was fully validated. These preliminary results encourage a more extensive sifting through of the data for the future development of new theories for the atmospheric surface-layer.

Acknowledgments

This research is part of the EU-FP7 ITN WAUDIT (http://www.waudit-itn.eu). The authors also highly acknowledge the courtesy of Electricité De France (EDF) for providing wind velocity and temperature data as well as enlightening discussions with Eric Dupont and Luc Musson Genon.

References

[1] Marusic, I., McKeon, B. J., Monkewitz, P. A., Nagib, H. M., Smits, A. J. & Sreenivasan, K. R. 2010 Wall-bounded turbulent flows at high Reynolds numbers: Recent advances and key issues *Phys. Fluid.*, **22**, 065103.

[2] Schertzer, D. & Lovejoy, S. 1984 On the Dimension of Atmospheric motions. In: T. Tatsumi (Editor), Turbulence and Chaotic phenomena in Fluids, Amsterdam, Elsevier Science Publishers B. V., pp. 505-512.

[3] Monin, A. S. & Yaglom, A. M. 1975 *Statistical Fluid Mechanics*, Cambridge, MIT-Press, Vol. 2, pp. 874.

[4] Kader, B. A., Yaglom, A. M., & Zubkovskii, S. L. 1989 Spatial Correlation Functions of Surface-Layer Atmospheric Turbulence in Neutral Stratification, *Bound.-Lay. Meteorol.* **47**, pp. 233-249.

[5] Faggio, G. & Jolin, C. 2003 Suivi ornithologique sur le parc dèoliennes dErsa- Rogliano (Haute Corse) - Rapport final-SIIF/AAPNRC-GOC, 100p.

[6] Lazarev, A., Schertzer, D., Lovejoy, S. & Chigirinskaya, Y. 1994 Unified multifractal atmospheric dynamics tested in the tropics: part II, vertical scaling and generalized scale invariance, 115-123.

[7] Bolgiano, R. 1959 Turbulent spectra in a stably stratified atmosphere, *J. Geophys. Res.* **64**, 2226.

[8] Obukhov, A. N. 1959 Effect of Archimedian forces on the structure of the temperature field in a temperature flow, *Sov. Phys. Dokl.* **125**, 1246.

[9] Pinus, N. Z., Reiter, E. R., Shur, G. N. & Vinnichenko, N. K. 1967 Power spectra of turbulence in the free atmosphere, *Tellus* **19**, 206.

The Anisotropic Multifractal Model and Wind Turbine Wakes

G. Fitton[1], I. Tchiguirinskaia[1], D. Schertzer[1] & S. Lovejoy[2]
[1]Universitè Paris Est, Ecole des Ponts ParisTech, LEESU,
6-8 avenue B. Pascal, Citè Descartes, 77455, Marne-la-Vallée cedex 02, France;
tel.: +33 1 64 15 36 07, fax: +33 1 64 15 37 64
McGill University, Physics department, 3600 University street, Montreal, Quebec, Canada
E-mail: fittong@cereve.enpc.fr

Keywords: Universal Multifractals, Spectral Analysis, Wind Velocity Fluctuations and Power Estimation.

1 Introduction

A typical routine in wind field resource assessment, at the most basic level, consists of first to third order statistics of times series data. The quality of the time series data can range between 0.05 to 600 seconds. More often than not the frequency of data will be the latter of the two since it is the cumulative power over long periods of time that define the financial return from turbines and thus high-resolution data is deemed unnecessary. It is now evident that such coarse time series data are no longer sufficient for a representative assessment of the wind and that estimations based on such data are associated with inaccurate power curve prediction and turbine damage. In particular it has been suggested that such problems are due to a lack of understanding of the somewhat intermittent nature of the wind velocity fields and the small-scale fluctuations thus associated. In order to address this there has been a significant increase in research involving coupled mesoscale-microscale models and stochastic downscaling methods. Our contribution is a demonstration that a good knowledge of small-scale variability is essential for a better understanding of the atmospheric boundary layer. We discuss the applicability of the stochastic anisotropic multifractal model to the complex conditions of wind farm potential and operational sites.

2 Data

Available to us is six-months of wind velocity and temperature measurements at the heights 22, 23 and 43m.

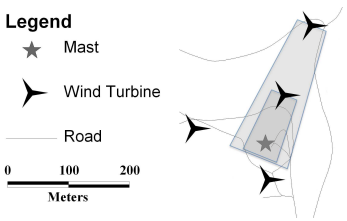

Figure 1: Schematic of turbine positions and wake effect due to North-Westerly winds (map courtesy of Julien Richard).

The measurements came from 3D sonic anemometers with a 10Hz data output rate positioned on a mast in a wind farm test site subject to wake turbulence effects (see Fig. 1). The quality of the data was of utmost importance so thorough pre-processing and verification was implemented to assure the reliability of the results.

3 Analysis

3.1 The Energy Spectrum and Scaling

A typical first-step-method to determine the overall scaling behaviour is the transformation of the velocity field into Fourier space. We 'should' then be able to observe power-law behaviour of the spectrum such that

$$E(\omega) \equiv A\omega^{-\beta} \tag{1}$$

where ω is the frequency, $E(\omega)$ is the energy at a given frequency, A is a coefficient of proportionality and β is the scaling exponent. The review of [Marusic et. al., 2010] discusses the existence of a -1 power law sub-range over small frequencies, adjoined by a classical Kolmogorov inertial sub-range with $\beta = 5/3$.

We will present shortly a more in-depth discussion on how our results compare to Kolmogorov's predictions however before this we would like to discuss the fact that there is no unique scaling regime i.e. there are three common scaling features, instead of the predicted universal law (see Figs. 2 and 3 also), that are:

- **High frequency scaling range** (R_{HF}:$\sim$ 0.1 secs to $\sim$5 mins) in which all three velocity components, u, v and w, follow (approximately) the same scaling law.
- **Mid-frequency w-component departure** from scaling at $\sim$5 minutes. Mid-Frequency, R_{MF}, corresponds to the ranges $\sim$ 5 mins to $\sim$1 hour.
- **Low frequency scaling reunification** (R_{LF}:$\sim$ 1 hr to $\sim$1 day) for all three velocity components at about an hour. The power law is not the same as that for small scales as will be discussed later.

The focus therefore of our more in-depth analysis is the behaviour of the horizontal u- and v-components over the mid-frequency-ranges i.e. $\sim$5 mins to $\sim$1 day. In fact what we

found was that our data fell into two categories; days (i.e., independent samples of 2^{19} measurements [$\approx$ 14.5 hours] per day) *without* a mid-frequency perturbation (Fig. 2) and days *with* a mid-frequency perturbation (Fig. 3). In the next section we will consider the simpler of the two regimes that are the non-perturbed days.

3.2 Non-perturbed Days & The Anisotropic Multifractal Model

The results from spectral analysis on non-perturbed days confirm a unique power law for all three velocity components over higher frequencies up to approximately 40 seconds at which the vertical wind w-component shows a clear scaling break followed by a -1 power law subrange as described in the previous section.

Moreover, such a clear separation of power law subranges allows us to obtain an estimate of the integral length scale for the vertical wind component as suggested in [Monin & Yaglom, 1975], which in turn leads to an estimate of the Reynolds number of about 60,000. Thus, from dimensional analysis one may obtain a minimum Reynolds number of about 14,000. These estimates confirm that the investigated wind field exhibits fully developed turbulence.

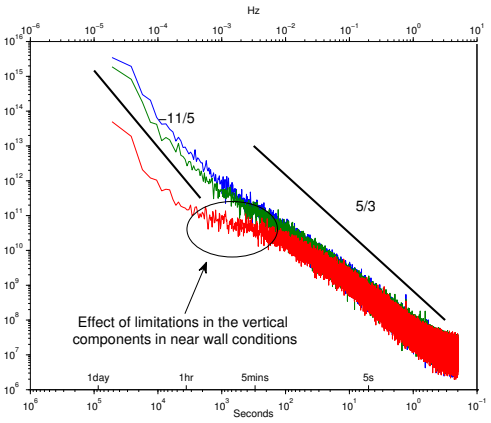

Figure 2: Averaged spectra for 11 non-perturbed days where the velocity component u is blue, v is green and w is red. The high-frequency range from $\sim$ 0.1 sec to 5 mins has spectral slope $\sim$ 1.4, less than the predicted 5/3. In addition we have highlighted the -1 adjoining range, from 5 mins to an hour, with the scale break being predictable based on the mast height (see [Fitton et. al., 2011] for more details). Low frequency scaling region is compatible with the -11/5 scaling law.

Over the high-frequency range Fig. 3 displays spectral exponents that differ from Kolmogorov's -5/3 law. The difference corresponds to an intermittency correction of spectral slopes and can be taken into account using the universal multifractal framework (Schertzer and Lovejoy, 1987), where:

- the energy density flux is a conserved (at any scale ratio λ) multifractal field proportional to a power law with singularity, γ, i.e.

$$\varepsilon_\lambda \propto \lambda^\gamma, \tag{2}$$

- the statistical moments of the energy density flux are defined by:

$$\langle \varepsilon_\lambda^q \rangle \propto \lambda^{K(q)}, \tag{3}$$

- and the scaling moment function $K(q)$ is defined by:

$$K(q) = \frac{C_1}{\alpha - 1}\left(q^\alpha - q\right). \tag{4}$$

Here, q, is the order of moment, C_1 is the codimension of the mean singularity and α is the multifractal Lévy index. The spectral exponent of Eq. 1 now becomes

$$\beta = 2H + 1 - K(2) \tag{5}$$

where $H = 1/3$ quantifies the degree of non-conservation of velocity increments. For spectra (i.e. for second order statistics), we estimated $K(2) = 0.27$. Such high intermittency corrections are expected over high frequencies in areas with high Reynolds numbers and complex terrain.

In addition we observed the Bolgiano-Obuhkov -11/5 power law at low frequencies illustrating the influence of large-scale vertical motions specific to the topography of our wind farm test site [Faggio & Jolin, 2003].

To take into account the dominant role of the vertical motion of large scale atmospheric structures, one may consider that the buoyancy force variance flux, ϕ, plays the same role as the energy flux, ε, in 3D turbulence but only along the vertical [Schertzer & Lovejoy, 1984]. This is contrary to the classical 'buoyancy subrange' that postulates an isotropic turbulence [Bolgiano, 1959, Obukhov, 1959] with two different (horizontal and vertical) scaling regimes. Thus we have the coupled sets of scaling equations [Schertzer & Lovejoy, 1984, Lazarev et. al., 1994]:

$$\left.\begin{aligned} \Delta V(\Delta x) &\stackrel{d}{=} (\varepsilon(\Delta x))^{1/3}\Delta x^{1/3} \\ \Delta V(\Delta z) &\stackrel{d}{=} (\phi(\Delta z))^{1/5}\Delta x^{3/5} \end{aligned}\right\} \tag{6}$$

$$\Longrightarrow (\varepsilon(\Delta x))^{1/3} \approx (\phi(\Delta z))^{1/5} \text{ when } \Delta x^{1/3} \approx \Delta z^{3/5} \tag{7}$$

where $\Delta V(\Delta x)$ and $\Delta V(\Delta z)$ denote the horizontal and vertical shears of the horizontal wind respectively and the symbol $\stackrel{d}{=}$ means equality in probability distribution.

Because the scaling fluctuations of both fluxes are not neglected (due to their explicit scale dependency) we can define anisotropic scaling (as defined by the anisotropic multifractal model [Schertzer & Lovejoy, 1984]) at all significant scales instead of two isotropic regimes, separated by a scaling break (see [Fitton et. al., 2011] for more details).

3.3 Perturbed Days, Wakes and Power Estimation

In [Fitton et. al., 2011] we put forward the argument that the non-perturbed days were a result of lack of influence of wind turbines justified by the low frequency power law (cross-diagonal mean wind) of the integrated cospectral analysis. The same argument allowed us to select days that were highly perturbed. By this we mean days where the mid-frequency range, R_{MF}, in which the scaling of horizontal

velocity components remained the same as described in the previous section, now have significant fluttering (see below [Fig. 3]).

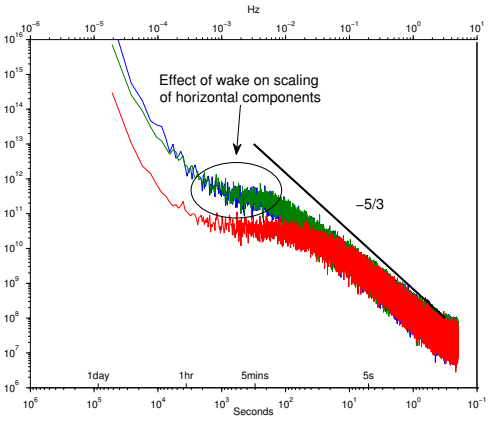

Figure 3: Averaged spectra for 11 perturbed days where the velocity component u is blue, v is green and w is red. The high-frequency range from ~ 0.1 sec to 5 mins has spectral slope ~ 1.6 which is much closer to the predicted 5/3. We have highlighted the fluttering for the horizontal components over R_{MF}. We can also see the fluttering of the vertical component is accentuated to a plateau. The 11/5 low frequency scaling regime remains, although with a lower coefficient of proportionality A (Eq. 1).

To see the effect of the turbines we can do a direct comparison of the integrated spectra, $\omega E(\omega)$, in log-linear coordinates of perturbed and non-perturbed days (11 of each see Fig. 4).

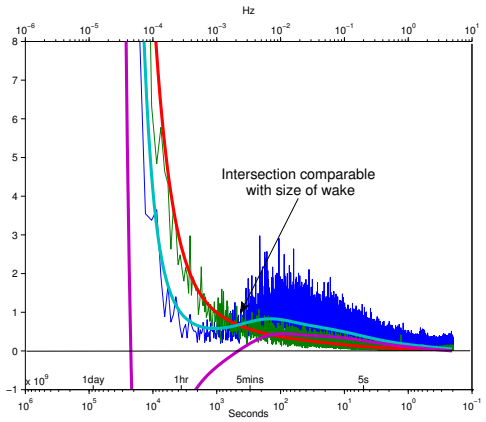

Figure 4: Comparison of perturbed and non-perturbed, u-component averaged integrated spectra, $\omega E(\omega)$, in log-linear coordinates; blue is perturbed days with light-blue moving average, green is non-perturbed with red moving average and purple is the differences of the moving averages.

This gives us a quantification of the energy per frequency increment making the overall evaluation of the energy gains and losses much easier. We have selected the horizontal u-component since there is no -1 adjoining range for non-perturbed days making it easier to make the comparison. Note the behaviour of the horizontal v-component is very similar (evidence of asymmetry at larger scales). From Fig. 4 we can draw the following intermediate conclusions based on the ranges defined in §3.1:

- **High frequency scaling range** (~ 0.1 secs to $\sim$5 mins) has an injection of energy since perturbed days (blue integrated spectra, light-blue moving average in Fig. 4) have more energy than the unperturbed days (green integrated spectra, red moving average in Fig. 4). This is confirmed by the positive difference of the moving average of the integrated spectra (purple curve of Fig. 4). If we consider the most basic approximation to a turbine, the actuator disc, then we can assume any eddy larger than the disc will be split into smaller eddies. This may explain the increase in high frequency energy. In fact, we can further confirm this idea since the transition of energy peaks at $\sim$ 5 mins highlighted again in Fig. 4 correspond to the size of the wake shown in Fig. 1.

- **Mid-frequency u-component** ($\sim$ 5 mins to $\sim$3 hours) shows evidence of energy pumping from the turbines for the perturbed days. This is more obvious when looking at the negative difference of the two integrated spectra over this range.

- **Low frequency** ($\sim$ 3 hours to $\sim$ 1 day [mesoscales]) shows that although there is similar scaling behaviour the energy for the perturbed days (red curve) is greater than the non-perturbed (light-blue curve) since the difference of the two (purple line) is positive. In [Fitton et. al., 2011] we suggested this was because the two particular types of wind the site was typically subject were strong North-Westerlys and weak South-Easterlys. This meant only the stronger winds would interact with the turbines (see Fig. 1).
  In addition we see at $\sim$ 3 hours the energy of the non-perturbed days becomes greater than perturbed. In the previous section we discussed how topographical features can change the scaling power law over the lower frequency data. This suggests there are similar topographical influences causing the loss of energy e.g. higher mean winds dissipate more energy over complex terrain.

Fig. 5 displays a schematic diagram that illustrates the corresponding inter-relations of different scaling ranges of the energy spectra. Over each of these ranges, two distinct power laws describe the corresponding scaling behaviour, with and without wake effects. Thus, from Eq. 5 we get:

$$E_1(\omega) = A_1 \omega^{-\beta_1}, \tag{8}$$

$$E_2(\omega) = A_2 \omega^{-\beta_2}. \tag{9}$$

Since the estimates of the multifractality parameter, α, remain stable for both perturbed and non-perturbed fields, the

ratio of the energy spectra is defined by the second order structure function:

$$\frac{E_1(\omega)}{E_2(\omega)} = \frac{A_1}{A_2}\omega^{-\zeta_\Delta(2)} \tag{10}$$

where $\zeta_\Delta = 2(\Delta H) - (\Delta C_1/(\alpha-1)) \cdot (2^\alpha - 2)$ from Eqs. 4 and 5.

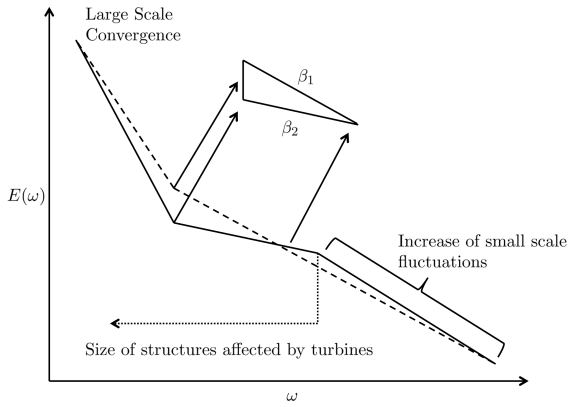

Figure 5: Schematic of the inter-relations of different scaling ranges of the energy spectra in a log-log plot.

From Fig. 5, Eq. 4 and the above equation (Eq. 10) we see an empirical spectral exponent closer to the theoretical values of $\beta = 5/3$ (over small scales) or $\beta = 11/5$ (over large scales), correspond to a smaller intermittency correction $K(2)$. Figs. 4 and 5 therefore suggest that by taking the energy over large scales, wind turbines create additional small-scale eddies and re-inject them as part of the energy over smaller scales, making the turbulence more homogeneous.

4 Conclusion

The aim of this study was to explore the scaling behaviour of atmospheric velocity measurements in a wind farm test site subject to wake turbulence effects. Based on this study we can make the following conclusions:

- Using long time series, 10Hz data, we identified (depending on the direction of the mean wind) two or three scaling sub-ranges.
- Through spectral analysis we found possible relations between wind velocity scaling breaks and associated theories of fully developed turbulence in the atmospheric surface-layer and used the universal multifractal framework to deal with the strong intermittency of the field.
- We have discussed how the anisotropic multifractal model can be applied to near wall atmospheric turbulence over complex terrain how it can be fully validated for days with no interaction with the wind turbine wakes.
- We found empirical evidence of the influence of wakes and suggested reasoning and scaling techniques that enable us to quantify the loss of energy with the potential of taking this into account using the anisotropic multifractal model.
- And finally, we discussed how the pumping of energy from wind turbines over mid-frequency scales, creates additional small-scale eddies which are re-injected as part of the energy over smaller scales. This makes the turbulence more homogeneous over the smaller scales in an analogous way to grid-generated homogeneous turbulence.

References

[Bolgiano, 1959] Bolgiano, R. 1959 Turbulent spectra in a stably stratified atmosphere, *J. Geophys. Res.* **64**, 2226.

[Faggio & Jolin, 2003] Faggio, G. & Jolin, C. 2003 Suivi ornithologique sur le parc dèoliennes dErsa- Rogliano (Haute Corse) - Rapport final-SIIF/AAPNRC-GOC, 100p.

[Fitton et. al., 2011] Fitton, G. F., Tchiguirinskaia, I., Schertzer D., & Lovejoy, S. 2011 Scaling Of Turbulence In The Atmospheric Surface-Layer: Which Anisotropy?, *Journal of Physics: Conference Series* (in review) Warsaw, ETC13.

[Lazarev et. al., 1994] Lazarev, A., Schertzer, D., Lovejoy, S. & Chigirinskaya, Y. 1994 Unified multifractal atmospheric dynamics tested in the tropics: part II, vertical scaling and generalized scale invariance, 115-123.

[Marusic et. al., 2010] Marusic, I., McKeon, B. J., Monkewitz, P. A., Nagib, H. M., Smits, A. J. & Sreenivasan, K. R. 2010 Wall-bounded turbulent flows at high Reynolds numbers: Recent advances and key issues *Phys. Fluid.*, **22**, 065103.

[Monin & Yaglom, 1975] Monin, A. S. & Yaglom, A. M. 1975 *Statistical Fluid Mechanics*, Cambridge, MIT-Press, Vol. 2, pp. 874.

[Obukhov, 1959] Obukhov, A. N. 1959 Effect of Archimedian forces on the structure of the temperature field in a temperature flow, *Sov. Phys. Dokl.* **125**, 1246.

[Pinus et. al., 1967] Pinus, N. Z., Reiter, E. R., Shur, G. N. & Vinnichenko, N. K. 1967 Power spectra of turbulence in the free atmosphere, *Tellus* **19**, 206.

[Schertzer & Lovejoy, 1984] Schertzer, D. & Lovejoy, S. 1984 On the Dimension of Atmospheric motions. In: T. Tatsumi (Editor), Turbulence and Chaotic phenomena in Fluids, Amsterdam, Elsevier Science Publishers B. V., pp. 505-512.

[Yaglom & Kader, 1989] Yaglom, A. M., Kader, B. A., & Zubkovskii, S. L. 1989 Spatial Correlation Functions of Surface-Layer Atmospheric Turbulence in Neutral Stratification, *Bound.-Lay. Meteorol.* **47**, pp. 233-249.

Multifractal Statistical Methods And Space-Time Scaling Laws For Turbulent Winds

Fitton, G., Tchiguirinskaia, I., Schertzer, D. and Lovejoy, S.

Abstract We discuss the results of a universal multifractal (UM) analysis performed on the GROWIAN wind speed dataset. Within this framework the wind speed can be reproduced, including the extremes, at all scales using just three parameters: α, C_1 and H [1]. We exploit the fact that the wind speed is simultaneously recorded at several positions (effectively two grids) on two masts. The first grid allows us to compare the scaling of the horizontal spatial increments of the wind speed (at three heights) with that of the temporal increments, thus enabling us to verify Taylor's hypothesis of frozen turbulence. The second grid allows us to test the hypothesis of scaling anisotropy between horizontal and vertical shears of the wind speed. The two scaling laws refer to the choice of either Kolmogorov energy or buoyancy force fluxes. The spatial structure function analyses assume the large number of data samples (approximately 150 samples of twenty minutes) reduces the uncertainties from the limited number of spatial points. The proof of universal scaling behaviour for different wind farm sites (see [2] for comparison) is an exciting concept that opens up the possibility of further areas of research and application within the field.

Data Courtesy of Dr. Peinke we were introduced to the GROWIAN dataset. The experiment consisted of two 150m masts positioned 65m East-South-East of a 3MW wind turbine with a 52m lateral distance between each mast. Installed on the masts were 20 propellor anemometers positioned in pairs on the ends of booms with a 12m length. This covered an effective area of 75×100m. Wind speed, direction and temperature were measured at 2.5Hz and the duration of one measuring run was approximately 20 minutes. A total of 300 runs were sampled between April 1984 and February 1987 at different inflow conditions, however, errors in the data meant

Fitton, G., Tchiguirinskaia, I. and Schertzer, D.
Universitè Paris Est, Ecole des Ponts ParisTech, LEESU, 6-8 avenue B. Pascal, Citè Descartes, 77455, Marne-la-Vallèee, France; tel.: +33 1 6415 3607, fax: +33 1 6415 3764.
e-mail: fittong@cereve.enpc.fr

Lovejoy, S.
McGill University, Physics department, 3600 University street, Montreal, Quebec, Canada

the number of usable samples varied between 150 to 290. For more details about the experiment see [3].

Spectra The field scales when the logarithm of the spectral energy, $E(\omega) \propto \omega^{\beta}$, has linear behaviour with a unique slope, $\beta = 2H + 1 - K(2)$ (see Fig. 1). The second order scaling moment function, $K(2)$, is an intermittency correction. The Hurst exponent, H, quantifies the divergence from conservation of a flux and is 1/3 for Kolmogorov energy and 3/5 for Bolgiano-Obukhov buoyancy fluxes. For data analysis, the horizontal wind speed, u, is represented as the two-dimensional vector, $\mathbf{u} = (u_x, u_y)$, preselected to be approximately perpendicular to the measuring array.

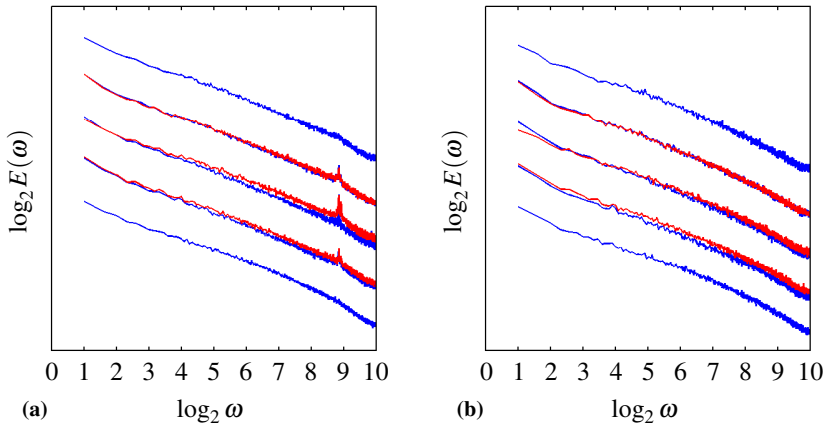

Fig. 1: Log-log plot of averaged wind speed spectra, $E(\omega)$ for all samples (a) and $E_{\perp}(\omega)$ for samples with direction approximately perpendicular to the array (b). The frequency, $\omega = 2^N/\ell_n = \lambda/0.4\text{s}$, where $\ell_n = 2^n \times 0.4\text{s}$ for $n \in [0:N]$. Plots (shifted) from bottom to top correspond to wind speeds at 50, 75, 100, 125 and 150m measured on Mast 2. The blue and red correspond to inner and outer positions on the masts.

Wind Speed Direction In Fig. 1a a spectral spike can be seen occurring at approximately $\log_2 \omega = 9$ or two seconds. In [4], a filtering criteria based on mean interpolated wind speed and turbulence intensity was used to supposedly remove measurements subject to a 'shadow effect' from the mast. The only way we could obtain the desired scaling (Fig. 1b) was to filter the wind speed so that it was perpendicular to the mast. This confirms the effect of the wakes of the anemometers causing the over representation of the two second frequency in Fig. 1a. In fact, we can further confirm this idea by estimating a characteristic length scale of 30m, given a mean wind speed of 10m/s, which is approximately the length of the boom.

UM Parameters After removing the 'problematic' data we estimated α and C_1 – the UM parameters that measure respectively the multifractality and mean intermittency of the scaling field – over two subranges: $\log_2 \omega \in [1:7]$ & [8:10] using the DTM method [1]. We use the DTM method [1] on the third power of the time-series of the wind speed increments, $\Delta u = \sqrt{[\Delta u_x^2 + \Delta u_y^2]}$, and component increments, Δu_x

and Δu_y, for α and C_1, and the first-order structure function for H (see Table 1 for the average estimates).

Table 1: Estimation of UM parameters over *high* (top) and *low* (bottom) frequency subranges.

Height	$\alpha_{\Delta u}$	$C_{1,\Delta u}$	$H_{\Delta u}$	$\alpha_{\Delta u_x}$	$C_{1,\Delta u_x}$	$H_{\Delta u_x}$	$\alpha_{\Delta u_y}$	$C_{1,\Delta u_y}$	$H_{\Delta u_y}$
150m	1.42	0.31	0.42	1.36	0.36	0.38	1.36	0.36	0.45
125m	1.40	0.32	0.37	1.36	0.37	0.33	1.35	0.36	0.42
100m	1.38	0.30	0.45	1.33	0.35	0.42	1.32	0.35	0.49
75m	1.39	0.30	0.45	1.35	0.36	0.42	1.34	0.36	0.49
50m	1.43	0.32	0.48	1.38	0.38	0.44	1.38	0.38	0.51
10m	1.50	0.34	0.47	1.47	0.43	0.43	1.47	0.42	0.51
150m	1.76	0.26	0.33	1.69	0.42	0.30	1.69	0.40	0.36
125m	1.71	0.26	0.30	1.64	0.37	0.26	1.64	0.37	0.34
100m	1.71	0.24	0.33	1.66	0.37	0.30	1.63	0.35	0.36
75m	1.66	0.24	0.31	1.59	0.37	0.30	1.54	0.31	0.34
50m	1.63	0.22	0.30	1.58	0.34	0.28	1.57	0.31	0.33
10m	1.67	0.20	0.26	1.61	0.33	0.23	1.61	0.30	0.29

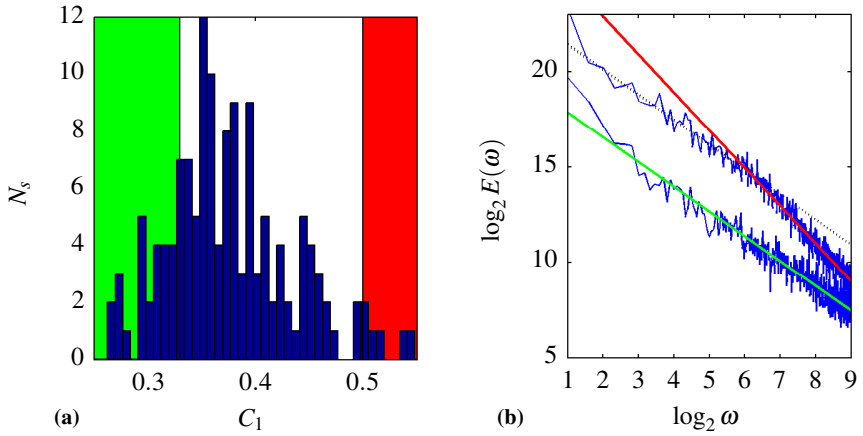

Fig. 2: Histogram of the parameter H for u_y at 75m (a), estimated from the first order structure function, using 152 subsamples, N_s. The estimates are comparable to those of Table 1. Summing the subsamples for extreme values $H < 0.33$ (green area) and $H > 0.5$ (red area) we get the corresponding spectral slopes (b) 2 (red), 1.4 (green) and 1.3 (dotted).

The estimates of H, show considerable variability, fluctuating around 0.3 and 0.6 i.e. between Kolmogorov and Bolgiano-Obukhov scaling (Fig. 2a). This is further supported by average spectra (Fig. 2b) selected so that they correspond to the extreme values of H. The mean codimension, C_1, fluctuates in a corresponding manner between 0.35 and 0.45. The multifractality, $\alpha \approx 1.5$, remains fairly stable at all heights and between horizontal components. The values are comparable with those found in [2]. To check the high frequency changes in scaling are not due to a smoothing procedure of the measuring device we can look at the compensated spectra, $\omega^{\beta} E(\omega)$ (Fig. 3).

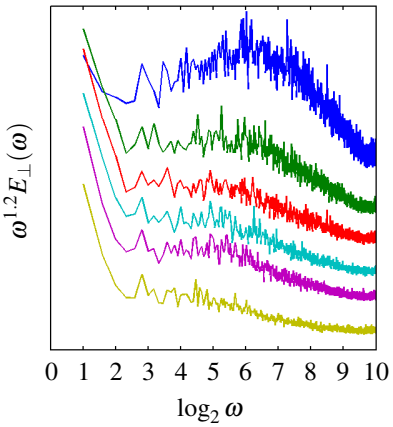

Fig. 3: Log-linear plot of *compensated* perpendicular wind spectra, $\omega^{1.2}E_\perp(\omega)$, vs. the normalised frequency, ω; Wind speeds at 10, 50, 75, 100, 125 and 150m, on the inner position of Mast 2 (shifted from top to bottom).

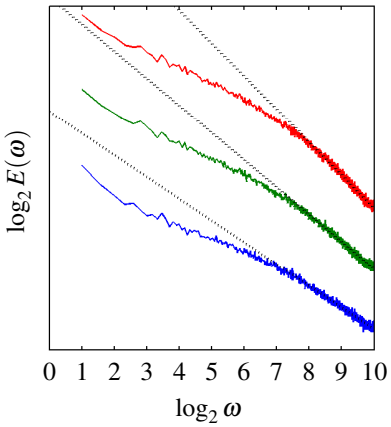

Fig. 4: Comparison of high frequency spectral slopes at 10m for u (blue), u_x (green) and u_y (red), shifted for easier comparison. The corresponding slopes of the dotted lines of best fit are 2.3, 1.9 and 1.5.

A characteristic height (or length scale), corresponds to the peaks in the compensated spectra. For wind speed spectra averaged over all subsamples the frequencies to the left of the peaks correspond to Kolmogorov and to the right Bolgiano-Obukhov scaling respectively. In addition to high and low frequency scaling anisotropy the UM parameters exhibit component wise anisotropy over high frequencies. The extent of the anisotropy leads to a majority of cases where u_x scales as Kolmogorov and u_y scales as Bolgiano-Obukhov (see estimates at 10m in Table 1). We can further confirm this by comparing the high frequency spectral slopes of the decomposed component vectors (see Fig. 4).

Structure Functions Using the UM parameters estimated on the wind speed time increments, $\Delta u(\tau) = u(t+\tau) - u(\tau)$, we can test the validity of Taylor's hypothesis by reconstructing a semi-analytic structure function, $\zeta_\tau(q)$, and the empirical structure function, $\zeta_{\mathbf{r}}(q)$, for the temporally averaged wind speed space increments, $\Delta u(\mathbf{r}) = u(\mathbf{x}+\mathbf{r}) - u(\mathbf{x})$:

$$\zeta_\tau(q) = qH - K(q) = qH - \frac{C_1}{\alpha - 1}\left(q^\alpha - q\right) \;\; \& \;\; \zeta_{\mathbf{r}}(q) = \log\langle|\Delta u(\mathbf{r})|^q\rangle/\mathbf{r}, \qquad (1)$$

where q is the order of moment and the operator $\langle\cdot\rangle$ denotes an averaging procedure in time. Fig. 5a illustrates that $\mathbf{x} = (x_i)$ is the position vector with reference $i \in [4 : 20]$ (see [3]) and $\mathbf{r}$ is the corresponding spacing between. In Figs. 5b-d, α and C_1 are fixed at 1.5 and 0.35 respectively and only the parameter, H, changes between the two theoretical values 1/3 (red) and 3/5 (blue). The hypothesis is valid when $\zeta_\tau(q) \approx \zeta_{\mathbf{r}}(q)$.

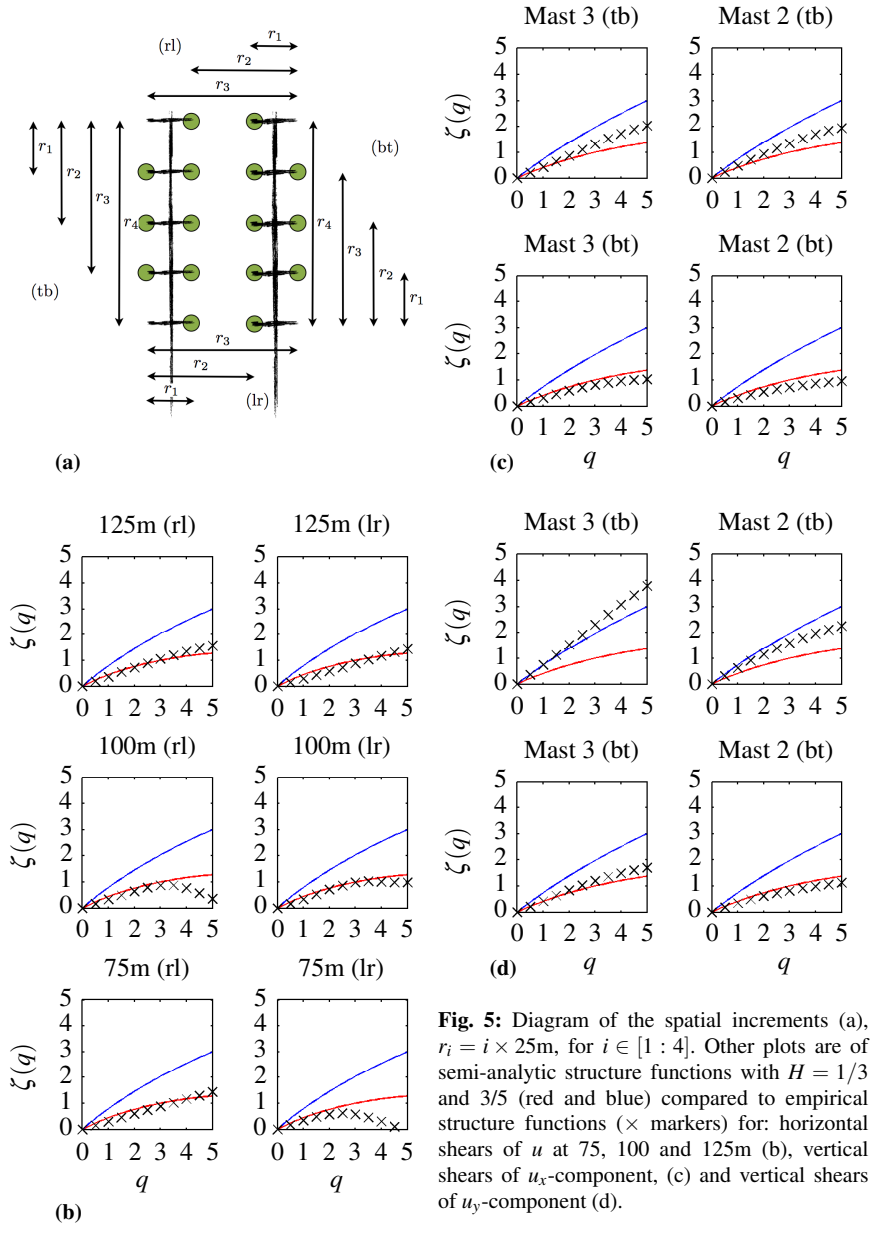

Fig. 5: Diagram of the spatial increments (a), $r_i = i \times 25$m, for $i \in [1:4]$. Other plots are of semi-analytic structure functions with $H = 1/3$ and 3/5 (red and blue) compared to empirical structure functions ($\times$ markers) for: horizontal shears of u at 75, 100 and 125m (b), vertical shears of u_x-component, (c) and vertical shears of u_y-component (d).

The plots of the structure functions in Fig. 5b confirm Taylor's hypothesis for the horizontal shears of u. Looking at the vertical shears of components, u_x and u_y, we find the anisotropic scaling displayed in the Hurst exponents in Table 1 (estimated on the high frequencies of the time-series velocity increments) and the spectra in Fig. 4 are replicated only for the shears taken from top to bottom (5a). This can be

explained with the help of Fig. 3 and the minimum spacing length, $r_1 = 25$m. Again, taking the mean wind speed as 10m/s, we see that taking the smallest vertical shear at the top of the mast, means we are within the Kolmogorov scaling range and taking the smallest vertical shear at the bottom of the mast means we are within the Bolgiano-Obukhov scaling range.

Perspectives For The Modelling Of Extremes The effect of the mean codimension can be seen through the $c(\gamma)$ function (Fig. 6); related to the probability distribution of a flux, ε_λ through:

$$\Pr(\varepsilon_\lambda \geq \lambda^\gamma) \simeq \lambda^{-c(\gamma)}, \quad \text{where} \quad c(\gamma - H) = C_1 \left(\frac{\gamma(\alpha-1)}{C_1 \alpha} + \frac{1}{\alpha} \right)^{\frac{\alpha}{\alpha-1}}.$$

Here, $\gamma = \log_\lambda \varepsilon_\lambda$, is a scale invariant singularity. In addition to being able to reproduce the theoretical $c(\gamma)$ curves (Fig. 6) from the UM parameters, the exponent, q_D, of the power law of the distribution of the extremes can be predicted from $K(q_D) = D(q_D - 1)$ with $D = 1$ for a time-series. Over small scales this gives $q_D \approx 4$ and 2.5 for $C_1 = 0.35$ and 0.42 when $\alpha \approx 1.5$, thus defining the extreme behaviour of the energy flux. This further implies $q_D \approx 7.5$ for the wind velocity, which is a crucial result for applications within the field of wind energy.

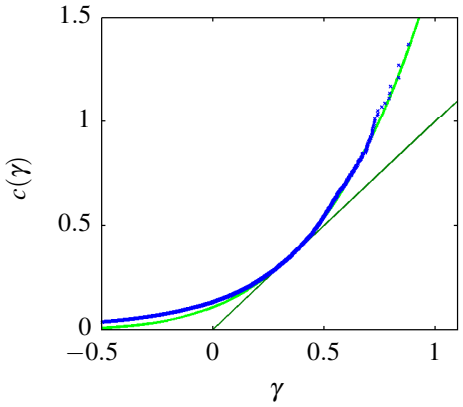

Fig. 6: Theoretical conservative function, $c(\gamma)$, with $\alpha = 1.35$ and $C_1 = 0.35$ for predominantly Kolmogorov scaling (green) compared to the empirical function (blue crosses) using the Weibull plotting position. The empirical data are the concatenated 13 subsamples of the third power of the u_y velocities from Fig. 2b, filtered such that $H < 0.33$. The horizontal shifting of the empirical curves is done so that they superimpose with the theoretical ones at $c(C_1) = C_1$. The shift (corresponding to $H = 0.2$) is comparable to the mean of the first order structure function estimates ($H = 0.25$, see also Fig. 2a).

Acknowledgements This research is part of the EU-FP7 ITN WAUDIT project.

References

1. D. Schertzer and S. Lovejoy, "Multifractals, Generalized Scale Invariance and Complexity in Geophysics," *International Journal of Bifurcation and Chaos*, vol. 21, no. 12, pp. 3417–3456, 2011.
2. G. Fitton, I. Tchiguirinskaia, D. Schertzer, and S. Lovejoy, "Scaling Of Turbulence In The Atmospheric Surface-Layer: Which Anisotropy?," *Journal of Physics: Conference Series*, vol. 318, p. 072008, Jan. 2011.
3. W. Palz, *European Wind Energy Conference 1984: Proceedings of an International Conference Held at Hamburg, FR Germany, 22-26 October, 1984*. Information Today Inc, 1985.
4. T. Mücke, D. Kleinhans, and J. Peinke, "Atmospheric turbulence and its influence on the alternating loads on wind turbines," *Wind Energy*, vol. 14, pp. 301–316, Mar. 2011.

Torque Fluctuations In The Framework Of A Multifractal 23/9-Dimensional Turbulence Model

G. Fitton[1], I. Tchiguirinskaia[1], D. Schertzer[1] and S. Lovejoy[2]

[1]Université Paris Est, Ecole des Ponts ParisTech, LEESU, 6-8 avenue B. Pascal, Cité Descartes, 77455, Marne-la-Vallée, France; tel.: +33 1 6415 3607, fax: +33 1 6415 3764

[2]McGill University, Physics department, 3600 University street, Montreal, Quebec, Canada

E-mail: `fittong@leesu.enpc.fr`

Abstract. We have carried out in-depth analyses of boundary-layer wind velocity data within the universal multifractal (UM) framework. Within the UM framework the statistics of a given field are characterised with the help of three parameters α, C_1 and H. With these three parameters one fully describes the wind velocity fields up to and including the order q_D after which the divergence of statistical moments intervenes. Studies at different sites have shown that the parameter α – the multifractality index – of the horizontal and vertical shears of the horizontal wind remains fairly constant at approximately 1.7. In this study we show how the two remaining parameters C_1 and H vary for two very different sites/datasets and discuss what the consequences of this variability are for the fluctuations of the torque.

1. Introduction

Modern wind turbines operate in the near-surface part of the atmospheric boundary-layer i.e. between 50 to 200m above ground level. An improved understanding of turbulence-induced complexities inherent in this region therefore holds central importance for the wind energy community ([8]). To understand such complexities, accurate wind measurements at these heights require expensive and non-traditional instrumentation. This has led to insufficient amounts of adequate experimental data. At present, wind speed observations at 10m heights from meteorological networks are used in conjunction with the standard similarity theory ([17]). The use of such methods does not fully represent the complexity of the vertical profile of the wind.

Within the so called surface-layer there exist highly complex three-dimensional time-dependent turbulent fields involving multi-scale structures whose non-linear interactions and statistics evolve with the turbulence generation mechanism. Moreover, these turbulent structures change drastically when generated mostly by buoyancy compared to those generated by wind shears only (see [16]). This is partially in agreement with the (isotropic) scaling 'buoyancy sub-range' hypothesised by Bolgiano-Obukhov ([3, 18]) hereafter referred to as BO.

In addition to the complexities involved in changing turbulence generation mechanisms further complexities arise when inhomogeneous terrains are involved. To take advantage of the wind speed-up induced by eddies forced up over a hill, turbines are frequently installed on hilltops. This is done even though there is only a limited amount of knowledge concerning the mechanisms responsible for the complex fluid dynamics that occur on the upwind side of the hill ([9]). What's more, if the upwind side of the hill contains tall vegetation the turbulent structures and atmospheric stability will be *even* further modified ([4]).

Removing the effects of a complex terrain i.e. when the surface satisfies a horizontally homogeneous terrain assumption, does not make the problem much simpler. A low-level jet phenomena occurring between 50 to 400m can also cause reason for concern ([1, 2]). In summary, to establish a reference of the observable space-time variability of wind-inflow events, in particular of extreme wind speed gusts, very detailed observations need to be made in a variety of locations and situations.

The wind energy community defines as 'extreme', those wind-inflow events, that can potentially produce, adverse, damaging impacts on modern wind turbines (see [8] for a review). This includes events such as: persistent wind gusts, rapid changes in the wind direction, and atmospheric coherent structures; events that are likely to generate critical loads on wind turbines. If these events occur too frequently the wind turbine will prematurely fatigue. It is thus of vital importance that the (statistical) predictions of the extreme wind-inflow events are improved. Improved predictions of the wind turbine loads will help to develop advanced torque gain controls thus minimising the potential damage caused by extreme wind events.

The significance of turbulence intensity on the optimal torque control gain for different time scales was investigated in [10]. The so called 'turbulence intensity', deeply rooted in the Reynolds decomposition, is defined as the standard deviation of the wind speed, normalised by the mean wind speed over a given interval of time. Within the wind energy community this time interval is typically from 10 minutes to one hour. Bearing in mind a torque controller must be responsive down to time scales comparable to the transition time of a few seconds – in order to mitigate the impact of extreme events – it is unlikely the study of such coarse time-scales could be truly representative of the variability in the system. Moreover, because the turbulence intensity is defined through the mean and therefore framework dependent velocity, the normalisation does not respect Galilean invariance. A tool that has been fundamental in the understanding of the multi-scale structures in turbulence is ironically lost in a term claiming to be that which it least describes. And yet, inspite of these facets, the turbulence intensity is still widely used as a classical measure of the 'gustiness' of the wind.

In light of these problems (and opportunities), current atmospheric and therefore torque measurements can be analysed using modern statistical methods. Statistical methods that are appropriate to the study of events considered to be extreme by the wind energy community. This paper argues that the current focus of research in wind resource assessment should be devoted to the multifractal modelling of atmospheric turbulence. A model that, instead of performing scale-by-scale developments in the design of separate features of a wind turbine, aims to integrate knowledge across the spatio-temporal scales.

Multifractals are scale invariant. They provide the scaling velocity field, power law statistics w.r.t. the scales. This allows us to understand and to model extremely variable space-time fields over a wide range of scales. At present one would expect the wind energy community to go beyond the Reynolds decomposition. This means taking into account the fundamental problem of intermittency and addressing the fact that the so-called 'mean' wind is frame dependent.

2. Intermittency And The Physics Of Extremes

Intermittency means that the activity of a process is confined to smaller and smaller fractions of the available space-time domain when observed at higher and higher resolutions. We define the resolution, λ, as the ratio of the largest scale, L, and the reference scale, ℓ. Examples of intermittency can easily be observed in wind farm wind velocity data. Figure 1 illustrates a twenty-second time-series of wind velocity increments from Corsica (France) with $\lambda = 200$. The velocity increments show a highly variable process with sporadically occurring extreme values. Given the flux of energy at a given ratio of scales, ε_λ, is proportional to the third power of the wind velocity increment, it may sometimes vary by orders of magnitude in time and in space. The highest values of the flux at any given scale relative to the mean, increase with increasing

Reynolds number. These values may be of an order fifteen times greater than the average energy flux in laboratory scale flows and fifty times that of the average energy flux in atmospheric flows.

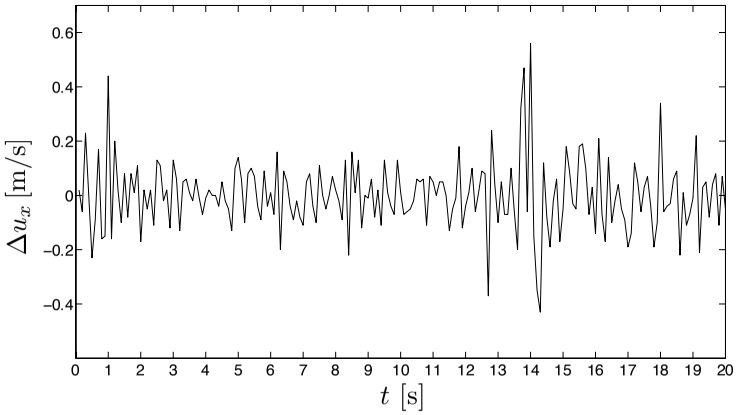

Figure 1: Twenty second time-series of wind velocity increments for the horizontal u_x-component of the Corsica dataset. The sporadic nature of the large fluctuations is characteristic of an intermittent process.

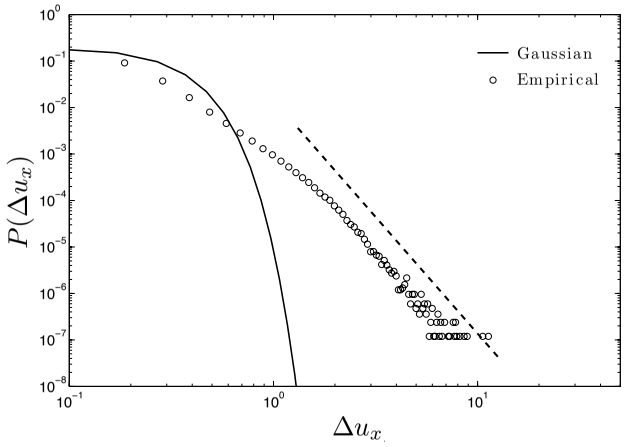

Figure 2: Log-log plot of the probability distribution, $P(\Delta u_x)$, of the (normalised) velocity increments, Δu_x, of the twenty second time-series in figure 1. The slope of the dashed line is 6 i.e. $q_D = 6$. This means velocity increment statistics above an order of 6 are random.

The irregular nature of the large fluctuations characteristic of an intermittent process will often result in the divergence of statistical moments (see figure 2). The statistical moments of order q of the wind velocity increments correspond to a non-linear form of the structure-function exponent $\zeta(q) = q/3 - K(q; 1/3)$. The scaling moment function $K(q; 1/3)$ characterises the intermittency of the velocity field.

The divergence of statistical moments of a random variable correspond to a hyperbolic (algebraic) fall-off of the probability distribution tail

$$P(X \geq s) \approx s^{-q_D} \implies \langle x^q \rangle = \infty, \ q > q_D \tag{1}$$

where s is a threshold of intensity with a tail exponent of critical order q_D. With respect to the scaling moment function the critical order $q_D > 1$ is the solution of $K(q_D; 1) = (q_D - 1)D$. The

exponent characterises the relative frequency of extreme events i.e. extremes are more frequent when the exponent q_D is smaller. This statistical behaviour is a consequence of the fact that the sum of the contributions is dominated by the strongest contribution; rare events have a dominant contribution ([19]).

3. Multifractal Behaviour Of Wind Velocity Shears

Over the past two years we have carried out two in-depth analyses of boundary-layer wind velocity data within a universal multifractal (UM) framework ([19]). Within this framework we consider that the wind shears scale as

$$\Delta u_\lambda \stackrel{d}{=} \varepsilon_\lambda^a \lambda^{-H}, \tag{2}$$

where $\stackrel{d}{=}$ denotes equal in distribution. Moreover, depending on whether the energy flux or the force variance flux is conserved one may consider that the buoyancy force variance flux, ϕ, plays the same role as the energy flux, ε, in 3D turbulence but only along the vertical:

$$\Delta u(\Delta x) \stackrel{d}{=} (\varepsilon(\Delta x))^{1/3}\Delta x^{1/3} \text{ and } \Delta u(\Delta z) \stackrel{d}{=} (\phi(\Delta z))^{1/5}\Delta z^{3/5}. \tag{3}$$

Within the UM framework the statistical moments of a given field are characterised with the help of a limited number of parameters: α, C_1, a and H. For a conservative field ($H = 0$) the scaling moment function reads as

$$K(q;a) = a^\alpha \frac{C_1}{\alpha - 1}\left(q^\alpha - q\right) \tag{4}$$

for $q < q_D$. In order to estimate the parameters α and C_1 we use the double trace moment method ([14] and [20] for a review). When the origin of the flux and hence its power, a, remains unknown, the estimate of C_1 absorbs the pre-factor and hence C_1 becomes slightly α-dependent.

The non-conservativeness parameter H is estimated through spectral analysis. The Fourier transform of the second-order-moment structure function yields the energy spectrum $E(\omega) \propto \omega^\beta$, where the scaling exponent $\beta = 2H + 1 - K(2;a)$. Note, using the first order structure-function will give the same result provided the same ranges of scales are used in the regression procedure.

Figure 3 displays log-log plots of the averaged u-component wind velocity spectra at 43m from the Corsica dataset. The Corsica dataset consists of high-resolution (10Hz) ultrasonic wind anemometer data taken over six-months. The measurements were taken at 22, 23 and 43m above the ground in a wind farm test site subject to complex terrain and buoyancy forces from the nearby sea. Very often, as in the Corsica dataset, only time-series measurements of the velocity are available from an anemometer in a fixed position r say. By Taylor's frozen turbulence hypothesis ([22]), if the mean wind, U, is much larger than the local fluctuations, u', we can consider $u(r, t + t') = u(r - Ut', t')$. Hence, the spectral exponent is still expected to be close to the Kolmogorov-Obukhov (KO) inertial range 5/3 value.

Figure 3a shows the average (over ten samples for each mean direction) of spectra for meteorological wind directions, θ_{met} = 9, 35, 62, 86, 116, 134, 162, 188, 210, 238, 260 and 281 degrees. The direction, θ_{met}, is where the wind is coming from with respect to true North e.g. 0° is North, 90° is East etc. Due to the effects resulting from the wakes of the turbine it was important to find a control sample from which to observe undisturbed scaling behaviour. Based on the spectra with the least amount of fluttering i.e. the least influence from the turbine (see figure 3 for details), the samples are then compared with even lower frequency spectra (see [6]). This is achieved by concatenating each individual sample (measured continuously over a day) into a larger continuous file. The largest concatenation consists of about 100 files giving a maximum ratio of scales, $\lambda = 2^{25}$ (figure 3b blue). The higher frequencies of the concatenated files have been removed to give a continuously scaling appearance.

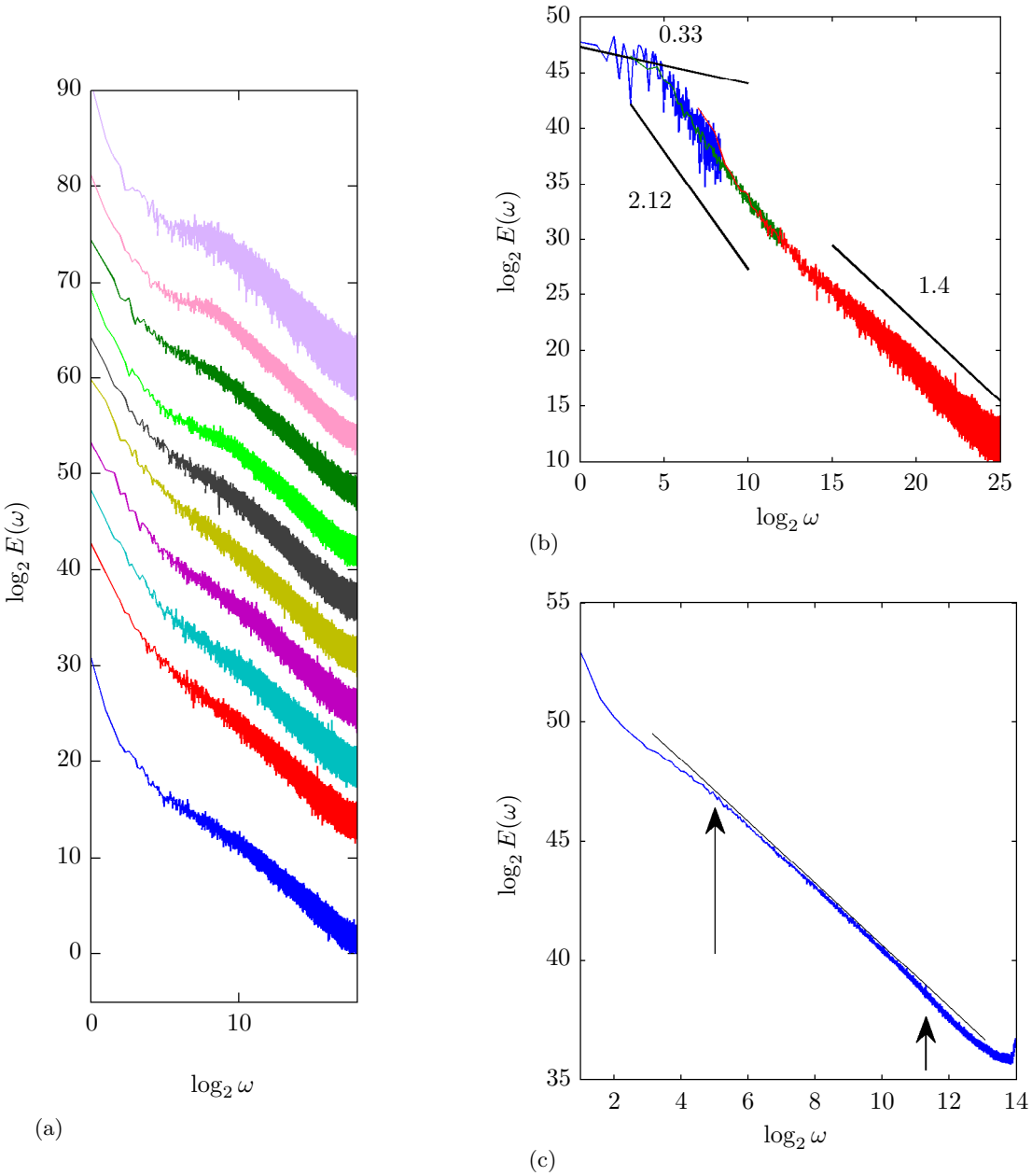

Figure 3: Plots of averaged u-component wind velocity spectra ($E_u(\omega)$) at a 43m height versus the normalised frequency, ω. The frequency is normalised such that $\omega = 2^N/\ell_n = \lambda/0.1$s, where $\ell_n = 2^n \times 0.1$s for $n \in [0 : N]$ and $N = 19$, 25 and 14 for (a), (b) and (c) respectively. (a) Spectra, $E_u(\omega)$, for meteorological varying wind directions (see text) shifted vertically for clarity from bottom to top; (b) The spectra assumed to have the least influence from the turbine (the second red plot) is compared with even lower frequency spectra achieved by concatenating each daily sample into a larger continuous file. The largest concatenation consists of about 100 files giving a maximum ratio of scales, $\lambda = 2^{25}$ (blue). The higher frequencies of the concatenated files have been removed to give a continuously scaling appearance; (c) Inversely each daily sample can be split into sub-samples and averaged in order to get smoother scaling over the higher frequencies. The slope of the line of best fit is 1.35.

Based on the pseudo-continuously scaling plot we can see there exist three distinct scaling sub-ranges. Over the lowest frequencies ($\log_2 \omega \in [0:5]$) of figure 3b we have a scaling exponent that is comparable with low frequency 'macro' weather (see [15]). This is then adjoined by an apparent BO scaling region over the frequencies $\log_2 \omega \in [5:12]$. And finally, for the frequencies $\log_2 \omega \in [12:25]$ we observe something close to KO scaling. Over this high frequency KO scaling sub-range the spectra are fairly noisy. We can improve the statistics over the higher frequencies in an inverse fashion to the concatenation for very low frequencies. That is, each daily sample can be split into sub-samples and the resulting spectra then averaged. Figure 3c displays the result of this procedure.

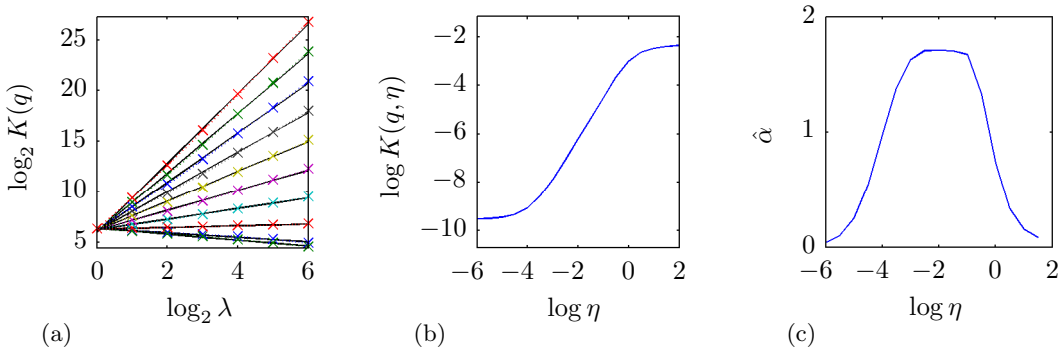

Figure 4: (a) Ensemble average of trace moments for $q = 1.5$ and $\log \eta \in [-6:2]$; (b) resulting double trace moment curve; (c) the local estimate $\hat{\alpha} = \Delta \log K(q,\eta)/\Delta \log \eta$, of α. The trace moments are estimated on the energy flux over the mid-frequency sub-range (the green plot from figure 3b) of the Corsica dataset. The parameters over these time-scales are: $\alpha = 1.67, C_1 = 0.56$ and $H = 0.64$.

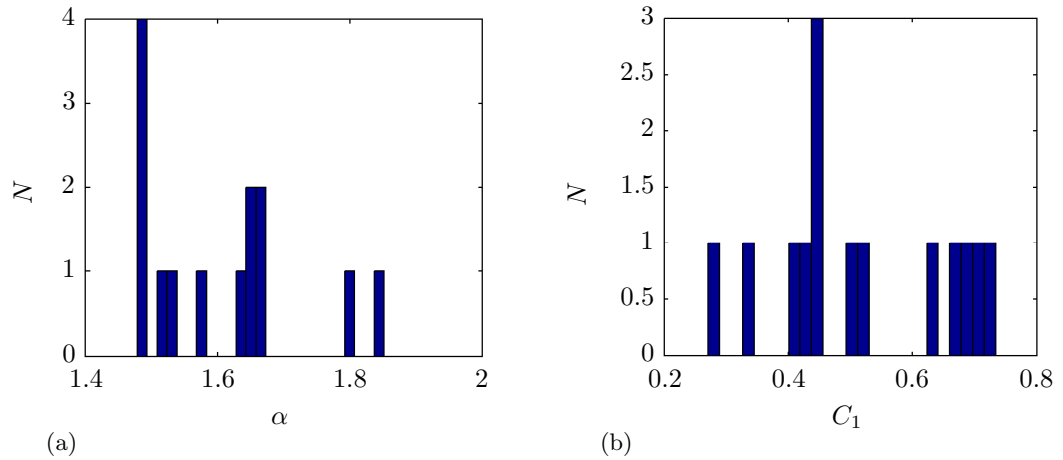

Figure 5: Distribution of UM parameters α (a) and C_1 (b) estimated on the energy flux of the Corsica dataset over the frequencies $\log_2 \omega \in [5:12]$. Estimates of $\alpha = 2$ and the corresponding C_1s have been removed leaving a total of 14 samples from 80.

Figures 4a, b and c show: the trace moments for $q = 1.5$ and $\log \eta \in [-6:2]$, the resulting double trace moment curve and the local estimate ($\hat{\alpha}$) of α, all estimated on the energy flux over the mid-frequency sub-range ($\log_2 \omega \in [5:12]$, see 3b) of the Corsica dataset. The trace

moments show the data scale well if the ensemble average are used. This gives an extended range of $\log \eta$ i.e. $\log \eta \in [-3 : -1]$ over which α is constant. The corresponding UM parameters are $\alpha = 1.67$ and $C_1 = 0.56$. Over the high-frequency range $\alpha = 1.66$ and $C_1 = 0.23$. Using equation 4 we get $H = 0.64$ over the mid-frequency range and $H = 0.23$ over the high-frequency range, with intermittency corrections $K(2; 1/3) = 0.16$ and 0.06 respectively (see equation 4).

Because the ensemble averaged trace moments give a more stable result we do not have error bars on the estimates. Figure 5 gives an idea of the dispersion of the individual estimates of the UM parameters.

Figure 6a displays a log-log plot of the averaged horizontal u-component spectra at 50m from the Growian dataset. The Growian experiment in Germany consisted of an array of cup anemometers recording horizontal wind speeds at 2.5Hz [13]. The array formed a grid of approximately 75 by 100m, with the lowest point being at 50m. This was comparable, in part, to the heights of the measurements taken in Corsica. However, due to the spatial distribution of the measurements, unlike in Corsica, we were able to test if the scaling laws were valid in space and in time [22]. For the Growian dataset the wind speed and direction are provided and the corresponding horizontal wind vectors are decomposed such that $u_x = u \cdot \cos\theta$ and $u_y = u \cdot \sin\theta$. For this study we selected a system of coordinates such that $\langle u_y \rangle = 0$ in order to impose 'mirror symmetry' as suggested in ([11]).

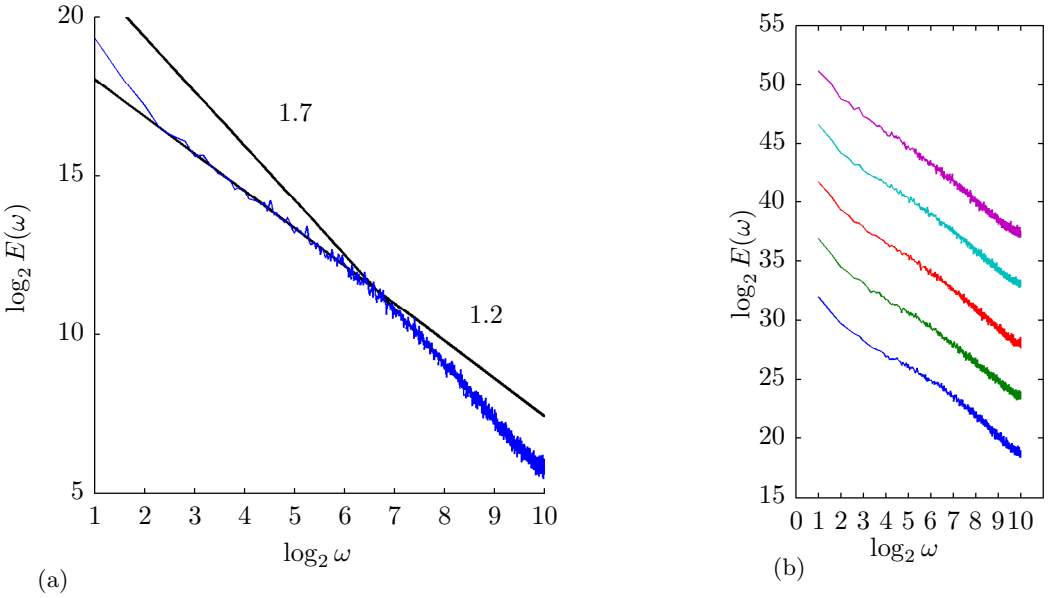

Figure 6: (a) Log-log plot of average horizontal wind speed spectra, $E_{u_x}(\omega)$, at 50m from the Growian dataset. The frequency is normalised such that $\omega = 2^N/\ell_n = \lambda/0.4$s, where $\ell_n = 2^n \times 0.4$s for $n \in [0 : N]$. The spectral slopes (black solid lines) are 1.2 over low frequencies ($\log_2 \omega \in [1 : 7]$) and 1.7 is over high frequencies ($\log_2 \omega \in [7 : 10]$); (b) Spectra of $E_{u_x}(\omega)$ at 50, 75, 100, 125 and 150m (from bottom to top [shifted for clarity]). Corresponding spectral slopes over higher frequencies are: 1.77, 1.58, 1.64, 1.56 and 1.51, and over lower frequencies are: 1.12, 1.24, 1.25, 1.28 and 1.39.

The velocity spectra exhibit scaling over two sub-ranges: approximately $\log_2 \omega \in [1 : 7]$ and [7:10]. Over the lower frequency sub-range there is a scaling exponent $\beta = 1.2$. Over the higher frequency sub-range the scaling exponent falls closer to homogeneous KO scaling with $\beta = 1.7$. The UM parameters over both low and high frequencies are the same i.e.: $\alpha \approx 1.8$ and $C_1 \approx 0.7$.

This gives an intermittency correction $K(2;1/3) = 0.18$ and therefore $H = 0.19$ and 0.44 over low and high-frequency sub-ranges respectively. The scaling of the spectra is consistent with that observed in [12] in which a -1 energy production scaling sub-range is adjoined by a KO scaling sub-range. Although this scaling behaviour is observable close to the ground we find with increasing height (figure 6b) the processes become mixed and the scaling exponents deviate from the two predicted adjoining sub-ranges.

4. Scaling Anisotropy And The Implications For The Torque Fluctuations

The Generalised Scale Invariance (GSI) approach posits scale invariance (scaling) as the main symmetry and then considers the remaining non-trivial symmetries. These symmetries are generally no longer isotropic (see [21] for details). The anisotropy exponent, H_z, measures the deviation of scaling laws (self-similarity) from isotropy between two directions. For example, when taking the horizontal and vertical shears of the horizontal wind, $H_z = H_h/H_v = C_{1,h}/C_{1,v} = 5/9$. The subscripts h and v correspond to two different scaling relations (equation 3). This corresponds to the multifractal 23/9-dimensional turbulence model.

When using time-series measurements, the dominant role of the vertical motion of large scale atmospheric structures may explain (e.g., [6]) why BO scaling becomes apparent over the range of corresponding frequencies. For the Corisca dataset we find that $H_h/H_v = 0.23/0.64 = 0.36$ and $C_{1,h}/C_{1,v} = 0.22/0.56 = 0.39$ which thus (indirectly) validates the anisotropic model of the wind shears (although with a lower anisotropy exponent $H_z = 0.4$). For the Growian dataset, since the co-dimension remains the same for all timescales when $\langle u_y \rangle = 0$, a much simpler model can be used in which only a modification of H is required. Indeed, the wind shears become about 0.43 times (i.e., $H_z = 0.19/0.44$) less convoluted over low frequencies.

Using dimensional analysis, the torque derivatives in time, t, which, as a first approximation, correspond to the derivatives in space, r, are the third power of the velocity increments i.e., $Q_t = [(u_t) \cdot r]_t = u_r^3$. This gives that the torque fluctuations will scale as the square of the velocity increments, $\Delta Q = (\Delta u)^2$, and hence, $\Delta Q \propto \varepsilon^{2/3}\ell^{2/3}$ according to equation 3a and $\Delta Q = \phi^{2/5}\ell^{6/5}$ according to equation 3b. Using the UM parameters estimated from the two sites we can then simulate the torque fluctuations.

In the context of the simulations the multifractality parameter remains the same however the non-conservativeness parameter increases two-fold. The mean co-dimension C_1 is modified by the pre-factor $(2a)^\alpha$. Figure 7 displays the resulting torque fluctuations.

Figures 7a and 7c correspond to the torque fluctuations resulting from an intermittent KO scaling velocity sub-range and a smoother sub-range (possibly a -1 power law energy production sub-range) respectively. Note that the deviations from the predicted scaling exponents in both cases suggests the processes are more complex, possibly mixed. Given the vertical scales in both plots are the same we can consider that both processes result in similarly strong variability of the torque increments, while the velocity increment variability is fully compatible with that displayed by figure 1.

Figure 7b corresponds to the torque fluctuations of a velocity field that appears to scale closer to a homogeneous KO 5/3s power law. From the estimates of C_1 and H we know however that again the processes are likely mixed between an 11/5s and 5/3s power law with intermittency corrections. We can hypothesise it is the mixing of such processes that gives the deviation of H_z from the predicted 5/9s. This less intermittent field is the result of an adjoining more convoluted sub-range predicted to follow an energy production sub-range.

The drastic qualitative difference of the variability displayed by figures 7a to 7d is mainly due to the difference of values of the exponent H. Indeed, its main role is to smooth out the field by precisely decreasing the field singularities by $-H$, i.e. dividing the spikes at resolution λ by a factor λ^H, when other UM parameters remain rather similar. This corresponds to a damping factor of $2^{8\times.9} \approx 2^7 = 128$, i.e. two orders of magnitudes, for figure 7d with respect to figure 7a.

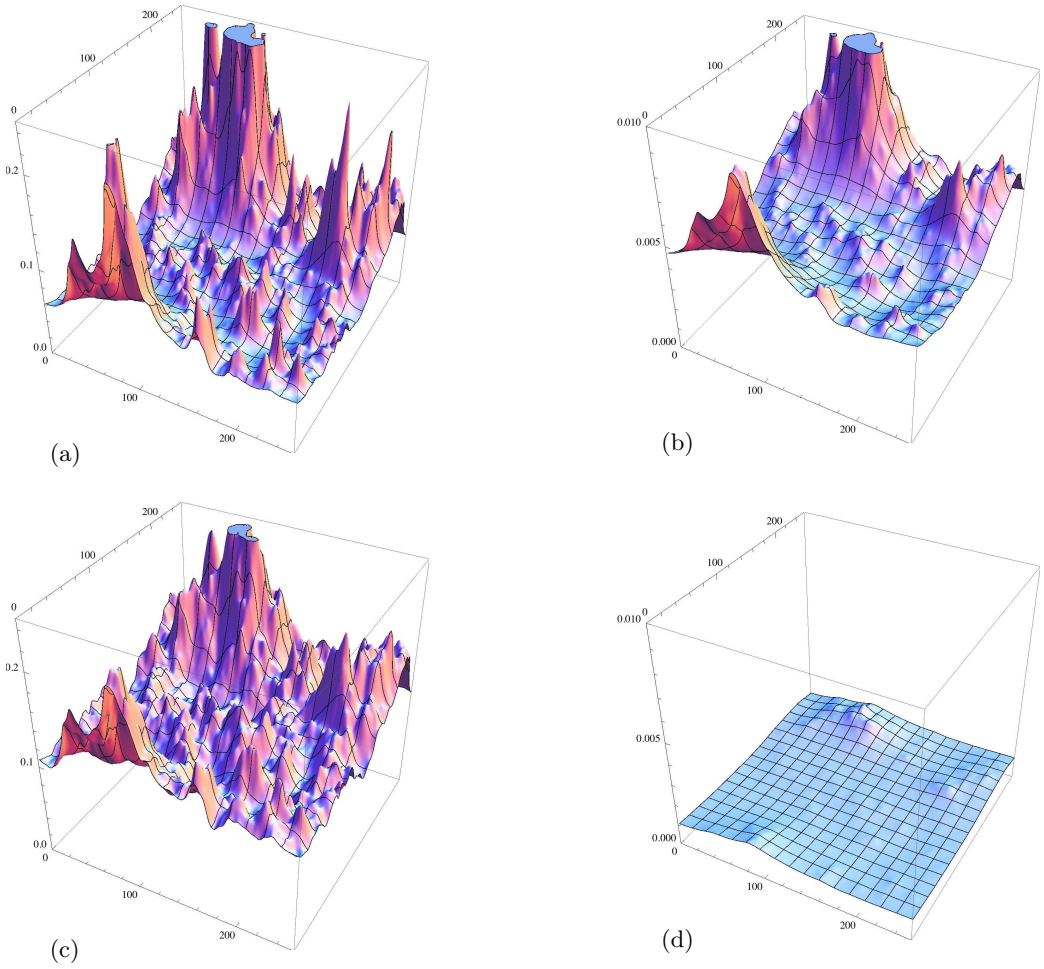

Figure 7: Two-dimensional (scalar) simulations of torque fluctuations, ΔQ, for a ratio of scales $\lambda = 2^8$. Plots (a) and (b) are simulated using the Growian dataset UM parameters for torque: $\alpha = 1.8$, $C_1 = 0.38$ and $H = 0.38$; $\alpha = 1.8$, $C_1 = 0.38$ and $H = 0.88$ respectively; and plots (c) and (d) are simulated using the Corsica dataset parameters for torque: $\alpha = 1.7$, $C_1 = 0.11$ and $H = 0.46$; $\alpha = 1.7$, $C_1 = 0.33$ and $H = 1.28$ respectively. Because the difference between the Hs is so large it was necessary to reduce the vertical scale in plots (b) and (d) by almost two orders of magnitude.

5. Concluding Remarks

Casting our minds back to figure 3a, for directions influenced by wind turbine wakes, there is a highly intermittent sub-range with a smoother spectral slope than KO that is followed by a less intermittent KO scaling sub-range (see [6] for more details). This suggests that there is an adjoining (high-frequency) range of time and therefore length-scales in which the strong velocity and therefore torque fluctuations can be smoothed depending on the process. The quantification of the effect of smoothing for different processes can be estimated with the help of the factor λ^{-H} for processes having rather similar other UM parameters. This reduction factor is also relevant for the estimation of the fatigue.

Finally, the probability tails of the Corsica dataset showed that the critical order above which statistical moments diverge is about $q_D = 6$. One of the consequences of the second order relation between the torque and the velocity increments is that for the torque fluctuations the critical

exponent is therefore twice smaller than that of the velocity fluctuations. This implies that for orders larger than three the empirical statistics will display larger and larger fluctuations with increasing sample size. Consequently standard statistical methods of analysis will underestimate the extremes.

6. Acknowledgments

The authors highly acknowledge the help of Joachim Peinke who facilitated the access to the Growian dataset and Eric Dupont and Luc Musson Genon who provided access to the data of the EDF wind farm in Corsica. Their illuminating discussions help to stimulate our research.

References

[1] Banta, R. M., Newsom, R. K., Lundquist, J. K., Pichugina, Y. L., Coulter, R. L., & Mahrt, L. (2002). Nocturnal low-level jet characteristics over Kansas during CASES-99. Boundary-Layer Meteorology, 105(2), 221252.

[2] Banta, R. M., Pichugina, Y. L., & Newsom, R. K. (2003). Relationship between low-level jet properties and turbulence kinetic energy in the nocturnal stable boundary layer. Journal of the atmospheric sciences, 60(20), 25492555.

[3] Bolgiano, R., Jr. (1959). Turbulent spectra in a stably stratified atmosphere. Journal of Geophysical Research, 64(12), 22262229.

[4] Finnigan, J. (2000). Turbulence in plant canopies. Annual Review of Fluid Mechanics.

[5] Fitton, G., Tchiguirinskaia, I., Schertzer, D., & Lovejoy, S. (2011). Scaling Of Turbulence In The Atmospheric Surface-Layer: Which Anisotropy? Journal of Physics: Conference Series, 318(7), 072008.

[6] Fitton, G., Tchiguirinskaia, I., Schertzer, D., & Lovejoy, S. (2011). The Anisotropic Multifractal Model and Wind Turbine Wakes. 7th PhD Seminar on Wind Energy in Europe, 115118.

[7] Fitton, G., Tchiguirinskaia, I., Schertzer, D., & Lovejoy, S. (2012) Wind Energy and the impact of turbulence on the conversion process. Euromech 528 proceedings (submitted).

[8] Hau, E. (2005). Wind turbines: Fundamentals, technologies, application, economics POD. 783 pp.

[9] Hunt, J., Leibovich, S., & Richards, K. J. (1988). Turbulent wind flow over smooth hills. QJR Meteorol Soc.

[10] Johnson, K. E. (2004). Adaptive torque control of variable speed wind turbines. Citeseer.

[11] Kader, B. A., & Yaglom, A. M. (1989). Spatial correlation functions of surface-layer atmospheric turbulence in neutral stratification. Boundary-Layer Meteorology.

[12] Katul, G., & Chu, C.-R. (1998). Boundary-Layer Meteorology, Volume 86, Number 2 - SpringerLink. Boundary-Layer Meteorology, 86(2), 279312. doi:10.1023/A:1000657014845.

[13] Korber, F., Besel, G., & Reinhold, H. (1988). Messprogramm an der 3 MW-Windkraftanlage GROWIAN: Forderkennzeichen 03E-4512-A. Forschungsbericht / Bundesministerium fur Forschung und Technologie, Nichtnukleare Energietechnik. Grosse Windenergieanlage Bau- u. Betriebsges.

[14] Lavalle, D., Lovejoy, S., Schertzer, D., & Schmitt, F. (1992). On the determination of universal multifractal parameters in turbulence. Topological aspects of the dynamics of fluids and plasmas, 463478.

[15] Lovejoy, S., Schertzer, D., & Varon, D. (2012). Do GCM's predict the climate. Or low frequency weather? EGU General Assembly.

[16] Moeng, C. H., & Sullivan, P. P. (1994). A comparison of shear-and buoyancy-driven planetary boundary layer flows. Journal of the atmospheric sciences.

[17] Monin, A. S., & Obukhov, A. M. (1959). Basic laws of turbulent mixing in the surface layer of the atmosphere. Contrib Geophys Inst Acad Sci USSR151, 24(151), 163187.

[18] Obukhov, A. (1959). Effect of Archimedean forces on the structure of the temperature field in a turbulent flow (Vol. 125, p. 1246). Presented at the Dokl. Akad. Nauk SSSR.

[19] Schertzer, D., S. Lovejoy, F. Schmitt, I. Tchiguirinskaia and D. Marsan (1997). "Multifractal cascade dynamics and turbulent intermittency." Fractals 5(3): 427-471.

[20] Schertzer, D., & Lovejoy, S. (2011). Multifractals, Generalized Scale Invariance and Complexity in Geophysics. International Journal of Bifurcation and Chaos, 21(12), 34173456.

[21] Schertzer, D., Tchiguirinskaia, I., Lovejoy, S., & Tuck, A. F. (2011). Quasi-geostrophic turbulence and generalized scale invariance, a theoretical reply. Atmos. Chem. Phys. Discuss, 11(1), 33013320. doi:10.5194/acp-12-327-2012

[22] Taylor, G. I. (1922). Diffusion by Continuous Movements. Proceedings of the London Mathematical Society, s2-20(1), 196212.

Scaling Anisotropy And Extremes In The Wake Of A Turbine

G. Fitton[a], I. Tchiguirinskaia[a], D. Schertzer[a] & S. Lovejoy[b]

a. *Université Paris Est, École des Ponts ParisTech, LEESU, 6-8 avenue B. Pascal, Cité Descartes, 77455, Marne-la-Vallée, France; tel. : +33 1 6415 3607, fax: +33 1 6415 3764*

b. *McGill University, Physics department, 3600 University street, Montreal, Quebec, Canada*

Résumé :

Dans cette étude, nous utilisons un repère tournant pour analyser l'anisotropie de la vitesse horizontale dans la couche de surface atmoshpèrique (SL). Cela nous permet de quantifier la dépendance angulaire de l'exposant de la loi d'échelle, souvent appelé exposant de Hurst. Les valeurs de cet exposant restent de façon générale conformes aux résultats publiés. Pour les échelles de temps supérieures à 10 secondes, les données de l'expérience Growian montrent une anisotropie scalante forte, qui décroît avec l'altitude. Nous mettons en évidence une expression analytique de la variation angulaire de l'exposant de Hurst, qui pilote la formation des extrêmes, y compris dans le sillage d'une turbine. Les cisaillements turbulents du vent peuvent être extrêmes au point que leur loi de distribution est une loi de puissance. Son exposant décroît lorsque l'anisotropie augmente, ce qui correspond à des extrêmes d'autant plus violents.

Abstract :

In this study we use a rotated frame of reference to analyse the anisotropy of the horizontal velocity in the atmospheric surface-layer (SL). This enables us to quantify the angular dependency of the scaling exponent, often called the Hurst exponent that overall remains consistent with surface-layer literature. For time-scales above 10 seconds, the data from the Growian experiment exhibits a strong, scaling anisotropy that decreases with height. We put forward an analytical expression for the angular variation of the Hurst exponent that determines the generation of wind shear extremes, including those in the wake of a turbine. Turbulent wind shears can be so extreme that their probability distributions follow a power law. The exponent of the latter decreases when anisotropy increases, this corresponds to wilder and wilder extremes.

Mots clefs : **Turbulence ; Anisotropy ; Extremes**

1 Introduction

Due to the massive worldwide expansion of wind energy production, as foreseen in the next decade [1], the number of wind farms there are and the number of turbines they consist of is rapidly increasing. The larger the wind farm, the greater the number of turbines subject to strong wake effects and, moreover, increased loads. In terms of modelling, this introduces additional complexities compared to a free inflow condition. There are two methods that are generally used to evaluate response time in wake operation : the method of equivalent turbulence intensity [2] and the dynamic wake meandering model [3]. Unfortunately both methods often underestimate extreme loads [4] since the results remain very sensitive to short-time, extreme fluctuations.

Within a scaling framework we can attempt to quantify the statistics of a given process across the scales. The main focus of the problem then becomes how to interpret scaling anisotropies through statistical scaling exponents as discussed in detail in [5]. Typically this has been done without the

mention of additional scaling changes and additionally extreme behaviours caused by the wake of the turbine (see [6] for discussion). For this study we will focus on the scaling anisotropies of the horizontal velocity components ; enabling us to better understand the complexity of the atmospheric surface-layer – as indicated by the variability of spectral exponents – and its consequences for extremes. The obtained results help to settle a more appropriate framework for future observations, analyses and flow simulations in and around the wake.

2 Spectral Look To The Data

For this study we will use the dataset that came from the Growian experiment [7, 8]. Two 150m masts were constructed 65m West-South-West of a 3MW wind turbine on flat, coastal terrain. Twenty cup anemometers were positioned at the heights 10, 50, 75, 100, 125 and 150m measuring wind speed and direction. The measurements were taken at 2.5Hz over twenty-minutes with 300 measuring runs done in total. Because the anemometers were positioned on booms, certain directions of the wind produced a shadow effect resulting in spurious spectral spikes over higher frequencies. Filtering the data such that the mean wind direction per twenty-minute sample was perpendicular to the masts removed the spurious effects but reduced the total number of samples to 225.

Due to the lack of a vertical velocity component in the Growian dataset we restrict our analyses to the horizontal components of the velocity. We define the horizontal velocity vector, $\boldsymbol{u}$, with components (u, v), that depend on the spatial coordinates, (x, y), of the position vector $\boldsymbol{r} = (x, y)$. In order to compare the scaling properties of the velocity components we use their energy spectrum, $E(\omega) = \|\mathcal{F}(\omega)\|^2$, where $\mathcal{F}$ is the Fourier transform of the required variable. If there is scaling, the spectra, in a log-log plot, will exhibit linear behaviour with a spectral slope β (see figure 1). The Hurst exponent can be defined by $H = (\beta - 1)/2$ and is the scaling exponent of the second-order structure function for $H \in [0 : 1]$. For spectral plots, the horizontal axes are normalised such that $\omega = 2^N/\tau_n$, where $\tau_n = 2^n \times 0.1\text{s}$ for $n \in [0 : N]$.

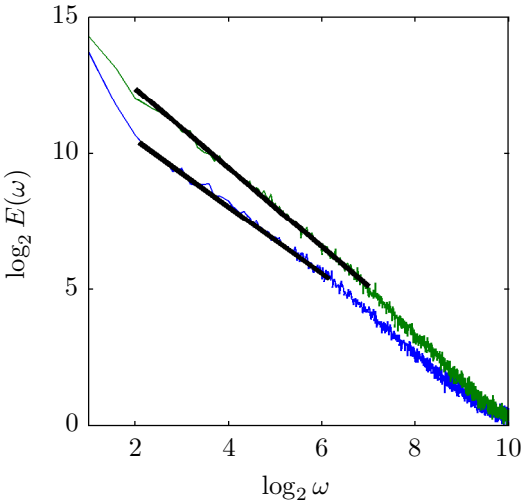

FIGURE 1 – Energy spectra of the velocity components u (blue) and v (green) for the Growian dataset. The corresponding spectral exponents for u over low and high frequency ranges respectively are 1.25 and 1.45 ; and for v are 1.45 and 1.70.

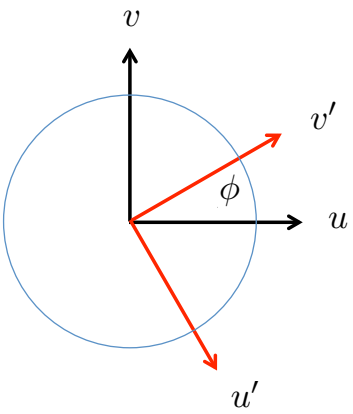

FIGURE 2 – Diagram showing a comparison between the initial two-dimensional Cartesian frame of reference R (black) with horizontal velocity vector components u and v and the rotated frame of reference $R'(\phi)$ (red) and its corresponding rotated velocities u' and v'.

For the Growian dataset the Cartesian wind components are not directly measured, but are easily obtained from the wind velocity modulus, $\tilde{u} = \|\boldsymbol{u}\|^2$, and the instantaneous angle θ with respect to a

fixed reference frame R :

$$u = \tilde{u} \cdot \cos(\theta) \text{ and } v = \tilde{u} \cdot \sin(\theta). \quad (1)$$

Figure 1 compares the scaling properties of the u and v components from the Growian dataset at 100m. Both components show two scaling sub-ranges : a small scale sub-range from 1 to 10 seconds and a larger scale sub-range from 10 seconds to 15 minutes. The scaling exponents for u over low and high frequency ranges respectively are 1.25 and 1.45 ; and for v are 1.45 and 1.7. There is no evidence of $\beta = 5/3$ as predicted by homogeneous isotropic turbulence contrary to the 'local isotropy' assumption. An assumption that has been commonly used in turbulence since Kolmogorov, and is often used for load simulations [9]. The relevance of this hypothesis to atmospheric turbulence has been brought into question numerous times, eventually leading to the birth of the concept of generalised scale invariance (GSI). GSI first posits scaling, not isotropy [10]. Statistical isotropy, i.e. $u \overset{d}{=} v$ (the symbol $\overset{d}{=}$ denotes equality in probability distribution), would correspond to rotational invariance of the statistics at all scales.

3 Scaling Anisotropy

The significant differences in spectral exponents on figure 1 correspond to a scaling anisotropy that is much stronger than a trivial anisotropy with a constant ratio of components different from unity. In order to quantify the scaling anisotropy (by means of the parameter H) we can rotate the frame of reference R by an angle ϕ giving the rotated frame of reference $R'(\phi)$ (see figure 2). We then compute the corresponding statistical exponents $H_u(\phi)$ and $H_v(\phi)$. This is in some way the inverse of the procedure typically performed in order to ensure isotropy, i.e. $E_u = E_v$ (see [11]).

The Cartesian components, defined through the direction and modulus, in a rotated reference frame $R'(\phi)$, are then simply given by $u'(\phi) = \tilde{u} \cdot \cos(\theta + \phi)$ and $v'(\phi) = \tilde{u} \cdot \sin(\theta + \phi)$. Since we are using the spectral exponent, β, to quantify statistical properties, it will be of interest to look at the analytical properties of the rotated vectors' energy spectra. The rotated time-dependent u-component and its Fourier transform are :

$$u'_\phi(t) = \cos(\phi)u(t) - \sin(\phi)v(t), \quad \widehat{u'_\phi}(\omega) = \cos(\phi)\hat{u}(\omega) - \sin(\phi)\hat{v}(\omega). \quad (2)$$

Considering now either the variance or the spectra of the field, their quadratic nature yields the following relations :

$$|u'_\phi(t)|^2 = \mathrm{Var}_\phi(t) = \cos^2(\phi)\mathrm{Var}_0(t) + \sin^2(\phi)\mathrm{Var}_{\pi/2}(t) - \sin(2\phi)\mathrm{Cov}_{u,v}(t), \quad (3)$$

$$|\widehat{u'_\phi}(\omega)|^2 = E_\phi(\omega) = \cos^2(\phi)E_0(\omega) + \sin^2(\phi)E_{\pi/2}(\omega) - \sin(2\phi)E_{u,v}(\omega), \quad (4)$$

where $\mathrm{Cov}_{u,v}$ is the covariance of u and v and, Var_0 and $\mathrm{Var}_{\pi/2}$ are the variances of u and v respectively ; $E_{u,v}$ is the co-spectrum and, E_0 and $E_{\pi/2}$ are the spectra of u and v respectively.

When the two velocity components u and v are identically distributed, but not independent, equations 3 and 4 become $\mathrm{Var}_\phi = \rho(\phi)\mathrm{Var}_0$ and $E_\phi = \rho(\phi)E_0$, where the correlation function $\rho(\phi)$ depends on r, the the correlation coefficient of u and v :

$$\rho(\phi) = 1 - r\sin(2\phi), \quad (5)$$

Equations 3-4 correspond to a given anisotropy of the velocity field u. This anisotropy becomes a scaling anisotropy if we consider, instead of the velocity field itself, similar relations for the singularities, $\gamma = \log_\lambda u$, where λ is the ratio of the total sample length and the time-scale of observation.

If we consider the same rotations for the singularities the equivalent equation to equation 3 readily holds for the (misnamed) log-normal model and therefore for the scaling exponent of the moment of order two, i.e., $K_\phi(2) = \rho(\phi)K_0(2)$. For the more general, universal multifractal (UM), case, the mathematics are more involved and will be discussed in detail elsewhere. We can however mention that the generalisation will lead to :

$$K_\phi(q) = \rho(\phi)K_0(q), \quad (6)$$

when considering the full hierarchy of multifractal singularities. Note that the UM scaling moment function $K_\phi(q)$ statistically describes the intermittency of atmospheric flows. Then from the above equation, this intermittency increases with $\rho(\phi)1$.

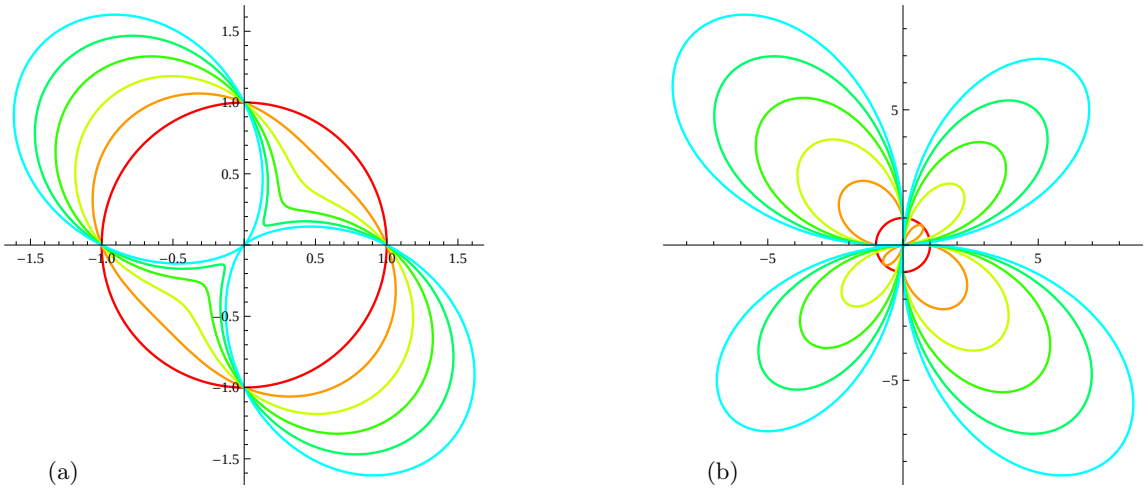

FIGURE 3 – (a) Plots of the function $\rho(\phi)$ in polar coordinates $(\rho, -\phi)$ for the correlation coefficient r. The coefficient is increased in increments 0.2 from $r = 0$ (red) to $r = 1$ (turquoise). The red circle corresponds to the isotropic case of independent identically distributed variables ; (b) The same as in (a) but for r being increased in increments 2 from $r = 0$ (red) to $r = 10$ (turquoise).

As expected in the isotropic turbulence model the scaling exponent will remain the same for varying ϕ. Figure 3a shows the continuous squeezing of the isotropic, circular structures due to an increase of the correlation coefficient (see equation 5) in the case of identically distributed, but not independent, singularities γ of the velocity field u. Note, the transformation $r \to -r$ only rotates the set of figures by $\pi/2$. On the contrary a stronger correlation with $r > 1$ doubles the amount of the structure squeezing (for figure 3b). For very large r the difference in the size of the sub-structures vanishes. This could be mimicked by doubling the periodicity of the process with $r = 1$ and re-normalising the results. This kind of scaling anisotropy is empirically visible within the Growian data.

4 From The Scaling Anisotropy To Wind Shear Extremes

The scaling exponents have been estimated on the Growian data over the (larger) scales, 10 seconds to 5 minutes ($\log_2 \omega$ from 2 to 6). Figure 4 displays the scaling exponents H_u and H_v as a function of the rotation, ϕ, of the frame of reference. Each plot (from left to right and from top to bottom from the figure 4a) corresponds to an increasing height : 10, 50, 75, 100, 125 and 150m. Note, these exponents represent statistically averaged estimates over all the data samples. The black solid line corresponds to the scaling exponent expected in the isotropic homogeneous case i.e. $H = 1/3$. The increasing values of H_u and H_v with height are, although well below the exponent predicted for homogeneous turbulence, consistent with other literature (see for example [11]). What is of particular interest is the clearly decreasing anisotropy between exponents with height. At 10m (top left) we see the scaling exponents exhibit the largest (relative) difference. The anisotropy exhibits symmetries consistent with the symmetries of equation 4. At 150m (bottom right) it is rather clear that with the addition of another 100m in height the scaling exponents would become isotropic to a point. Note, even though the scaling exponent is isotropic it remains far from being homogeneous. This is due to strong intermittency corrections assimilated into the estimation of H that make them differ from the expected $H = 1/3$!

Filtering the data by the mean wind direction per twenty-minute sample was useful to obtain the average statistical estimates of the scaling exponents. Over the time-scales 10 seconds to 5 minutes, this mean direction is rarely representative due to very strong small-scale wind fluctuations. This implies that the average scaling exponents represent a mixed process between undisturbed and disturbed

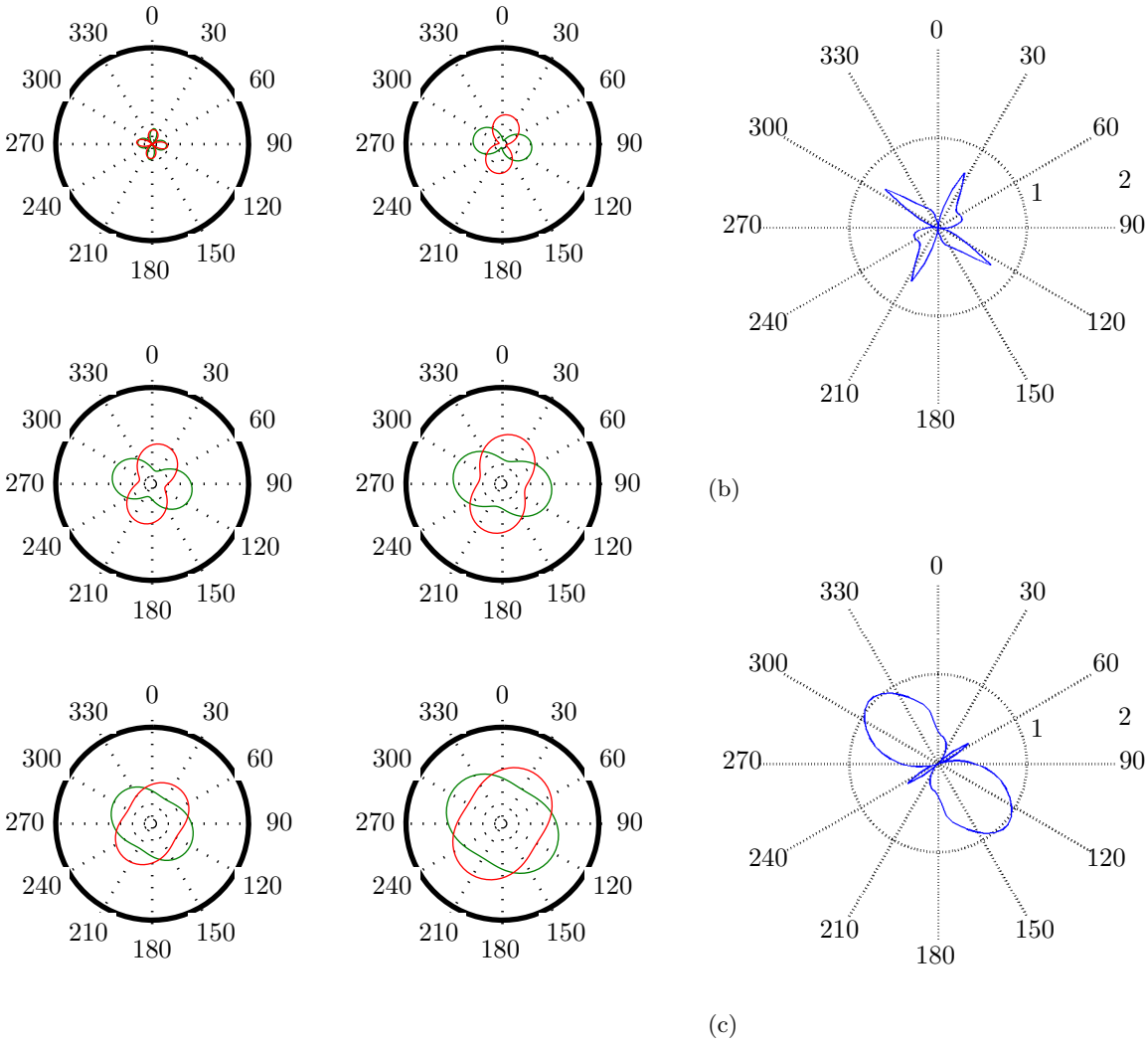

FIGURE 4 – (a) Plots of H_u (red) and H_v (green) versus ϕ at 10, 50, 75, 100, 125 and 150m from left to right and from top to bottom. The black solid line corresponds to $H = 1/3$.

(within the wake) flows. To get an idea of how the scaling anisotropy differs in and out of the wake, we selected two individual data samples at 50m for which the mean wind direction remains perpendicular to the masts and corresponds to two opposite inflow conditions. The results displayed in figures 4 b and c, demonstrate that although the estimates of scaling exponent for individual samples naturally differs from the average statistics, the flow within the wake is marked by a much stronger scaling anisotropy with $r \gg 1$. An anisotropy this strong modifies the extreme loads, bringing into question the many traditional isotropic methods in use at the moment.

Turbulent wind shears can be so extreme that their probability distributions follow a power law at all scales providing there are sufficient data. The exponent of the power law, q_D, is the critical exponent of the divergence of moments [5]. It is the critical exponent because the statistical moments of order q_D are theoretically finite and can be estimated with the help of standard statistical methods. For orders $q > q_D$ the theoretical moments are infinite and their empirical estimates are both random and sample size dependent. The velocity measurements taken during the Growian experiment yield multiple data samples exhibiting the aforementioned divergence of moments. We found that if q_D is observable in the data sample, the multifractal intermittency could be difficult to estimate. This corresponds to the

fact that exponent of the power law, q_D, is defined by :

$$K_0(q_D) = D(q_D - 1), \tag{7}$$

where D corresponds to the Euclidean dimension of the isotropic data. Equation 6 indicates that the scaling anisotropy with $\rho(\phi) > 1$ increases the initial intermittency $K_0(q_D)$, or equivalently it reduces the dimension D that defines the exponent q_D. The latter implies that extremes are concentrated on much smaller fractions of the space in statistically anisotropic flows. This significantly complicates their detection and quantification by traditional statistical methods.

5 Conclusions

In this work we have discussed the component-wise scaling properties of the horizontal velocity in the atmospheric surface-layer. Using the Growian dataset, scaling anisotropy was observed over the time-scales 10 seconds to 5 minutes, and analytically framed. Over these time-scales, the anisotropy decreases with height. Preliminary findings suggest that when $\rho(\phi) > 1$ the scaling anisotropy increases the turbulent wind shear extremes. To precisely define the relation between the extremes and the scaling anisotropy, a general UM framework is required. This is out of the scope of this publication. Furthermore, we need to analyse the full hierarchy of multifractal singularities to estimate the mean intermittency, as well as that of the extremes, i.e. the multifractality of intermittency. Our future work will therefore focus on the determination of the UM parameters of the fields.

Since our measurements are well within the surface-layer we can expect that the instability of the atmosphere will contribute significantly to anisotropic changes in shear stresses (see [11]). An in-depth study of this question is indeed another interesting scientific perspective. In fact, the component-wise scaling anisotropy inspires many questions that could be answered through better observations, multifractal analyses and simulations in and around the wake.

Acknowledgements This study was supported by the EU-INT WAUDIT project.

Références

[1] S Gsänger. World Wind Energy Report 2010, in. *World Wind Energy Association*, 2010.

[2] S T Frandsen. Turbulence and turbulence-generated structural loading in wind turbine clusters. 2007.

[3] Kenneth Thomsen and Helge Aagaard Madsen. A new simulation method for turbines in wake applied to extreme response during operation. *Wind Energy*, 8(1) :35–47, 2004.

[4] K Thomsen, H A Madsen, G C Larsen, and T J Larsen. Comparison of methods for load simulation for wind turbines operating in wake. *Journal of Physics : Conference Series*, 75(1) :012072, August 2007.

[5] Shaun Lovejoy and Daniel Schertzer. *The weather and Climate : emergent laws and multifractal cascades*. Cambridge University Press, 2013.

[6] G Fitton, I Tchiguirinskaia, D Schertzer, and S Lovejoy. The Anisotropic Multifractal Model and Wind Turbine Wakes. *7th PhD Seminar on Wind Energy in Europe*, pages 115–118, 2011.

[7] Friedrich Körber, Günter Besel, and Hans Reinhold. *Meßprogramm an der 3 MW-Windkraftanlage GROWIAN : Förderkennzeichen 03E-4512-A*. Große Windenergieanlage Bau- u. Betriebsges., 1988.

[8] H Günther and B Hennemuth. Erste Aufbereitung von flächenhaften Windmessdaten in Höhen bis 150m. *Deutscher Wetter Dienst, BMBF-Projekt A*, 329372 :1998, 1988.

[9] Jakob Mann. Wind field simulation. *Probabilistic engineering mechanics*, 13(4) :269–282, 1998.

[10] D Schertzer and S Lovejoy. Generalised scale invariance in turbulent phenomena. *PhysicoChemical Hydrodynamics*, 6 :623–635, January 1985.

[11] P Drobinski, P Carlotti, R K Newsom, R M Banta, R C Foster, and J L Redelsperger. The structure of the near-neutral atmospheric surface layer. *Journal of the atmospheric sciences*, 61(6) :699–714, 2004.

Programs

function used to calculate the double trace moments

```
% input arguments:
% - flux should be of length 2^n
% - the double structure function (DSF) requires only flux = dU.

function [phi] = DTM(q,eta,flux)

L = length(flux);

phi = zeros(log2(L),numel(q),numel(eta));

[m,n] = size(flux);

if m > n
  flux = flux';
end

for i = 1:(log2(L)+1)

  % calculate (normalised) psuedo flux
  flux_prime = bsxfun(@power,abs(flux),eta');
  flux_prime = bsxfun(@rdivide,flux_prime,mean(flux_prime,2));

  % calculate the trace moments of the psuedo flux
  phi(i,:,:) = mean(bsxfun(@power,permute(flux_prime,[3 1 ...
      2]),q'),3);

  % upscale/downgrade the flux
  flux_odd = flux(1:2:(end-1));
  flux_even = flux(2:2:end);

  flux = (flux_odd+flux_even);
  flux = flux./2;

end
```

function used for fractional integration

```
% input arguments:
% - u is variable to be convoluted (of length 2^n)
% - pow is the exponent of the k-vector
% - f0 is the highest frequency measurement

function [phi] = frac_flux(u,pow,f0)

  m = length(u);          % Window length
  n = pow2(nextpow2(m));  % Transform length
  y = fft(u);             % DFT
  f = (0:n-1)*(f0/n);     % Frequency range

  trans_vec = ([f(1:end/2) f(end/2:-1:1)]).^(pow);

  % needed for negative powers as spurious values occur at ...
     k_0 and k_N
  trans_vec(end) = trans_vec(end-1);
  trans_vec(1) = trans_vec(2);

  Y = y'.*trans_vec;

  u = (ifft(Y));

  phi = abs(real(u));

end
```

function used to optimise h

```
% arguments:
% - u is the variable to be operated on (length = 2^n)
% - H_vec is the range of values of convolution
% - f0 is the highest measured frequency
% - q and eta should be scalar

function [H] = optimise_h(u,H_vec,f0,q,eta)

L = log2(length(u));

temp = zeros(1,length(H_vec));

for i = 1:length(H_vec)

  [flux] = frac_flux(u,H_vec(i),f0);

  [dtm] = DTM_fastest(q,eta,flux);

  [p] = polyfit(1:L,log2(dtm),1);
    y = polyval(p,1:L);
      R = mean(abs(log2(dtm)-y));

  temp(i) = R;

end

[~,b] = min(temp);

H = H_vec(b);
```